DISSERTATION

PHOTOELECTROCHEMICAL CELLS EMPLOYING MOLECULAR LIGHT-HARVESTING MATERIALS FOR THE CAPTURE AND CONVERSION OF SOLAR ENERGY

Submitted by

Joel Thomas Kirner

Department of Chemistry

In partial fulfillment of the requirements

For the Degree of Doctor of Philosophy

Colorado State University

Fort Collins, Colorado

Spring 2017

Doctoral Committee:

Advisor: Richard G. Finke

Melissa Reynolds
Alan Van Orden
Walajabad Sampath

ABSTRACT

PHOTOELECTROCHEMICAL CELLS EMPLOYING MOLECULAR LIGHT-HARVESTING MATERIALS FOR THE CAPTURE AND CONVERSION OF SOLAR ENERGY

Solar light has the potential to be a substantial contributor to global renewable energy production. The diffuse nature of solar energy requires that commercially viable devices used to capture, convert, and store that energy be inexpensive relative to other energy-producing technologies. Towards this end, photoelectrochemical cells have been the subject of study for several decades. Particularly interesting to chemists, molecular light-harvesting materials can be employed in photoelectrochemical cells. For example, a dye-sensitized solar cell (DSSC) is a type of photoelectrochemical cell designed to capture solar energy and convert it to electricity. Alternatively, molecular light-harvesting materials have also been employed in water-splitting photo*electrolysis* cells (PECs), which capture solar energy and store it in the form of chemical bonds such as H_2 and O_2.

The work presented in this dissertation falls into two major projects. The first involves fundamental studies of water-oxidizing PECs employing a novel perylene diimide molecule as the light-harvesting unit. Background is provided in Chapter II, composed of a comprehensive literature review of water-oxidizing PEC systems that employ light-harvesting materials composed of earth-abundant elements. Chapter III describes preliminary studies of a water-oxidizing PEC composed of a perylene diimide organic thin-film (OTF) and cobalt oxide catalyst, the first of its kind in the literature. Characterization of this novel device provided knowledge of the efficiency-limiting processes that would need to be addressed in order to

improve device performance. Subsequently, Chapter IV describes preliminary studies of the same perylene diimide molecule in an alternative, literature-precedented, dye-sensitized photoelectrolysis cell (DS-PEC) architecture aimed at improving the efficiency-limiting processes of the first OTF-PEC. Characterization of this DS-PEC architecture reveals that the efficiency-limiting processes of the OTF-PEC were indeed improved. However, deposition of the cobalt oxide catalyst onto the DS-PEC did not successfully result in water oxidation. Alternative catalyst-deposition strategies from the literature are described as direction for future studies.

The second project of this dissertation involves the study of novel high-redox-potential organometallic cobalt complexes as redox mediators in DSSCs, and is presented in Chapter V. Therein, it was found that the use of electron-withdrawing functional groups on cobalt-coordinating ligands not only increased the redox potential, but also increased the lability of the ligands. The resulting complex instability caused performance-limiting electron-recombination reactions in assembled DSSCs. These results point future researchers towards the study of higher-chelating ligands for enhanced stability in high-potential cobalt complexes.

ACKNOWLEDGEMENTS

I would like to thank my research co-advisors, Prof. Richard Finke and Prof. C. Michael Elliott, for their scientific tutelage throughout graduate school. I would not be the chemist I am today without their guidance. I acknowledge my supporting group of colleagues, classmates, and friends who have helped to make this phase of life an adventure, not monotony. Last, but certainly not least, I would like to thank my wife Anna for her patience and support through the long years of graduate school.

TABLE OF CONTENTS

I. INTRODUCTION

This dissertation follows a "journal's format" where each chapter is a manuscript that has been prepared for, submitted for, or accepted for publication in a peer-reviewed scientific journal. Therefore, each chapter follows the formatting guidelines for its respective journal. For manuscripts that were submitted with Supporting Information, those materials are added at the end of their respective chapters. Dissertation chapters are not presented in historical order of journal submission, but instead they have been arranged into two main projects, both of which involve the study of photoelectrochemical cells employing molecular light-harvesting materials for the capture and conversion of solar energy. The main project involves the study of photoelectrochemical anodes for the capture of solar energy and its conversion to chemical energy by performing photocatalytic water oxidation (Chapters II–IV). A secondary project involves the study of dye-sensitized solar cells for the capture of solar energy and its conversion to electrical energy (Chapter V). In order to compile a cohesive dissertation document, the following sections have been added: (i) this Chapter I Introduction, (ii) brief connecting footnotes at the beginning of Chapters II–V, and (iii) a Chapter VI Summary at the end of the document. Chapters II–VI are briefly described below.

Chapter II serves to provide important background material and to place the original work of this dissertation in the context of known literature. The chapter contains a comprehensive literature review of water-oxidizing photoelectrolysis cell (PEC) systems that employ light-harvesting materials composed of earth-abundant elements. This manuscript was formatted for the journal *Energy & Environmental Science*, and was submitted for review on February 16, 2017 (Kirner, J. T.; Finke, R. G. *Energy Environ. Sci.* **2017**, Submitted). The review consists of: (i) an

Introduction section describing important background of light-driven water-splitting strategies, various water-splitting PEC configurations, a justification for the focus on organic light-harvesting materials, properties that distinguish organic semiconductors from inorganic semiconductors, and the two major device architectures for water-oxidizing photoanodes in the literature that are composed of organic light-harvesting materials; (ii) a summary of the major performance metrics by which literature PEC systems will be compared; (iii) detailed reviews of published water-oxidizing PEC systems employing an organic thin-film architecture; (iv) detailed reviews of published water-oxidizing PEC systems employing a dye-sensitized metal oxide architecture; and (v) a Summary and Outlook section.

Chapter III describes preliminary studies of a water-oxidizing PEC composed of a perylene diimide organic thin-film (OTF) and cobalt oxide catalyst, the first of its kind in the literature. This chapter was published in the journal *ACS Applied Materials & Interfaces* (Kirner, J. T.; Stracke, J. J.; Gregg, B. A.; Finke, R. G. *ACS Appl. Mater. Interfaces* **2014,** *6*, 13367–13377. http://pubs.acs.org/doi/full/10.1021/am405598w). The study details the preparation and characterization of our prototype photoanode. Characterization provided knowledge of the efficiency-limiting processes that will be addressed in attempts to improve device performance in the following chapter.

Chapter IV describes preliminary studies of the same perylene diimide molecule in an alternative dye-sensitized photoelectrolysis cell (DS-PEC) architecture. This architecture was chosen in order to improving the efficiency-limiting processes that were determined in Chapter III for the OTF architecture. This manuscript has been prepared for submission to the journal *ACS Applied Materials & Interfaces* (Kirner, J. T.; Finke, R. G. *ACS Appl. Mater. Interfaces* **2017**, to be submitted). Characterization of the DS-PEC architecture reveals that the efficiency-limiting

processes of the OTF-PEC were indeed improved. However, deposition of the cobalt oxide catalyst onto the DS-PEC did not successfully result in water oxidation. Alternative catalyst-deposition strategies from the literature are described as direction for future studies.

Chapter V describes work done on a secondary project focused on dye-sensitized solar cells (DSSCs) for solar energy capture and conversion to electricity. Rather than focusing on the light-harvesting dye, this project focused on the use of organometallic cobalt complexes as alternative redox mediators designed to increase the voltage (and therefore the power output) of DSSCs. This project was carried out under the direction of co-advisor Prof. C. Michael Elliott. The manuscript was completed after Prof. Elliott's untimely death, and was published in *The Journal of Physical Chemistry C* (Kirner, J. T.; Elliott, C. M. *J. Phys. Chem. C* **2015**, *119*, 17502–17514. http://pubs.acs.org/doi/full/10.1021/acs.jpcc.5b02513). The results from this project demonstrated that the use of electron-withdrawing functional groups on cobalt-coordinating ligands successfully increased the complexes' redox potentials, but also increased the lability of the ligands. The resulting complex instability caused performance-limiting electron-recombination reactions in assembled DSSCs. These results point future researchers towards the study of higher-chelating ligands for enhanced stability in high-potential cobalt complexes.

Chapter VI summarizes the results from both main projects described in this dissertation. The results and conclusions from each study are combined with literature knowledge to predict the most impactful future directions for each project.

II. WATER-OXIDATION PHOTOANODES USING ORGANIC LIGHT-HARVESTING MATERIALS: A REVIEW[i]

Overview

Solar energy storage by photoelectrochemical water splitting has garnered significant research attention in recent years. While the majority of water-splitting systems are composed of inorganic semiconductor light-harvesting materials, an increasing amount of research has studied the use of earth-abundant organic semiconductors and dyes as an inexpensive alternative. Herein, we provide a comprehensive review of published water-oxidizing photoanodes which employ organic light-harvesting materials, including both organic thin-film and dye-sensitized photoelectrochemical cell architectures. We highlight the different materials that have been employed, summarize recent advancements, and provide insights for future improvements of device efficiencies and stabilities.

2.1 Introduction

Meeting mankind's thirst for sustainable energy is one of the scientific grand challenges of our time.[1–4] The harvesting of sustainable solar energy and its conversion into useful electricity or heat is one promising strategy.[1,3] However, solar energy is diffuse, making it challenging to collect efficiently. Furthermore, solar energy is not always available on demand due to the diurnal cycle of the sun and intermittent cloud cover. Therefore, there is a need to efficiently store solar energy

[i] This chapter provides important background material and places the original work of this dissertation in the context of the known literature. It also includes a brief description of the work that is detailed in Chapter III. A version of this manuscript has been submitted for publication to the journal *Energy & Environmental Science* (Kirner, J. T.; Finke, R. G. *Energy Environ. Sci.* Submitted February 16, 2017). A list of abbreviations is provided at the end of this dissertation.

when it is available so that the energy can be used when needed. The conversion of solar energy into solar fuels can be achieved by artificial photosynthetic water splitting, which includes the steps of light capture, charge separation, water-oxidation catalysis (WOC), and CO_2 or proton-reduction catalysis.[4–10] In this way, solar energy is stored in the chemical bonds of the hydrogen and oxygen products of the water splitting reaction, and these molecules can be stored until their energy is needed. The energy can then be released as heat by combustion, or as electricity in a fuel cell.[3,8]

The two half cells that make up the water splitting reaction are the hydrogen-evolving reaction (HER) and the oxygen-evolving reaction (OER) (eqs 2.1 and 2.2, respectively). The OER

$$2H^+ + 2e^- \rightarrow H_2 \quad (2.1)$$

$$H_2O \rightarrow \tfrac{1}{2}O_2 + 2H^+ + 2e^- \quad (2.2)$$

$$H_2O \rightarrow H_2 + \tfrac{1}{2}O_2 \quad (2.3)$$

requires the reaction of two water molecules with four hole equivalents to form O_2, and is well-established to be the kinetic bottleneck of water-splitting catalysis.[10] Hence, the OER takes on additional importance and significance in energy storage research. The net electrochemical water-splitting reaction (eq 2.3) stores 237 kJ per mole of H_2,[4,6,7,10] which corresponds to an electromotive force for the cell reaction, E_{rxn}, of −1.23 V by the equation $\Delta G = -nFE_{rxn}$,[11] where n is the number of electrons transferred (n = 2 in eq 2.3) and F is Faraday's constant. According to the Plank–Einstein relation ($E = hc/\lambda$, where E is photon energy, h is Plank's constant, c is the speed of light, and λ is the photon wavelength)), the energy (1.23 eV) required to transfer an electron from half cell (2.2) to (2.1) can be provided by electromagnetic radiation with wavelengths smaller than ~1010 nm. However, electron–hole recombination reactions and concentration gradients during these multiple-electron reactions often necessitate ≥400 mV of overpotential beyond the thermodynamic limit of 1.23 eV in order to maintain the reactions at reasonable rates,[12] even in the presence of efficient catalysts. As a result, the energy required to perform water splitting is

often at least 1.6 eV,[1,12] corresponding to light with wavelengths ≤ 775 nm. Fortunately, this wavelength range includes ~60% of the incident solar power at the earth's surface, as calculated from the air mass 1.5 global (AM1.5G) solar reference standard (ASTM G173-03).[13] Therefore, light-driven water splitting is a promising strategy to help mankind meet its energy needs.

Light-Driven Water-Splitting Strategies. Solar energy storage through light-driven water splitting can be achieved by a number of strategies,[6,7,10,14] three of which are depicted in Fig. 2.1 in order to clarify the focus of this review. Perhaps the easiest method to conceptualize is simply to wire a p–n junction photovoltaic (PV) device (or multiple PV cells in series, to provide sufficient voltage) to a commercial electrolyzer (Fig. 2.1, left). Alternatively, light-driven water splitting can be accomplished by an integrated *photoelectrochemical* cell (Fig. 2.1, center), wherein the light-collecting panel (a single-bandgap semiconductor (SC) film, a PV film, or multiple SC or PV films integrated together) is submerged directly in aqueous solution. In this strategy, the water-splitting half reactions to produce H_2 and O_2 occur directly at the semiconductor–liquid junction (SCLJ). A third strategy is to prepare the light-harvesting materials as tiny particulates to be suspended in solution as a colloid (Fig. 2.1, right). Such *photocatalytic*

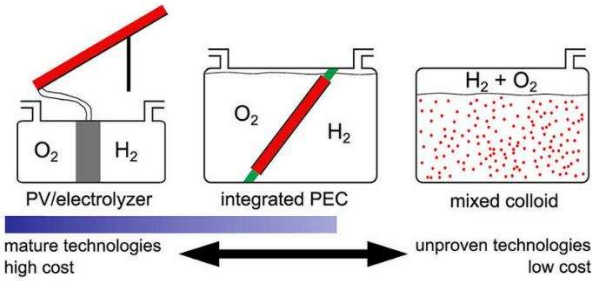

Fig. 2.1 Schematic diagrams of various water splitting engineering strategies: (left) a photovoltaic (PV) cell (or multiple cells in series) wired to an electrolyzer; (center) a submerged (integrated) photoelectrolysis cell (PEC) wherein water-splitting reactions occur at the surface of a semiconductor panel in solution; (right) a suspended colloid (photocatalytic) system wherein water-splitting reactions occur at the surface of semiconductor particles throughout solution. Reprinted with permission from Ref. 14. Copyright 2014, American Chemical Society.

(suspended colloid) systems generate H_2 and O_2 at the SCLJ throughout the bulk of the solution, often within the same compartment.

While the PV/electrolyzer strategy is well-established, it has been proposed[7,10,14] that the strategy will remain too costly for broad commercialization because of the need for (historically) relatively expensive solar power, the use of noble metal water-splitting catalysts, and because of the costs associated with wiring the devices together. However, recent work has focused on lowering the costs of PV/electrolyzer systems by employing inexpensive organic solar cells in series[15] or triple-junction configurations.[16,17] A recent 2016 study has also demonstrated a PV/electrolyzer system composed entirely of inexpensive, earth-abundant inorganic materials, and which is capable of 14.2% solar-to-hydrogen efficiency[18] (above the threshold for practical commercialization of 10%).[7]

The photoelectrochemical strategy (the focus of this review) has the advantage of avoiding the costs associated with wiring the PV and electrolyzer together, but has the added challenging requirement that the light-harvesting cell must be stable against photo-corrosion under harsh water-splitting conditions.[6,19,20] A promising strategy to protect the light-absorbing semiconductor against photo-corrosion is to coat the material with thin layers of metal oxide or metal catalysts.[6,7,10] On the other end of the spectrum, the photocatalytic (colloidal) strategy shows promise for low cost, but has yet to be demonstrated on a large scale. A number of review articles have highlighted the strategies and materials used in photocatalytic water-splitting systems.[21–26]

Published analyses have compared the promise and challenges of the photocatalytic and photoelectrochemical water-splitting strategies from engineering and economic perspectives.[27,28] Such studies have confirmed that the estimated cost for hydrogen production is significantly lower for the photocatalytic strategy compared to the photoelectrochemical strategy.[28] However, the

photocatalytic strategy is a largely unproven technology, and often has the added safety concern of co-generating H_2 and O_2 gases in the same compartment, creating a flammable mixture (the flammable range of H_2 is 4–75% in air or 4–94% in O_2 at standard temperature and pressure).[29] Importantly, the above economic analysis also concluded that the cost of hydrogen produced by photoelectrochemical strategies could be significantly reduced by increasing the solar-to-hydrogen efficiency beyond 10% and by lowering the cost of the panel-based photoelectrochemical cells.[28] The latter strategy of reducing cost is one of the major motivations behind the focus of this review. Before continuing, we will next describe several different configurations for photoelectrochemical water-splitting cells.

Water-Splitting Photoelectrolysis Cell (PEC) Configurations. An integrated PEC can take on many forms. The simplest is a single-bandgap SC photoelectrode (n-type photoanode or p-type photocathode) submerged in an electrolyte solution with a metal counter electrode, sometimes called a Schottky-type PEC.[6] This name arose because the device is functionally similar to a Schottky-barrier solar cell,[30] which is composed of a semiconductor sandwiched between two metal contacts. A SCLJ behaves similarly to a SC–metal junction in that they both form a Schottky barrier, the physics of which are described in detail elsewhere.[6,10] Briefly, charges transfer across the interface in order to reach thermodynamic equilibrium, resulting in the buildup of a space charge layer within the SC near the interface. The electric field in the space charge region affects the local energy of electrons, which is expressed as band banding in an energy band diagram (Fig. 2.2). For an n-type semiconductor (n-SC), bands are bend upwards at the SCLJ (Fig. 2.2a). When illuminated, this band bending causes photo-generated holes in the valence band to migrate towards the SCLJ where they can induce oxidation reactions, and electrons in the conduction band to migrate towards the bulk of the SC where they can be collected by the conductive substrate.

For a single semiconductor (Schottky-type PEC) to achieve unassisted light-driven water splitting (Fig. 2.2a), it must have a band gap energy, E_g, ≥ ~1.6 eV (to provide sufficient kinetic overpotential, see above), and the bands must also be appropriately positioned relative to the half-cell reactions. The electrochemical potential of the SC conduction band (E_{CB}) must be positioned more negative than the proton-reduction reaction (eq 2.1, by definition 0 V vs the reversible hydrogen electrode, RHE), and the SC valence band potential (E_{VB}) must be positioned positive of the water-oxidation reaction (eq 2.2, +1.23 V vs RHE). It has proved quite difficult to find SC

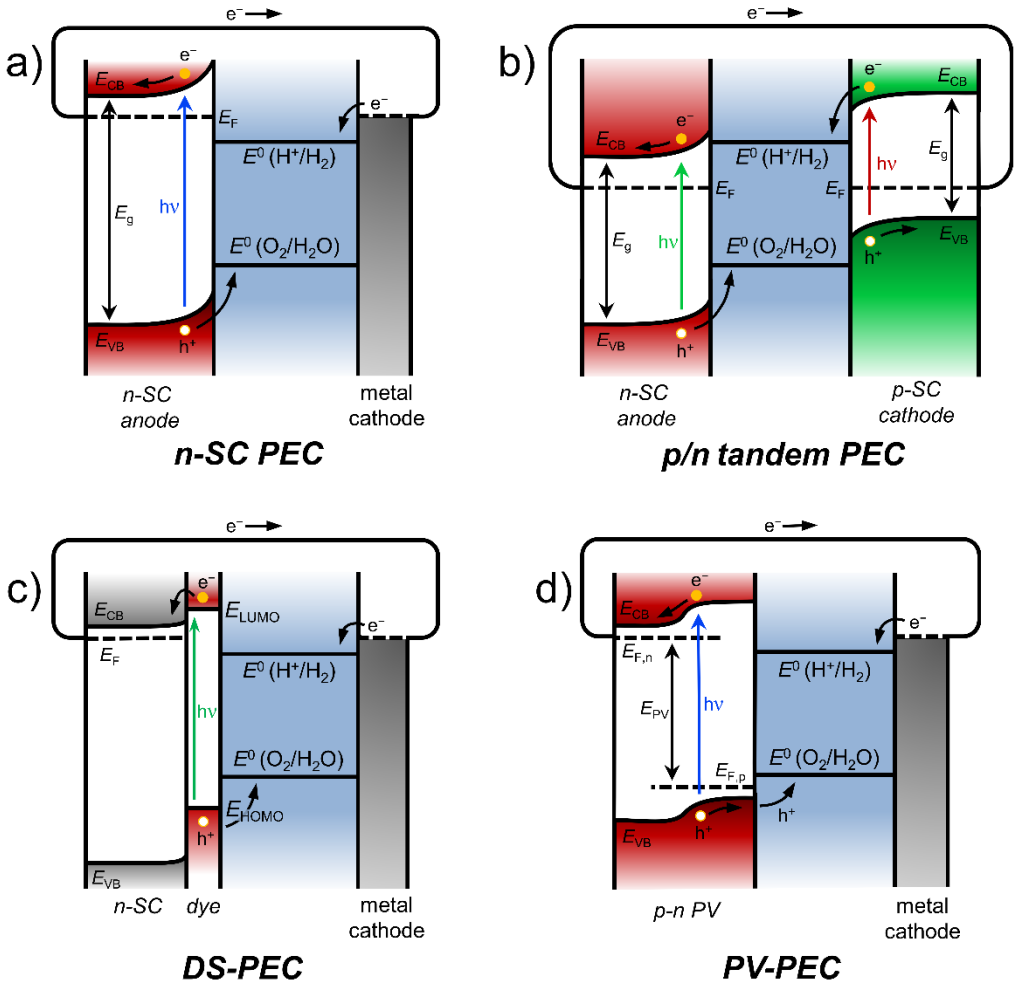

Fig. 2.2 Representative band diagrams of various liquid-junction water splitting systems: (a) a single-bandgap, n-type semiconductor photoanode with metal cathode (n-SC PEC); (b) a dual bandgap (tandem) cell with n-type photoanode and p-type photocathode (p/n tandem PEC); (c) a dye-sensitized metal oxide photoanode with metal cathode (DS-PEC); (d) a submerged p–n junction photovoltaic photoanode with metal cathode (PV-PEC).

materials that meet all the above requirements, let alone the additional requirement of stability against photo-corrosion.[6,19,20] Of the dozens of materials that were the subject of early studies, only a handful of n-type metal oxides met all the above criteria, including $SrTiO_3$, $KTaO_3$, Ta_2O_2, and ZrO_2.[6] Of these, only the former two successfully confirmed unassisted (no applied bias) light-driven water splitting.[31,32] Unfortunately, these materials also have $E_g \geq 3.4$ eV, and so can only absorb light with wavelengths ≤ 365 nm. This includes only ~4% of the incident power in the AM1.5G solar reference standard.[13]

To avoid placing all the above requirements on one semiconductor material, a common strategy is to employ a tandem[10,33] (or p/n-type[6,34]) PEC (Fig. 2.2b). A tandem PEC is a dual bandgap configuration employing both an n-SC photoanode and p-SC photocathode. These systems allow the use of materials with smaller and complementary bandgaps (absorbing complementary wavelength ranges of light) compared to single-bandgap systems, and therefore have a higher theoretical water splitting efficiency as a result of absorbing more of the incident solar radiation.[12] An example band diagram of a p/n-PEC is shown in Fig. 2.2b. In this configuration, two photons (one at each electrode) must be absorbed to generate each usable electron–hole pair, where holes reach the SCLJ of the photoanode to oxidize water, and electrons reach the SCLJ of the photocathode to reduce protons. Therefore, the photoanode must have a VB more positive than the potential of the OER, and the photocathode must have a CB more negative than the potential of the HER.

Another strategy to improve the visible absorptivity of a stable, wide-bandgap SC is *dye sensitization*, wherein dye molecules at the SC surface absorb visible light (dependent on the dye's absorbance spectrum) followed by a rapid charge-transfer reaction between the photoexcited dye and one of the SC energy bands.[6,7] This dye sensitization strategy was studied as early as 1968 by

Gerischer *et al.*[35] but resulted in sub-nanoampere photocurrents, likely because sensitization only occurs from a monolayer of dye molecules adsorbed to the planar semiconductor surface,[36] achieving a visible absorptance of only ~1%.[37] Tsubomura et al. later tried enhancing light absorption by employing thicker films of insoluble dye, but this strategy failed because the dye layers were electrically insulating.[37]

A breakthrough came in 1976 when Tsubomura *et al.* demonstrated a photoelectrochemical cell with greatly improved power efficiency by employing a high-surface-area electrode of sintered ZnO powder coated with dye adsorbed from solution, thus allowing a "large total absorption of light".[37] Furthermore, their use of KI as a redox mediator in solution allowed for the rapid regeneration of photo-oxidized dye at the surface, resulting in a power conversion efficiency of 1.5%.[37] This strategy was significantly enhanced in 1991 by O'Regan and Grätzel, who employed a porous film of sintered TiO_2 nanoparticles (15 nm average diameter) with an internal surface area ~780 times that of a planar surface.[38] When these films were sensitized by adsorption of a Ru-based organometallic dye with carboxylic acid anchor groups and submerged in electrolyte containing iodide redox mediator, they achieved 97% incident-photon-to-current efficiency (IPCE) at the λ_{max} of the dye and a solar conversion efficiency of over 7%.[38] Such an accomplishment demonstrated the commercial promise of the dye-sensitized solar cell (DSSC),[39,40] opening up a huge field of research with >21,700 journal publications as of January, 2017.[41]

In a DSSC, the reduction reaction at the cathode is simply the reverse of the oxidation reaction at the anode, both of which involve a redox mediator in solution. A DSSC is therefore a *photoelectrochemical photovoltaic cell*, which converts light energy into electrical power.[6] Dye-sensitized films of sintered colloidal metal oxides can also be decorated with water-splitting

catalysts for use as *photoelectrolysis cells*, wherein light energy is collected and stored in the chemical bonds of the H_2 and O_2 solar fuels.[6] Such water-splitting dye-sensitized photoelectrolysis cells (DS-PECs) have been the subject of several recent reviews.[42–51] The band energy diagram of an n-type DS-PEC is shown in Fig. 2.2c. In this case, the photo-excited dye injects an electron into the CB of the metal oxide, after which the photo-oxidized dye must accept an electron from a water-oxidation catalyst (WOCatalyst) to avoid the back-electron-transfer recombination reaction.

A fourth type of PEC, Fig. 2.2d, consists of a p–n junction PV in solution to provide the photovoltage required to split water. One could also use multiple PV in tandem, or a PV integrated in series with a single SC photoanode/cathode.[10] In such integrated devices, the PV cell is considered to be a "buried" photoelectrochemical junction, because it is not in direct contact with the electrolyte, and can be classified as a photovoltaic photoelectrolysis cell (PV-PEC).[10] Tandem and integrated PECs can also be prepared in a wireless configuration where each component is sandwiched together by ohmic contacts. Such cells are often referred to as photochemical diodes, monoliths, or artificial leaves,[6,10,52] and have the potential for low cost manufacturing. However, it is common to study the photoanodes and photocathodes in separate Schottky-type PECs before they are integrated into a tandem device.

To summarize, a variety of configurations are possible for water-splitting photoelectrochemical cells. When highlighting specific systems from the literature below, we may reference Fig. 2.2 to clarify the configuration used.

A Focus on Organic Light-Harvesting Materials. Since Fujishima and Honda demonstrated the first example of photoelectrochemical water splitting by a TiO_2 photoanode and Pt cathode (n-SC-PEC) under UV light,[53] hundreds of other inorganic SCs have been studied for PECs[21,22,54] (most of which require UV light and/or sacrificial reagents to function). A select few

PEC systems[55–58] have achieved solar-to-hydrogen efficiencies, η_{STH},[59] above the threshold for practical commercialization of 10%.[7] However, those systems often exhibit poor long-term stability and are composed of rare and expensive elements (In and Ga, for example). These features are likely to limit their commercial application.[60,61] Many researchers have focused their studies on water-splitting PECs composed of *inexpensive, earth-abundant materials* (Fig. 2.3), especially the light-harvesting SC materials and water-splitting catalyst(s).

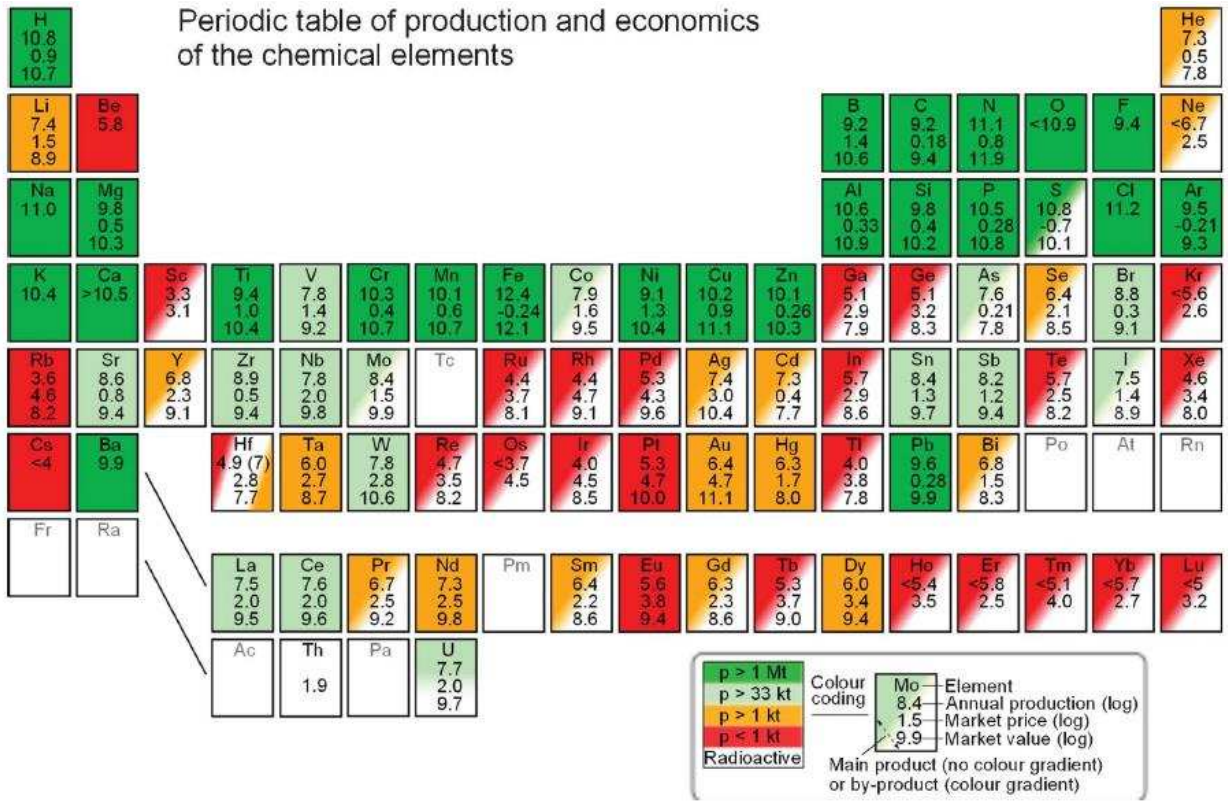

Fig. 2.3 "Periodic table of the elements with data for production, price and implied value for the year 2010. The colour coding (green, light-green, orange and red) corresponds to overall production level (medium to high, low, very low and extremely low, respectively). Solid colour is used for elements which are chiefly main economic products of their respective ores while a diagonal gradient in colour is used for elements which are mostly by-products of other elements." Figure and caption reproduced from Ref. 60 with permission from The Royal Society of Chemistry.

Organic semiconductor (OSC) materials show promise for electronic and light-harvesting applications because of their low cost, earth-abundance, low-temperature manufacturing processes, and perhaps especially because of the structural tunability of their properties by well-established organic synthesis techniques.[62,63] The present review will highlight literature examples of water-splitting systems that employ organic semiconductors and dyes (organic molecules, organometallic complexes with earth-abundant transition metals, and polymers) as light-harvesting materials in light-driven water-splitting cells. Our focus is photoelectrochemical systems; photocatalytic (suspended colloid) systems that employ organic SC polymers[64–69] or dye-sensitized colloids systems[69,70] will not be covered. We further narrow our focus to the more kinetically limiting OER by giving preferential attention to PEC *photoanodes* that have confirmed WOC by the direct detection of O_2 product. We have made our best effort to be comprehensive in our inclusion of such systems, and we apologize in advance to the authors of any important systems that we may have inadvertently missed.

Properties of Organic Semiconductors (OSCs). Before continuing, it is prudent to highlight some of the major differences between molecular and polymeric *organic* semiconductors and more traditional *inorganic* semiconductors. Perhaps the most important difference between OSCs and inorganic SCs is the low dielectric constant of OSC materials.[63] Organic materials are composed primarily of second-row elements where valence shell electrons are held more tightly to the nuclei than in lower-row elements, making organic materials less polarizable and less efficient at shielding electric fields between charges. As a result, light absorption by OSCs generally leads to the formation of *excitons* (coulombically bound electron–hole pairs).[63] By contrast, the higher dielectric constant of inorganic semiconductors generally allows for the photo-generation of free charge carriers (that is, thermal energy even at room temperature is sufficient to

overcome the binding energy between electrons and holes). In order to generate usable charge carriers in OSCs, photo-generated excitons must diffuse to a heterojunction interface with a band offset sufficient to overcome the exciton binding energy.[63]

A second major difference is the relatively weak electronic coupling between neighboring molecules in an organic film when compared to the coupling between covalently bound atoms in inorganic semiconductors.[63] This results in relatively narrow valence and conduction bands, more localized charge carriers, lower carrier mobilities, and anisotropic carrier mobilities.[63] Such mobility limitations allow excitons in organic materials to diffuse only a short distance before relaxing (typically on the order of tens of nanometers), and often the diffusion distance is much shorter than the depth that light can penetrate into the film (a function of the material's wavelength-dependent extinction coefficient).[63] If excitons are generated by light absorption too far from a materials heterojunction, they will relax before dissociation and their energy is wasted. In planar heterojunction configurations, the thickness of organic thin-films is therefore limited to roughly the exciton diffusion length, greatly limiting the light absorption efficiency. A common strategy to overcome this limitation is to nanostructure the interface.[63]

Device Architectures for PECs Composed of Organic Light-Harvesting Materials. Modern studies of PECs employing organic light-harvesting materials generally come in one of two main architectures, both of which are based on emerging PV technologies: organic photovoltaics (OPVs)[63,71,72] and DSSCs.[39,40] Both OPVs and DSSCs have recently reached PV efficiencies nearing 12%.[73] If the energy bands of such PV devices are appropriately positioned for one or both of the half-cell reactions for water splitting, the cells can potentially be decorated with water-splitting catalysts and submerged in aqueous solutions as PECs. We will refer to OPV-type water-splitting architectures as an organic thin-film photoelectrolysis cells (OTF-PEC), and

DSSC-type architecture as dye-sensitized photoelectrolysis cells (DS-PEC). Simplified representations of each architecture are provided in Fig. 2.4.

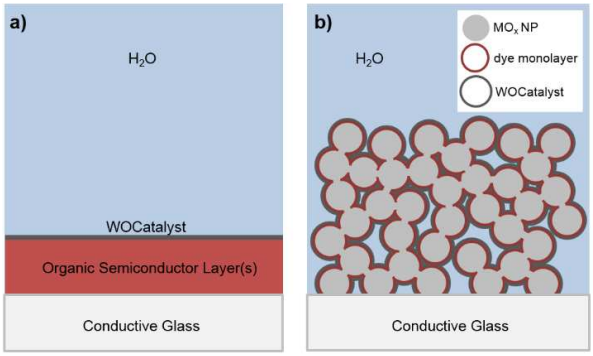

Fig. 2.4 Schematic cross-sections of two common device architectures for PECs composed of earth-abundant materials. (a) Organic-thin-film photoelectrolysis cells (OTF-PEC); (b) Dye-sensitized photoelectrolysis cells (DS-PEC).

The OTF-PEC architecture (Fig. 2.4a) is composed of a planar thin-film of OSC(s). This thin-film may be composed of a single OSC material, or may contain a planar bilayer heterojunction between two different OSC materials; a bulk heterojunction wherein the two OSC materials are mixed with nanoscale phase domains; or a trilayer junction wherein a blended bulk heterojunction layer is sandwiched between two single-OSC layers. The DS-PEC architecture (Fig. 2.4b), on the other hand, is typically composed of a sintered nanoparticle (NP) film of semiconducting metal oxide (with resulting internal surface area often 1000-times larger than a planar surface, depending on thickness)[40] which is then sensitized to visible light by adsorption of a monolayer of dye. When illuminated, the photo-excited dye can inject a charge carrier into the metal oxide, where the carrier then diffuses through the interconnected nanoparticle film to be collected at the conductive substrate, and the dye is subsequently regenerated by charge transfer from a water-splitting catalyst.

2.2 Performance Metrics

The water-oxidizing photoanode systems highlighted in this review will be compared by a number of performance metrics. To our knowledge, none of the OTF-PEC or DS-PEC photoanodes studied to date achieve sufficient photovoltage to perform overall water splitting without additional applied bias. As a result, these photoanodes are typically characterized in a 3-electrode configuration, and would require a complementary photocathode in a tandem configuration (Fig. 2.2b) in order to achieve unassisted water splitting (a few examples of tandem OTF-PEC[74] and DS-PEC[75] devices for unassisted light-driven water splitting have emerged in the literature,[74,75] although most photoanodes are still at early fundamental stages of research). As such, the overall solar-to-hydrogen efficiencies, η_{STH},[59] are not a relevant (or possible) metric of comparison for these systems. It has recently been highlighted that photolysis cells measured in a 3-electrode configuration can still be compared using "intrinsic solar-to-chemical conversion efficiency"[76] or "ratiometric power saved"[77] metrics. None of the systems highlighted in this review had adopted such performance metrics, though they should certainly be considered for future studies.

The most widely reported performance metric for water-oxidizing photoanodes is the photocurrent density, J (μA/cm²), taken as the difference in current density at the working electrode measured under illumination and in the dark. The measurement is typically done in a 3-electrode configuration,[59] wherein currents are measured between the (working) photoelectrode and a metal counter electrode as a function of potential applied to the photoelectrode vs a reference electrode (typically Ag/AgCl or saturated calomel electrode, SCE). Photocurrents are obtained from separate *J*–*V* experiments performed in the dark and under illumination, or from one *J*–*V* experiment with transient illumination (a light source is cycled on and off throughout the scan). In

the latter case, currents often show a spike-like behavior, wherein the current peaks when the light is turned on and quickly decays towards a steady-state value over the course of seconds (see, for example, Fig.s 2.6 and 2.11 in the following section). In such cases, we report the *steady-state* photocurrent value. Of course, photocurrents depend highly on the measurement conditions,[59,78] so herein we report both the measured photocurrent density for each system as well as the specific conditions for the measurement, including solution pH, electrolyte identity, applied potential, illumination intensity, and illumination wavelength distribution.

For direct comparison across different systems we convert applied potentials reported vs various reference electrodes to the reversible hydrogen electrode (RHE) by the following conversion factors to the normal hydrogen electrode (NHE):[11]

Table 2.1. Conversion factors for applied potential vs various reference electrodes to NHE.[11]

Reference Electrode	Conversion to NHE
Ag/AgCl (sat. KCl)	$+0.197$ V
Ag/AgCl (3 M KCl)	$+0.210$ V
SCE	$+0.241$ V
RHE	$-(0.0591\ \text{V} \times \text{pH})$

Conveniently, this conversion allows for the comparison of applied potentials to the thermodynamic potential required for water oxidation (+1.23 V vs RHE, independent of pH). Efficient photoanodes should reach saturated water-oxidation photocurrents at potentials well-negative of +1.23 V vs RHE.

A major concern with organic light-harvesting materials is that they may not have sufficient photo- and oxidative stability for high-turnover water oxidation catalysis. Therefore, an especially important metric of such systems is the *faradaic efficiency*, or the fraction of the photocurrent that actually corresponds to O_2 production. For inorganic systems, this is typically done by the quantitative detection of O_2 product in the gas phase above solution by gas chromatography.[59] For organic systems, which typically exhibit lower and less-stable photocurrents, O_2 quantification is

often measured in solution using commercial probes based on fluorescence-quenching by O_2[79] or by electrochemical methods such as Clark electrodes[80] or a Generator–Collector method[81–83] (see details in Sec. 4.1 below). By tracking both the O_2 concentration and the current passed by the photoelectrode over time, the faradaic efficiency can then be calculated.

A final performance metric we will use for comparison is the incident photon-to-current conversion efficiency, IPCE.[59] The IPCE spectrum is calculated from a photocurrent action spectrum experiment, wherein amperometric photocurrent (*J*–*t*) is measured as a function of monochromatic illumination wavelength. By measuring the power of the incident light at each wavelength step, the photon flux can be calculated. Subsequently, dividing the steady-state photocurrent by the incident photon flux yields the IPCE value at each wavelength.[59] The IPCE of a device is a combination of several characteristic efficiencies,[59] including light-harvesting efficiency (and therefore the IPCE spectrum is expected to correspond well to the photoelectrode light-absorptance spectrum), charge-separation efficiency (exciton dissociation), charge-transport efficiency through the material to the SCLJ, and charge-transfer efficiency *across* the SCLJ.[59]

The characteristic efficiencies that determine the IPCE can be partially deconvoluted by a combination of action spectrum experiments with and without a facile redox couple, and the UV–vis absorptance spectrum of the photoelectrode.[59] As mentioned above, the photoanodes highlighted in this review do not have sufficient reducing potential to carry out overall water splitting. IPCE measurements for such systems are generally performed at an applied bias in order to provide additional potential to the counter electrode to carry out the HER and/or to provide sufficient electric field for efficient carrier collection at the working photoelectrode.[59] As such, we report both the maximum IPCE value achieved by each system (usually at the λ_{max} of the organic light collector) and the applied potential vs RHE.

2.3 Water Oxidizing Organic Thin-Film Photoelectrolysis Cells (OTF-PECs)

Herein we will highlight literature examples of water oxidizing OTF-PECs. Many of these systems employ classic organic semiconductor materials[63,71,72] including phthalocyanine derivatives (Pc), porphyrin derivatives (Por), or perylene derivatives, as well as the classic fullerene, [6,6]-phenyl-C_{61}-butyric acid methyl ester (PCBM). The former three classes of molecules garnered early attention because of their high molar extinction coefficients, high chemical and thermal stabilities, and strong π-stacking in the solid state resulting in beneficial charge-transport properties.[63] Furthermore, Por and Pc molecules can be considered as synthetically tractable analogues of chlorin, the core structure found in chlorophyll pigments used by many photosynthetic systems in nature.[84] On the other hand, fullerenes such as PCBM are far and away the most common acceptor materials in OPVs because of their positive redox potentials, and their spherical structure results in small reorganization energies upon electron transfer and direction-independent accepting ability.[63,71,72]

Literature examples of OTF-PECs fall within two sub-categories. The first is based on classic OPVs,[63,71,72] wherein free charge generation is presumably achieved at the materials heterojunction between two organic semiconductors. The second type is composed of a single-bandgap OSC thin-film material, and *may* be considered as a Schottky-type PEC[6,30] such as that in Fig. 2.2a (see the discussion at the end of Sec. 3.2 below). We will introduce literature examples of water-oxidizing OTF-PEC systems historically and separated by device sub-category. A summary of the highlighted systems is provided in Table 2.2.

Table 2.2. Summary of the 6 known OTF-PEC water-oxidizing photoanodes.

System[a]	WOCatalyst[a]	Max Steady-State Photocurrents (Conditions)[b]	Faradaic Efficiency	Max IPCE (appl. bias)[b,c]	Corresponding Author(s)
PTCBI/**H_2Pc** bilayer	Nf-IrO_2	**6 μA/cm²** (pH 10 KOH, +1.19 V vs RHE, ~70 mW/cm²)	≥90%	0.04% (+1.2)	Abe & Nagai[85]
PTCBI/**CoPc** bilayer	**CoPc**	**20 μA/cm²** (pH 11 NaOH, +1.25 V vs RHE, ~70 mW/cm²)	ND	ND	Abe & Nagai[86]
PTTh:**MnPor**	**MnPor**	**23 μA** (pH 7 Na_2SO_4, +1.51 V vs RHE)	ND	ND	Chen & Swiegers[87]
PTCDA/**PTCDA**:**PCBM**/**PCBM** trilayer	Unknown	**110 μA/cm²** (pH 2 KNO_3/H_2SO_4, +1.16 V vs RHE, ~110 mW/cm², λ>420 nm)	ND	1.2% (+1.16V)	Zhao[88]
PMPDI single layer	CoO_x	**150 μA/cm²** (pH 7 KPi, +1.56 V vs RHE, ~100 mW/cm², λ=315–710 nm)	80±15%	0.12% (none)	Gregg & Finke[80]
BBL polymer single layer	ALD TiO_2/ Ni-Co	**20 μA/cm²** (pH 7 Na_2SO_4/KPi, +0.90 V vs RHE, 100 mW/cm²)	82±16%	1.0% (+1.23V)	Sivula[89]

[a] Abbreviations are defined throughout the text and summarized in a List of Abbreviations at the end of this dissertation. [b] Applied bias has been converted to the RHE reference electrode for direct comparison between systems. [c] Note that IPCEs measured under applied bias ≠ η_{STH}.

Organic Heterojunction Photoelectrolysis Cells. In 2006, the PIs Abe and Nagai (*et al.*) published an OPV-PEC system[85] (Fig. 2.2d) composed of an organic thin-film bilayer of the electron acceptor material 3,4,9,10-perylenetetracarboxyl-benzimidazole (**PTCBI**, hereafter, we will abbreviate specific molecules in bold), and the electron donor material 29H,31H-phthalocyanine (**H_2Pc**), Fig. 2.5a. The OPV was prepared on indium tin oxide-coated glass (ITO) by vacuum vapor deposition of **PTCBI** (450 nm) followed by **H_2Pc** (160 nm). Subsequently, the film was "coated" (by an unspecified procedure) with finely-ground IrO_2 powder as a WOCatalyst (~1.2×10^{-5} mol/cm²), which was then immobilized by a top coating of ~30 nm-thick water- and proton-permeable Nafion membrane (Nf, a copolymer of tetrafluoroelthylene and sulfonated tetrafluoroethylene). These ITO/**PTCBI**/**H_2Pc**/Nf-IrO_2 photoanodes were immersed in pH 10 (KOH) aqueous solution for photoelectrochemical studies.[85] A schematic energy diagram of the system (Fig. 2.5b) shows that light absorption in either of the OSC layers should drive electrons to transfer towards the ITO

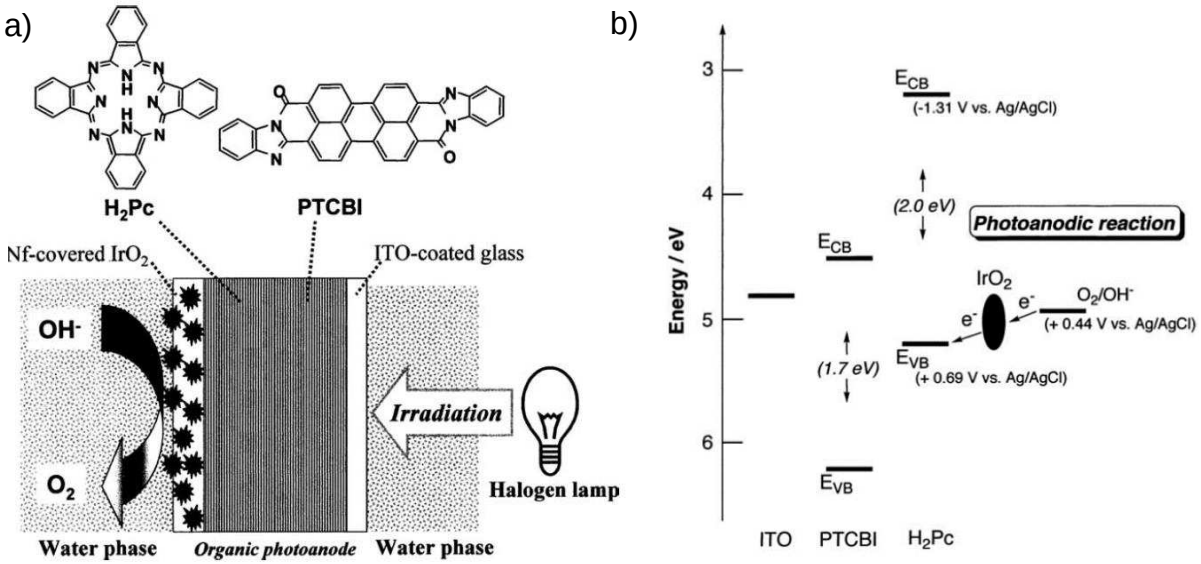

Fig. 2.5 (a) Chemical structures of **PTCBI** and **H_2Pc,** and a device schematic for O_2 production from an organic bilayer photoanode modified with Nafion-covered IrO_2 catalyst. (b) An approximate energy diagram for the ITO/**PTCBI**/**H_2Pc**/Nf-IrO_2 bilayer device. Figures reprinted from Ref. 85, Copyright 2005, with permission from Elsevier.

interface (from **H_2Pc** donor to **PTCBI** acceptor) and holes to transfer towards the SCLJ. Furthermore, holes in the **H_2Pc** VB should be sufficiently oxidizing for the OER.

Control experiments showed that the Nf-IrO_2 layer was necessary to observe photocurrents, indicating that IrO_2 catalyzes the WOC reaction (faradaic efficiencies were ≥90% as determined by gas chromatography of the head space gasses after electrolysis carried out over 1.5 h).[85] Additional controls found that ITO/**PTCBI**/Nf-IrO_2 films (without the **H_2Pc** layer) were able to achieve comparable photocurrents, but for unknown reasons no O_2 was detected.[85] When illuminated with 70 mW/cm² white light from a halogen lamp and held at +0.4 V vs Ag/AgCl (+1.19 V vs RHE), ITO/**PTDBI**/**H_2Pc**/Nf-IrO_2 photoanodes achieved steady-state photocurrents of ~6 μA/cm². During transient photocurrent experiments in which the light source is repeatedly switched on and off, photocurrents spiked and quickly decayed towards the steady-state values over tens of seconds, Fig. 2.6. The authors interpreted this behavior as indicating that the water

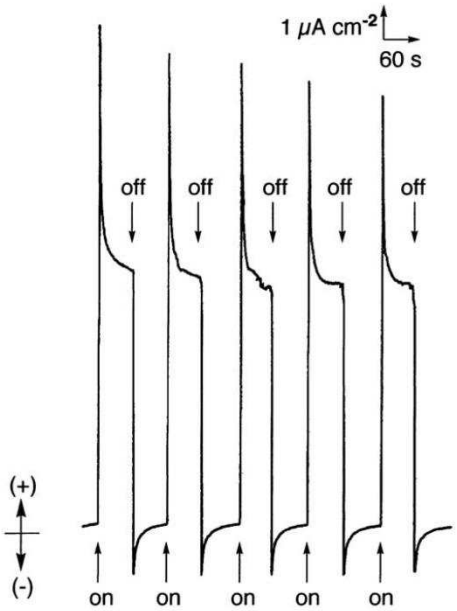

Fig. 2.6 Oxidative photocurrents produced at an ITO/**PTCBI**/**H_2Pc**/Nf-IrO_2 anode under transient illumination with an applied potential of +0.4 V vs Ag/AgCl in pH 10 KOH. Film thicknesses were 450 nm (**PTCBI**)/160 nm (**H_2Pc**) coated with 1.2×10^{-5} mol IrO_2. Reprinted from Ref. 85, Copyright 2005, with permission from Elsevier.

oxidation reaction at the SCLJ was kinetically slow, in spite of the well-established, highly-active IrO_2 WOCatalyst.[85]

Action spectra for the ITO/**PTDBI**/**H_2Pc**/Nf-IrO_2 system at +1.19 V vs RHE indicated a maximum IPCE value of ~0.04%. Interestingly, the action spectrum was *not* a match for the absorption spectrum of the **PTCBI**/**H_2Pc** bilayer OPV, but was closer to that of the **PTCBI** layer alone. In other words, only excitons generated by light absorbed in the **PTCBI** layer apparently contribute to photocurrents, in contrast to comparable dry-type OPV cells.[85] The authors hypothesized that this was likely because the overall kinetics of the PEC system are limited by the electrochemical process at the SCLJ.[85] In the end, Abe *et al.* proposed that the use of a more efficient WOCatalyst would be the most promising route to improving the photolysis efficiency of their device.[85] However, given that IrO_2 is among the most active of heterogeneous, metal oxide WOCatalysts,[90] an alternative hypothesis is that the above kinetic bottleneck is more likely relatedto a low catalyst surface area or the efficiency of charge transfer (that is, the electronic coupling) from the **H_2Pc** layer to the IrO_2 WOCatalyst than to the turnover frequency of the catalyst itself.

In the same year, Abe and Nagai *et al*. published a subsequent paper describing an analogous OPV-PEC system in which the IrO_2 WOCatalyst was omitted, and instead cobalt(II) phthalocyanine (**CoPc**) was used as the p-type OSC[86] (Fig. 2.7). As before, the OPV was prepared by the vacuum vapor deposition of **PTCBI** followed by **CoPc**. When submerged in pH 11 (NaOH) aqueous solution and illuminated with ~70 mW/cm² white light, ITO/**PTCBI**/**CoPc** electrodes exhibited photocurrents on the order of ~20 μA/cm² at an applied bias of +0.4 V vs Ag/AgCl (+1.25 V vs RHE).[86] Controls showed essentially no currents in the dark, and negligible photocurrents for single-layer ITO/**CoPc** films or ITO/**PTCBI**/**H_2Pc** films without cobalt. This

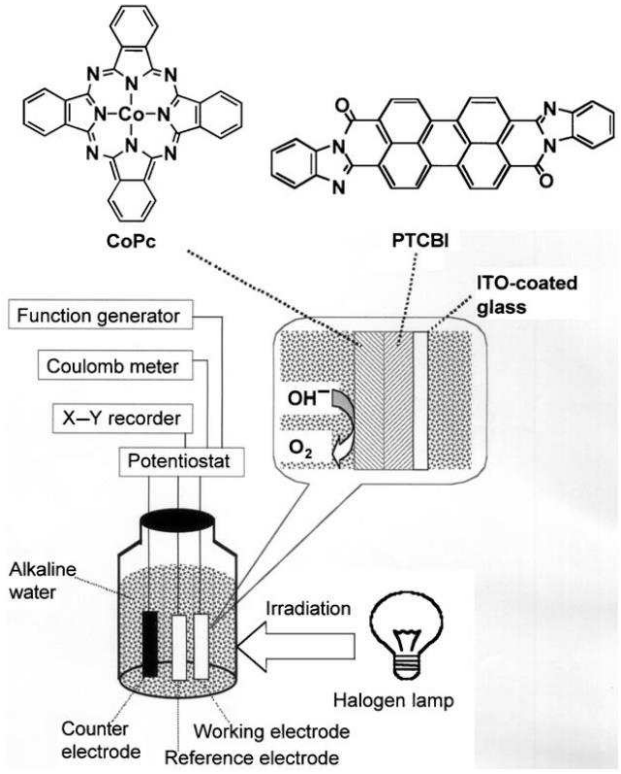

Fig. 2.7 Chemical structures of **PTCBI** and **CoPc**, and a schematic illustration of the ITO/**PTCBI**/**CoPc** organic bilayer thin-film photoanode and testing apparatus for photoelectrochemical measurements. Reprinted from Ref. 86 with permission from John Wiley and Sons. Copyright 2006 Wiley-VCH.

work from Abe and Nagai *et al.*[86] is the first example in the literature of photoelectrochemical WOC using **CoPc** as the likely WOCatalyst. An important, yet untested, alternative hypothesis from subsequent literature[91–93] is that labile Co(II) may have leached from the **CoPc** film and re-deposited on the electrode as heterogeneous CoO_x.

Importantly, WOC was confirmed by the detection of O_2 formed in the headspace by gas chromatography, though the faradaic efficiency was not reported.[86] Furthermore, isotopic studies in $H_2{}^{18}O$ produced only $^{18}O^{18}O$ product, demonstrating that all O_2 produced originated from water.[86] Extended electrolysis studies showed that O_2 was still being produced well beyond 3 h (with a **CoPc** turnover number >35,000 estimated under the assumption that only **CoPc** on the surface participates), indicating a relatively stable performance for the ITO/**PTCBI**/**CoPc** system.

IPCE measurements (under applied bias and with the sacrificial electron donor triethylamine, **TEA**) were again a closer match for the absorbance spectrum of the **PTCBI** portion of the film alone, suggesting that light absorption by the **CoPc** layer does not contribute to photocurrents. Instead, the authors suggested that the **CoPc** layer must aid in exciton dissociation at the p–n interface, allow hole conduction to the SCLJ, and also act as a catalyst through the inter-sphere interaction between $Co^{III}Pc$ (hole-doped $Co^{II}Pc$) and OH^-.[86] Importantly, this publication presented the first example in the literature of a water-oxidizing OTF-PEC system composed entirely of earth abundant elements (excluding the indium in the ITO substrate), including both the light-harvesting material and the WOCatalyst.

In early 2012, the groups of Chen and Swiegers *et al*. published a second example of a water-oxidizing organic heterojunction thin-film system composed entirely of earth-abundant materials.[87] Specifically, their thin-film consisted of an anionic Mn-porphyrin dispersed throughout a poly(thiophene) film (poly(thiophene) being one of the most-studied conducting polymers due to its high stability and structural versatility[94]). In their system, thin-films were formed by the oxidative electrochemical polymerization of terthiophene to poly(terthiophene) (PTTh) on ITO substrates in ethanol-dichloromethane (1:1) solution, while in the presence of the dissolved 5,10,15,20-tetra(4-sulfonophenyl)porphyrin tetrasodium salt (**MnPor**, Fig. 2.8). The resulting ITO/PTTh:**MnPor** film was characterized by SEM to show a porous surface structure and a film thickness of ~500 nm. EDX-mapping showed that the **MnPor** was uniformly distributed throughout the film, and elemental analysis suggested a ratio of 1:3 **MnPor** : terthiophene monomer.

When submerged in pH 7, 0.1 M Na_2SO_4 and held at +0.9 V vs Ag/AgCl (+1.51 V vs RHE), ITO/PTTh:**MnPor** anodes showed practically zero current in the dark and photocurrents as

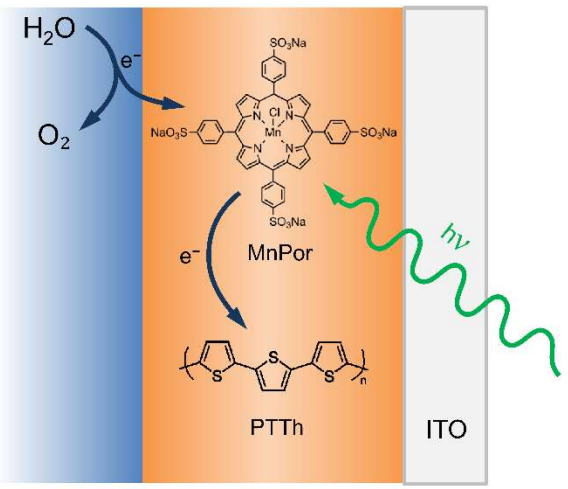

Fig. 2.8 Schematic illustration of the OTF-PEC photoanode studied in Ref. 87. The thin-film was deposited by electrochemical polymerization of poly(terthiophene) (PTTh) in the presence of 5,10,15,20-tetra(4-sulfonophenyl)porphyrin tetrasodium salt (**MnPor**).

high as 23 μA (not normalized for surface area) when illuminated with a halogen lamp (light intensity was not reported).[87] Furthermore, when submerged in pH 8.6 filtered sea water and held at +0.9 V vs Ag/AgCl (+1.60 V vs RHE), ITO/PTTh:**MnPor** films exhibited sustained photocurrents of ~7.5 μA. Surprisingly, after 24 h of photolysis in sea water, analysis by GC-MS and analytical test strips revealed O_2 product but no Cl_2 was detected, despite the fact that the overpotential for Cl^- oxidation is far less than WOC on most known catalysts.[87] Hence, the apparent selectivity of the PTTh:**MnPor** film for H_2O over Cl^- oxidation is noteworthy, but merits independent verification and explanation.

The action spectrum of an ITO/PTTh:**MnPor** anode was generally featureless, with a maximum current at 375 nm, decaying to near zero by 550 nm.[87] While the authors claimed that the action spectrum was in good agreement for light absorption from one band of **MnPor,**[87] the overall action spectrum was not a match for **MnPor** nor the PTTh:**MnPor** composite film. Nevertheless, control experiments attempting photolysis using bare ITO and dissolved **MnPor** showed no photocurrents. Additional controls of ITO/PTTh with p-toluenesulfonate (to mimic the hydrophilic groups of **MnPor**) showed only small photocurrents of ~1 μA. Therefore, Chen and

Swiegers *et al*. concluded that **MnPor** is indeed required for photolysis of water.[87] Upon illumination, they suggest that **MnPor** must transfer an electron into the PTTh matrix, which then conducts the electron to the ITO substrate, and the photo-oxidized **MnPor** must then oxidize water (Fig. 2.8).[87] We note, however, that the band energies of PTTh and **MnPor** were not provided to confirm that the proposed electron transfer is thermodynamically favored. This is of particular interest because the poly(thiophene) derivative P3HT, or poly(3-hexylthiophene), is one of the most common electron *donor* materials in polymer–fullerene solar cells,[71,72] as well as in a bilayer device with a Por derivative.[95] That being said, the energy bands of poly(thiophene) are expected to be slightly more positive than P3HT,[96] and can vary depending on preparation method, extent of polymerization, film thickness, and even substrate electrode.[94]

As for the proposed water oxidation by **MnPor**, a previous study found that covalently bound dimers of analogous manganese porphyrins do function as water oxidation catalysts, while individual monomers do not[97] (suggesting a bimolecular mechanism). Therefore, Chen and Swiegers *et al*.[87] proposed that water oxidation in their system occurs by a bimolecular interaction between two neighboring **MnPor** molecules, which were at high concentration within the PTTh film. They also hypothesized that the hydrophilic sulfonic acid groups of **MnPor** may be beneficial because they could be providing H^+-conduction pathways throughout the film.[87]

Later in 2012, the Zhao group published an additional example of a water-oxidizing OPV-PEC photoanode composed entirely of earth-abundant elements.[88] In that study, the researchers prepared OPV films by vacuum vapor deposition of 3,4,9,10-perylenetatracarboxylic dianhydride (**PTCDA**) and/or [6,6]-phenyl-C_{61}-butyric acid methyl ester (**PCBM**) on ITO (Fig. 2.9). Notably, **PCBM** is being used as a *donor* material in this study, whereas it is the most common *acceptor* material in OPVs.[71,72] Several compositions for the organic thin-film were tested, including: single

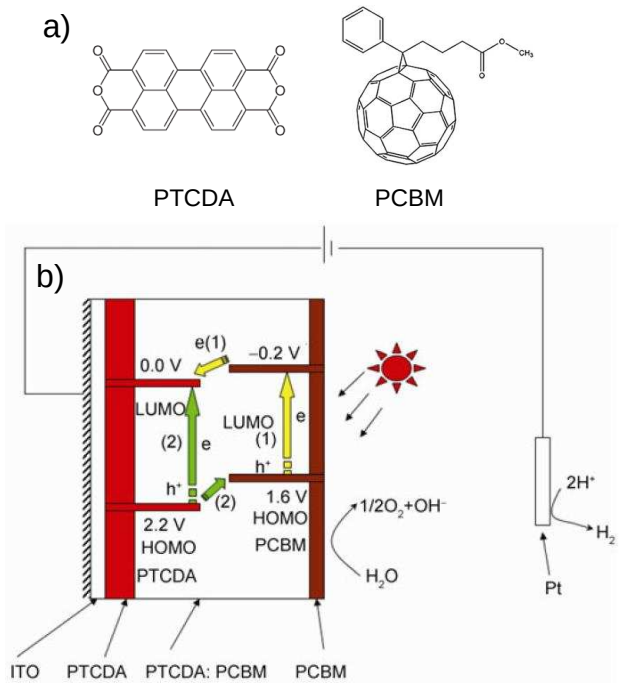

Fig. 2.9 (a) Chemical structures of **PTCDA** and **PCBM**. (b) The trilayer film configuration **PTCDA**/**PTCDA**:**PCBM**/**PCBM**. Also shown are two possible charge separation mechanisms under light illumination: (1) electron transfer from the LUMO of excited **PCBM** to the LUMO of **PTCDA** (yellow arrows); (2) hole transfer from the HOMO of excited **PTCDA** to the HOMO of **PCBM** (green arrows). Both processes would produce free charge carriers. Reprinted from Ref. 88 (Copyright 2011, Science China Press and Springer-Verlag Berlin Heidelberg) with permission from Springer.

layers of **PTCDA** or **PCBM**; a mixed (bulk heterojunction) **PTCDA**:**PCBM** layer; a bilayer **PTCDA**/**PCBM** heterojunction; a three-layer **PTCDA**/**PTCBA**:**PCBM**/**PCMB** film consisting of an initial layer of **PTCDA** (20 nm), followed by a bulk heterojunction of **PTCBA**:**PCBM** (35 nm, 11.6:1 molar ratio), and finally a thin layer of **PCBM** (3 nm). For electrochemical testing, these films were then submerged in aqueous solution containing 35 mM KNO_3 and adjusted to pH 2 with H_2SO_4, and illuminated with a halogen lamp (110 mW/cm²) with a UV filter ($\lambda > 420$ nm).

Current–voltage curves for all films showed negligible photocurrents in the dark. In the light, most of the films showed photocurrents up to tens of μA/cm². Of all the films tested, the trilayer (ITO/**PTCDA**/**PTCDA**:**PCBM**/**PCBM**) film showed the largest photocurrents, reaching as high as 110 μA/cm² at an applied potential of +0.8 V vs SCE (+1.16 V vs RHE). This presents

a significant improvement relative to the previous planar bilayer systems from Abe *et al*.[85,86] Interestingly, when Zhao *et al*. tested a planar-heterojunction, bilayer film (ITO/**PTCDA**/**PCBM)** similar to the architectures used by Abe *et al*.,[85,86] it showed the worst performance of all films tested, reaching only ~5 μA/cm².[88] This seems to indicate that, relative to the planar-heterojunction, the increased surface area of the bulk heterojunction in the trilayer film significantly enhances the exciton dissociation efficiency. Furthermore, the use of the thin **PCBM** film at the SCLJ of the trilayer film likely helped with the preferential collection of holes at that interface (in comparison to the single-layer heterojunction, ITO/**PTCDA**:**PCBM**).[88]

The stability of the system was probed by extended photolysis experiments. First, in the presence of a redox mediator, KI, the trilayer film (held at +1.16 V vs RHE) exhibited an initial photocurrent spike which decayed over the course of ~200 s to a steady-state value of 150 μA/cm². The authors attributed this spike/decay behavior to "photoelectrical charging" of the film.[88] The steady-state current then remained unchanged throughout 50 min of illumination. In the absence of a sacrificial reductant, the authors were able to use a Clark electrode to detect O_2 product in solution (a faradaic efficiency was not reported). This is surprising, given the fact that no known WOCatalyst was deposited on the film. Interestingly, a recent study has detected light-induced water oxidation by a colloidal suspension of **PTCDA** nanorods, even in the absence of intentionally added WOCatalyst[98] (though this does not rule out the possibility of water oxidation by trace metal impurities).[99] It has also been shown that **PCBM** can be chemically oxidized when illuminated in air[100] and even by water vapor in the dark.[101] It is therefore conceivable that **PTCDA**, some oxidized decomposition product of **PCBM**, or trace metal impurity[99] may be functioning as a WOCatalyst in this system,[88] hypotheses which merit further experimental investigation.

During extended photolysis in the absence of a sacrificial reductant, photocurrents gradually decayed by ~50% over the first 15 min of illumination before reaching a steady state.[88] Despite this, the O_2 evolution rate over time appeared to increase slightly over 100 min of illumination. After extended electrolysis, the UV–vis spectrum of the film had decreased by less than 10% relative to before electrolysis, indicating the relatively high stability of the film. However, mass spectrometry did indicate some destruction of an unspecified "small quantity"[88] of the **PCBM**. The IPCE spectrum indicates that absorbance from both film components, **PTCDA** and **PCBM**, likely contribute to photocurrents. At an applied bias of +1.16 V vs RHE, a maximum IPCE value of 1.2% was reached at the λ_{max} of **PCBM**,[88] which is somewhat surprising given the low extinction coefficient and low mass loading of **PCMB** in the film. Overall, this system demonstrates that a trilayer OPV architecture with a bulk heterojunction provided superior performance to a planar, bilayer heterojunction.

A final example of an OPV-PEC meriting mention came from Gustafson *et al*. in 2014,[74] though we do not include their results in Table 2.2 because water-splitting catalysis was not confirmed *by the direct detection of H_2 and O_2 products*. Their system was composed of a typical[71,72] OPV cell printed on ITO-coated plastic, Fig. 2.10. They used the common OPV active materials of P3HT and **PCBM** in a 1:1 weight ratio to form a bulk heterojunction film, which was printed from an organic-solvent ink onto either an electron-blocking interfacial layer (PEDOT:PSS) for photocathodes or a hole-blocking interfacial layer (ZnO) for photoanodes. The interfacial layers served to ensure the desired electron flow direction in each bulk heterojunction electrode (Fig. 2.10). Next, these films were sputter-coated with Pt to function as water-splitting catalyst and films were laminated with plastic except for a small window to allow contact with

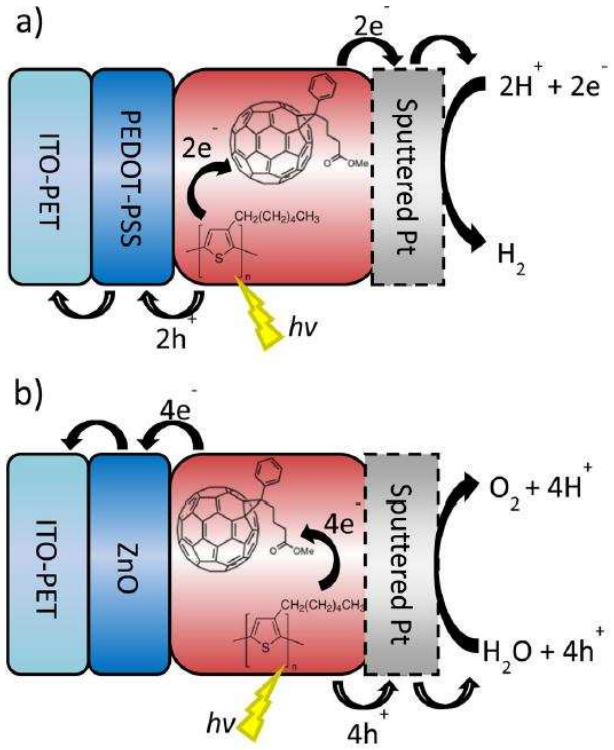

Fig. 2.10 Water-splitting photoelectrodes composed of a bulk-heterojunction organic active layer containing **PCBM** and P3HT (structures shown in red). The photocathode (a) includes a PEDOT:PSS electron-blocking interfacial layer, and the photoanode (b) contains a ZnO hole-blocking layer. Arrows indicate electron and hole pathways. Reprinted from Ref. 74, Copyright 2014, with permission from Elsevier.

solution. In this way, these cells can be considered as "buried junction" OPV-PECs,[10] where none of the OSC materials are in direct contact with solution.

When submerged in pH 7 phosphate buffer and illuminated by 300–400 mW/cm² white light, their photocathode achieved photocurrent densities of 10 μA/cm² with an applied bias of +0.51 V vs RHE, and their photoanode achieved photocurrent densities of 77 μA/cm² with an applied bias of +1.31 V vs RHE.[74] However, without the detection of water-splitting products, H_2 and O_2, it cannot be known if these photocurrents truly correspond to the HER and OER, respectively. This is especially crucial because E_{VB} of the P3HT polymeric electron donor (hole acceptor) material is not innately positive enough to drive the water oxidation reaction.[102,103]

Hence, further investigations of this interesting system are warranted, especially those focusing on photolysis products, and perhaps also on band bending and band edge positions during operation.

Importantly, Gustafson *et al*. also noted a degradation in electrochemical response over time.[74] They measured an increasing resistance across their cells as a function of time soaked in water, which they interpreted as possible ITO delamination and/or morphological changes to the active layer as a result of swelling from electrolyte intake.[74] This brings up a serious concern for PECs based on traditional OPV materials, especially since it is well-documented in the OPV literature that exposure to water vapor and O_2 leads to accelerated device degradation caused by oxidation of the active materials and conductive contacts as well as morphological changes and delamination of films.[101,104–107] Clearly, the application of such technology to photoelectrochemical water oxidation will require either extremely effective encapsulation methods or the engineering of alternative materials that are compatible with water and oxygen.

Single Organic Semiconductor Photoelectrolysis Cells. As described in Section 1.2, PECs composed of a single-bandgap (inorganic) semiconductor (Fig. 2.2a) are often referred to as Schottky-type PECs[6] because of their parallel structure to a Schottky-barrier solar cell.[30] Early studies of photoelectrochemical cells employing porphyrin and phthalocyanine thin-films were also well-explained by semiconductor band-bending phenomena of Schottky junctions at the substrate and/or electrolyte interfaces.[108–114] Significantly, one example from the Armstrong group demonstrated the first example of light-assisted hydrogen evolution by a single organic-semiconductor thin-film, specifically, a chlorogallium phthalocyanine film decorated with Pt.[111]

To our knowledge, the first example of a water-*oxidizing* single-layer OTF-PEC (composed entirely of earth-abundant materials) came in 2014 from Gregg and Finke *et al*.[80] In that system, the authors designed and synthesized a novel perylene diimide (PDI) dye derivative

with phosphonate groups under the hypothesis that it should enhance coupling between the organic light-harvesting material and a popular, earth-abundant, heterogeneous WOCatalyst, CoO_x (CoPi).[115] Previous studies had shown that this CoO_x catalyst film contains phosphate groups as a disordered component of the structure when formed electrochemically from phosphate-buffered solution.[116]

The OTF-PEC was prepared by spin coating the phosphonate-derivatized PDI dye, N,N'-bis(phosphonomethyl)-3,4,9,10-perylenediimide (**PMPDI**, Fig. 2.11a), from basic aqueous solution onto ITO, then dipping the film in acid to protonate the phosphonate groups and render the dye film insoluble in neutral water. These 40–50 nm-thick films were then submerged in pH 7 potassium phosphate (KPi)-buffered aqueous solution containing 1 mM $Co(NO_3)_2$. With white light illumination and an applied bias of +0.7 V vs Ag/AgCl (providing a driving force for electron collection but below the oxidation potential of Co^{II}), Co^{II} in solution was oxidized by photo-generated holes in the **PMPDI** valence band and CoO_x was therefore photoelectrochemically

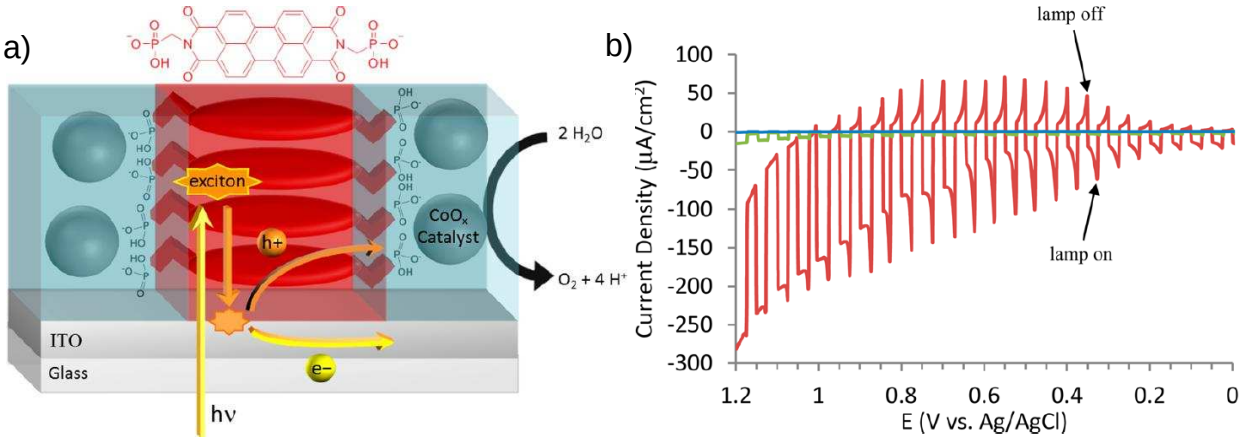

Fig. 2.11 (a) Schematic illustration of the ITO/**PMPDI**/CoO_x OTF-PEC photoanode, where **PMPDI** is N,N'-bis(phosphonomethyl)-3,4,9,10-perylenediimide. (b) *J*–*V* curve with transient illumination for ITO/**PMPDI**/CoOx (red line), ITO/**PMPDI** (green line), and bare ITO (blue line) in pH 7 KPi buffer, 5 mV/s scan rate starting from 0.0 V with 5 s light transients. Reprinted with permission from Ref. 80. Copyright 2014, American Chemical Society.

deposited throughout the film. XPS studies confirmed that cobalt was retained by the film after rinsing.[80]

The *J–V* curve for these ITO/**PMPDI**/CoO_x anodes submerged in pH 7 KPi with transient illumination by a Xe arc lamp (100 mW/cm², λ = 315–710 nm) reveal anodic photocurrents with initial spikes that then decay to steady-state values over the course of several seconds (Fig. 2.11b, red trace). The authors attributed this behavior to a balance between the rates of exciton dissociation, charge recombination, and WOC reactions.[80] As the applied bias to the ITO substrate was increased, both the spike and steady-state photocurrents steadily increased, likely a result of enhanced rates of exciton dissociation and decreased rates of recombination reactions. The steady-state anodic photocurrents reached as high as 150 μA/cm² at +0.95 V vs Ag/AgCl (+1.56 V vs RHE).[80] According to Table 2.2, these are the highest water-oxidizing photocurrents reached by an OTF-PEC, which is somewhat surprising given the simple composition of the device. Control experiments with bare ITO (Fig. 2.11b, blue trace) showed photocurrents <1 μA/cm², and ITO/**PMPDI** films without CoO_x (Fig. 2.11b, green trace) showed photocurrents <10 μA/cm², indicating that CoO_x was indeed necessary to improve the efficiency of the OER, and must be electronically coupled with the **PMPDI** film for charge transfer to occur.

During the scan, dark cathodic current spikes were present for ITO/**PMPDI**/CoO_x anodes but not for ITO/**PMPDI** controls without CoO_x (Fig. 2.11b). At higher applied potentials, these spikes decrease. This suggests that recombination reactions with hole equivalents stored in the CoO_x catalyst are kinetically competitive with the desired OER, but become less favored at higher applied potentials. *Steady-state* dark currents were negligible at potentials up to +1.0 V vs Ag/AgCl (1.61 V vs RHE). At higher potentials, anodic dark currents flowed, corresponding to the onset potential for direct electrochemical WOC by the CoO_x catalyst.[80] Taken together, these

data suggest that the **PMPDI** film is porous, with CoO_x catalyst near to the ITO substrate. Therefore, one hypothesis is that the hydrophilic, anionic phosphonate groups of PMPDI provide H^+-conduction channels throughout the organic film, similar to those proposed above for sulfonate groups in the PTTh:**MnPor** system by Chen and Swiegers *et al*.[87]

IPCE experiments were performed in a 2-electrode configuration at short-circuit with a Pt wire counter electrode. The resulting action spectrum was a good match for the absorptance spectrum of the **PMPDI** film, and reached a maximum IPCE of 0.12%. Unfortunately, given that the E_{CB} of the **PMPDI** film is not sufficiently negative for the HER,[80] the photocurrents flowing during the IPCE measurements could not have corresponded to the overall water-splitting reaction (that is, the reduction reaction at the Pt counter electrode is unknown, and may have been limiting photocurrents). However, **IPCE** measurements with added sacrificial reductants $K_4Fe(CN)_6$ or hydroquinone (H_2Q) also matched the **PMPDI** absorptance spectrum, and reached IPCE values of 0.32% and 0.69%, respectively.[80]

Importantly, extended photolysis experiments were performed for ITO/**PMPDI**/CoO_x photoanodes at a bias of +1.51 V vs RHE and O_2 product was detected by a Clark electrode with a Faradaic efficiency of 80 ± 15%.[80] During such experiments, steady-state photocurrents gradually decayed by ~30% within only 5 min, suggesting some unknown, gradual deactivation of the system that remains to be characterized. In an efficiency analysis, it was determined that the ITO/**PMPDI**/CoO_x system is most limited by the efficiency of charge dissociation and transport[80] (that is, recombination reactions dominate), which may explain why such high applied potentials were needed to reach maximum photocurrents (Fig. 2.11b). Performance was also significantly limited by the low light absorbance of the thin **PMPDI** films. Thicker films showed *worse* performance, likely due to the longer exciton diffusion distance.[80] In the end, Gregg and Finke *et*

al. predicted that their system may be improved by employing their dye in a DS-PEC architecture (such as those in the following section) due to improved light absorption and possibly decreased recombination.[80] An initial paper testing this hypothesis has been submitted for publication.[117]

A second example of a water-oxidizing single-layer OTF-PEC system was recently published by Sivula *et al*. in 2015.[89] This system is based on the n-type conjugated polymer poly(benzimidazobenzophananthroline) (BBL, structure shown in Fig. 2.12). In that study, two separate film deposition methods were used to test the effect of film morphology. In one strategy, films were dip coated onto glass coated with conducting fluorine-doped tin oxide (FTO) from a BBL solution in methanesulfonic acid. In a second strategy, an aqueous solution of BBL nanofibers was prepared by a "wet spinning" method, which was then spray coated onto a hot FTO substrate. The different film morphologies are shown in SEM images in Fig 2.12. The dip-coated

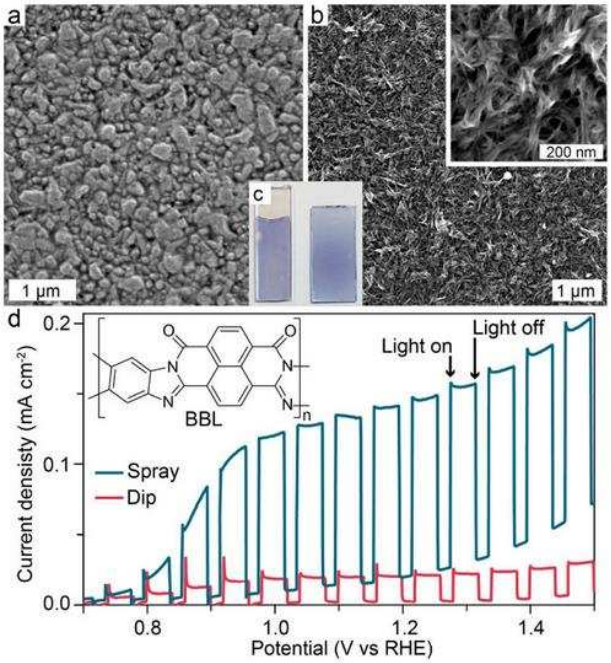

Fig. 2.12 SEM images of BBL films on FTO prepared by dip-coating (a) and spraying (b), along with optical images of each electrode (c). Panel (d) shows *J*–*V* curves for a sprayed film (blue line) and a dip-coated film (red line) in sacrificial electrolyte (0.5 M Na_2SO_3, pH 7) while under transient illumination to the substrate. Scan rate was 10 mV/s. Reprinted from with permission Ref. 89. Copyright 2015, American Chemical Society.

film shows homogeneous coverage of the FTO with globular BBL particles ranging from 100–500 nm, whereas the spray-coated films show a rough, interconnected network of BBL nanofibers.[89] We note that the nano-structure and film porosity of the latter architecture could potentially result in (i) fully depleted, field-free semiconductor and (ii) facile electrolyte transport throughout the film. Both of these factors could eliminate the contribution of charge carrier migration influenced by macroscopic electric fields, leaving diffusion as the major charge transport process, similar to nanoporous TiO_2 in DSSC applications.[118,119]

When the two FTO/BBL films of similar thickness (~40 nm) and similar light absorptance were submerged in pH 7 electrolyte with the sacrificial reductant Na_2SO_3, *J*–*V* curves with transient illumination (100 mW/cm² white light) revealed that photocurrents for the spray-coated film were 6.5-fold higher than the dip-coated film. This suggests that the nanofiber morphology offers advantages of shorter exciton transport distances and higher surface area at the SCLJ where hole transfer occurs.[89] In this way, we propose that it may be more appropriate to consider such an architecture as an "organic semiconductor–electrolyte bulk heterojunction" than a typically planar, Schottky-type PEC. In the absence of sacrificial reductant, thicker spray-coated BBL films (still without WOCatalyst) were subjected to electrochemical impedance spectroscopy and Mott–Schottky analysis in aqueous solutions of varying pH. The results showed evidence for the formation of a depletion region at high applied potentials, and that band energies were approximately constant within the pH range of 3.5 to 10.5.[89] As such, higher photocurrents observed for FTO/BBL anodes in higher-pH solutions are consistent with a higher driving force for the OER (which shifts negatively with pH).[89]

IPCE measurements for FTO/BBL anodes in pH 7 buffer with an applied bias of +1.23 V vs RHE matched the absorptance spectrum of the BBL film. However, O_2 product was not

observed by GC analysis of the headspace gases under these conditions, so photocurrents observed from the FTO/BBL films could not be attributed to the desired OER. In pH 7 buffer without a sacrificial reductant, a fluorescence probe technique provided evidence that illumination of FTO/BBL anodes generated trace hydroxyl radical, a possible byproduct of photoelectrochemically generated H_2O_2.[89] This suggests that BBL may be capable of the direct (that is, without an added WOCatalyst) photo-oxidation of water to H_2O_2, a reaction which requires a higher thermodynamic potential than the OER, but which involves only two electrons instead of four. These FTO/BBL films in pH 7 buffer were subjected to extended photolysis for at least 120 min. Photocurrents decayed by 43% within the first 10 min, then stabilized at a steady-state value. Over the extended electrolysis, the film passed more charge than would have been theoretically required to oxidize the entire BBL film, suggesting that currents did not originate from BBL degradation.[89] Furthermore, SEM and Raman characterizations of the film before and after the extended photolysis revealed no discernible morphological or structural changes by those physical methods.

In order to catalyze the desired OER, ~230-nm-thick BBL films were decorated with an earth-abundant Ni-Co WOCatalyst. Attempts to load the catalyst directly onto the BBL surface did not produce O_2, possibly due to poor adhesion and/or poor electrical contact. However, when the BBL films were first coated with a thin-film (1 nm) of TiO_2 by atomic layer deposition (ALD), then spin coated with nickel and cobalt salts and annealed, a successful interface was achieved.[89] In pH 7 buffer, such "buried junction"[10] FTO/BBL/TiO_2/Ni-Co films reached steady-state photocurrents as high as ~20 μA/cm² at an applied potential of +0.9 V vs RHE. While the application of the TiO_2 and Ni-Co catalyst did not significantly enhance photocurrents, they were necessary to observe O_2 product, with a faradaic efficiency of 82 ± 16%.

Overall, the Sivula *et al*. system provides important evidence that the morphology of the OSC film and SCLJ can significantly affect photoelectrochemical performance. Specifically, the small domain size of BBL nanofibers achieved by "wet spinning" and spray coating appear to enhance the charge collection efficiency by decreasing the distance that excitons had to travel in order to dissociate at the SCLJ. The high surface area of the SCLJ also likely enhances the efficiency of hole transfer to the electrolyte. Furthermore, the BBL material exhibits promising stability for an organic material, with no detected evidence for oxidative degradation. Finally, the use of ALD TiO_2 proved to be an effective method to couple the WOCatalyst to the organic dye. Still, Sivula *et al.* hypothesized that performance was likely limited by interfacial exciton dissociation, and suggested that improvements might be achieved through the use of a solid-state semiconductor heterojunction or charge-separating overlayers.[89]

Before continuing, we would like to point the interested reader towards additional OTF-PEC photo*cathode*s for the HER,[66,74,102,103,111,120–130] though it is beyond the scope of this review to detail each specific system. These include single-bandgap OSC thin-films[66,111,122] as well as organic-bilayer heterojunctions[120,121] and bulk-heterojunction systems.[74,102,103,123–130] This field has benefitted from the fact that the model polymer–fullerene (P3HT:**PCBM**) bulk-heterojunction OPV has appropriate band energies to drive the HER, which has led to faster progress relative to OTF-PEC photo*anodes*. Major improvements in cell performance and stability have been achieved not by making significant changes to the active layer, but by judicious selection and application of various interfacial layers to enhance charge-collecting efficiencies.[74,103,123–129] Additional systems of note include multi-junction OPV/electrolyzer systems,[15,16] as well as a (buried) triple-junction OPV artificial leaf.[17] Such multi-junction architectures allow for the generation of sufficient photovoltage for overall water splitting.

2.4 Water Oxidizing Dye-Sensitized Photoelectrolysis Cells (DS-PECs)

Compared to water-oxidizing OTF-PECs, far more DS-PEC systems have been published, and are the subject of several recent review articles.[42–51] However, the vast majority of DS-PECs employ $Ru^{II}(bpy)_3$-type sensitizer dyes (bpy = 2,2'-bipyridine) which are historically popular and well-understood in DSSC studies.[39,40,131] Indeed, the two top-performing water-oxidizing DS-PECs employ TiO_2 nanoparticle films with surface-anchored $Ru^{II}(bpy)_3$-type dyes and Ru-based organometallic WOCatalysts.[132,133] These cells exhibit steady-state photocurrents as high as ~1,100 μA/cm² and maximum incident photon-to-current efficiencies (IPCEs)[59] as high as 14% (while using an applied electrochemical bias and under ~*3-sun*, 300 mW/cm² illumination).[132,133] Unfortunately, these Ru-based dyes and catalysts depend on a low-abundance, relatively expensive transition-metal.[60] Therefore, this review will highlight the important fundamental studies which have tested DS-PECs containing all-organic sensitizer dyes or organometallic dyes containing first-row transition metals.

Many all-organic dyes have been studied in DSSCs[40,131,134], as well as dye-sensitized photocatalytic (colloidal suspension) systems.[70] Broadly, all-organic dyes tend to have higher molar extinction coefficients than metal complexes, but are more prone to aggregation on the nano-MO_x surface, which can enhance non-radiative relaxation processes and result in poor excited-state-injection efficiency.[40,131,134] To alleviate aggregation, co-adsorber molecules are sometimes added to the dying solution, or molecular engineering of the dye can include sterically bulky groups to make π-stacking unfavorable.[40,131,134] However, it should be noted that examples exist where aggregation has enhanced efficiency due to improved light absorption by the dye aggregates.[135]

Organic dyes have also been employed in water-splitting DS-PECs. In what follows, we highlight literature examples of water-oxidizing DS-PEC photoanodes (summarized in Table 2.3),

Table 2.3. Summary of the known DS-PEC water-oxidizing photoanodes using organic sensitizers.

Sensitizer[a]	WOCatalyst[a]	Substrate	Max Steady-State Photocurrents (Conditions)[b]	Faradaic Efficiency	Max IPCE (appl. bias)[b,c]	Corresponding Author(s)
ZnPor1	**Cp*Ir**	TiO_2	**30 μA/cm²** (pH 7 Na_2SO_4, +0.91 V vs RHE, 200 mW/cm², λ>400nm)	ND	ND	Schmuttenmaer, Crabtree, & Brudvig[136]
H_2Por(s)	IrO_2 NPs	TiO_2	**40 μA/cm²** (pH 6.8 NaPi, +0.70 V vs RHE, "AM 1.5", λ>410 nm)	102±5%	0.036% (+0.70 V)	Mallouk[137]
ZnPor2	**Ru–bda1** (covalent dyad)	TiO_2	**110 μA/cm²** (pH 7.3 NaPi, +0.23 V vs RHE, 35 mW/cm², λ>380 nm)	33%	17±1% (+0.42 V)	Sun & Imahori[138]
SubPor	**Ru–bda2**	TiO_2	**60 μA/cm²** (pH 7.3 NaF, +0.64 V vs RHE, 100 mW/cm², λ>420nm)	64%	6% (+0.64 V)	Sundström, Sun, & Imahori[139]
TEPDI	IrO_2 NPs	WO_3	**70 μA/cm²** (pH 3 $NaClO_4$, +0.92 V vs RHE, 100 mW/cm², λ>435nm)	ND	0.8% (+0.92 V)	Prato, Caramori, & Bignozzi[140]
PMI	**Cp*Ir-Sil**	TiO_2/Al_2O_3 core/shell	**15 μA/cm²** (pH 5.8, KNO_3, +0.71 V vs RHE, 100 mW/cm², λ>420nm)	20%	ND	Wasielewski[141]
D–A	**Ru–pdc1**	TiO_2	**300 μA/cm²** (pH 7 KPi, +0.61 V vs RHE, 100 mW/cm², λ>400nm)	73%	ND	Sun[75]
D-π-A	**Ru–bda3**	SnO_2/TiO_2 core/shell	**100 μA/cm²** (pH 7 Pi, +0.86 V vs RHE, 100 mW/cm², λ>400 nm)	8.2%	ND	Meyer[142]
g-C_3N_4	IrO_2 NPs	TiO_2	**120 μA/cm²** (pH 7 Pi, +1.42 V vs RHE, λ>420nm)	19%	7±1% (+1.42 V)	Beranek[79,143]

[a] Abbreviations are defined throughout the text and summarized in a List of Abbreviations at the end of this dissertation. [b] Applied bias has been converted to the RHE reference electrode for direct comparison between systems. [c] Note that IPCEs measured under applied bias ≠ η_{STH}.

covered in semi-historical order, but organized by sensitizer type. Before continuing, we again point the interested reader towards several published DS-PEC photo*cathodes* for the HER,[75,144–152] including many that employ earth-abundant sensitizer dyes.[75,145–147,149–152] We note, however, that the performance of DS-PEC photocathodes tend to lag behind that of photoanodes due to the lack of a highly efficient hole-conducting nano-porous substrate, the most common being NiO.[40]

Aromatic Macrocycle Dyes. As mentioned above, porphyrin and phthalocyanine derivatives have long been studied as light collectors in OPVs, DSSCs, and PECs, in part because of their relation to chlorophyll pigments used in natural photosynthesis.[84] In fact, a porphyrin derivative is responsible for the top-performing DSSC to date.[153] As such, it is not surprising that the first example of an organic dye used in a water-oxidizing DS-PEC was a porphyrin, published in 2011 from the groups of Schmettenmaer, Crabtree, and Brudvig.[136] Their system employed a zinc-porphyrin sensitizer dye (**ZnPor1**, Fig. 2.13) anchored on the surface of a sintered TiO_2 nanoparticle (NP) film. To our knowledge, this was also the first example in the literature to use the strategy of co-loading the nano-TiO_2 film with an anchored, molecular WOCatalyst. The specific catalyst used was an Ir

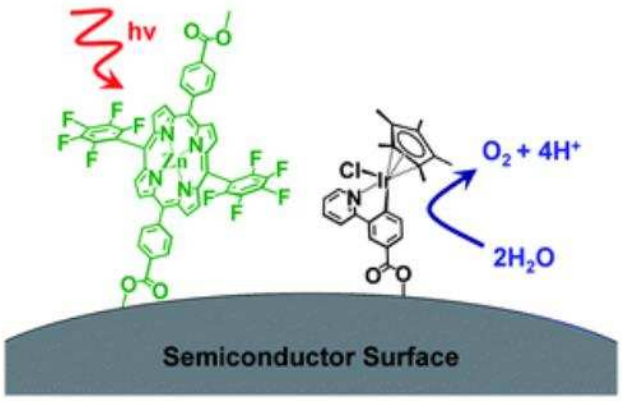

Fig. 2.13 Schematic representation of the water-oxidizing DS-PEC employing a high-potential Zn-porphyrin (**ZnPor1)** and Ir organometallic WOCatalyst (**Cp*Ir**), co-anchored on a sintered TiO_2 nanoparticle film. Reproduced from Ref. [136] with permission of The Royal Society of Chemistry.

complex with a carboxylic acid anchor group (**Cp*Ir**, Fig. 2.13), belonging to a class of Cp*Ir-type WOCatalyst[154] originally developed by the groups of Eisenstein, Crabtree, and Brudvig.[155] The specific Por dye was functionalized with pentafluorophenyl electron-withdrawing groups (Fig. 2.13) which shift the oxidation potential of the dye positive of the onset potential of the Ir-complex WOCatalyst.[136]

When submerged in pH 7, 0.1 M Na_2SO_4 and illuminated with 200 mW/cm² white light (through a 400 nm long-pass filter, to eliminate direct bandgap excitation of TiO_2 by UV light), TiO_2 films sensitized with both **ZnPor1** and the **Cp*Ir** WOCatalyst (TiO_2/**ZnPor1**:**Cp*Ir**) exhibited photocurrents of ~30 μA/cm² at an applied bias of +0.3 V vs Ag/AgCl (+0.91 V vs RHE). Controls with only **ZnPor1** or **Cp*Ir** anchored to TiO_2 both reached photocurrents of only ~5 μA/cm². Rotating ring-disc experiments were used to confirm O_2 production for TiO_2 films loaded with **Cp*Ir** WOCatalyst under electrochemical conditions, albeit not for the full device under photoelectrochemical conditions. The authors concluded that the photocurrent controls were consistent with light-activation of the catalyst by electron injection from the photo-excited dye into the TiO_2 CB, followed by hole transfer from the photo-oxidized dye(s) to Ir sites.[136] Overall, the system by Schmettenmaer, Crabtree, and Brudvig constitutes the first example of a water-oxidizing DS-PEC employing a dye composed only of earth-abundant elements, and also the first example of any DS-PEC to use the strategy of co-anchoring a molecular WOCatalyst.[136]

In 2015, the Mallouk group reported the results of a study in which they employed a series of metal-free porphyrin derivatives (H_2Por) as sensitizers on TiO_2 films, along with co-loaded IrO_2 NP WOCatalyst.[137] Following a previous study,[83] citrate-capped IrO_x NPs (~2 nm diameter) were loaded onto bare TiO_2 films (prior to dye loading) by soaking from colloidal solution, followed by calcination at 450 °C to burn off the ligands and crystallize the IrO_2 NPs. Such crystalline IrO_2

particles are more active WOCatalyst, but their location directly on the surface of TiO_2 makes the scavenging of TiO_2 CB electrons by the catalyst the dominant recombination pathway.[83] To minimize recombination, the concentration of IrO_2 NPs was kept low. However, this strategy adds the requirement that the dye monolayer be conductive to holes in order for the highly dispersed catalyst to regenerate many surrounding dye molecules (Fig. 2.14).

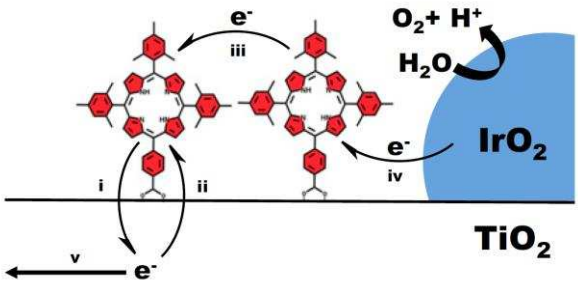

Fig. 2.14 Schematic of the DS-PEC system composed of H_2Por-sensitized TiO_2 co-loaded with IrO_2 nanoparticle WOCatalyst. The scheme displays various electron transfer processes: (i) injection, (ii) recombination, (iii) hole transfer, (iv) regeneration of oxidized sensitizer, and (v) diffusion to the FTO substrate. Reproduced from Ref. [137].

The series of porphyrin derivatives included differing numbers and positions of sterically bulky mesityl (electron donating) groups, as well as a few derivatives with multiple carboxylate (electron withdrawing) groups. These varying substitutions shifted the oxidation potentials of the dyes over a range of roughly 200 mV.[137] In pH 6.8 sodium phosphate (NaPi) buffer and illumination by a Xe arc lamp through AM1.5 and 410 nm long-pass filters, TiO_2/H_2Por:IrO_2 photoanodes exhibited peak photocurrent spikes followed by steady, gradual decay. The top porphyrin dye reached a peak photocurrent spike of ~85 μA/cm², which decayed down to ~40 μA/cm² after 15 s and down to ~10 μA/cm² after 10 min.[137] Other dyes in the series exhibited photocurrents within the same order of magnitude. Differences in performance were somewhat less pronounced than expected by the varying electronic properties. The authors rationalized this result based on energetic tradeoffs; dyes with more negative HOMO and LUMO energies had a higher driving force for electron injection into TiO_2, but a lower driving force for the OER.[137]

Most of the $TiO_2/H_2Por:IrO_2$ anodes studied showed no appreciable change in the UV–vis spectra after 10 min of electrolysis, indicating their general stability at least over that timescale. IPCE values were estimated by the lamp power and the integrated current collected over 10 min, reaching only 0.036 ± 0.007% at best.[137]

The faradaic efficiency for O_2 production measured for one representative dye was 102 ± 5%.[137] For this calculation, O_2 product was detected electrochemically in solution by a previously developed Generator–Collector method[81–83] wherein a planar platinized electrode (collector) is sandwiched several mm away from the working electrode (generator) and held at a potential sufficient to reduce any O_2 that diffuses from the working electrode. While this technique is not rigorously selective for O_2 (any chemical species that reaches the collector and that can also be reduced at equal or more positive potential could also contribute to collector current), controls using various applied potentials for both generator and collector electrodes can improve confidence that O_2 is the product being detected.[156] Furthermore, the high collection efficiencies achievable by the Generator–Collector method make it especially useful in the DS-PEC field where photocurrents are often quite small and can decay quickly.

As a control, results for the H_2Por dyes were compared to the better-studied $[Ru^{II}(bpy)_2(4,4'\text{-}(PO_3H_2)_2bpy)]^{2+}$ dye under the same conditions.[137] Despite absorption of a wider portion of visible light by the H_2Por dyes and comparable dye surface loading, photocurrents for the H_2Por dyes were roughly half those achieved by the $Ru^{II}(bpy)_3$-type dye. The authors determined that this result was at least partially caused by (i) lower excited-state electron injection efficiencies (estimated at approximately 2.4 to 7.4% for the various H_2Por dyes vs 21% for the $Ru^{II}(bpy)_3$-type dye), despite similar thermodynamic driving force for injection of ~130 mV, and (ii) low hole diffusion coefficients through the dye monolayer (not detectable, $<10^{-11}$ cm^2/s for the

H_2Por dyes compared to 10^{-9}–10^{-10} cm²/s typically for $Ru^{II}(bpy)_3$-type dyes).[137] All in all, this valuable study demonstrated that a variety of all-organic H_2Por dyes are capable of photoelectrochemically-driven water oxidation in DS-PEC architectures, and with IrO_2 NP WOCatalyst.

In early 2016, the groups of Sun and Imahori co-published a third example of a water-oxidizing DS-PEC employing an aromatic macrocycle sensitizer dye, specifically another Zn-Por derivative.[138] This group used an alternative strategy wherein the sensitizer and the WOCatalyst are covalently attached as a *molecular dyad* (**Ru-ZnP**, Fig. 2.15). The WOCatalyst chosen has the

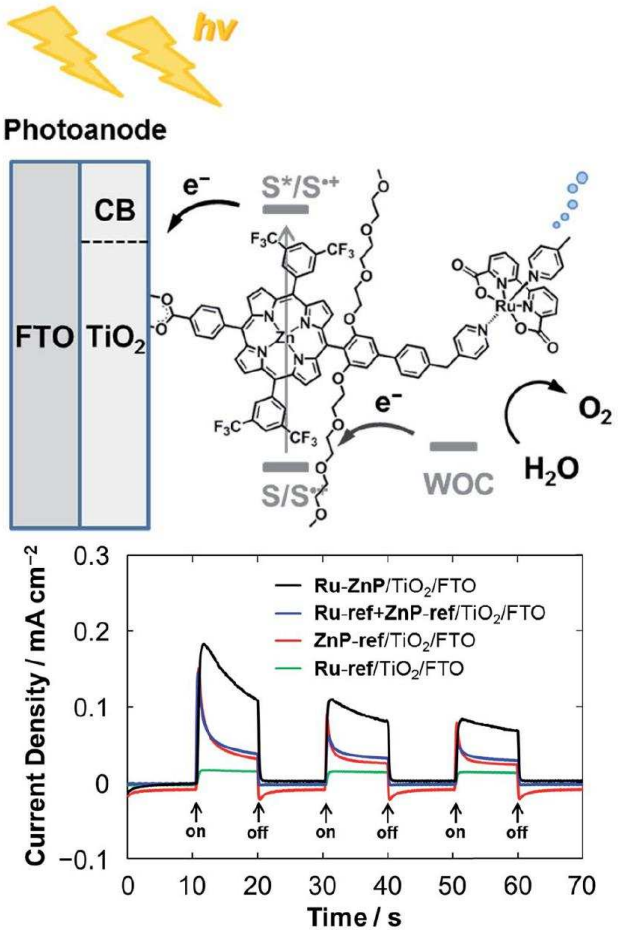

Fig. 2.15 (upper) A schematic diagram of the DS-PEC composed of a molecular sensitizer–catalyst dyad (**Ru-ZnP**) anchored to nano-TiO_2. (lower) The current–time responses for TiO_2/**Ru-ZnP** (black), TiO_2/**ZnP-ref:Ru-ref** (blue), TiO_2/**ZnP-ref** (red), and TiO_2/**Ru-ref** (green) electrodes under transient white light illumination in pH 7.3 buffer and at +0.23 V vs RHE. Reproduced from Ref. [138]-Published by The Royal Society of Chemistry.

[Ru(bda)(pic)$_2$] structural motif[154] (bda = 2,2'-bipyridine-6,6'-dicarboxylate, pic = 4-picoline) developed by the Sun group.[157] Hereafter, we will use the nomenclature of Ru–bda to describe this class of catalyst which contains both bda and pic ligands, either of which may be functionalized with anchor or linking groups. Note that in Table 2.3, we refer to the **Ru-ZnP** dyad as separate components **ZnPor2** and **Ru–bda1** to indicate the respective molecular components. The molecular dyad strategy follows from the hypothesis that a covalent linkage will ensure that the WOCatalyst is always in close proximity to the sensitizer dye and should promote rapid electron transfer from the WOCatalyst to the photo-oxidized dye after excited state electron injection into the TiO_2 conduction band (Fig. 2.15). Such a configuration should also negate the need for extended hole conductivity across the dye monolayer, as required for the previous system depicted in Fig. 2.14.

When submerged in pH 7.3, 0.1 M NaPi buffer and illuminated with a halogen lamp (35 mW/cm², $\lambda > 380$ nm; note the possible direct bandgap excitation of TiO_2) and held at a potential of +0.23 V vs RHE, a TiO_2 film dyed with the molecular dyad (**Ru-ZnP**) exhibited a peak photocurrent of ~180 μA/cm², which quickly decayed to ~110 μA/cm² after 10 s of illumination. At the end of two additional 10 s light transients, steady-state photocurrent had decayed by ~35% to 70 μA/cm² (Fig. 2.15). The photocurrent action spectrum was a good match for the dye's absorptance spectrum, with a maximum IPCE value of 17% at the λ_{max} of the dye. Notably, this maximum IPCE value for the TiO_2/**Ru-ZnP** system is higher than the best-performing water-oxidizing DS-PEC to date,[132] which used the common $[Ru^{II}(bpy)_2(4,4'\text{-}(PO_3H_2)_2bpy)]^{2+}$ dye with a co-anchored Ru–bda catalyst (TiO_2/Ru(bpy)$_3$:Ru–bda).[132] That system reached an IPCE of 14%, though with a higher faradaic efficiency of 83%.[132]

As an important control, individual molecular analogues of the individual components of the **Ru-ZnP** dyad were also prepared (**ZnP-ref** and **Ru-ref**, respectively).[138] Control photoanodes were prepared by adsorbing only **ZnP-ref**, only **Ru-ref**, or co-adsorbed **ZnP-ref** : **Ru-ref** in a 1:1 molar ratio. Under the same conditions as above, TiO_2/**ZnP-ref** anodes without catalyst showed steady-state photocurrents of ~30 μA/cm² and TiO_2/**Ru-ref** anodes without dye showed steady-state photocurrents of ~10 μA/cm² (Fig. 2.15). Surprisingly, co-adsorbed TiO_2/**ZnP-ref**:**Ru-ref** anodes showed no photocurrent enhancement relative to the TiO_2/**Zn-ref** anode (Fig. 2.15), which suggests inefficient intermolecular electron transfer from the Ru–bda WOCatalyst to the ZnPor dye when they are not covalently linked.[138]

The rapid decay in photocurrent for the TiO_2/**Ru-ZnP** anode shown in Fig. 2.15 suggests some instability to the system. Consistent with this, O_2 detection experiments found a faradaic efficiency of only 33% after 1h of electrolysis, with a turnover number of only 1.3 per **Ru-ZnP** dyad. UV–visible, IR, and XPS studies of the films before and after 1h of electrolysis gave no indication that the **Ru-ZnP** dimer degraded or desorbed, but the Ru component had evolved to higher oxidation states. Therefore, the authors concluded that the Zn-Por dye was not sufficiently oxidizing to generate the higher oxidation states of Ru at appreciable turnover rates.[138] An alternative hypothesis here is that oxidation of the poly(ethylene glycol) chains of the dye structure (Fig. 2.15, the purpose of which were not discussed in the paper) may have contributed to the low faradaic efficiencies.

Near the end of 2016, the groups of Sundström, Sun, and Imahori published an additional DS-PEC system which employed a novel subporphyrin sensitizer dye, **SubPor**.[139] **SubPor** incorporates a carboxyphenyl electron-withdrawing anchor group and two triphenylamine electron-donating groups (Fig. 2.16). The molecule can therefore be considered a donor–acceptor

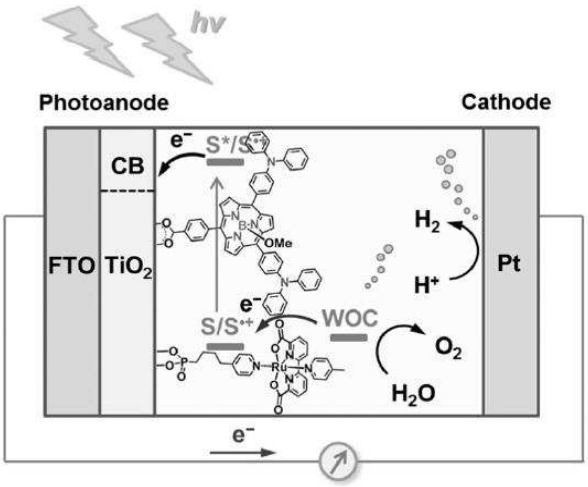

Fig. 2.16 Schematic diagram of the DS-PEC system composed of a "push–pull" subporphyrin sensitizer dye (**SubPor**) and a Ru–bda type WOCatalyst (**Ru–bda2**) co-anchored on nano-TiO_2. Reproduced from Ref. [139]-Published by The Royal Society of Chemistry.

(D–A) type dye, or "push–pull" dye, wherein the electron density of the HOMO is spatially distributed closer to the triphenylamine groups and the electron density of the LUMO is spatially distributed closer to the anchor group.[139] This type of electronic engineering of the dye is expected to enhance electron injection from the excited state into TiO_2 via the anchor group, and decrease recombination because the hole (empty HOMO) is distributed further away from the TiO_2 surface. Anodes were prepared by stepwise co-adsorption of **SubPor** and a Ru–bda type WOCatalyst (**Ru–bda2**) in a ratio of 7.5:1 (Fig. 2.16). The groups of Gao and Sun had previously found that using a propylene spacer between the Ru–bda WOCatalyst and the phosphonate anchor group showed superior performance relative to a methylene spacer.[158] This may be a result of enhanced linker flexibility improving the efficiency with which the catalyst can regenerate surrounding photo-oxidized dye, or possibly a result of a decreased rate of recombination between the catalyst and the CB electrons in the MO_x because of the increased linker distance.

When submerged in pH 7, 0.1 M NaF solution (this electrolyte showed a ~50% improvement in photocurrent relative to NaPi) and illuminated with white LED light (100

mW/cm², λ > 420 nm), anodes with co-loaded TiO_2/**SubPor**:**Ru–bda2** exhibited photocurrents which stabilized at ~60 μA/cm² after 30 s. Controls using anodes with only **SubPor** or only **Ru–bda2** loaded on TiO_2 showed photocurrents of 6 and 0 μA/cm², respectively. The action spectrum for TiO_2/**SubPor**:**Ru–bda2** anodes was a close match for the absorptance spectrum of **SubPor**, with a maximum IPCE of 6% at the λ_{max} of the dye. Oxygen gas was measured by GC after 1 h of photolysis with a faradaic efficiency of only 64% and a catalytic turnover number of 27 ± 4. Additionally, $H_2{}^{18}O$-labeling studies showed $^{18}O_2$ product as well as trace ^{18}O-labeled CO_2, indicating that oxidative decomposition of **SubPor** and/or the **Ru–bda2** catalyst occurred along with water oxidation.[158]

Importantly, transient-absorption spectroscopy (TAS) experiments helped elucidate some of the kinetics of the relevant electron-transfer processes. The formation of photo-oxidized **SubPor** on TiO_2 (without catalyst) was observed with a time constant of 800 fs after a pump light pulse, providing evidence for the expected rapid electron injection from photo-excited **SubPor*** into TiO_2. The oxidized dye was returned to the ground state (by back-electron-transfer) with a half-life on the order of tens of ns, despite the push–pull dye engineering. However, the ground state recovery fitted rate constant was accelerated 85% in the presence of co-adsorbed **Ru–bda2** catalyst, indicating competitive electron transfer from the catalyst to the oxidized dye. The authors concluded that undesired rapid back-electron-transfer from TiO_2 to the photo-oxidized dye greatly limits the water-splitting efficiency, and as such, improving electron–hole separation should be the focus of future systems.[158]

In early 2016, the Jiang group published a rather non-conventional DS-PEC,[159] in that the high-surface-area, charge-transporting substrate was composed of carbon nanotubes (CNTs, rolled sheets of graphene) instead of sintered MO_x nanoparticles. CNTs are known to have excellent

charge transport properties due to their high conductivity and high aspect ratios.[159] Previously the Jiang group also showed that multi-walled carbon nanotubes (MWCNTs, concentric tubes) with 2–3 walls showed promising electrochemical water oxidation activity relative to those with higher numbers of walls or single-walled nanotubes.[160] In the current study, commercial MWCNTs (5–30 μm length) were purified and separated into fractions by a series of acid washes with sonication, and then suspended in ethanol solutions with 10% Nafion and various dyes: zinc(II) phthalocyanine (**ZnPc**), cobalt(II) phthalocyanine (**CoPc**), and $[Ru^{II}(bpy)_3]^{2+}$. These solutions were pipetted onto FTO glass and dried to form photoactive films of ~1 μm thickness, containing dye adsorbed on CNTs suspended within the water-and H^+-permeable Nafion matrix. A representative film was 60 wt% **ZnPc**, which was uniformly adsorbed onto MWCNTs by π–π stacking as determined by STEM-EDS.[159]

The **ZnPc** dye on MWCNTs showed a relatively weak light-absorption band in the visible region with λ_{max} of 665 nm, but strong absorption at $\lambda < 350$ nm. Light absorption by dyed CNT films was a distinct function of the nanotube composition (that is, the average number of CNT walls in the sample), with the highest light absorption by samples composed of mostly 3-walled CNTs (57% 3-walled CNTs, 20% 4-walled CNTs, and 19% 5-walled CNTs).[159,160] This phenomenon was not explained, but may be a result of the differing surface areas of the CNT films,[160] differing electronic coupling between the dyes and CNTs as a function of CNT diameter, or possibly a combination of the two. When submerged in 1 M KOH (pH 14) and illuminated with a transient white light from a xenon arc lamp (100 mW/cm², $\lambda > 250$ nm), FTO/CNT/**ZnPc** anodes showed varying photocurrents, which were also a function of the CNT film composition. Consistent with the light absorption trends, FTO/CNT/**ZnPc** samples composed of mostly 3-walled CNTs showed the highest photocurrents of 280 μA/cm² at +1.2 V vs RHE, which is quite

high compared to other water-oxidizing DS-PEC systems (Table 2.3). By contrast, FTO/CNT/**ZnPc** films composed of mostly *single-walled* CNTs showed roughly 2.5-fold lower photocurrents, and those composed of CNTs with >12 walls showed 4-fold lower photocurrents. Bubbles were observed on CNT/**ZnPc** films during photolysis, although analysis of the evolved gas to confirm O_2 product was not reported.[159]

For comparison, un-dyed CNT films containing mostly 3-walled CNTs displayed photocurrents of <50 μA/cm² at +1.2 V vs RHE. Films dyed with **CoPc** or $[Ru(bpy)_3]^{2+}$ dyes showed photocurrents that were roughly 2-fold lower and 2-fold higher, respectively, when compared to **ZnPc**-dyed CNT films at +1.2 V vs RHE.[159] The authors hypothesized that the films composed of mostly 3-walled CNTs showed the highest PEC activity because of enhanced electron–hole separation, as represented in Fig. 2.17. They propose that electron injection from the photo-excited dye to the outer CNT is followed by rapid electron tunneling to the inner tube(s), where the electron then diffuses to the conductive FTO substrate.[159] Given the previously

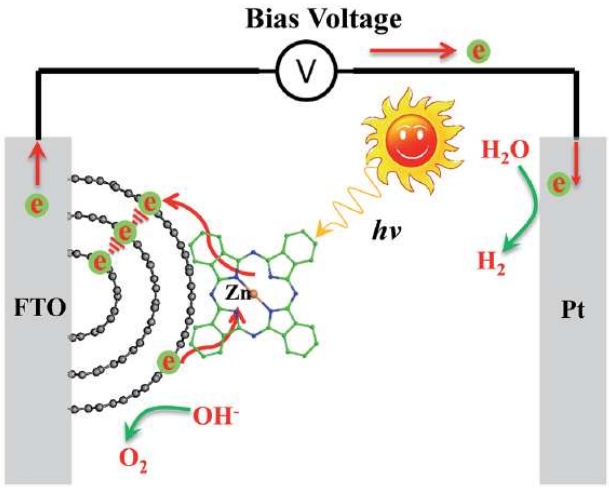

Fig. 2.17 Scheme for a PEC composed of a film of multi-walled carbon nanotubes (MWCNTs) sensitized with a zinc-phthalocyanine (**ZnPc**) dye. Electron injection is postulated to occur from the photo-excited dye into the outer carbon nanotube, followed by electron tunneling to the interior of the nanotube providing electron–hole separation. Reproduced from Ref. 159 with permission of The Royal Society of Chemistry.

demonstrated activity of MWCNTs for WOC,[160] the authors hypothesized that the outer-most CNT may transfer an electron to regenerate the photo-oxidized dye, and the OER may occur on the CNT surface.[159] Additional studies are needed to confirm that these resultant electron-transfer processes are energetically favorable.

Finally, we would like to draw attention to an alternative, noteworthy strategy for preparing a water-oxidizing DS-PEC. Instead of sensitizing nanostructured anodes with molecular analogues of the natural water-oxidizing photosystem II, several research groups have extracted the actual photosystem II complex from biological samples and loaded them on high-surface-area electrodes to perform photoelectrochemical WOC.[161–163] While such systems have achieved impressive oxygen-evolving photocurrents as high as ~275 μA/cm² at +0.5 V vs NHE in pH 6.5 buffer (+0.88 V vs RHE), the rapid decay of photocurrents with half-lives of <5 min indicate major stability concerns that remain to be addressed and overcome.[163]

In summary, aromatic macrocycle sensitizer dyes such as porphyrins, subporphyrins, and phthalocyanines have been the most commonly studied organic dyes for water-oxidizing DS-PECs. In fact, there are many additional studies concerning aromatic macrocycle dyes in DS-PECs en-route to water oxidation.[164–174] While these dyes are inspired by chromophores found in natural photosynthesis and absorb farther into the visible than the most common $[Ru^{II}(bpy)_2(4,4'\text{-}(PO_3H_2)_2bpy)]^{2+}$ sensitizer, they still have not extended light absorption beyond ~650 nm, leaving room for additional improvements.

Perylene Dyes. Like porphyrins and phthalocyanines, perylene diimide (PDI) molecules garnered early attention for OPV and PEC studies due to their unique properties, including high molar extinction coefficients, low band energies, liquid crystalline behavior, high electron mobility, as well as high thermal, oxidative, and photochemical stability.[63] The same properties

have made perylenes popular materials for water-splitting applications, such as the OTF-PEC systems highlighted above.[80,85,86,88,175] In addition, it has recently been demonstrated that suspended colloidal **PTCDA** or PDI nanostructures in the presence of sacrificial reductant are capable of light-driven water oxidation even without an intentionally added WOCatalyst.[98,176,177] Several studies have demonstrating the ability of PDIs to advance the oxidation states of WOCatalyst,[175,178–180] and to sensitize metal oxides in DS-PEC architectures,[179–182] though successful water oxidation has remained difficult to confirm.

In 2015 the groups of Prato, Caramori, and Bignozzi published the first example of a water-oxidizing DS-PEC system using the cationic perylene derivative, [N,N'-bis(2-(trimethylammonium)-ethylene)-3,4,9,10-perylenediimide]$(PF_6)_2$ (**TEPDI**), co-loaded onto a nanostructured WO_3 substrate with citrate-stabilized IrO_2 NP WOCatalyst (Fig. 2.18).[140] In addition to WO_3, the group also studied the sensitization of nanostructured TiO_2 and SnO_2 with their cationic PDI. This allowed for the comparison of injection dynamics from the relatively positive LUMO of **TEPDI** into substrates with different CB energies. **TEPDI** was able to adsorb on each of these materials, despite its lack of a traditional carboxylate or phosphonate anchor

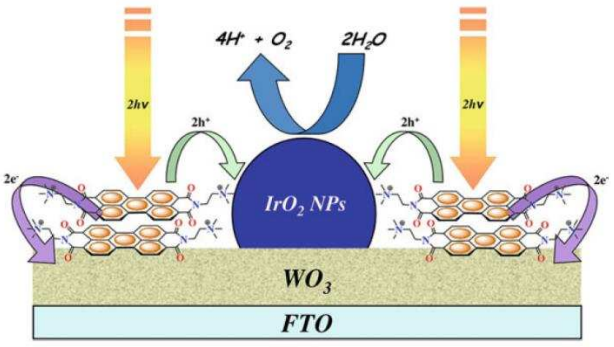

Fig. 2.18 Schematic of the DS-PEC device composed of a nanostructured WO_3 film sensitized with a cationic PDI dye, **TEPDI**, and decorated with IrO_2 NP WOCatalyst. "Photoinduced electron injection by PBI loaded on WO_3 by exploiting aggregation forces, triggers water oxidation at co-deposited IrO_2 nanoparticles." Reproduced from Ref. 50 (Copyright 2016 Springer International Publishing Switzerland) with permission from Springer.

groups. The authors hypothesized that the sensitization was caused by "aggregation/hydrophobic interactions".[140] In a DSSC configuration with LiI redox mediator, photocurrents were highest on WO_3, followed by SnO_2, then TiO_2. Consistently, transient spectroscopy experiments showed decreasing rates of injection from photo-excited **TEPDI** into the semiconductor CB in the order $WO_3 > SnO_2 > TiO_2$,[140] likely caused by a decreasing thermodynamic driving force in that order.[6,117] Furthermore, the WO_3 surface is the most acidic (lowest isoelectric point)[183] in the series, so the authors hypothesized that its negative surface charge even at low pH may enhance electronic coupling to the cationic **TEPDI**.[140]

After decoration with IrO_2 NP WOCatalyst, optimized WO_3/**TEPDI**/IrO_2 anodes were submerged in pH 3, 0.1 M $NaClO_4$ and illuminated with AM1.5G light (~100 mW/cm², $\lambda > 435$ nm). Steady-state photocurrents reached as high as ~70 A/cm² at +0.92 V vs RHE. For comparison, WO_3/**TEPDI** anodes without IrO_2 under the same conditions reached photocurrents of only ~16 μA/cm², and WO_3/IrO_2 anodes without dye reached photocurrents of ~8 μA/cm². WOC *was not confirmed* by the detection of O_2 products, but instead inferred from the previously demonstrated[184] activity of the IrO_2 NP catalyst. Action spectra were not a direct match to the **TEPDI** absorption spectrum, indicating that some light absorption by the yellow WO_3 may contribute to photocurrents, and a maximum IPCE of 0.8% was reached. Transient spectroscopy showed that regeneration of photo-oxidized **TEPDI** by IrO_2 occurs on the same timescale as back-electron-transfer recombination, and therefore is likely the kinetic bottleneck of the device.[140]

A second example of a water-oxidizing DS-PEC using a perylene sensitizer was published in 2017 from the group of Wasielewski *et al.*[141] In that study, a perylene monoimide (**PMI**, Fig. 2.19) dye was used to sensitize nano-TiO_2. Following literature precedent,[185,186] the dyed anode was subsequently treated with varying thicknesses of Al_2O_3 overlayer by atomic layer deposition

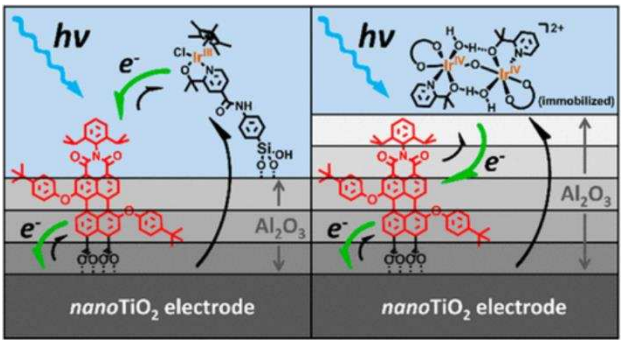

Fig. 2.19 Schematic representation of a nano-TiO_2 film sensitized with perylene monoimide (**PMI**). The dyed film was subsequently treated with an Al_2O_3 overlayer by atomic layer deposition to partially encapsulate the dye, increasing its stability. The TiO_2/**PMI**/Al_2O_3 films were subsequently decorated with monomeric **Cp*Ir-Sil** (left panel) or dimeric **IrIr** (right panel) WOCatalysts. Reproduced with permission from Ref. [141]. Copyright 2017, American Chemical Society.

(ALD). The Al_2O_3 overlayers were found to enhance the stability of **PMI** on the TiO_2 surface relative to untreated films.[141] ALD overlayers have also previously been shown to reduce recombination between conduction band electrons and oxidants at the surface or in solution, due to the passivation of MO_x surface states and the creation of a tunneling barrier for electron transfer.[187,188] After ALD treatment, TiO_2/**PMI**/Al_2O_3 films were decorated with either a dimeric, **IrIr,** WOCatalyst which binds directly to the MO_x surfae[189] (Fig. 2.19, right panel) or a monomeric Cp*Ir-type WOCatalyst with a phenylene spacer and strongly-binding silatrane anchor group, **Cp*Ir-Sil**[190] (Fig. 2.19, left panel).

Transient absorption spectroscopy of the dry films suggested that TiO_2/**PMI** can oxidize both **IrIr** and **Cp*Ir-Sil** to form the TiO_2^-/**PMI**/Al_2O_3/Cat^+ charge-separated state.[141] Thicker Al_2O_3 layers slow the rate of charge transfer between catalyst and dye, but also increase the lifetime of the TiO_2^-/**PMI**/Al_2O_3/Cat^+ charge-separated state.[141] In aqueous electrolyte and illumination (~100 mW/cm², $\lambda > 420$ nm), photocurrents for TiO_2/**PMI**/Al_2O_3 anodes without catalyst were enhanced for samples with thicker Al_2O_3 layers up to 20 deposition cycles, likely due to passivation of recombination-active TiO_2 surface states and an increased tunneling barrier

for recombination from any redox active species in solution.[141] The addition of **IrIr** catalyst always produced lower photocurrents than without catalyst, likely due to relatively fast recombination with **IrIr**$^{+}$ bound directly to the surface. Indeed, increased thicknesses of Al_2O_3 between TiO_2 and **IrIr** resulted in improved photocurrents as a result of the increased tunneling barrier.[141]

In the case of **Cp*Ir-Sil**, photocurrents were always higher than without catalyst, and the presence and thickness of the Al_2O_3 layer had minimal effect.[141] This likely indicates the effectiveness of the phenyl spacer group to decrease the rate of recombination. In pH 5.8, 0.1 M KNO_3 solution, TiO_2/**PMI**/Al_2O_3/**Cp*Ir-Sil** anodes reached ~15 μA/cm² at +0.4 V vs NHE (+0.71 V vs RHE). However, photocurrents decayed by ~66% over 5 min of repeated scans, despite the Al_2O_3 encapsulation. Given the demonstrated improved stability of **PMI** dye with ALD Al_2O_3 encapsulation, we propose the most likely degradation mechanism is catalyst instability.

Oxygen quantification was done by the Generator–Collector method, which indicated roughly 20% faradaic efficiency for films with either **IrIr** or **Cp*Ir-Sil** catalyst, or even without catalyst (Wasielewski *et al.* also cautioned that the G–C method could detect degradation products in addition to O_2).[141] All in all, this study provides a second example where a spacer group between the WOCatalyst and its anchor group (**Cp*Ir-Sil**) can reduce recombination. It also demonstrates that encapsulation of dye with ALD overlayers may be an important strategy to improve stability of dye molecules in DS-PECs. However, such overlayers may also interfere with charge transfer from oxidized dye to WOCatalyst, and so a balance between overlayer thickness and WOCatalyst spacer length may be required for efficient water-oxidation catalysis.

All Organic Donor–Acceptor (D–A) Dyes. Many donor–acceptor (D–A), or "push–pull" type dyes have been employed in DSSC studies.[40,131,134] In 2015, the Sun group published the first example of a water-oxidation DS-PEC using this class of sensitizer dye.[75] In this work, they employed a D–A dye consisting of a common triphenylamine donor group and a cyanoacrylic acid acceptor/anchor group (**D–A**, Fig. 2.20). This dye was co-loaded onto TiO_2 with a derivative of the [Ru(pdc)(pic)$_3$] (pdc = 2,6-pyridinedicarboxylate) WOCatalyst structural motif (Fig. 2.19), which was also developed by the Sun group.[191] Hereafter, we will use the nomenclature of Ru–pdc to describe this class of catalyst containing the pdc and pic ligands, either of which may be functionalized with anchor or linking groups. We will refer to the specific catalyst used in this study as **Ru–pdc1**, which employed a pdc ligand as a strong anchoring group. Impressively, this paper demonstrated a rare example of a p/n-DS-PEC tandem cell capable of overall water splitting without an applied bias. The photocathode also utilized a different D–A type dye, co-loaded onto NiO with a cobalt complex proton-reduction catalyst (Fig. 2.20).[75]

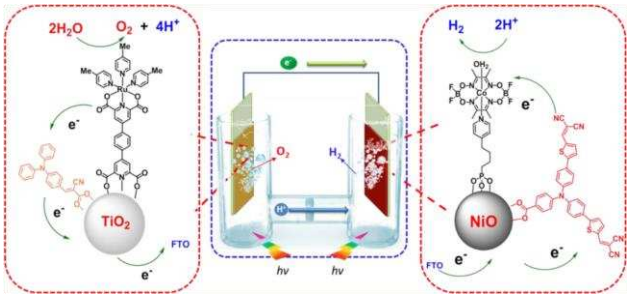

Fig. 2.20 Schematic representation of a published p/n-DS-PEC tandem cell. The photoanode is composed of a **D–A** sensitizer dye co-loaded onto TiO_2 with Ru–pdc WOCatalyst (**Ru–pdc1**). The photocathode is composed of a different D–A type sensitizer dye co-loaded onto NiO with a cobalt complex proton-reduction catalyst. Reprinted with permission from Ref. 75. Copyright 2015, American Chemical Society.

Focusing on the OER, when submerged in pH 7, 0.05 M KPi buffer and illuminated with white LED light (100 mW/cm², $\lambda > 400$ nm), TiO_2/**D–A**:**Ru–pdc1** anodes achieved steady-state photocurrents of ~300 μA/cm² at 0 V vs Ag/AgCl (3M KCl) (+0.62 V vs RHE). These

photocurrents are 3-fold higher and achievable at a lower applied potential than similar photoanodes prepared with the $[Ru^{II}(bpy)_2(4,4'\text{-}(PO_3H_2)_2bpy)]^{2+}$ sensitizer dye and the same WOCatalyst.[192] Under the same conditions, controls of TiO_2/**D–A** with no catalyst showed photocurrents of ~30 μA/cm² (10-fold lower), and TiO_2/**Ru–pdc1** with no dye showed photocurrents of only 6 μA/cm² (50-fold lower). Notably, in the TiO_2/**D–A**:**Ru–pdc1** anodes, light absorbance from **Ru–pdc1** catalyst is stronger and covers a broader wavelength range than **D–A**, yet photocurrents for TiO_2/**Ru–pdc1** without **D–A** were not significant.[75] Therefore, it is possible that **D–A** functions as both a sensitizer and an electron-transfer mediator for injection from photo-excited **Ru–pdc1** catalyst. This could be elucidated by the action spectrum of the TiO_2/**D–A**:**Ru–pdc1** anode, although one was not reported.

During extended photolysis at +0.62 V vs RHE, steady-state photocurrents from TiO_2/**D–A**:**Ru–pdc1** anodes decayed by ~30% to 200 μA/cm² after 5 min, and by ~70% to 80 μA/cm² after 60 min, indicating some degree of instability. Consistent with this, O_2 product generated over the 60 min period was detected by GC with a faradaic efficiency of just 73%. For the fully-assembled tandem cell depicted in Fig. 2.19, photocurrents of ~70 μA/cm² were achieved in a 2-electrode configuration with no applied bias, and a faradaic efficiency for H_2 generation of 55% was measured. This corresponds to an overall solar-to-hydrogen efficiency, η_{STH}, of 0.05%. Interestingly, it was found that the photo*cathode* was the kinetic bottleneck of this tandem device, owing to the poor hole-transport properties of the nanostructured NiO film.[75]

The Sun group published a second DS-PEC system in late 2016 employing a subporphyrin D–A dye,[139] which has already been detailed in Sec. 4.1 above. In early 2016, the Meyer group published their own system[142] employing a dye molecule with donor and acceptor units separated by a π-conjugated bridge, a structural motif commonly abbreviated[134] as D-π-A. The specific dye

employed in the Meyer group study consisted of a triphenylphosphine donor group, π-conjugated thiophene bridge, and a cyano acceptor group with phosphonate anchor, **D-π-A**. This dye was co-loaded onto the substrate with a Ru–bda type WOCatalyst with phosphonate anchor groups, **Ru–bda3** (Fig. 2.21).

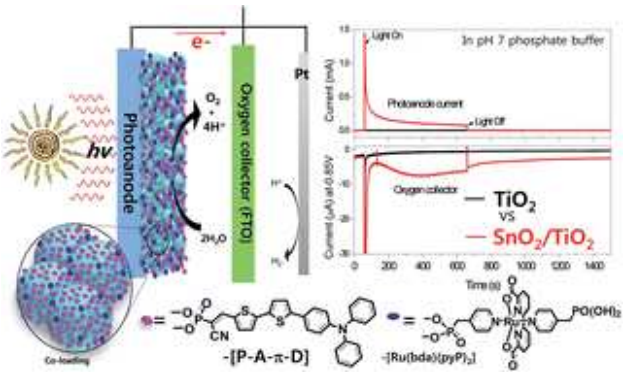

Fig. 2.21 Schematic of a DS-PEC composed of **D-π-A** sensitizer dye co-loaded with a Ru–bda type WOCatalyst (**Ru–bda3**) on a nanoparticle film of core/shell SnO_2/TiO_2. The green electrode represents the generator–collector technique used to detect photogenerated O_2 in solution. Upper plot: current−time trace for the generator electrode composed of TiO_2/**D-π-A**:**Ru–bda3** (black line) and core/shell SnO_2/TiO_2/**D-π-A**;**Ru–bda3** (red line) electrodes with 100 mW/cm² illumination in pH 7 Pi with +0.88 V vs RHE. Lower plot: current–time traces at the O_2-collector electrode at −0.20 V vs RHE. Reproduced from Ref. [142] with permission from The Royal Society of Chemistry.

An additional strategy employed in this work was to use a nanostructured SnO_2/TiO_2 core/shell film, wherein a sintered film of SnO_2 nanoparticles (~20 nm diameter) was subsequently treated by atomic layer deposition to form a 3 nm thick TiO_2 shell, then dyed.[142] As shown in Fig. 2.22, the core/shell strategy can be viewed as a functional analogue of photosystem II, in that a cascade of electronic energy levels is designed to thermodynamically drive electrons and holes in different spatial direction in order to decrease the probability of recombination.[84]

Nanosecond transient-absorption spectroscopy experiments indicated rapid injection (complete within 20 ns) from photo-excited **D-π-A** into both TiO_2 and SnO_2/TiO_2 core/shell films.[142] By following the decay of the absorption signature of photo-oxidized **D-π-A** (due to back-electron-transfer recombination), it was found that the half-life for the oxidized dye on TiO_2 films

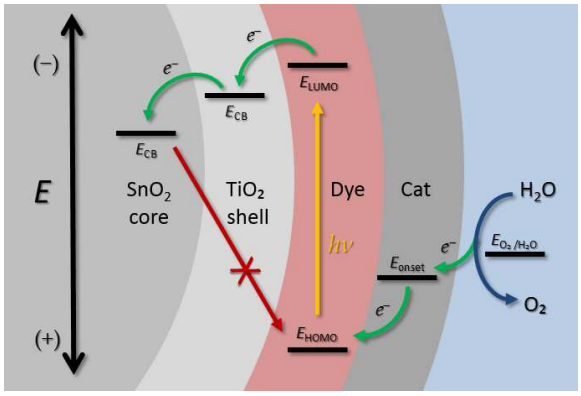

Fig. 2.22 Schematic energy diagram for a DS-PEC employing a core/shell semiconductor substrate. Photo-excitation of the dye is followed by injection into the CB of the TiO_2 shell, followed by injection into the CB of the SnO_2 core. This enhances spatial separation of the injected electron and the hole on the oxidized dye molecule, thus reducing the rate of recombination by back electron transfer and allowing more time for regeneration by the WOCatalyst.

was 170 ns, whereas on SnO_2/TiO_2 core/shell films the half-life was 1,020 ns, or six-fold longer, and thereby confirming the expected decrease in recombination by employing the core/shell strategy. Photocurrent–time measurements in pH 7, 0.1 M phosphate buffer *with 20 mM hydroquinone sacrificial reductant* and illumination with white light (100 mW/cm², $\lambda > 400$ nm) produced photocurrents up to ~2,500 μA/cm² for SnO_2/TiO_2/**D-π-A** anodes at +0.2 V vs SCE (+0.86 V vs RHE) as compared to only ~100 μA/cm² in controls for TiO_2/**D-π-A** anodes examined under the same conditions, results which again demonstrate the enhanced charge separation for the core/shell film. The action spectrum for SnO_2/TiO_2/**D-π-A** (still in the presence of hydroquinone as a sacrificial reductant) were a good match for the dye's absorption spectrum, reaching a maximum IPCE value of ~21%.[142]

To explore water oxidation catalysis, **D-π-A** dye and **Ru–bda3** WOCatalyst were co-loaded onto SnO_2/TiO_2 films with a ratio of 5:1, respectively. Photolysis experiments with SnO_2/TiO_2/**D-π-A**:**Ru–bda3** anodes in pH 7 buffer (now in the absence of hydroquinone) produced steady state photocurrents of ~100 μA/cm² after 60 s. For comparison, TiO_2/**D-π-A:Ru–**

bda3 anodes without the core/shell structure produced no photocurrent under the same conditions, indicating that back-electron-transfer recombination out-competes hole transfer to the WOCatalyst. Curiously, SnO_2/TiO_2**/D-π-A** anodes without catalyst also produced comparable photocurrents to those with catalyst.[142] The O_2 product was detected directly in solution by the generator–collector technique adapted from the Mallouk group.[83] Representative current profiles for generator (photolysis) and collector (O_2 detection) electrodes are includes in the upper-right portion of Fig. 2.21. Significant O_2 product was not detected for either SnO_2/TiO_2/**D-π-A** anodes without catalyst, or TiO_2/**D-π-A**:**Ru–bda3** anodes without the core/shell structure. Dioxygen product *was* detected for SnO_2/TiO_2/**D-π-A**:**Ru–bda3** anodes, but even then the faradaic efficiency was only 8.2%, indicating that the majority of photocurrent did not yield the desired O_2 product.[142]

The oxidative stability of **D-π-A** was studied by CV on nanoparticle TiO_2 films in both acetonitrile and water solutions. In acetonitrile, a reversible oxidative wave was observed even after 50 repeated CV cycles. By contrast, in pH 7 aqueous electrolyte the oxidative wave was irreversible and gradually decayed to practically zero within 50 cycles. This indicates the oxidative instability of **D-π-A** in aqueous solution, which in turn provides the most likely explanation for the low faradaic efficiency measured under water-oxidation conditions. Importantly, the authors pointed out that photocurrents from SnO_2/TiO_2/**D-π-A** anodes in aqueous solution were much more stable over the course of 15 min when in the presence of hydroquinone sacrificial reductant, indicating that even this relatively unstable dye could cycle repeatedly when kinetically protected against oxidative degradation by rapid electron transfer from an excess of the easily oxidized hydroquinone.[142] Put more generally, the results imply that even all-organic dyes may be capable of *kinetic stability* in water-oxidizing DS-PECs if strategies can be devised to promote rapid

regeneration of the photo-oxidized dye on a timescale competitive with recombination and degradative oxidation reactions. This highlights the need for efficient hole transfer from light-harvesting materials to WOCatalysts and for highly active (rapid turnover rate) WOCatalysts.

Polymeric Sensitizers. In addition to molecular sensitizers, light-absorbing conjugated organic polymers have also been studied in water-splitting applications. One common example is a material called graphitic carbon nitride (g-C_3N_4), or polyheptazine (structure shown in Fig. 2.23a). This g-C_3N_4 material has been studied as a highly stable OSC in photocatalytic (colloidal suspension) H_2-production studies.[65,66,69] To our knowledge, the first to apply this material to a

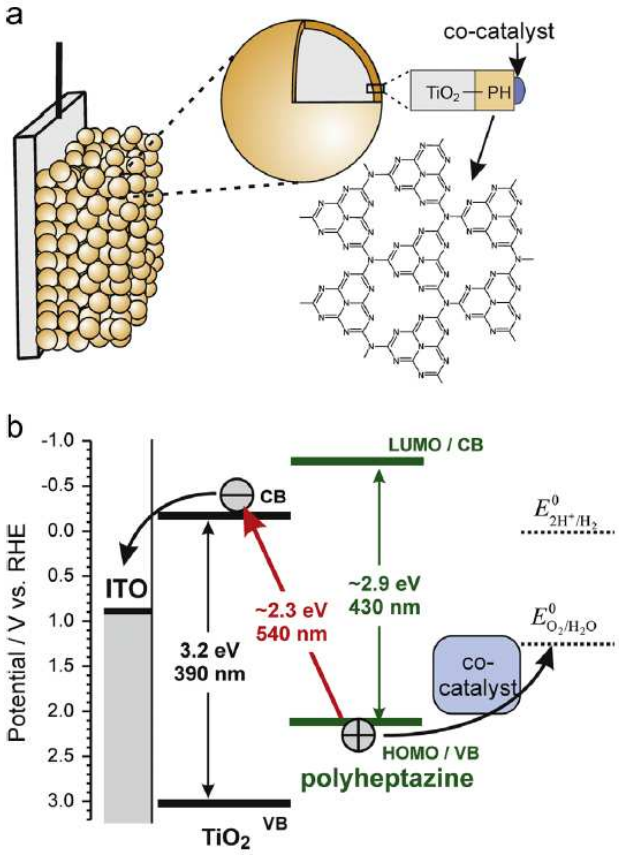

Fig. 2.23 (a) Schematic of a DS-PEC consisting of nano-TiO_2 modified at the surface with g-C_3N_4 (polyheptazine); (b) Energy diagram illustrating visible light absorption by TiO_2/g-C_3N_4 based on direct optical charge-transfer excitation of an electron from the g-C_3N_4 HOMO into the conduction band of TiO_2 (red arrow). Reprinted from Ref. [194], Copyright 2013, with permission from Elsevier.

water-oxidizing DS-PEC was the Beranek group in 2011.[79] Photoanodes were prepared by heating nanostructured TiO_2 films at 425 °C in the presence of gaseous urea pyrolysis products to form g-C_3N_4 on the TiO_2 surface. The UV–vis absorption spectrum of the TiO_2/g-C_3N_4 composite had a broad light-absorption feature extending out to λ < ~540 nm, which corresponds to a bandgap smaller than either TiO_2 or g-C_3N_4 alone.[79] This suggests a *direct optical electron transfer* from the HOMO of g-C_3N_4 to the CB of TiO_2 (Fig. 2.23b, red arrow) due to strong electronic coupling, as opposed to the more common *photoinduced electron transfer* from the sensitizer's LUMO. Subsequent studies provided TEM data showing that the g-C_3N_4 layer thickness ranges from 1–3 nm,[143] and XRD evidence that the planar g-C_3N_4 sheets lie flat on the TiO_2 surface.[193]

In pH 7, 0.1 M phosphate buffer, TiO_2/g-C_3N_4 electrodes illuminated with visible light (Xe lamp, λ > 420 nm, irradiance not reported) and held at +0.5 V vs Ag/AgCl (+1.42 V vs RHE) reached photocurrents of ~35 μA/cm², which were stable over the course of 10 min. After the anodes were loaded with IrO_2 NPs by soaking in a colloidal IrO_2 solution overnight, photocurrents were enhanced to ~120 μA/cm² and decayed only slightly over the course of 1 h. During this time, O_2 product was confirmed by a commercial O_2 sensor, though a faradaic efficiency was not reported. Under the same conditions, TiO_2/IrO_2 anodes without g-C_3N_4 showed no photocurrent and no O_2 product.[79] A subsequent study revealed that TiO_2/g-C_3N_4 anodes with no IrO_2 showed significant photocurrents but no O_2 product, and slightly lower photocurrent stability during extended photolysis than anodes with IrO_2.[143] Furthermore, the maximum IPCE for TiO_2/g-C_3N_4/IrO_2 anodes in pH 7 buffer was 7 ± 1% at +1.42 V vs RHE, and the faradaic efficiency was determined to be only 19%, suggesting poor electronic coupling between the organic film and inorganic catalyst.[143]

Subsequent optimization studies from the Beranek group further improved the performance of their system.[193–196] One study tested the effect of Nb-doping in the TiO_2 substrate.[194] Therein it was found that 0.1 atomic % was optimal, and Nb-TiO_2/g-C_3N_4 achieved roughly 4-fold higher photocurrents and 30% higher IPCE in pH 7 buffer than un-doped TiO_2/g-C_3N_4, presumably due to increased electron conductivity in TiO_2 and reduced recombination.[194] Other studies tested alternative WOCatalysts and deposition strategies.[193,195,196] One paper showed that decorating their (un-doped) TiO_2/g-C_3N_4 anodes with an earth-abundant CoO_x catalyst by a photoelectrochemical method rather than loading IrO_2 NPs from a colloidal solution resulted in improved photocurrents and O_2 yield, presumably because the photoelectrochemical deposition method allowed for improved adhesion and electrical coupling of the CoO_x catalyst.[193,195] This was the first example (and to our knowledge, the only example so far) of a water-oxidizing DS-PEC composed entirely of earth-abundant materials, including both sensitizer and catalyst.

Subsequently, it was also shown that the IrO_x catalyst could be deposited by the same photoelectrochemical method.[196] Comparing the performance of TiO_2/g-C_3N_4/IrO_2 anodes prepared from colloidal IrO_2 NPs to those prepared by the photoelectrochemical deposition method, both had remarkably similar photocurrents at short times. However, at longer times, films prepared from colloidal IrO_2 NPs showed steady decrease in photocurrent and O_2 yield, suggesting instability of IrO_2 loading. By contrast, films prepared by photoelectrochemical deposition displayed more stable photocurrents and continual O_2 production over the course of 1h. Further optimization experiments demonstrated that the faradaic efficiency for TiO_2/g-C_3N_4/IrO_2 anodes was affected by buffer anion,[196] showing lowest performance with phosphate buffer (which is known to reduce the activity of IrO_2),[197,198] and highest performance with sulfate buffer. Finally, it was also found that anode performance was optimized at pH $\leq$ 6. Higher pH, up to 10, resulted

in lower (but stable) photocurrents and constant faradaic efficiency, possibly caused by deprotonation of g-C_3N_4 and decreased IrO_2 activity.[196] Finally, pH 12 buffer resulted in high, but unstable photocurrent and loss of faradaic efficiency, likely due to decomposition of g-C_3N_4.[196] In summary, Beranek *et al*. have demonstrated water-oxidizing DS-PECs based on sensitization by the robust, earth-abundant polymer material g-C_3N_4, and demonstrated that photoanode performance can be optimized by doping of the MO_x semiconductor, by varying the WOCatalyst and catalyst deposition methods, and by varying the electrolyte.

A final system of note was published in 2013 by Xiao *et al*.[199] wherein ZnO nanorods were decorated with poly(pyrrole) (PPy) conducting polymer. Zinc oxide is a common wide-bandgap semiconductor for PECs and has a higher conductivity than TiO_2.[199] In this study, ZnO nanorods (~150 × 1,500 nm) were electrochemically grown on ITO from pH 7.5 aqueous solution $Zn(NO_3)_2$. The nanorod anode was subsequently chemically etched to make a rough ZnO surface, and PPy was deposited by in-situ chemical polymerization of pyrrole by $FeCl_3$ oxidant. SEM images indicated that the ZnO surface was uniformly decorated with PPy nanoparticles of 30 nm diameter. When submerged in pH 7 aqueous buffer (0.5 M Na_2SO_4) and illuminated with a Xe arc lamp (irradiance not reported), ZnO/PPy reached very impressive steady-state photocurrents of ~680 μA/cm² at +0.8 V vs Ag/AgCl (+1.4 V vs RHE), which actually grew slightly over 10 minutes of transient illumination. For comparison, bare ZnO anodes reached photocurrents of ~475 μA/cm² under the same conditions. In the dark, all anodes had currents ≤ 10 μA/cm².[199] While such photocurrents are promising, O_2 product quantification was not reported, an especially important omission given that ZnO is unstable under such conditions and is known to photocorrode[20,200,201] (though the PPy coating may help prevent corrosion).[201] Furthermore, O_2 production is in question given the fact that a WOCatalyst was not intentionally added, although Fe impurity from the

chemical polymerization of PPy[199] is certainly possible, if not likely (trace Fe impurity has been shown to greatly enhance the WOC activity of select transition metal oxides).[99] Regardless, this interesting ZnO/PPy system warrants further study.

2.5 Summary And Outlook

Herein we have compiled a comprehensive review of literature systems that employ earth-abundant, organic light harvesting materials in photoelectrochemical water-oxidizing anodes. These materials include derivatives of aromatic heterocycles including porphyrin, subporphyrin, and phthalocyanine, perylene derivatives, as well as conducting polymers and fullerenes. Architectures include organic thin-films composed of a single-bandgap organic semiconductor material or heterojunctions between two organic semiconductor materials, as well as dye-sensitized nanostructured semiconductor films. The use of organic materials in such devices takes advantage of their low materials cost, the synthetic tunability of their properties, and low-temperature manufacturing processes.

OTF-PECs. Progress in water-oxidizing OTF-PECs has largely paralleled the OPV field,[63,71,72] showing that planar heterojunctions between two OSC materials can improve performance by enhancing charge separation efficiency relative to the individual layers.[85,86] However, film thicknesses in this planar bilayer architecture are limited by the exciton diffusion length, usually on the order of tens of nanometers,[63] resulting in poor light-harvesting efficiency. Therefore, bulk-heterojunctions with nanomorphology allow thicker active layers while maintaining short distances between the two phases, and have been successfully employed in water-oxidizing photoanodes.[74,88] However, systems are rare in which the bulk-heterojunction electron donor (hole acceptor) material has a HOMO energy sufficiently positive to oxidize water,

with only one such system published to date.[88] As such, further improving the efficiency of OTF-PEC photoanodes will likely require enhanced efforts to develop high-efficiency bulk-heterojunction active layer materials with more positive energy bands, or further studies of multi-junction cell architectures.[16,17] Film morphology was also found to have a large effect on performance, especially for photoanodes composed of a single organic-semiconductor material. For example, a film of conducting polymer showed much higher activity when prepared with nanofiber morphology instead of globular morphology.[89] We have proposed herein that such a morphology may best be described as an "organic semiconductor–electrolyte bulk heterojunction", and also merit further study.

One of the great challenges in the OTF-PEC field is to ensure both strong physical and electronic coupling between the organic light harvesting materials and inorganic water-splitting catalysts. The identity and deposition method of the WOCatalyst can also greatly affect performance. Successful strategies to date include the immobilization of catalyst within a Nafion thin-film at the electrolyte interface[85] or within a conductive polymer film,[87] the use of organometallic catalyst as part of an organic bilayer,[86] the use of an interfacial layer such as TiO_2 (by atomic layer deposition) between the OSC and catalyst,[89] and the use of incorporation of ionic linking groups such as phosphonate as part of the OSC.[80] It has also been hypothesized that the incorporation of ionic groups such as sulfonate or phosphonate throughout the OSC film may enhance electrolyte uptake and provide H^+-conduction channels.[80,87]

Finally, perhaps the most promising developments in the field of OTF-PECs includes the selective use of charge-rectifying interfacial layers. Such layers can decrease recombination between active materials and charge-collecting substrate, enhance coupling with the water-splitting catalyst, and can also enhance the stability of the organic active materials.[74] The study of

various interfacial layers has been especially pronounced in the field of OTF-PEC bulk-heterojunction photo*cathodes*,[103,123–128] and advancements in that field promise to inform similar strategies for use in bulk-heterojunction photo*anodes* as additional high-potential active materials are developed.

DS-PECs. A variety of organic dyes and polymers have been employed in water-oxidizing DS-PEC architectures, though there is no clear trend in performance to indicate if one type of sensitizer offers a clear advantage over another (Table 2.3). In general, the DS-PECs highlighted here show lower faradaic efficiencies and shorter lifetimes compared to the OTF-PEC systems. This suggests that the organic light-harvesting materials in a DS-PEC architecture may be more prone to oxidative decomposition or perhaps desorption. WOCatalysts have been loaded by a variety of strategies. The most common (and to date the most successful[75,132,133]) strategy is to load the nano-MO_x surface with both anchored dye and anchored molecular WOCatalyst.[75,136,139,141,142] It has also been shown that performance can be enhanced by anchoring the molecular catalyst through a longer, aliphatic linker group.[141,158] This strategy may enhance the efficiency with which the catalyst can regenerate surrounding photo-oxidized dye, and/or decrease the rate of recombination between the catalyst and the CB electrons in the MO_x. Alternatively, the MO_x surface can be loaded with a heterogeneous WOCatalyst such as IrO_2 nanoparticles,[79,137,140] although this strategy tends to enhance recombination between the catalyst and CB electrons.[83] Beranek *et al*. have demonstrated that DS-PEC performance and lifetime can be enhanced by the photoelectrochemical deposition of heterogeneous WOCatalyst such as IrO_x and CoO_x, likely because of enhanced coupling between sensitizer and catalyst.[193,195,196]

Note that the above strategies of co-loading the MO_x surface with WOCatalyst, while successful for demonstrating photoelectrochemical water oxidation, can have the added

disadvantages of (i) competing with dye for surface loading, thereby reducing the light-harvesting efficiency; and (ii) if catalyst concentration is low relative to dye, the dye layer must be conductive to photogenerated holes in order to allow for regeneration of oxidized dye molecules that are not in direct contact with catalyst. A third catalyst-loading strategy involves the covalent coupling of dye and catalyst to form a molecular dyad,[138] which is expected to provide a fast regeneration of the photo-oxidized dye and negate the need for hole conductivity throughout the dye layer. However, cases exist where the dye component may not be sufficiently oxidizing for efficient complete turnover of the catalyst.[47,138]

We note that all the water-oxidizing DS-PEC systems highlighted in Table 2.3 employ WOCatalyst composed of rare transition metals. However, the literature does contain one system by the Beranek group composed entirely of earth-abundant elements (TiO_2/g-C_3N_4/CoO_x) wherein CoO_x was photoelectrochemically deposited.[193,195] There is an additional recent example where a CoO_x nanoparticle catalyst was co-anchored to nano-TiO_2 through long linker groups alongside the common $[Ru^{II}(bpy)_2(4,4'\text{-}(PO_3H_2)_2bpy)]^{2+}$ sensitizer dye.[202] Furthermore, alternative molecular WOCatalysts exist[154] that are composed of earth-abundant transition metals yet still exhibit turnover frequencies $\geq 0.5\ s^{-1}$, the approximate rate achievable by the photon flux at 1-sun illumination.[47] However, the stability of such catalysts may not be sufficient for long-lived devices,[154] and they have yet to be employed in DS-PECs.

IPCE values for the best DS-PECs to date reach only 14%[132] and 17%[138], falling far short of the 80% achieved by the top DSSC.[153] This major difference comes from regeneration rates of the oxidized dye after photoinjection. In DSSCs, this is accomplished by fast electron transfer from a redox couple in solution on the microsecond timescale.[40] In DS-PECs, this step is limited by the rate of hole transfer to the WOCatalyst, which can be much slower, on the order of milliseconds

for dye-ligated IrO_2 nanoparticles, for example.[203] Clearly, it is of great interest to enhance rates of dye regeneration by catalyst oxidation. It has already been shown that hole transfer can occur within ~500 ps for some covalent chromophore–catalyst dyads,[47] leading to longer lifetimes for that charge-separated state.

It also appears that recombination rates in DS-PECs may be faster than in DSSCs. Nanosecond transient absorption spectroscopy studies on dye-sensitized SnO_2 and TiO_2 in aqueous media have shown that a significant fraction of injected electrons can recombine even on the timescale of tens of nanoseconds,[204] though recombination is not complete for hundreds of microseconds to milliseconds.[204] This indicates that back-electron transfer is likely competitive with catalyst oxidation in most systems, and is therefore a dominant recombination pathway in DS-PECs. The Mallouk group has recently found evidence for proton intercalation into the nano-TiO_2 of DS-PECs, which cause long-lived, electron-trapping surface states.[205,206] Such trap states were shown to enhance the recombination rate constant with surface-bound, oxidized sensitizer dye by a factor of 4.[206] Protons are constantly generated at the surface of water-oxidizing photoanodes, and are likely driven to intercalate into the MO_x in order to compensate the charge of injected electrons. Overall, continued efforts are needed to improve efficiencies of DS-PECs by retarding rates of back-electron transfer, and proton-management at the surface of DS-PECs may prove to be of key importance to decrease recombination. The Al_2O_3 encapsulation method highlighted above (Fig. 2.19) was shown to decrease recombination with oxidized catalyst,[141] and the SnO_2/TiO_2 core/shell structure (Fig. 2.22) was shown to decrease the rate of back-electron transfer to oxidized dye by almost an order of magnitude.[142] Most likely, a combination of charge-separation strategies (the use of interfacial layers as well as dye and catalyst structural engineering) will be required to achieve highly efficient DS-PECs.

Stability. The "elephant in the room" for water oxidation systems that employ organic light-harvesting materials is stability. Practically all systems highlighted in this review exhibit deactivation in the form of gradual photocurrent decay over the course of minutes. In general, DS-PECs seem to exhibit faster deactivation and lower faradaic efficiencies than OTF-PEC systems. Improving device stabilities can only be accomplished by understanding the cause(s) of degradation. In this regard, very little is known in the field. In one instance, the Meyer group probed the degradation of their DS-PEC by performing repeated cyclic voltammetry sweeps (x50) of their dyed photoanode in acetonitrile and in water, finding that the oxidative wave of their **D-π-A** dye was highly reversibly in the former but highly irreversible in the latter, thus indicating the dye's oxidative instability in the presence of water.[142] In another example, Hanson *et al*. followed the change in the visible absorbance spectrum of a dyed photoanode during extended photolysis, assigning broadband absorbance decay to dye desorption and a spectral change with an isosbestic point to chemical degradation of the dye.[207] Knowledge of the major deactivation pathway can inform subsequent strategies to improve stability, such as the use of alternative anchor groups or surface treatments to prevent dye desorption,[47,141,185,186] or molecular structural changes to replace oxidatively unstable units.

A variety of stability tests have been recommended for photoelectrochemical water splitting,[59] which should be applied to this field of PECs based on organic light-harvesting materials. A starting point is to track photocurrents over extended photolysis times. To our knowledge, the longest test of an OTF-PEC lasted only 24 hours.[87] Future studies should take systems to their end of lifetime in order to determine their total turnovers. Subsequently, the electrolysis solution can be analyzed for degradation products, for example by ICP-MS to detect metal ions from the corrosion of MO_x substrate or catalyst decomposition. Additional analyses of

the electrode can be performed both before and after extended electrolysis, including optical and electron microscopy, XRD, XPS, and vibrational spectroscopies.[59] It may also be of interest to recover the organic material from the device for analysis by NMR and mass spectrometry to detect oxidation products. Hopefully, such analyses will provide insights on how to improve the stability of future organic-based systems. It is worth noting that even the $[Ru(bpy)_3]^{2+}$-type sensitizers common in DSSCs are oxidatively unstable,[208] although dyes in such devices are *kinetically* stabilized for high total turnovers when a redox couple is present to quickly regenerate the oxidized dye. Likewise, oxidatively unstable organic materials in water-splitting PECs may be kinetically stabilized if efficient coupling to fast water-oxidation catalysts can be achieved. Overall, in-depth studies of the deactivation pathways, degradation products, and the kinetic and thermodynamic stability of organic light-harvesting materials in water-oxidizing photoanodes are important topics for future research.

REFERENCES

(1) Turner, J. A. A Realizable Renewable Energy Future. *Science* **1999**, *285*, 687–689.

(2) Smalley, R. E. Future Global Energy Prosperity: The Terawatt Challenge. *MRS Bull.* **2005**, *30*, 412–417.

(3) Lewis, N. S.; Nocera, D. G. Powering the Planet: Chemical Challenges in Solar Energy Utilization. *Proc. Natl. Acad. Sci. U. S. A.* **2006**, *103*, 15729–15735.

(4) Cook, T. R.; Dogutan, D. K.; Reece, S. Y.; Surendranath, Y.; Teets, T. S.; Nocera, D. G. Solar Energy Supply and Storage for the Legacy and Nonlegacy Worlds. *Chem. Rev.* **2010**, *110*, 6474–6502.

(5) Balzani, V.; Moggi, L.; Manfrin, M. F.; Bolletta, F.; Gleria, M. Solar Energy Conversion by Water Photodissociation. *Science* **1975**, *189*, 852–856.

(6) Nozik, A. J. Photoelectrochemistry: Applications to Solar Energy Conversion. *Annu. Rev. Phys. Chem.* **1978**, *29*, 189–222.

(7) Bard, A. J.; Fox, M. A. Artificial Photosynthesis: Solar Splitting of Water to Hydrogen and Oxygen. *Acc. Chem. Res.* **1995**, *28*, 141–145.

(8) Crabtree, G. W.; Dresselhaus, M. S. The Hydrogen Fuel Alternative. *MRS Bull.* **2008**, *33*, 421–428.

(9) Gray, H. B. Powering the Planet with Solar Fuel. *Nat. Chem.* **2009**, *1*, 7.

(10) Walter, M. G.; Warren, E. L.; McKone, J. R.; Boettcher, S. W.; Mi, Q.; Santori, E. A.; Lewis, N. S. Solar Water Splitting Cells. *Chem. Rev.* **2010**, *110*, 6446–6473.

(11) Bard, A. J.; Faulkner, L. R. *Electrochemical Methods: Fundamentals and Applications*; 2nd ed.; John Wiley & Sons, Inc.: Hoboken, NJ, 2001.

(12) Bolton, J. R.; Strickler, S. J.; Connolly, J. S. Limiting and Realizable Efficiencies of Solar Photolysis of Water. *Nature* **1985**, *316*, 495–500.

(13) Reference Solar Spectral Irradiance: Air Mass 1.5. http://rredc.nrel.gov/solar/spectra/am1.5/ (accessed May 18, 2016).

(14) McKone, J. R.; Lewis, N. S.; Gray, H. B. Will Solar-Driven Water-Splitting Devices See the Light of Day? *Chem. Mater.* **2014**, *26*, 407–414.

(15) Aoki, A.; Naruse, M.; Abe, T. Series Circuit of Organic Thin-Film Solar Cells for Conversion of Water into Hydrogen. *ChemPhysChem* **2013**, *14*, 2317–2320.

(16) Esiner, S.; van Eersel, H.; Wienk, M. M.; Janssen, R. A. J. Triple Junction Polymer Solar Cells for Photoelectrochemical Water Splitting. *Adv. Mater.* **2013**, *25*, 2932–2936.

(17) Esiner, S.; Willems, R. E. M.; Furlan, A.; Li, W.; Wienk, M. M.; Janssen, R. A. J. Photoelectrochemical Water Splitting in an Organic Artificial Leaf. *J. Mater. Chem. A* **2015**, *3*, 23936–23945.

(18) Schüttauf, J.-W.; Modestino, M. A.; Chinello, E.; Lambelet, D.; Delfino, A.; Dominé, D.; Faes, A.; Despeisse, M.; Bailat, J.; Psaltis, D.; *et al.* Solar-to-Hydrogen Production at 14.2% Efficiency with Silicon Photovoltaics and Earth-Abundant Electrocatalysts. *J. Electrochem. Soc.* **2016**, *163*, F1177–F1181.

(19) Bard, A. J.; Wrighton, M. S. Thermodynamic Potential for the Anodic Dissolution of n-Type Semiconductors A Crucial Factor Controlling Durability and Efficiency in Photoelectrochemical Cells and an Important Criterion in the Selection of New Electrode/Electrolyte Systems. *J. Electrochem. Soc.* **1977**, *124*, 1706–1710.

(20) Gerischer, H. On the Stability of Semiconductor Electrodes against Photodecomposition. *J. Electroanal. Chem. Interfacial Electrochem.* **1977**, *82*, 133–143.

(21) Kudo, A.; Miseki, Y. Heterogeneous Photocatalyst Materials for Water Splitting. *Chem. Soc. Rev.* **2008**, *38*, 253–278.

(22) Chen, X.; Shen, S.; Guo, L.; Mao, S. S. Semiconductor-Based Photocatalytic Hydrogen Generation. *Chem. Rev.* **2010**, *110*, 6503–6570.

(23) Maeda, K.; Domen, K. Photocatalytic Water Splitting: Recent Progress and Future Challenges. *J. Phys. Chem. Lett.* **2010**, *1*, 2655–2661.

(24) Maeda, K. Photocatalytic Water Splitting Using Semiconductor Particles: History and Recent Developments. *J. Photochem. Photobiol. C Photochem. Rev.* **2011**, *12*, 237–268.

(25) Osterloh, F. E. Inorganic Nanostructures for Photoelectrochemical and Photocatalytic Water Splitting. *Chem. Soc. Rev.* **2013**, *42*, 2294–2320.

(26) Hisatomi, T.; Kubota, J.; Domen, K. Recent Advances in Semiconductors for Photocatalytic and Photoelectrochemical Water Splitting. *Chem. Soc. Rev.* **2014**, *43*, 7520–7535.

(27) Xing, Z.; Zong, X.; Pan, J.; Wang, L. On the Engineering Part of Solar Hydrogen Production from Water Splitting: Photoreactor Design. *Chem. Eng. Sci.* **2013**, *104*, 125–146.

(28) Pinaud, B. A.; Benck, J. D.; Seitz, L. C.; Forman, A. J.; Chen, Z.; Deutsch, T. G.; James, B. D.; Baum, K. N.; Baum, G. N.; Ardo, S.; *et al.* Technical and Economic Feasibility of Centralized Facilities for Solar Hydrogen Production via Photocatalysis and Photoelectrochemistry. *Energy Environ. Sci.* **2013**, *6*, 1983–2002.

(29) Coward, H. F.; Jones, G. W. *Limits of Flammability of Gases and Vapors*; Bulletin 503; Bureau of Mines, United States Department of the Interior, 1952.

(30) Badawy, W. A. Photovoltaic and Photoelectrochemical Cells Based on Schottky Barrier Heterojunctions. In *Modern Aspects of Electrochemistry*; White, R. E.; Conway, B. E.; Brockris, J. O., Eds.; Springer US: New York, 1997; Vol. 30, pp. 187–259.

(31) Mavroides, J. G.; Kafalas, J. A.; Kolesar, D. F. Photoelectrolysis of Water in Cells with $SrTiO_3$ Anodes. *Appl. Phys. Lett.* **1976**, *28*, 241–243.

(32) Ellis, A. B.; Kaiser, S. W.; Wrighton, M. S. Semiconducting Potassium Tantalate Electrodes. Photoassistance Agents for the Efficient Electrolysis of Water. *J. Phys. Chem.* **1976**, *80*, 1325–1328.

(33) Prévot, M. S.; Sivula, K. Photoelectrochemical Tandem Cells for Solar Water Splitting. *J. Phys. Chem. C* **2013**, *117*, 17879–17893.

(34) Nozik, A. J. P-N Photoelectrolysis Cells. *Appl. Phys. Lett.* **1976**, *29*, 150–153.

(35) Gerischer, H.; Michel-Beyerle, M. E.; Rebentrost, F.; Tributsch, H. Sensitization of Charge Injection into Semiconductors with Large Band Gap. *Electrochimica Acta* **1968**, *13*, 1509–1515.

(36) Gerischer, H. Electrochemical Techniques for the Study of Photosensitization. *Photochem. Photobiol.* **1972**, *16*, 243–260.

(37) Tsubomura, H.; Matsumura, M.; Nomura, Y.; Amamiya, T. Dye Sensitised Zinc Oxide: Aqueous Electrolyte: Platinum Photocell. *Nature* **1976**, *261*, 402–403.

(38) O'Regan, B.; Grätzel, M. A Low-Cost, High-Efficiency Solar Cell Based on Dye-Sensitized Colloidal TiO_2 Films. *Nature* **1991**, *353*, 737–740.

(39) Ardo, S.; Meyer, G. J. Photodriven Heterogeneous Charge Transfer with Transition-Metal Compounds Anchored to TiO_2 Semiconductor Surfaces. *Chem. Soc. Rev.* **2009**, *38*, 115–164.

(40) Hagfeldt, A.; Boschloo, G.; Sun, L.; Kloo, L.; Pettersson, H. Dye-Sensitized Solar Cells. *Chem. Rev.* **2010**, *110*, 6595–6663.

(41) A SciFinder search for the concept "Dye-sensitized Solar Cells", including Journal articles, Letters, and Reviews yielded 21,704 results. https://scifinder.cas.org (accessed Jan 12, 2017).

(42) Youngblood, W. J.; Lee, S.-H. A.; Maeda, K.; Mallouk, T. E. Visible Light Water Splitting Using Dye-Sensitized Oxide Semiconductors. *Acc. Chem. Res.* **2009**, *42*, 1966–1973.

(43) Caramori, S.; Cristino, V.; Meda, L.; Argazzi, R.; Bignozzi, C. A. Hydrogen Production with Nanostructured and Sensitized Metal Oxides. *Top. Curr. Chem.* **2011**, *303*, 39–94.

(44) Young, K. J.; Martini, L. A.; Milot, R. L.; Snoeberger, R. C.; Batista, V. S.; Schmuttenmaer, C. A.; Crabtree, R. H.; Brudvig, G. W. Light-Driven Water Oxidation for Solar Fuels. *Coord. Chem. Rev.* **2012**, *256*, 2503–2520.

(45) Alibabaei, L.; Luo, H.; House, R. L.; Hoertz, P. G.; Lopez, R.; Meyer, T. J. Applications of Metal Oxide Materials in Dye Sensitized Photoelectrosynthesis Cells for Making Solar Fuels: Let the Molecules Do the Work. *J. Mater. Chem. A* **2013**, *1*, 4133–4145.

(46) Swierk, J. R.; Mallouk, T. E. Design and Development of Photoanodes for Water-Splitting Dye-Sensitized Photoelectrochemical Cells. *Chem. Soc. Rev.* **2013**, *42*, 2357–2387.

(47) Ashford, D. L.; Gish, M. K.; Vannucci, A. K.; Brennaman, M. K.; Templeton, J. L.; Papanikolas, J. M.; Meyer, T. J. Molecular Chromophore–Catalyst Assemblies for Solar Fuel Applications. *Chem. Rev.* **2015**, *115*, 13006–13049.

(48) Yu, Z.; Li, F.; Sun, L. Recent Advances in Dye-Sensitized Photoelectrochemical Cells for Solar Hydrogen Production Based on Molecular Components. *Energy Environ. Sci.* **2015**, *8*, 760–775.

(49) Brennaman, M. K.; Dillon, R. J.; Alibabaei, L.; Gish, M. K.; Dares, C. J.; Ashford, D. L.; House, R. L.; Meyer, G. J.; Papanikolas, J. M.; Meyer, T. J. Finding the Way to Solar Fuels with Dye-Sensitized Photoelectrosynthesis Cells. *J. Am. Chem. Soc.* **2016**, *138*, 13085–13102.

(50) Caramori, S.; Ronconi, F.; Argazzi, R.; Carli, S.; Boaretto, R.; Busatto, E.; Bignozzi, C. A. Solar Energy Conversion in Photoelectrochemical Systems. In *Applied Photochemistry*; Bergamini, G.; Silvi, S., Eds.; Lecture Notes in Chemistry; Springer International Publishing, 2016; pp. 67–143.

(51) Yamamoto, M.; Tanaka, K. Artificial Molecular Photosynthetic Systems: Towards Efficient Photoelectrochemical Water Oxidation. *ChemPlusChem* **2016**, *81*, 1028–1044.

(52) Nozik, A. J. Photochemical Diodes. *Appl. Phys. Lett.* **1977**, *30*, 567–569.

(53) Fujishima, A.; Honda, K. Electrochemical Photolysis of Water at a Semiconductor Electrode. *Nature* **1972**, *238*, 37–38.

(54) Osterloh, F. E. Inorganic Materials as Catalysts for Photochemical Splitting of Water. *Chem. Mater.* **2008**, *20*, 35–54.

(55) Aharon-Shalom, E.; Heller, A. Efficient p-InP (Rh-H Alloy) and p-InP (Re-H Alloy) Hydrogen Evolving Photocathodes. *J. Electrochem. Soc.* **1982**, *129*, 2865–2866.

(56) Khaselev, O.; Turner, J. A. A Monolithic Photovoltaic-Photoelectrochemical Device for Hydrogen Production Via Water Splitting. *Science* **1998**, *280*, 425–427.

(57) Licht, S.; Wang, B.; Mukerji, S.; Soga, T.; Umeno, M.; Tributsch, H. Over 18% Solar Energy Conversion to Generation of Hydrogen Fuel; Theory and Experiment for Efficient Solar Water Splitting. *Int. J. Hydrog. Energy* **2001**, *26*, 653–659.

(58) Verlage, E.; Hu, S.; Liu, R.; Jones, R. J. R.; Sun, K.; Xiang, C.; Lewis, N. S.; Atwater, H. A. A Monolithically Integrated, Intrinsically Safe, 10% Efficient, Solar-Driven Water-Splitting System Based on Active, Stable Earth-Abundant Electrocatalysts in Conjunction with Tandem III–V Light Absorbers Protected by Amorphous TiO_2 Films. *Energy Environ. Sci.* **2015**, *8*, 3166–3172.

(59) Chen, Z.; Dinh, H. N.; Miller, E. *Photoelectrochemical Water Splitting: Standards, Experimental Methods, and Protocols*; SpringerBriefs in Energy; Springer New York: New York, NY, 2013.

(60) Vesborg, P. C. K.; Jaramillo, T. F. Addressing the Terawatt Challenge: Scalability in the Supply of Chemical Elements for Renewable Energy. *RSC Adv.* **2012**, *2*, 7933–7947.

(61) Woodhouse, M.; Goodrich, A.; Margolis, R.; James, T. L.; Lokanc, M.; Eggert, R. Supply-Chain Dynamics of Tellurium, Indium, and Gallium Within the Context of PV Manufacturing Costs. *IEEE J. Photovolt.* **2013**, *3*, 833–837.

(62) Kelley, T. W.; Baude, P. F.; Gerlach, C.; Ender, D. E.; Muyres, D.; Haase, M. A.; Vogel, D. E.; Theiss, S. D. Recent Progress in Organic Electronics: Materials, Devices, and Processes. *Chem. Mater.* **2004**, *16*, 4413–4422.

(63) Hains, A. W.; Liang, Z.; Woodhouse, M. A.; Gregg, B. A. Molecular Semiconductors in Organic Photovoltaic Cells. *Chem. Rev.* **2010**, *110*, 6689–6735.

(64) Yanagida, S.; Kabumoto, A.; Mizumoto, K.; Pac, C.; Yoshino, K. Poly(p-Phenylene)-Catalysed Photoreduction of Water to Hydrogen. *J. Chem. Soc. Chem. Commun.* **1985**, 474–475.

(65) Wang, X.; Maeda, K.; Thomas, A.; Takanabe, K.; Xin, G.; Carlsson, J. M.; Domen, K.; Antonietti, M. A Metal-Free Polymeric Photocatalyst for Hydrogen Production from Water under Visible Light. *Nat. Mater.* **2009**, *8*, 76–80.

(66) Zhang, J.; Chen, X.; Takanabe, K.; Maeda, K.; Domen, K.; Epping, J. D.; Fu, X.; Antonietti, M.; Wang, X. Synthesis of a Carbon Nitride Structure for Visible-Light Catalysis by Copolymerization. *Angew. Chem. Int. Ed.* **2010**, *49*, 441–444.

(67) Zhang, Z.; Long, J.; Yang, L.; Chen, W.; Dai, W.; Fu, X.; Wang, X. Organic Semiconductor for Artificial Photosynthesis: Water Splitting into Hydrogen by a Bioinspired $C_3N_3S_3$ Polymer under Visible Light Irradiation. *Chem. Sci.* **2011**, *2*, 1826–1830.

(68) Sprick, R. S.; Jiang, J.-X.; Bonillo, B.; Ren, S.; Ratvijitvech, T.; Guiglion, P.; Zwijnenburg, M. A.; Adams, D. J.; Cooper, A. I. Tunable Organic Photocatalysts for Visible-Light-Driven Hydrogen Evolution. *J. Am. Chem. Soc.* **2015**, *137*, 3265–3270.

(69) Chen, S.; Wang, C.; Bunes, B. R.; Li, Y.; Wang, C.; Zang, L. Enhancement of Visible-Light-Driven Photocatalytic H_2 Evolution from Water over g-C_3N_4 through Combination with Perylene Diimide Aggregates. *Appl. Catal. Gen.* **2015**, *498*, 63–68.

(70) Zhang, X.; Peng, T.; Song, S. Recent Advances in Dye-Sensitized Semiconductor Systems for Photocatalytic Hydrogen Production. *J. Mater. Chem. A* **2016**, *4*, 2365–2402.

(71) Hoppe, H.; Sariciftci, N. S. Organic Solar Cells: An Overview. *J. Mater. Res.* **2004**, *19*, 1924–1945.

(72) Brabec, C. J.; Gowrisanker, S.; Halls, J. J. M.; Laird, D.; Jia, S.; Williams, S. P. Polymer–Fullerene Bulk-Heterojunction Solar Cells. *Adv. Mater.* **2010**, *22*, 3839–3856.

(73) Research Cell Record Efficiency Chart http://www.nrel.gov/pv/assets/images/efficiency_chart.jpg (accessed Jan 27, 2017).

(74) Gustafson, M. P.; Clark, N.; Winther-Jensen, B.; MacFarlane, D. R. Organic Photovoltaic Structures as Photo-Active Electrodes. *Electrochimica Acta* **2014**, *140*, 309–313.

(75) Li, F.; Fan, K.; Xu, B.; Gabrielsson, E.; Daniel, Q.; Li, L.; Sun, L. Organic Dye-Sensitized Tandem Photoelectrochemical Cell for Light Driven Total Water Splitting. *J. Am. Chem. Soc.* **2015**, *137*, 9153–9159.

(76) Dotan, H.; Mathews, N.; Hisatomi, T.; Grätzel, M.; Rothschild, A. On the Solar to Hydrogen Conversion Efficiency of Photoelectrodes for Water Splitting. *J. Phys. Chem. Lett.* **2014**, *5*, 3330–3334.

(77) Coridan, R. H.; Nielander, A. C.; Francis, S. A.; McDowell, M. T.; Dix, V.; Chatman, S. M.; Lewis, N. S. Methods for Comparing the Performance of Energy-Conversion Systems for Use in Solar Fuels and Solar Electricity Generation. *Energy Environ. Sci.* **2015**, *8*, 2886–2901.

(78) Buriak, J. M.; Kamat, P. V.; Schanze, K. S. Best Practices for Reporting on Heterogeneous Photocatalysis. *ACS Appl. Mater. Interfaces* **2014**, *6*, 11815–11816.

(79) Bledowski, M.; Wang, L.; Ramakrishnan, A.; Khavryuchenko, O. V.; Khavryuchenko, V. D.; Ricci, P. C.; Strunk, J.; Cremer, T.; Kolbeck, C.; Beranek, R. Visible-Light Photocurrent Response of TiO_2–polyheptazine Hybrids: Evidence for Interfacial Charge-Transfer Absorption. *Phys. Chem. Chem. Phys.* **2011**, *13*, 21511–21519.

(80) Kirner, J. T.; Stracke, J. J.; Gregg, B. A.; Finke, R. G. Visible-Light-Assisted Photoelectrochemical Water Oxidation by Thin Films of a Phosphonate-Functionalized Perylene Diimide Plus CoO_x Cocatalyst. *ACS Appl. Mater. Interfaces* **2014**, *6*, 13367–13377. http://pubs.acs.org/doi/abs/10.1021/am405598w.

(81) Johnson, C. D.; Paul, D. W. In Situ Calibrated Oxygen Electrode. *Sens. Actuators B Chem.* **2005**, *105*, 322–328.

(82) Lee, S.-H. A.; Zhao, Y.; Hernandez-Pagan, E. A.; Blasdel, L.; Youngblood, W. J.; Mallouk, T. E. Electron Transfer Kinetics in Water Splitting Dye-Sensitized Solar Cells Based on Core–Shell Oxide Electrodes. *Faraday Discuss.* **2012**, *155*, 165–176.

(83) Swierk, J. R.; McCool, N. S.; Saunders, T. P.; Barber, G. D.; Strayer, M. E.; Vargas-Barbosa, N. M.; Mallouk, T. E. Photovoltage Effects of Sintered IrO_2 Nanoparticle Catalysts in Water-Splitting Dye-Sensitized Photoelectrochemical Cells. *J. Phys. Chem. C* **2014**, *118*, 17046–17053.

(84) McConnell, I.; Li, G.; Brudvig, G. W. Energy Conversion in Natural and Artificial Photosynthesis. *Chem. Biol.* **2010**, *17*, 434–447.

(85) Abe, T.; Nagai, K.; Ogiwara, T.; Ogasawara, S.; Kaneko, M.; Tajiri, A.; Norimatsu, T. Wide Visible Light-Induced Dioxygen Evolution at an Organic Photoanode Coated with a Noble Metal Oxide Catalyst. *J. Electroanal. Chem.* **2006**, *587*, 127–132.

(86) Abe, T.; Nagai, K.; Kabutomori, S.; Kaneko, M.; Tajiri, A.; Norimatsu, T. An Organic Photoelectrode Working in the Water Phase: Visible-Light-Induced Dioxygen Evolution by a Perylene Derivative/Cobalt Phthalocyanine Bilayer. *Angew. Chem. Int. Ed.* **2006**, *45*, 2778–2781.

(87) Chen, J.; Wagner, P.; Tong, L.; Wallace, G. G.; Officer, D. L.; Swiegers, G. F. A Porphyrin-Doped Polymer Catalyzes Selective, Light-Assisted Water Oxidation in Seawater. *Angew. Chem.* **2012**, *124*, 1943–1946.

(88) Liu, G.; Chen, C.; Ji, H.; Ma, W.; Zhao, J. Photo-Electrochemical Water Splitting System with Three-Layer n-Type Organic Semiconductor Film as Photoanode under Visible Irradiation. *Sci. China Chem.* **2012**, *55*, 1953–1958.

(89) Bornoz, P.; Prévot, M. S.; Yu, X.; Guijarro, N.; Sivula, K. Direct Light-Driven Water Oxidation by a Ladder-Type Conjugated Polymer Photoanode. *J. Am. Chem. Soc.* **2015**, *137*, 15338–15341. http://pubs.acs.org/doi/full/10.1021/jacs.5b05724.

(90) McCrory, C. C. L.; Jung, S.; Peters, J. C.; Jaramillo, T. F. Benchmarking Heterogeneous Electrocatalysts for the Oxygen Evolution Reaction. *J. Am. Chem. Soc.* **2013**, *135*, 16977–16987.

(91) Stracke, J. J.; Finke, R. G. Electrocatalytic Water Oxidation Beginning with the Cobalt Polyoxometalate $[Co_4(H_2O)_2(PW_9O_{34})_2]^{10-}$: Identification of Heterogeneous CoOx as the Dominant Catalyst. *J. Am. Chem. Soc.* **2011**, *133*, 14872–14875.

(92) Artero, V.; Fontecave, M. Solar Fuels Generation and Molecular Systems: Is It Homogeneous or Heterogeneous Catalysis? *Chem. Soc. Rev.* **2013**, *42*, 2338–2356.

(93) Stracke, J. J.; Finke, R. G. Distinguishing Homogeneous from Heterogeneous Water Oxidation Catalysis When Beginning with Polyoxometalates. *ACS Catal.* **2014**, 909–933.

(94) Roncali, J. Conjugated Poly(thiophenes): Synthesis, Functionalization, and Applications. *Chem. Rev.* **1992**, *92*, 711–738.

(95) Huijser, A.; Savenije, T. J.; Shalav, A.; Siebbeles, L. D. A. An Experimental Study on the Molecular Organization and Exciton Diffusion in a Bilayer of a Porphyrin and poly(3-Hexylthiophene). *J. Appl. Phys.* **2008**, *104*, 034505.

(96) Lubis, P.; Saito, M. Band Gap Design of Thiophene Polymers Based on Density Functional Theory. *Jpn. J. Appl. Phys.* **2014**, *53*, 071602.

(97) Naruta, Y.; Sasayama, M.; Sasaki, T. Oxygen Evolution by Oxidation of Water with Manganese Porphyrin Dimers. *Angew. Chem. Int. Ed. Engl.* **1994**, *33*, 1839–1841.

(98) Li, J.-X.; Li, Z.-J.; Ye, C.; Li, X.-B.; Zhan, F.; Fan, X.-B.; Li, J.; Chen, B.; Tao, Y.; Tung, C.-H.; *et al.* Visible Light-Induced Photochemical Oxygen Evolution from Water by 3,4,9,10-Perylenetetracarboxylic Dianhydride Nanorods as an n-Type Organic Semiconductor. *Catal. Sci. Technol.* **2016**, *6*, 672–676.

(99) Burke, M. S.; Enman, L. J.; Batchellor, A. S.; Zou, S.; Boettcher, S. W. Oxygen Evolution Reaction Electrocatalysis on Transition Metal Oxides and (Oxy)hydroxides: Activity Trends and Design Principles. *Chem. Mater.* **2015**, *27*, 7549–7558.

(100) Reese, M. O.; Nardes, A. M.; Rupert, B. L.; Larsen, R. E.; Olson, D. C.; Lloyd, M. T.; Shaheen, S. E.; Ginley, D. S.; Rumbles, G.; Kopidakis, N. Photoinduced Degradation of Polymer and Polymer–Fullerene Active Layers: Experiment and Theory. *Adv. Funct. Mater.* **2010**, *20*, 3476–3483.

(101) Bao, Q.; Liu, X.; Braun, S.; Fahlman, M. Oxygen- and Water-Based Degradation in [6,6]-Phenyl-C_{61}-Butyric Acid Methyl Ester (PCBM) Films. *Adv. Energy Mater.* **2014**, *4*, 1301272.

(102) Lanzarini, E.; Antognazza, M. R.; Biso, M.; Ansaldo, A.; Laudato, L.; Bruno, P.; Metrangolo, P.; Resnati, G.; Ricci, D.; Lanzani, G. Polymer-Based Photocatalytic Hydrogen Generation. *J Phys Chem C* **2012**, *116*, 10944–10949.

(103) Comas Rojas, H.; Bellani, S.; Fumagalli, F.; Tullii, G.; Leonardi, S.; T. Mayer, M.; Schreier, M.; Grätzel, M.; Lanzani, G.; Fonzo, F. D.; *et al.* Polymer-Based Photocathodes with a Solution-Processable Cuprous Iodide Anode Layer and a Polyethyleneimine Protective Coating. *Energy Environ. Sci.* **2016**, *9*, 3710–3723.

(104) Reese, M. O.; Morfa, A. J.; White, M. S.; Kopidakis, N.; Shaheen, S. E.; Rumbles, G.; Ginley, D. S. Pathways for the Degradation of Organic Photovoltaic P3HT:PCBM Based Devices. *Sol. Energy Mater. Sol. Cells* **2008**, *92*, 746–752.

(105) Norrman, K.; Gevorgyan, S. A.; Krebs, F. C. Water-Induced Degradation of Polymer Solar Cells Studied by $H_2{}^{18}O$ Labeling. *ACS Appl. Mater. Interfaces* **2009**, *1*, 102–112.

(106) Madogni, V. I.; Kounouhéwa, B.; Akpo, A.; Agbomahéna, M.; Hounkpatin, S. A.; Awanou, C. N. Comparison of Degradation Mechanisms in Organic Photovoltaic Devices upon Exposure to a Temperate and a Subequatorial Climate. *Chem. Phys. Lett.* **2015**, *640*, 201–214.

(107) Djurišić, A. B.; Liu, F.; Ng, A. M. C.; Dong, Q.; Wong, M. K.; Ng, A.; Surya, C. Stability Issues of the next Generation Solar Cells. *Phys. Status Solidi RRL – Rapid Res. Lett.* **2016**, *10*, 281–299.

(108) Kawai, T.; Tanimura, K.; Sakata, T. Mechanism of Photocurrent Generation at Zinc-Tetraphenylporphine/Metal Electrodes. *Chem. Phys. Lett.* **1978**, *56*, 541–545.

(109) Fan, F.-R.; Faulkner, L. R. Phthalocyanine Thin Films as Semiconductor Electrodes. *J. Am. Chem. Soc.* **1979**, *101*, 4779–4787.

(110) Ayers, W. M. Analysis of the Mass and Charge Transfer Limits of Copper Phthalocyanine Photoelectrochemistry. *Faraday Discuss. Chem. Soc.* **1980**, *70*, 247–254.

(111) Rieke, P. C.; Armstrong, N. R. Light-Assisted, Aqueous Redox Reactions at Chlorogallium Phthalocyanine Thin-Film Photoconductors: Dependence of the Photopotential on the Formal Potential of the Redox Couple and Evidence for Photoassisted Hydrogen Evolution. *J. Am. Chem. Soc.* **1984**, *106*, 47–50.

(112) Rieke, P. C.; Linkous, C. L.; Armstrong, N. R. Chlorogallium Phthalocyanine Thin-Film Photoelectrochemistry. Effect of Surface Coverage and Physical Distribution of Microcrystallites on the Photoelectrochemical Response. *J. Phys. Chem.* **1984**, *88*, 1351–1357.

(113) Buttner, W. J.; Rieke, P. C.; Armstrong, N. R. Evidence for Charge Trapping at the Gold/Chlorogallium Phthalocyanine Interface Using Photocurrent Spectroscopy with One or Two Illumination Sources. *J. Phys. Chem.* **1985**, *89*, 1116–1121.

(114) Rieke, P. C.; Armstrong, N. R. Pulsed Laser Coulostatic Studies of Phthalocyanine Photoconductor Electrodes. *J. Phys. Chem.* **1985**, *89*, 1121–1126.

(115) Kanan, M. W.; Nocera, D. G. In Situ Formation of an Oxygen-Evolving Catalyst in Neutral Water Containing Phosphate and Co^{2+}. *Science* **2008**, *321*, 1072–1075.

(116) Du, P.; Kokhan, O.; Chapman, K. W.; Chupas, P. J.; Tiede, D. M. Elucidating the Domain Structure of the Cobalt Oxide Water Splitting Catalyst by X-Ray Pair Distribution Function Analysis. *J. Am. Chem. Soc.* **2012**, *134*, 11096–11099.

(117) Kirner, J. T.; Finke, R. G. Sensitization of Nanocrystalline Metal Oxides with a Phosphonate-Functionalized Perylene Diimide: A Photoelectrochemical Anode En Route to Water Oxidation Catalysis. *ACS Appl. Mater. Interfaces* **2017**, To be submitted for publication.

(118) Zaban, A.; Meier, A.; Gregg, B. A. Electric Potential Distribution and Short-Range Screening in Nanoporous TiO_2 Electrodes. *J. Phys. Chem. B* **1997**, *101*, 7985–7990.

(119) Peter, L. M. Dye-Sensitized Nanocrystalline Solar Cells. *Phys. Chem. Chem. Phys.* **2007**, *9*, 2630–2642.

(120) Abe, T.; Tobinai, S.; Taira, N.; Chiba, J.; Itoh, T.; Nagai, K. Molecular Hydrogen Evolution by Organic p/n Bilayer Film of Phthalocyanine/Fullerene in the Entire Visible-Light Energy Region. *J. Phys. Chem. C* **2011**, *115*, 7701–7705.

(121) Abe, T.; Chiba, J.; Ishidoya, M.; Nagai, K. Organophotocatalysis System of p/n Bilayers for Wide Visible-Light-Induced Molecular Hydrogen Evolution. *RSC Adv.* **2012**, *2*, 7992–7996.

(122) Zhang, J.; Zhang, M.; Sun, R.-Q.; Wang, X. A Facile Band Alignment of Polymeric Carbon Nitride Semiconductors to Construct Isotype Heterojunctions. *Angew. Chem. Int. Ed.* **2012**, *51*, 10145–10149.

(123) Bourgeteau, T.; Tondelier, D.; Geffroy, B.; Brisse, R.; Laberty-Robert, C.; Campidelli, S.; Bettignies, R. de; Artero, V.; Palacin, S.; Jousselme, B. A H_2-Evolving Photocathode Based on Direct Sensitization of MoS_3 with an Organic Photovoltaic Cell. *Energy Environ. Sci.* **2013**, *6*, 2706–2713.

(124) Guerrero, A.; Haro, M.; Bellani, S.; Antognazza, M. R.; Meda, L.; Gimenez, S.; Bisquert, J. Organic Photoelectrochemical Cells with Quantitative Photocarrier Conversion. *Energy Environ. Sci.* **2014**, *7*, 3666–3673.

(125) Balapanuru, J.; Chiu, G.; Su, C.; Zhou, N.; Hai, Z.; Xu, Q.; Loh, K. P. Photoactive PDI–Cobalt Complex Immobilized on Reduced Graphene Oxide for Photoelectrochemical Water Splitting. *ACS Appl. Mater. Interfaces* **2015**, *7*, 880–886.

(126) Bourgeteau, T.; Tondelier, D.; Geffroy, B.; Brisse, R.; Cornut, R.; Artero, V.; Jousselme, B. Enhancing the Performances of P3HT:PCBM–MoS_3-Based H_2-Evolving Photocathodes with Interfacial Layers. *ACS Appl. Mater. Interfaces* **2015**, *7*, 16395–16403.

(127) Haro, M.; Solis, C.; Molina, G.; Otero, L.; Bisquert, J.; Gimenez, S.; Guerrero, A. Toward Stable Solar Hydrogen Generation Using Organic Photoelectrochemical Cells. *J. Phys. Chem. C* **2015**, *119*, 6488–6494.

(128) Bourgeteau, T.; Tondelier, D.; Geffroy, B.; Brisse, R.; Campidelli, S.; Cornut, R.; Jousselme, B. All Solution-Processed Organic Photocathodes with Increased Efficiency and Stability via the Tuning of the Hole-Extracting Layer. *J. Mater. Chem. A* **2016**, *4*, 4831–4839.

(129) Fumagalli, F.; Bellani, S.; Schreier, M.; Leonardi, S.; Rojas, H. C.; Ghadirzadeh, A.; Tullii, G.; Savoini, A.; Marra, G.; Meda, L.; *et al.* Hybrid Organic–inorganic H_2-Evolving Photocathodes: Understanding the Route towards High Performance Organic Photoelectrochemical Water Splitting. *J. Mater. Chem. A* **2016**, *4*, 2178–2187.

(130) Morozan, A.; Bourgeteau, T.; Tondelier, D.; Geffroy, B.; Jousselme, B.; Artero, V. Noble Metal-Free Hydrogen-Evolving Photocathodes Based on Small Molecule Organic Semiconductors. *Nanotechnology* **2016**, *27*, 355401.

(131) Giribabu, L.; Kanaparthi, R. K.; Velkannan, V. Molecular Engineering of Sensitizers for Dye-Sensitized Solar Cell Applications. *Chem. Rec.* **2012**, *12*, 306–328.

(132) Gao, Y.; Ding, X.; Liu, J.; Wang, L.; Lu, Z.; Li, L.; Sun, L. Visible Light Driven Water Splitting in a Molecular Device with Unprecedentedly High Photocurrent Density. *J. Am. Chem. Soc.* **2013**, *135*, 4219–4222.

(133) Zhang, L.; Gao, Y.; Ding, X.; Yu, Z.; Sun, L. High-Performance Photoelectrochemical Cells Based on a Binuclear Ruthenium Catalyst for Visible-Light-Driven Water Oxidation. *ChemSusChem* **2014**, *7*, 2801–2804.

(134) Mishra, A.; Fischer, M. K. R.; Bäuerle, P. Metal-Free Organic Dyes for Dye-Sensitized Solar Cells: From Structure: Property Relationships to Design Rules. *Angew. Chem. Int. Ed.* **2009**, *48*, 2474–2499.

(135) Mann, J. R.; Gannon, M. K.; Fitzgibbons, T. C.; Detty, M. R.; Watson, D. F. Optimizing the Photocurrent Efficiency of Dye-Sensitized Solar Cells through the Controlled Aggregation of Chalcogenoxanthylium Dyes on Nanocrystalline Titania Films. *J. Phys. Chem. C* **2008**, *112*, 13057–13061.

(136) Grätzel, M. The Artificial Leaf, Bio-Mimetic Photocatalysis. *CATTECH* **1999**, *3*, 4–17.

(137) Gardner, J. M.; Beyler, M.; Karnahl, M.; Tschierlei, S.; Ott, S.; Hammarström, L. Light-Driven Electron Transfer between a Photosensitizer and a Proton-Reducing Catalyst Co-Adsorbed to NiO. *J. Am. Chem. Soc.* **2012**, *134*, 19322–19325.

(138) Li, L.; Duan, L.; Wen, F.; Li, C.; Wang, M.; Hagfeldt, A.; Sun, L. Visible Light Driven Hydrogen Production from a Photo-Active Cathode Based on a Molecular Catalyst and Organic Dye-Sensitized p-Type Nanostructured NiO. *Chem. Commun.* **2012**, *48*, 988–990.

(139) Tong, L.; Iwase, A.; Nattestad, A.; Bach, U.; Weidelener, M.; Götz, G.; Mishra, A.; Bäuerle, P.; Amal, R.; Wallace, G. G.; *et al.* Sustained Solar Hydrogen Generation Using a Dye-Sensitised NiO Photocathode/$BiVO_4$ Tandem Photo-Electrochemical Device. *Energy Environ. Sci.* **2012**, *5*, 9472–9475.

(140) Ji, Z.; He, M.; Huang, Z.; Ozkan, U.; Wu, Y. Photostable p-Type Dye-Sensitized Photoelectrochemical Cells for Water Reduction. *J. Am. Chem. Soc.* **2013**, *135*, 11696–11699.

(141) Click, K. A.; Beauchamp, D. R.; Huang, Z.; Chen, W.; Wu, Y. Membrane-Inspired Acidically Stable Dye-Sensitized Photocathode for Solar Fuel Production. *J. Am. Chem. Soc.* **2016**, *138*, 1174–1179.

(142) Kaeffer, N.; Massin, J.; Lebrun, C.; Renault, O.; Chavarot-Kerlidou, M.; Artero, V. Covalent Design for Dye-Sensitized H_2-Evolving Photocathodes Based on a Cobalt Diimine–Dioxime Catalyst. *J. Am. Chem. Soc.* **2016**, *138*, 12308–12311.

(143) Khusnutdinova, D.; Beiler, A. M.; Wadsworth, B. L.; Jacob, S. I.; Moore, G. F. Metalloporphyrin-Modified Semiconductors for Solar Fuel Production. *Chem. Sci.* **2017**, *8*, 253–259.

(144) Kamire, R. J.; Majewski, M. B.; Hoffeditz, W. L.; Phelan, B. T.; Farha, O. K.; Hupp, J. T.; Wasielewski, M. R. Photodriven Hydrogen Evolution by Molecular Catalysts Using Al_2O_3-Protected Perylene-3,4-Dicarboximide on NiO Electrodes. *Chem. Sci.* **2017**, *8*, 541–549.

(145) Moore, G. F.; Blakemore, J. D.; Milot, R. L.; Hull, J. F.; Song, H.; Cai, L.; Schmuttenmaer, C. A.; Crabtree, R. H.; Brudvig, G. W. A Visible Light Water-Splitting Cell with a Photoanode Formed by Codeposition of a High-Potential Porphyrin and an Iridium Water-Oxidation Catalyst. *Energy Environ. Sci.* **2011**, *4*, 2389–2392.

(146) Swierk, J. R.; Méndez-Hernández, D. D.; McCool, N. S.; Liddell, P.; Terazono, Y.; Pahk, I.; Tomlin, J. J.; Oster, N. V.; Moore, T. A.; Moore, A. L.; *et al.* Metal-Free Organic Sensitizers for Use in Water-Splitting Dye-Sensitized Photoelectrochemical Cells. *Proc. Natl. Acad. Sci.* **2015**, *112*, 1681–1686.

(147) Yamamoto, M.; Wang, L.; Li, F.; Fukushima, T.; Tanaka, K.; Sun, L.; Imahori, H. Visible Light-Driven Water Oxidation Using a Covalently-Linked Molecular Catalyst–Sensitizer Dyad Assembled on a TiO_2 Electrode. *Chem. Sci.* **2016**, *7*, 1430–1439.

(148) Yamamoto, M.; Nishizawa, Y.; Chábera, P.; Li, F.; Pascher, T.; Sundström, V.; Sun, L.; Imahori, H. Visible Light-Driven Water Oxidation with a Subporphyrin Sensitizer and a Water Oxidation Catalyst. *Chem. Commun.* **2016**, *52*, 13702–13705.

(149) Ronconi, F.; Syrgiannis, Z.; Bonasera, A.; Prato, M.; Argazzi, R.; Caramori, S.; Cristino, V.; Bignozzi, C. A. Modification of Nanocrystalline WO_3 with a Dicationic Perylene Bisimide: Applications to Molecular Level Solar Water Splitting. *J. Am. Chem. Soc.* **2015**, *137*, 4630–4633.

(150) Kamire, R. J.; Materna, K. L.; Hoffeditz, W. L.; Phelan, B. T.; Thomsen, J. M.; Farha, O. K.; Hupp, J. T.; Brudvig, G. W.; Wasielewski, M. R. Photodriven Oxidation of Surface-Bound Iridium-Based Molecular Water-Oxidation Catalysts on Perylene-3,4-Dicarboximide-Sensitized TiO_2 Electrodes Protected by an Al_2O_3 Layer. *J. Phys. Chem. C* **2017**, *121*, 3752–3764.

(151) Wee, K.-R.; Sherman, B. D.; Brennaman, M. K.; Sheridan, M. V.; Nayak, A.; Alibabaei, L.; Meyer, T. J. An Aqueous, Organic Dye Derivatized SnO_2/TiO_2 Core/Shell Photoanode. *J. Mater. Chem. A* **2016**, *4*, 2969–2975.

(152) Wang, L.; Bledowski, M.; Ramakrishnan, A.; König, D.; Ludwig, A.; Beranek, R. Dynamics of Photogenerated Holes in TiO_2-Polyheptazine Hybrid Photoanodes for Visible Light-Driven Water Splitting. *J. Electrochem. Soc.* **2012**, *159*, H616–H622.

(153) Mathew, S.; Yella, A.; Gao, P.; Humphry-Baker, R.; Curchod, B. F. E.; Ashari-Astani, N.; Tavernelli, I.; Rothlisberger, U.; Nazeeruddin, M. K.; Grätzel, M. Dye-Sensitized Solar Cells with 13% Efficiency Achieved through the Molecular Engineering of Porphyrin Sensitizers. *Nat. Chem.* **2014**, *6*, 242–247.

(154) Kärkäs, M. D.; Verho, O.; Johnston, E. V.; Åkermark, B. Artificial Photosynthesis: Molecular Systems for Catalytic Water Oxidation. *Chem. Rev.* **2014**, *114*, 11863–12001.

(155) Hull, J. F.; Balcells, D.; Blakemore, J. D.; Incarvito, C. D.; Eisenstein, O.; Brudvig, G. W.; Crabtree, R. H. Highly Active and Robust Cp* Iridium Complexes for Catalytic Water Oxidation. *J. Am. Chem. Soc.* **2009**, *131*, 8730–8731.

(156) Ashford, D. L.; Sherman, B. D.; Binstead, R. A.; Templeton, J. L.; Meyer, T. J. Electro-Assembly of a Chromophore–Catalyst Bilayer for Water Oxidation and Photocatalytic Water Splitting. *Angew. Chem.* **2015**, *127*, 4860–4863.

(157) Duan, L.; Fischer, A.; Xu, Y.; Sun, L. Isolated Seven-Coordinate Ru(IV) Dimer Complex with [HOHOH]− Bridging Ligand as an Intermediate for Catalytic Water Oxidation. *J. Am. Chem. Soc.* **2009**, *131*, 10397–10399.

(158) Gao, Y.; Zhang, L.; Ding, X.; Sun, L. Artificial Photosynthesis – Functional Devices for Light Driven Water Splitting with Photoactive Anodes Based on Molecular Catalysts. *Phys. Chem. Chem. Phys.* **2014**, *16*, 12008–12013.

(159) Cheng, Y.; Memar, A.; Saunders, M.; Pan, J.; Liu, C.; Gale, J. D.; Demichelis, R.; Shen, P. K.; Jiang, S. P. Dye Functionalized Carbon Nanotubes for Photoelectrochemical Water Splitting – Role of Inner Tubes. *J. Mater. Chem. A* **2016**, *4*, 2473–2483.

(160) Cheng, Y.; Xu, C.; Jia, L.; Gale, J. D.; Zhang, L.; Liu, C.; Shen, P. K.; Jiang, S. P. Pristine Carbon Nanotubes as Non-Metal Electrocatalysts for Oxygen Evolution Reaction of Water Splitting. *Appl. Catal. B Environ.* **2015**, *163*, 96–104.

(161) Terasaki, N.; Iwai, M.; Yamamoto, N.; Hiraga, T.; Yamada, S.; Inoue, Y. Photocurrent Generation Properties of Histag-Photosystem II Immobilized on Nanostructured Gold Electrode. *Thin Solid Films* **2008**, *516*, 2553–2557.

(162) Mersch, D.; Lee, C.-Y.; Zhang, J. Z.; Brinkert, K.; Fontecilla-Camps, J. C.; Rutherford, A. W.; Reisner, E. Wiring of Photosystem II to Hydrogenase for Photoelectrochemical Water Splitting. *J. Am. Chem. Soc.* **2015**, *137*, 8541–8549.

(163) Sokol, K. P.; Mersch, D.; Hartmann, V.; Zhang, J. Z.; Nowaczyk, M. M.; Rögner, M.; Ruff, A.; Schuhmann, W.; Plumeré, N.; Reisner, E. Rational Wiring of Photosystem II to Hierarchical Indium Tin Oxide Electrodes Using Redox Polymers. *Energy Environ. Sci.* **2016**, *9*, 3698–3709.

(164) Moore, G. F.; Konezny, S. J.; Song, H.; Milot, R. L.; Blakemore, J. D.; Lee, M. L.; Batista, V. S.; Schmuttenmaer, C. A.; Crabtree, R. H.; Brudvig, G. W. Bioinspired High-Potential Porphyrin Photoanodes. *J. Phys. Chem. C* **2012**, *116*, 4892–4902.

(165) Martini, L. A.; Moore, G. F.; Milot, R. L.; Cai, L. Z.; Sheehan, S. W.; Schmuttenmaer, C. A.; Brudvig, G. W.; Crabtree, R. H. Modular Assembly of High-Potential Zinc Porphyrin Photosensitizers Attached to TiO_2 with a Series of Anchoring Groups. *J. Phys. Chem. C* **2013**, *117*, 14526–14533.

(166) Milot, R. L.; Moore, G. F.; Crabtree, R. H.; Brudvig, G. W.; Schmuttenmaer, C. A. Electron Injection Dynamics from Photoexcited Porphyrin Dyes into SnO_2 and TiO_2 Nanoparticles. *J. Phys. Chem. C* **2013**, *117*, 21662–21670.

(167) Negre, C. F. A.; Milot, R. L.; Martini, L. A.; Ding, W.; Crabtree, R. H.; Schmuttenmaer, C. A.; Batista, V. S. Efficiency of Interfacial Electron Transfer from Zn-Porphyrin Dyes into TiO_2 Correlated to the Linker Single Molecule Conductance. *J. Phys. Chem. C* **2013**, *117*, 24462–24470.

(168) Brennan, B. J.; Durrell, A. C.; Koepf, M.; Crabtree, R. H.; Brudvig, G. W. Towards Multielectron Photocatalysis: A Porphyrin Array for Lateral Hole Transfer and Capture on a Metal Oxide Surface. *Phys. Chem. Chem. Phys.* **2015**, *17*, 12728–12734.

(169) Brennan, B. J.; Lam, Y. C.; Kim, P. M.; Zhang, X.; Brudvig, G. W. Photoelectrochemical Cells Utilizing Tunable Corroles. *ACS Appl. Mater. Interfaces* **2015**, *7*, 16124–16130.

(170) Poddutoori, P. K.; Thomsen, J. M.; Milot, R. L.; Sheehan, S. W.; Negre, C. F. A.; Garapati, V. K. R.; Schmuttenmaer, C. A.; Batista, V. S.; Brudvig, G. W.; van der Est, A. Interfacial Electron Transfer in Photoanodes Based on Phosphorus(V) Porphyrin Sensitizers Co-Deposited on SnO_2 with the Ir(III)Cp* Water Oxidation Precatalyst. *J. Mater. Chem. A* **2015**, *3*, 3868–3879.

(171) Antoniuk-Pablant, A.; Terazono, Y.; Brennan, B. J.; Sherman, B. D.; Megiatto, J. D.; Brudvig, G. W.; Moore, A. L.; Moore, T. A.; Gust, D. A New Method for the Synthesis of *β*-Cyano Substituted Porphyrins and Their Use as Sensitizers in Photoelectrochemical Devices. *J. Mater. Chem. A* **2016**, *4*, 2976–2985.

(172) Nayak, A.; Roy, S.; Sherman, B. D.; Alibabaei, L.; Lapides, A. M.; Brennaman, M. K.; Wee, K.-R.; Meyer, T. J. Phosphonate-Derivatized Porphyrins for Photoelectrochemical Applications. *ACS Appl. Mater. Interfaces* **2016**, *8*, 3853–3860.

(173) Sherman, B. D.; Bergkamp, J. J.; Brown, C. L.; Moore, A. L.; Gust, D.; Moore, T. A. A Tandem Dye-Sensitized Photoelectrochemical Cell for Light Driven Hydrogen Production. *Energy Environ. Sci.* **2016**, *9*, 1812–1817.

(174) Jiang, J.; Swierk, J. R.; Materna, K. L.; Hedström, S.; Lee, S. H.; Crabtree, R. H.; Schmuttenmaer, C. A.; Batista, V. S.; Brudvig, G. W. High-Potential Porphyrins Supported on SnO_2 and TiO_2 Surfaces for Photoelectrochemical Applications. *J. Phys. Chem. C* **2016**, *120*, 28971–28982.

(175) Rawls, M. T.; Johnson, J.; Gregg, B. A. Coupling One Electron Photoprocesses to Multielectron Catalysts: Towards a Photoelectrocatalytic System. *J. Electroanal. Chem.* **2010**, *650*, 10–15.

(176) Liu, D.; Wang, J.; Bai, X.; Zong, R.; Zhu, Y. Self-Assembled PDINH Supramolecular System for Photocatalysis under Visible Light. *Adv. Mater.* **2016**, *28*, 7284–7290.

(177) Wang, J.; Shi, W.; Liu, D.; Zhang, Z.; Zhu, Y.; Wang, D. Supramolecular Organic Nanofibers with Highly Efficient and Stable Visible Light Photooxidation Performance. *Appl. Catal. B Environ.* **2017**, *202*, 289–297.

(178) Vagnini, M. T.; Smeigh, A. L.; Blakemore, J. D.; Eaton, S. W.; Schley, N. D.; D'Souza, F.; Crabtree, R. H.; Brudvig, G. W.; Co, D. T.; Wasielewski, M. R. Ultrafast Photodriven Intramolecular Electron Transfer from an Iridium-Based Water-Oxidation Catalyst to Perylene Diimide Derivatives. *Proc. Natl. Acad. Sci. U. S. A.* **2012**, *109*, 15651–15656.

(179) Brennaman, M. K.; Norris, M. R.; Gish, M. K.; Grumstrup, E. M.; Alibabaei, L.; Ashford, D. L.; Lapides, A. M.; Papanikolas, J. M.; Templeton, J. L.; Meyer, T. J. Ultrafast, Light-Induced Electron Transfer in a Perylene Diimide Chromophore-Donor Assembly on TiO_2. *J. Phys. Chem. Lett.* **2015**, *6*, 4736–4742.

(180) Lindquist, R. J.; Phelan, B. T.; Reynal, A.; Margulies, E. A.; Shoer, L. E.; Durrant, J. R.; Wasielewski, M. R. Strongly Oxidizing Perylene-3,4-Dicarboximides for Use in Water Oxidation Photoelectrochemical Cells. *J. Mater. Chem. A* **2016**, *4*, 2880–2893.

(181) Ferrere, S.; Zaban, A.; Gregg, B. A. Dye Sensitization of Nanocrystalline Tin Oxide by Perylene Derivatives. *J. Phys. Chem. B* **1997**, *101*, 4490–4493.

(182) Chen, H.-C.; Williams, R. M.; Reek, J. N. H.; Brouwer, A. M. Robust Benzo[ghi]perylenetriimide Dye-Sensitized Electrodes in Air-Saturated Aqueous Buffer Solution. *Chem. Eur. J.* **2016**, *22*, 5489–5493.

(183) Parks, G. A. The Isoelectric Points of Solid Oxides, Solid Hydroxides, and Aqueous Hydroxo Complex Systems. *Chem. Rev.* **1965**, *65*, 177–198.

(184) Hara, M.; Waraksa, C. C.; Lean, J. T.; Lewis, B. A.; Mallouk, T. E. Photocatalytic Water Oxidation in a Buffered Tris(2,2‘-Bipyridyl)ruthenium Complex-Colloidal IrO_2 System. *J. Phys. Chem. A* **2000**, *104*, 5275–5280.

(185) Son, H.-J.; Prasittichai, C.; Mondloch, J. E.; Luo, L.; Wu, J.; Kim, D. W.; Farha, O. K.; Hupp, J. T. Dye Stabilization and Enhanced Photoelectrode Wettability in Water-Based Dye-Sensitized Solar Cells through Post-Assembly Atomic Layer Deposition of TiO_2. *J. Am. Chem. Soc.* **2013**, *135*, 11529–11532.

(186) Hanson, K.; Losego, M. D.; Kalanyan, B.; Ashford, D. L.; Parsons, G. N.; Meyer, T. J. Stabilization of $[Ru(bpy)_2(4,4'\text{-}(PO_3H_2)bpy)]^{2+}$ on Mesoporous TiO_2 with Atomic Layer Deposition of Al_2O_3. *Chem. Mater.* **2013**, *25*, 3–5.

(187) Hamann, T. W.; Farha, O. K.; Hupp, J. T. Outer-Sphere Redox Couples as Shuttles in Dye-Sensitized Solar Cells. Performance Enhancement Based on Photoelectrode Modification via Atomic Layer Deposition. *J. Phys. Chem. C* **2008**, *112*, 19756–19764.

(188) Prasittichai, C.; Hupp, J. T. Surface Modification of SnO_2 Photoelectrodes in Dye-Sensitized Solar Cells: Significant Improvements in Photovoltage via Al_2O_3 Atomic Layer Deposition. *J. Phys. Chem. Lett.* **2010**, *1*, 1611–1615.

(189) Sheehan, S. W.; Thomsen, J. M.; Hintermair, U.; Crabtree, R. H.; Brudvig, G. W.; Schmuttenmaer, C. A. A Molecular Catalyst for Water Oxidation That Binds to Metal Oxide Surfaces. *Nat. Commun.* **2015**, *6*, 6469.

(190) Materna, K. L.; Rudshteyn, B.; Brennan, B. J.; Kane, M. H.; Bloomfield, A. J.; Huang, D. L.; Shopov, D. Y.; Batista, V. S.; Crabtree, R. H.; Brudvig, G. W. Heterogenized Iridium Water-Oxidation Catalyst from a Silatrane Precursor. *ACS Catal.* **2016**, *6*, 5371–5377.

(191) Duan, L.; Xu, Y.; Gorlov, M.; Tong, L.; Andersson, S.; Sun, L. Chemical and Photochemical Water Oxidation Catalyzed by Mononuclear Ruthenium Complexes with a Negatively Charged Tridentate Ligand. *Chem. – Eur. J.* **2010**, *16*, 4659–4668.

(192) Fan, K.; Li, F.; Wang, L.; Daniel, Q.; Gabrielsson, E.; Sun, L. Pt-Free Tandem Molecular Photoelectrochemical Cells for Water Splitting Driven by Visible Light. *Phys. Chem. Chem. Phys.* **2014**, *16*, 25234–25240.

(193) Mei, B.; Byford, H.; Bledowski, M.; Wang, L.; Strunk, J.; Muhler, M.; Beranek, R. Beneficial Effect of Nb Doping on the Photoelectrochemical Properties of TiO_2 and TiO_2-Polyheptazine Hybrids. *Sol. Energy Mater. Sol. Cells* **2013**, *117*, 48–53.

(194) Bledowski, M.; Wang, L.; Ramakrishnan, A.; Bétard, A.; Khavryuchenko, O. V.; Beranek, R. Visible-Light Photooxidation of Water to Oxygen at Hybrid TiO_2–Polyheptazine Photoanodes with Photodeposited Co-Pi (CoO_x) Cocatalyst. *ChemPhysChem* **2012**, *13*, 3018–3024.

(195) Bledowski, M.; Wang, L.; Ramakrishnan, A.; Beranek, R. TiO_2-Polyheptazine Hybrid Photoanodes: Effect of Cocatalysts and External Bias on Visible Light-Driven Water Splitting. *J. Mater. Res.* **2013**, *28*, 411–417.

(196) Bledowski, M.; Wang, L.; Neubert, S.; Mitoraj, D.; Beranek, R. Improving the Performance of Hybrid Photoanodes for Water Splitting by Photodeposition of Iridium Oxide Nanoparticles. *J. Phys. Chem. C* **2014**, *118*, 18951–18961.

(197) Owe, L.-E.; Tsypkin, M.; Sunde, S. The Effect of Phosphate on Iridium Oxide Electrochemistry. *Electrochimica Acta* **2011**, *58*, 231–237.

(198) N. Kushner-Lenhoff, M.; D. Blakemore, J.; D. Schley, N.; H. Crabtree, R.; W. Brudvig, G. Effects of Aqueous Buffers on Electrocatalytic Water Oxidation with an Iridium Oxide Material Electrodeposited in Thin Layers from an Organometallic Precursor. *Dalton Trans.* **2013**, *42*, 3617–3622.

(199) Wang, Z.; Xiao, P.; Qiao, L.; Meng, X.; Zhang, Y.; Li, X.; Yang, F. Polypyrrole Sensitized ZnO Nanorod Arrays for Efficient Photo-Electrochemical Splitting of Water. *Phys. B Condens. Matter* **2013**, *419*, 51–56.

(200) De Zoubov, M.; Pourbaix, M. Section 15.1-Zinc. In *Atlas of Electrochemical Equilibria in Aqueous Solutions*; Permagon Press Inc.: New York, 1966; pp. 406–413.

(201) Wippermann, K.; Schultze, J. W.; Kessel, R.; Penninger, J. The Inhibition of Zinc Corrosion by Bisaminotriazole and Other Triazole Derivatives. *Corros. Sci.* **1991**, *32*, 205–230.

(202) Wei, P.; Hu, B.; Zhou, L.; Su, T.; Na, Y. New Strategy to Incorporate Nano-Particle Sized Water Oxidation Catalyst into Dye-Sensitized Photoelectrochemical Cell for Water Splitting. *J. Energy Chem.* **2016**, *25*, 345–348.

(203) Youngblood, W. J.; Lee, S.-H. A.; Kobayashi, Y.; Hernandez-Pagan, E. A.; Hoertz, P. G.; Moore, T. A.; Moore, A. L.; Gust, D.; Mallouk, T. E. Photoassisted Overall Water Splitting in a Visible Light-Absorbing Dye-Sensitized Photoelectrochemical Cell. *J. Am. Chem. Soc.* **2009**, *131*, 926–927.

(204) Knauf, R. R.; Brennaman, M. K.; Alibabaei, L.; Norris, M. R.; Dempsey, J. L. Revealing the Relationship between Semiconductor Electronic Structure and Electron Transfer Dynamics at Metal Oxide–Chromophore Interfaces. *J. Phys. Chem. C* **2013**, *117*, 25259–25268.

(205) Swierk, J. R.; McCool, N. S.; Saunders, T. P.; Barber, G. D.; Mallouk, T. E. Effects of Electron Trapping and Protonation on the Efficiency of Water-Splitting Dye-Sensitized Solar Cells. *J. Am. Chem. Soc.* **2014**, *136*, 10974–10982.

(206) McCool, N. S.; Swierk, J. R.; Nemes, C. T.; Saunders, T. P.; Schmuttenmaer, C. A.; Mallouk, T. E. Proton-Induced Trap States, Injection and Recombination Dynamics in Water-Splitting Dye-Sensitized Photoelectrochemical Cells. *ACS Appl. Mater. Interfaces* **2016**, *8*, 16727–16735.

(207) Hanson, K.; Brennaman, M. K.; Luo, H.; Glasson, C. R. K.; Concepcion, J. J.; Song, W.; Meyer, T. J. Photostability of Phosphonate-Derivatized, Ru^{II} Polypyridyl Complexes on Metal Oxide Surfaces. *ACS Appl. Mater. Interfaces* **2012**, *4*, 1462–1469.

(208) Ghosh, P. K.; Brunschwig, B. S.; Chou, M.; Creutz, C.; Sutin, N. Thermal and Light-Induced Reduction of the Ruthenium Complex Cation $Ru(bpy)_3^{3+}$ in Aqueous Solution. *J. Am. Chem. Soc.* **1984**, *106*, 4772–4783.

III. VISIBLE-LIGHT-ASSISTED PHOTOELECTROCHEMICAL WATER OXIDATION BY THIN FILMS OF A PHOSPHONATE-FUNCTIONALIZED PERYLENE DIIMIDE PLUS COBALT OXIDE COCATALYST[ii]

Overview

A novel perylene diimide dye functionalized with phosphonate groups, N,N′-bis(phosphonomethyl)-3,4,9,10-perylenediimide (PMPDI), is synthesized and characterized. Thin films of PMPDI spin-coated onto indium tin oxide (ITO) substrates are further characterized, augmented by photoelectrochemically depositing a CoO_x catalyst, and then investigated as photoanodes for water oxidation. These ITO/PMPDI/CoO_x electrodes show visible-light-assisted water oxidation with photocurrents in excess of 150 $\mu A/cm^2$ at 1.0 V applied bias vs. Ag/AgCl. Water oxidation is confirmed by the direct detection of O_2, with a faradaic efficiency of 80 ± 15% measured under 900 mV applied bias vs. Ag/AgCl. Analogous photoanodes prepared with another PDI derivative with alkyl groups in place of PMPDI's phosphonate groups do not function,

---

[ii] This study details the preparation and characterization of a prototype, organic thin-film photoanode architecture. Characterization of this device provides knowledge of the efficiency-limiting processes that will be addressed in Chapter IV. This chapter contains the complete published manuscript (Kirner, J. T.; Stracke, J. J.; Gregg, B. A.; Finke, R. G. *ACS Appl. Mater. Interfaces* **2014,** *6,* 13367–13377. http://pubs.acs.org/doi/full/10.1021/am405598w.) which has been reproduced with permission. The article is licensed under ACS AuthorCoice, and further permission requests related to the article should be directed to the ACS. The project was the brainchild of the PIs, Dr. Gregg and Prof. Finke. Graduate student J. Stracke was the first to synthesize the novel perylene diimide dye and performed preliminary spin coating, catalyst deposition, and photocurrent measurement experiments. All such experiments were repeated by the first author, and all additional characterization experiments were performed by the first author alone. Minor changes to the manuscript have been made to meet dissertation formatting requirements. For example, table and figure numbers have been changed to indicate that they are specific to this chapter, and Supporting Information have been moved to Appendix I. A List of Abbreviations has been combined from all chapters and is provided as a Supplementary Section at the end of this dissertation.

providing evidence that PMPDI's phosphonate groups may be important for efficient coupling between the inorganic CoO_x catalyst and the organic dye. Our ITO/PMPDI/CoO_x anodes achieve internal quantum efficiencies for water oxidation ~1%, and for hydroquinone oxidation of up to ~6%. The novelty of our system is that, to the best of our knowledge, it is the first device to achieve photoelectrochemically driven water oxidation by a single-layer molecular organic semiconductor thin film coupled to a water-oxidation catalyst.

3.1 Introduction

The growing need for clean and renewable energy has led to considerable interest in the development of systems to harvest and store earth's abundant solar energy resources.[1] One promising solution is to store solar energy in the form of chemical bonds by forming solar fuels such as hydrogen gas. Indeed, the efficient photocatalytic conversion of liquid water to hydrogen and oxygen gases by artificial photosynthesis has been named as one of the "Holy Grails of Chemistry".[2,3] Since Honda and Fujishima first reported light-induced water oxidation by a TiO_2 semiconductor electrode,[4] photoelectrochemical water-splitting systems have received a great deal of attention. Although several inorganic solar water-splitting systems have achieved solar-to-hydrogen efficiencies above 10%[5–7] (the threshold for practical commercialization),[3] they are limited by the use of expensive materials or by poor long-term stability. It is, therefore, of continuing, significant interest to study alternative water-splitting systems based on semiconductors and catalysts that are composed of cheap and abundant materials.

Organic semiconductors are promising materials for electronics and photovoltaics due to the synthetic tunability of their properties, to their low cost, and to the low-temperature manufacturing processes they generally have available. If a suitable system were found, then these

three favorable properties could help make organic-semiconductor-based water-splitting systems economically viable. Several examples of water splitting photoelectrochemical cells employing organic materials are present in the literature.[8–17] These systems generally use organic or organometallic dyes as light collectors (a one electron/hole per photon process), coupled with catalysts to assist in water oxidation (a multi-electron process). Architectures include organic photovoltaic bilayers,[8,9] trilayers,[10] and dye-sensitized mesoporous semiconductor architectures using either organometallic[11–16] or organic polymer dye sensitizers.[17]

The hypothesis on which the current research is based is that perylene diimide dyes (PDI dyes; see the List of Abbreviations at the end of this dissertation) are promising organic molecules to study for organic water-splitting schemes, because of their robust nature and strong visible light absorption (they are relatively cheap, industrial dyes commonly used as colorants in car paints and plastics).[18] PDIs exhibit high thermal stability, with decomposition temperatures typically in the range of 300–600 °C,[19] and high oxidative stability in air and water, even resisting photobleaching in concentrated hypochlorite solutions.[20] Many PDIs exhibit a highest occupied molecular orbital (HOMO) that has a positive enough potential to oxidize water.[21] In the solid state, PDIs tend to π-stack, which often leads to a high degree of molecular order and strong electronic coupling between neighboring PDI molecules. Indeed, a polycrystalline PDI derivative has shown one of the longest exciton-transfer lengths (2.5 ± 0.5 μm) reported for an organic material.[22] These favorable properties have led several groups to propose the use of perylene derivatives in organic water oxidation systems.[8,9,10,23,24]

Herein we examine a water-oxidation photoelectrochemical cell based on light absorption by a novel PDI derivative, N,N'-bis(phosphonomethyl)-3,4,9,10-perylenediimide (PMPDI), shown in Figure 3.1. A sub-hypothesis of this research is that the phosphonate groups of PMPDI

should be beneficial when coupling the dye with, specifically, a heterogeneous cobalt-oxide catalyst (CoO_x or Co-Pi)[25] which has been shown to have phosphate groups as a disordered component of its structure when electrochemically formed from phosphate-containing solutions.[26] We show herein that thin films of PMPDI on indium tin oxide (ITO) plus photoelectrochemically deposited[27] CoO_x (ITO/PMPDI/CoO_x) are capable of photo-assisted water oxidation with current densities in excess of 150 μA/cm^2 under a positive bias of 1.0 V vs. Ag/AgCl. We confirm the water-oxidation reaction through the direct detection of O_2, with a faradaic efficiency of 80 ± 15% under positive applied bias. We compare the performance of ITO/PMPDI/CoO_x anodes to those using another PDI derivative, N,N'-bis(1-ethylpropyl)-3,4,9,10-perylenediimide (EPPDI), as a way to probe the importance of phosphonate groups in the structure, the results of which do implicate a role for the phosphonate groups in PMPDI. Finally, we hypothesize about the performance-limiting factors of our current system and propose future directions for optimization of the system.

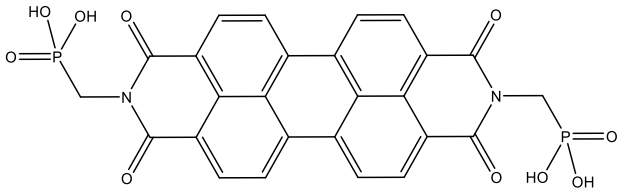

Figure 3.1 Structure of N,N´-bis(phosphonomethyl)-3,4,9,10-perylenediimide (PMPDI).

3.2 Results and Discussion

Synthesis and characterization of PMPDI. PMPDI was conveniently synthesized by adjusting a literature procedure[28] for an N,N'-bis(phosphono*ethyl*) PDI derivative. Specifically, PMPDI (Figure 3.1) was formed from the dehydration reaction between perylene tetracarboxylic dianhydride (PTCDA) and (aminomethyl)phosphonic acid in molten imidazole. The crude product

was purified by two cycles of dissolving the product in water by deprotonating it to the tetra-potassium salt in basic solution, filtering out any remaining PTCDA, precipitating the product by adding acid until pH 1, then collecting the solid on a filter to separate it from residual imidazole dissolved in the acidic solution. The purified product was dried overnight in a vacuum oven, giving a 90% yield. The product was pure by proton and phosphorus NMR (see Figures S3.1 and S3.2 in the Supporting Information), although the proton NMR showed highly broadened peaks, especially for the aromatic protons. Peak broadening is commonly observed for PDIs and has been attributed to π-stacking aggregation.[28,29] HPLC showed evidence of trace PTCDA (see Figure S3.3 in the Supporting Information), though it is likely that this impurity was due to the slow hydrolysis of PMPDI under the basic chromatography conditions, not from remaining starting material. Mass spectrometry was used to confirm PMPDI by the identification of its mono- and di-deprotonated ions ($[M-H]^-$ and $[M-2H]^{2-}$, respectively). Elemental analysis of the product, as collected, was consistent with the monopotassium, dihydrate salt of PMPDI (K1-PMPDI· $2H_2O$).

Cyclic voltammetry of PMPDI (aq) was performed in pH 10 potassium carbonate buffer degassed with argon (Figure 3.2a). At this pH, PMPDI is actually the fully-deprotonated, $PMPDI^{4-}$ (see below). A boron-doped diamond working electrode was used for its low background currents in the scan region. Voltammetry was started at 0.0 V vs. Ag/AgCl and scanned in the negative direction. The voltammogram of $PMPDI^{4-}$ (aq) shows two reduction waves, typical of PDIs,[21] with the $E_{1/2}$ of the first reduction at −0.55 V, and the second at −0.78 V vs. Ag/AgCl. The second reductive wave shows less chemical reversibility than the first, and if dissolved oxygen is present in solution, both reduction waves become almost completely chemically irreversible. This is to be expected, due to the known reactivity of reduced PDIs with oxygen, even leading to their use as oxygen sensors.[30]

The oxidation potentials of PDIs cannot typically be determined in aqueous solutions, as their oxidation potential lies more positive than that of water.[31] Interestingly, we did see a catalytic oxidative wave for $PMPDI^{4-}$ (aq) on a boron-doped diamond electrode at potentials slightly negative of the background water oxidation (see Figure S3.4a in the Supporting Information). Bulk electrolysis experiments coupled with oxygen detection indicates that the majority of this oxidative current does not yield O_2 (see Figure S3.4a in the Supporting Information and the accompanying

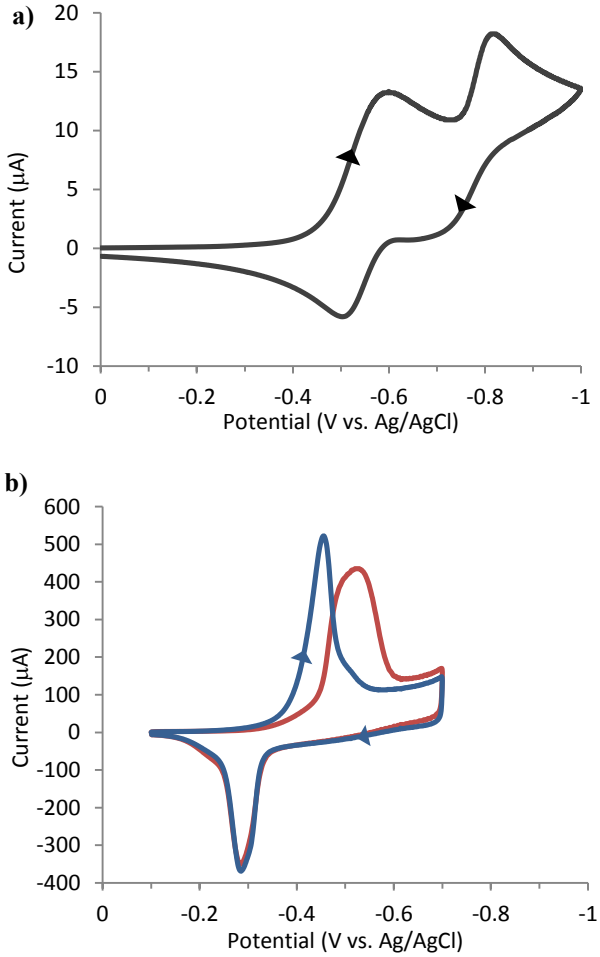

Figure 3.2 (a) CV of PMPDI dissolved in degassed 0.1 M carbonate buffer (pH 10) using a diamond working electrode, Pt wire counter electrode, Ag/AgCl reference, 50 mV/s scan rate. (b) CV of ITO/PMPDI electrode in degassed 0.1 M pH 7 potassium phosphate buffer, Pt wire counter electrode, Ag/AgCl reference, 50 mV/s scan rate, showing the first and second sweeps (red and blue lines, respectively).

discussion). This indicates that the catalytic oxidative wave in the CV in Fig. S3.4 in the Supporting Information may originate from the irreversible degradation of oxidized PMPDI or by some other PMPDI-catalyzed oxidation reaction that does not yield O_2. Even if these currents are caused by the degradation of PMPDI, this does not necessarily reflect the dye's oxidative stability under the photoelectrochemical conditions below when it is used as a water-oxidation photoanode, as these anodes have CoO_x catalyst present to help regenerate, and thus kinetically protect, any photo-oxidized dye.

Thin films of PMPDI were prepared by spin coating PMPDI from basic water solution onto cleaned ITO slides, then protonating the PMPDI by dipping the film in acidic solution to render it insoluble. X-ray photoelectron spectroscopy (XPS) was used to determine the C:K ratio in the films at various stages of preparation (see Figure S3.6 in the Supporting Information). The films, as spun from basic solutions, showed C:K ratios consistent with the tetrapotassium salt, K4-PMPDI. After submerging in acidic solution, no potassium was detected, consistent with the fully-protonated PMPDI. After submerging in pH 7 potassium phosphate (KPi) buffer, the C:K ratio was consistent with the dipotassium salt, K2-PMPDI.

Cyclic voltammetry was performed on the ITO/PMPDI films in 0.1 M pH 7 KPi buffer solution, in which the dye should be in the K2-PMPDI form. Similar to the dissolved, K4-PMPDI dye, K2-PMPDI films also show two reductive waves (Figure S3.4b in the Supporting Information); however, the voltammogram does not show the behavior expected for an ideal nernstian reaction of a surface-confined film (i.e., where anodic and cathodic waves are mirror-images reflected across the potential axis, and where the peak anodic current and potential equals the peak cathodic current and potential).[32] Instead, the films showed significant chemical irreversibility (as indicated by unequal peak heights) and poor electrochemical reversibility (as

indicated by a 170 mV offset in the peak potential between the anodic and cathodic waves at 50 mV/s scan rate). The chemical irreversibility is likely due to a combination of 1) reaction of reduced PMPDI with trace dissolved oxygen, and 2) loss of the twice-reduced dye from the film due to dissolution. Indeed, the chemical reversibility is greatly improved if the scan is reversed before the second reduction (Figure 3.2b). It should also be noted that the initial reduction wave of a virgin film is quite broad (red line, Figure 3.2b), but subsequent cycles consistently result in a sharper reduction wave which peaks at a less negative potential (blue line, Figure 3.2b). The peak potential of the reduction wave after the first sweep occurs at −0.46 V, while the subsequent reoxidation peak is shifted positive to −0.29 V vs. Ag/AgCl. Furthermore, the integrated charge under the reoxidation wave is only about half of that under the reduction wave. This behavior of significant potential shift between anodic and cathodic peaks has been reported previously for thin films of a liquid crystal PDI derivative.[31] In that case the results were rationalized as a reversible molecular reorganization or phase change in the film as a result of the reduction or oxidation (likely as a result of counterions diffusing into or out of the film), causing the reverse electron-transfer process to occur at a different potential.[31]

When preparing PMPDI films, it was noted that after they are immersed in acid solution to protonate the phosphonate groups, the film tint visibly changes from red to a darker violet color. This change can be seen in the UV–vis as a broadening of the absorbance, especially in the longer wavelengths, as shown in Figure 3.3a. The absorbance broadens further after the films are submerged in pH 7 KPi solution (the electrolyte used for subsequent experiments). A similar color change was also observed in small isolated regions of PMPDI films that were left on the benchtop under ambient conditions for several weeks. Red and black phases have been reported for many PDI films,[33–36] forming both spontaneously and under solvent vapor annealing. These different

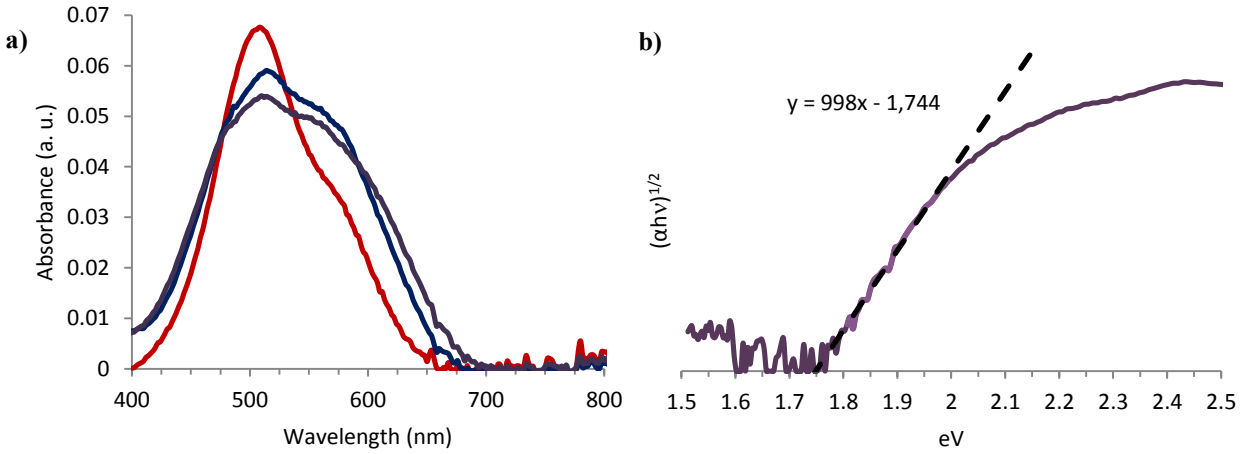

Figure 3.3. (a) Absorbance spectra of PMPDI thin films on ITO taken after spin coating from basic solution (red line), after dipping in acid solution (blue line) and after dipping in pH 7 KPi buffer (purple line). A clean ITO slide was used as background. (b) Tauc plot[38] of the KPi-rinsed film used to estimate the band gap (see the main text below).

phases are attributed to a slight shift in the π-stacking offset between neighboring perylene molecules, leading to a lower-energy intermolecular charge transfer transition.[36,37]

A Tauc plot can be used to estimate the optical band gap of amorphous thin film materials,[38] plotting $(\alpha h\nu)^{1/2}$ vs. the photon energy, $h\nu$, where α is the absorption coefficient, h is Planck's constant, and ν is the photon frequency. The exponent of 1/2 is used for amorphous solids derived under the assumption that the density of states at the band edges have a parabolic shape.[38] The solid-state optical band gap of the KPi-rinsed PMPDI film was estimated by this method to be 1.75 eV (Figure 3.3b).

Construction of an Approximate Band Diagram. The electrochemical and optical information gathered for PMPDI can be used to estimate the energies of the HOMO and LUMO (or, more accurately, the valence band and conduction band, respectively, in the solid state) in order to generate an approximate band diagram for our system. Although the field of organic semiconductors and their applications are growing rapidly, there is not yet a consensus in the

literature as to the best way of measuring their electronic energy levels.[39–41] The most direct methods are based on surface photoelectron spectroscopy,[41] which take measurement of solid films in a vacuum; however, approximations are also frequently made by measurement of electrochemical reduction and/or oxidation potentials, sometimes combined with measurements of the optical band gap.[40] The latter method was chosen for this study, since the electrochemical experiments are done on wet films suspended in electrolyte solution, nearly identical to the operating conditions of our final photoelectrochemical cell.

While the LUMO energy of PMPDI can be estimated from the $E_{1/2}$ of its first reductive wave when dissolved in solution, this LUMO energy is likely different from the conduction band edge of PMPDI films because of strong intermolecular interactions between nearest neighbors.[42] Therefore, the energy of the conduction band edge is likely best estimated by the reduction potential of PMPDI in the solid-state film. Unfortunately, the irreversibility of the ITO/PMPDI voltammograms shown in Figure 3.2b makes the precise determination of a formal reduction potential problematic; however, a rough estimation of the conduction band edge can be made from the average onset potential of the first reductive wave.[40] (The peak reduction potential would be a more straightforward estimation, but the peak potential shifts significantly with scan rate, as shown in Figure S3.5 in the Supporting Information.) The average onset potential for four voltammograms of different scan rates was −0.39 V vs. Ag/AgCl (see Figure S3.5 in the Supporting Information). Combining this value with the optical band gap of the PMPDI film as determined above, an *approximate* band diagram for our system is shown in Figure 3.4. Potentials of materials other than PMPDI are estimated as described below.

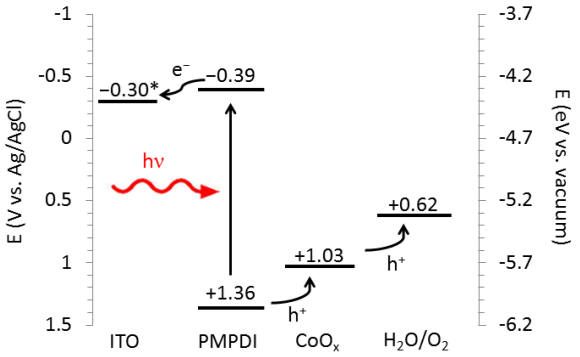

Figure 3.4 Band diagram for the ITO/PMPDI/CoO_x system. Estimated energy levels are given vs. Ag/AgCl, though a secondary y-axis is shown vs. vacuum as an additional reference. Arrows indicate the absorption of light by the perylene layer, and the energy-storing transfer of indicated charge. *The actual potential of ITO in most experiments in this study is that applied via potentiostat vs. Ag/AgCl.

The work function of ITO under similar cleaning conditions has been reported as 4.40 eV vs. vacuum,[43] although the actual potential in most of the experiments in this study is the applied potential vs. Ag/AgCl from the potentiostat. The catalytic onset of water oxidation by CoO_x on an ITO electrode is reported as (and was confirmed by us at) 1.23 V vs. NHE in pH 7 KPi buffer.[25] By the Nernst equation, the potential of water oxidation is 0.82 V vs. NHE at pH 7. The above potentials can be reported relative to the Ag/AgCl reference electrode employed by the following relationships:[32]

$$E_{\text{eV vs. vacuum}} - 4.5\ eV = eE_{\text{V vs. NHE}} \tag{3.1}$$

$$E_{\text{V vs. NHE}} - 0.20\ V = E_{\text{V vs. Ag/AgCl}} \tag{3.2}$$

Importantly, it is clear from the band diagram in Figure 3.4 that *photogenerated holes in the PMPDI film should have sufficient thermodynamic potential to oxidize water*.

Photoelectrochemical Deposition of CoO_x Catalyst. Photoelectrochemical deposition of the catalyst was chosen since it has the advantage of preferentially depositing catalyst in areas where there is a high concentration of photogenerated holes.[17,44] Briefly, ITO/PMPDI anodes were

immersed in 0.1 M pH 7 KPi buffer containing 1 mM $Co(NO_3)_2$. The catalyst was deposited at a potential of 700 mV vs. Ag/AgCl for 5 min while illuminated by a xenon arc lamp at approximately 100 mW/cm^2 intensity. Controls varying the process by using different cobalt concentrations, deposition times, and applied bias did not yield significantly different photo-assisted water-oxidation photocurrents. After depositing the catalyst, anodes were removed from cobalt solution and rinsed with DI water before further use. XPS spectra of PMPDI films were taken before and after the deposition in order to confirm that cobalt remains on the film after the catalyst deposition and a water rinse (see Figure S3.7a in the Supporting Information).

Photoelectrochemistry of ITO/PMPDI/CoO_x Anodes. Photocurrent transients vs. applied potential of an ITO/PMPDI/CoO_x anode in 0.1 M pH 7 KPi buffer are shown in Figure 3.5a. Importantly, practically no photocurrent (<1 μA/cm^2) is observed for bare ITO controls (blue line, Figure 3.5a, or Figure S3.10b in the Supporting Information for better scale), and relatively small photocurrents (<10 μA/cm^2) are observed for ITO/PMPDI controls (green line, Figure 3.5a,

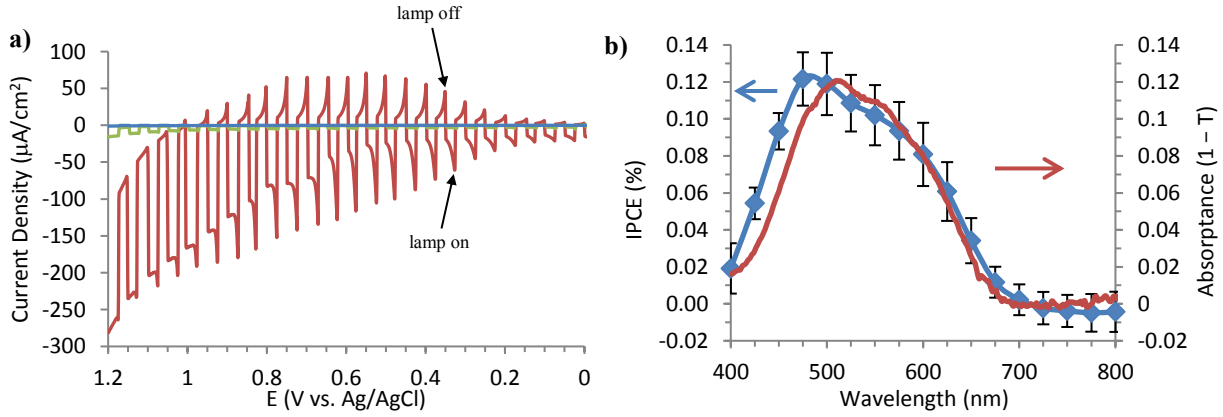

Figure 3.5. (a) Photocurrent transients vs. applied potential for ITO/PMPDI/CoO_x (red line), ITO/PMPDI (green line), and bare ITO (blue line), in 0.1 M pH 7 KPi buffer, 5 mV/s scan rate starting from 0.0 V (i.e., from right to left) with 5 s light transients. (b) average IPCE and standard deviation (blue squares and line) using a two-electrode configuration at short circuit in degassed 0.1 M pH 7 KPi buffer solution. The absorptance (1 – T) spectrum (red line) of a dry PMPDI film is overlaid for comparison.

or Figure S3.10a in the Supporting Information for better scale). The origin of the photocurrent at ITO/PMPDI anodes is not known, but could possibly be due to photo-oxidation of trace impurities by PMPDI, low levels of water oxidation by PMPDI, or some destructive oxidation of PMPDI itself. When the CoO_x cocatalyst is present on ITO/PMPDI anodes, photocurrents grow ten-fold from about 15 $\mu A/cm^2$ at zero applied bias to over 150 $\mu A/cm^2$ at 1.0 V applied bias. At applied biases higher than 1.0 V vs. Ag/AgCl, oxidation currents begin to flow even in the dark (red line, Figure 3.5a).

The photocurrent transients of ITO/PMPDI/CoO_x anodes exhibit a spikelike behavior, with an initial peak in anodic current when the light is turned on. This indicates the generation of charge carriers from exciton dissociation, where electrons are collected at the ITO/PMPDI interface and holes are transferred to CoO_x at the opposite interface where they can then oxidize water. The initial photocurrent spike is followed by a gradual decay to a steady-state photocurrent, indicating that a fraction of the photogenerated holes are lost to bulk or surface recombination before they can contribute to the faradaic current.[45]

When the light is turned off, a reverse, cathodic current peaks and quickly decays to zero, indicating that recombination of the hole reservoir (i.e., the oxidized catalyst or water-oxidation intermediates at the surface) is competitive with the forward water-oxidation process. When a one-electron redox couple is added to the electrolyte solution, such as $Fe^{II}(CN)_6^{4-}$ (i.e., a kinetically more facile, *one-electron* redox reaction vs. the four-electron, two-water-molecule water-oxidation reaction), the cathodic spikes are greatly reduced, especially at lower potentials (see Figure S3.8 in the Supporting Information). Also, when no catalyst is present (i.e., the ITO/PMPDI control, Figure S3.10a in the Supporting Information) there are no cathodic current spikes when the light is turned off, consistent with the cathodic current being associated with the CoO_x catalyst.

It should be noted that many of the phenomena occurring during the photocurrent transient experiments (such as exciton dissociation efficiency, the amount of charge buildup, and all charge-transfer rate constants) are potential dependent. As the applied potential is increased, the peak anodic currents also increase, indicating that more holes are reaching the interface to oxidize water. This buildup of holes also leads to higher recombination currents, as indicated by the increasing dark, peak cathodic currents as the applied potential increases from 0 to 0.5 V vs. Ag/AgCl. At applied potentials positive of 0.5 V, the cathodic peaks begin to decrease despite the still-rising anodic peaks, indicating a decreasing rate of recombination, which then leads to the higher steady-state anodic photocurrents observed in Figure 3.5a.

As for the general stability of our anodes, they can be stored under ambient conditions for months, and still show comparable photocurrents when tested in a transient experiment as described above. Also, the photocurrents tend to increase slightly for freshly-prepared anodes after repeating such transient experiments.

Cell Efficiency Studies. A few diagnostic cell efficiencies[46] can help to determine the shortcomings of our ITO/PMPDI/CoO_x water-oxidation anodes. First, the incident photon-to-current efficiency (IPCE), or external quantum efficiency, can be measured in a two-electrode configuration by a chronoamperometry experiment while holding the electrodes at short circuit. A device's IPCE is a measure of three fundamental processes: the efficiency of light absorption to create excitons (η_{abs}), the efficiency of charge dissociation and transport of those charge carriers to their respective interfaces (η_{trans}), and the efficiency of interfacial charge transfer (η_{int}).[46] The IPCE spectrum averaged for several ITO/PMPDI/CoO_x anodes is shown in Figure 3.5b. The absorptance (1 – T) spectrum of a dry PMPDI film (KPi-rinsed, K2-PMPDI) is shown for

comparison, indicating that the photocurrents observed during these measurements coincide with absorption of light by PMPDI.

If all other processes were 100% efficient, a device's IPCE could only reach as high as its light harvesting efficiency (η_{abs}), that is, its absorptance spectrum. The low absorptance values measured for our ITO/PMPDI/CoO_x anodes (12% at the λ_{max}) clearly indicate that light harvesting limitations are a major contributor to our low IPCE values. To investigate the other limitations to performance, a system's *internal* quantum efficiency, or *absorbed* photon-to-current conversion efficiency (APCE), can be calculated by dividing the IPCE values by the film's absorptance values at each wavelength. The APCE thus measures only the efficiencies of charge dissociation and transport, and the efficiency of interfacial charge transfer, η_{trans} and η_{int}, respectively.[46] By this treatment, our anodes typically show APCEs between 1 and 2%.

Finally, if the IPCE experiment is carried out with an added facile redox couple, and if η_{int} can be taken as ≈1, then the APCE should be a measure of only η_{trans}.[46] For our ITO/PMPDI/CoO_x anodes, we repeated the IPCE measurements with added $K_4Fe(CN)_6$ (a kinetically more facile, albeit one-electron, redox couple), which resulted in IPCE values that were generally double those without any Fe^{2+} (see Figure S3.9 in the Supporting Information). The APCE values (which should reflect only the charge transport efficiency) were then estimated to be ~3% (assuming the efficiency of the interfacial hole transfer to $Fe^{II}(CN)_6^{4-}$ is ≈1; the control performed next suggests that it is actually <1).

As a control, we also ran an IPCE experiment with added hydroquinone, a two-electron, two-proton redox couple, a therefore closer model to the four-electron, four-proton water oxidation reaction. Interestingly, the IPCE values measured in the presence of hydroquinone are roughly double the values when $Fe^{II}(CN)_6^{4-}$ was used at the same concentration (~5 mM, see Figure S3.9

in the Supporting Information), giving APCE values of ~6%. As an additional control, we ran an IPCE with much more concentrated hydroquinone (200 mM), but the photocurrents were essentially unchanged. Therefore, with the assumption that the η_{int} for hydroquinone is 1, then the estimated maximum η_{trans} in our ITO/PMPDI/CoO_x anodes is ~6%.

Preliminary Optimization Studies and Controls. Because the efficiency of light absorption is a major performance-limiting factor in our system, one key question to answer was whether or not our efficiencies could be improved by employing thicker PMPDI films to absorb more of the incident light. Attempts to alter the spin coating parameters employed to produce thicker films (e.g., lowering the spin rate) yielded only small changes in thickness. Thicker films, although not very uniform, were prepared by drop coating PMPDI solutions and letting the water slowly evaporate. A few of these films, roughly 3 times thicker than typical spin-coated films according to UV–vis, were used to prepare ITO/PMPDI/CoO_x anodes following the same standard procedures. Under photoelectrochemical testing, these thicker ITO/PMPDI/CoO_x anodes showed roughly one-tenth the steady-state photocurrents as our standard, thinner-film anodes (see Figure S3.10a in the Supporting Information).

The low dielectric constant of most organic materials causes excitons in such media to be strongly bound because of the coulombic attraction between electrons and holes. Therefore, excitons often must reach a materials interface in order to dissociate into separated charge carriers.[42] Exciton diffusion lengths in most organic materials are short (between 5 and 30 nm); hence, if films are prepared that are thicker than the exciton diffusion length, most excitons formed in the film bulk are expected to relax before reaching an interface to dissociate.[42] Through a combination of UV–vis and optical profilometry measurements, the absorption coefficient of PMPDI films (KPi rinsed, K2-PMPDI) was estimated at 2.0×10^4 cm^{-1} (see Figure S3.11 and its

discussion in the Supporting Information). This absorption coefficient was used to determine that typical thicknesses of our spin-coated PMPDI films are 40-50 nm. The thicker, drop-cast films were then roughly 150 nm thick, and therefore about an order of magnitude thicker than typical exciton diffusion lengths. Therefore, it can be expected that the majority of excitons formed in these thicker films will relax before they can dissociate into useable charges.

To test the hypothesis that the phosphonate groups of PMPDI are important for the overall performance of the device, we also prepared anodes using another PDI derivative, EPPDI, with 1-ethylpropyl groups in the place of PMPDI's phosphonomethyl groups. The ITO/EPPDI films were prepared by spin-coating EPPDI from $CHCl_3$ solutions. Interestingly, these films remained a bright-red color upon submerging in aqueous solution (no black phase was observed). Regardless of film thickness, photocurrents during CoO_x catalyst depositions and subsequent photoelectrochemical testing were about an order of magnitude *smaller* than our typical ITO/PMPDI/CoO_x anodes (see Figure S3.10b in the Supporting Information). XPS spectra were collected both before and after catalyst deposition, and showed that only trace cobalt was present on the EPPDI films (see Figure S3.7b in the Supporting Information), which is further supported by the lack of any dark cathodic peaks during transient experiments (see Figure S3.10b in the Supporting Information), as such peaks were characteristic of the CoO_x catalyst on PMPDI films. These results are consistent with phosphonate groups being important for efficiently linking the CoO_x catalyst to the organic film; however, the results could also be explained by poor conductivity of the film, which could be caused by film morphology, poor interaction with the ITO substrate, or other unknown factors. Indeed, we found that EPPDI films did not adhere well to ITO, and often delaminated upon rinsing. Needed here is a systematic study of the photoelectrochemical properties of more PDI films, including testing derivatives with different

functionalities (i.e., studies of dyes with and without phosphonate groups, but with otherwise similar structures) to see if PDI dyes with different functional groups are also capable of visible-light- and CoO_x-assisted water oxidation. Such studies are currently underway.

Evolved Oxygen Quantification. To confirm that photocurrents observed from the ITO/PMPDI/CoO_x anodes originate from oxidation of water and not from some other undesired process, it was necessary to directly quantify any photoelectrochemically produced O_2.[46] Previous studies have followed the concentration of oxygen in the headspace above solution in the photoelectrochemical cell,[25] or dissolved oxygen in the working electrolyte itself.[11,12,17] We chose the latter, well-established method for our studies due to the relatively small photocurrents produced by our anodes, and due to an observed gradual deactivation of our photoanodes over the five minute time scale of water-oxidation experiments (see Figure S3.12 in the Supporting Information). Details for oxygen-quantification experiments are provided in the Experimental Section; attention to those details matter for anyone reproducing this work as it took on the order of 3 months of research to optimize, and then make, the O_2 yield measurements and controls reported herein. Briefly, a Clark-type electrode was used to measure the dissolved oxygen concentration in the working compartment solution both before and after a 5 min, illuminated, amperometric water-oxidation experiment. The change in dissolved oxygen concentration and the known volume of solution in the working compartment were used to calculate the number of micromoles of oxygen produced. By recording the amount of current passed during the 5 min water oxidation, and using the stoichiometry for the water-oxidation reaction ($2H_2O \rightarrow 4H^+ + O_2 + 4e^-$), the theoretical yield for a perfect faradaic reaction can be calculated as:

$$\left(\frac{6.241\times10^{18}\ e^-}{1\ Coulomb}\right)\left(\frac{1\ molec\ O_2}{4\ e^-}\right)\left(\frac{1\ mol}{6.022\times10^{23} molec}\right)\left(\frac{10^6\ \mu mol}{1\ mol}\right) = 2.591\ \mu mol\ O_2/Coulomb\ passed \tag{3.3}$$

Then, the faradaic efficiency was calculated by dividing the measured oxygen yield by the theoretical yield.

The literature reports that ITO/CoO_x has a faradaic efficiency of 100% in 0.1 M KPi buffer at pH 7, with an applied bias of 1.1 V vs. Ag/AgCl.[25] Several controls were done in order to both verify the literature result in our hands and to check our multipoint calibration. First, ITO/CoO_x anodes were prepared as published,[25] except that a more concentrated Co^{2+} solution was used (1 mM vs. 0.5 mM) and the deposition was stopped after 5 min (depositing less catalyst) in order to closely mimic our conditions for CoO_x formation on ITO/PMPDI. The ITO/CoO_x anodes thus prepared were used for a 5 min amperometric water-oxidation experiment held at or below 1.1 V vs. Ag/AgCl (slightly lowering the potential decreases currents to more closely parallel the currents in the ITO/PMPDI/CoO_x systems) and under both illuminated and dark conditions (ITO/CoO_x anodes have little light absorption in the visible, and therefore exhibit no additional photocurrent; however, these controls provided confidence in our Clark electrode calibration concerning temperature changes in solution caused by illumination). Results of 17 ITO/CoO_x water-oxidation control experiments, both dark and illuminated, resulted in an average faradaic efficiency of 100 ± 14%. These controls provide confidence in the method used for oxygen detection and its accuracy.

Finally, the same method was used to determine the faradaic efficiency for our ITO/PMPDI/CoO_x anodes under illumination and held at 900 mV vs. Ag/AgCl. Nine anodes yielded an average faradaic efficiency of 80 ± 15%, near the theoretical limit of 100% within our experimental error. Of course, it cannot be ruled out that other oxidative side reactions may be occurring, such as oxidation of trace impurities, degradative oxidation of PMPDI, or the formation of other water-oxidation products, such as hydrogen peroxide. Controls of ITO/PMPDI films

without the CoO_x catalyst yielded no detectable oxygen, even when illuminated and held at 900 mV positive bias vs. Ag/AgCl. Overall, the results are quite pleasing in that a high, 80 ± 15% faradaic efficiency for water oxidation was achieved with our novel ITO/PMPDI/CoO_x system developed and studied herein. Further study of PDI-based photoelectrochemical water oxidation systems and their optimization and longer-term stability studies are, therefore, of interest in our opinion.

3.3 Conclusions

Although other perylene derivatives have been studied as components in organic bi- (or tri-) layer PV and water-oxidation devices,[8–10] the current study is, to our knowledge, the first device to achieve photochemically-driven water oxidation by a single-layer molecular organic semiconductor thin film coupled to a water-oxidation catalyst. Our comparison with anodes using another PDI dye, ITO/EPPDI/CoO_x yielded much lower performance. This indicates that the phosphonate groups found in PMPDI *may* be important for close electronic coupling between PMPDI and the CoO_x catalyst, but continued studies of other PDI derivatives will be required to further support or refute this hypothesis, and are currently under investigation.

It is important to note that the photocurrent densities generated by our ITO/PMPDI/CoO_x anodes, just over 150 $\mu A/cm^2$ at 1.0 V applied bias vs. Ag/AgCl, are small relative to many photoelectrochemical water-oxidation cells based on inorganic semiconductors.[5–7] However, our observed current densities are quite comparable to those achieved using other organic semiconductors,[8,9,11,12,17] despite ours being a largely unoptimized system. Current transient experiments revealed that the rate of recombination between holes in the oxidized catalyst and conduction band electrons is competitive with the desired water-oxidation reaction. While

improvements can be expected for the current system through the use of a faster water-oxidation catalyst, such catalysts are generally composed of less earth-abundant, more expensive metals than cobalt (i.e., iridium or ruthenium). We can, however, expect at least some improvement in the performance of our current system by the use of different interfacial layer materials to enhance charge separation and prevent recombination between ITO and the perylene film. Such interfacial layers may also help to reduce the large applied bias required in our current system to reach its maximum photocurrents, given that the estimated HOMO of PMPDI should have more than sufficient overpotential to oxidize water (Figure 3.4).

Efficiency measurements of our system reveal that our anodes only reach a maximum IPCE of 0.12%. APCE calculations show that light absorption is a large limitation. Our PMPDI thin films are optically quite thin, absorbing only about 12% of incident light at the maximum absorbance. IPCE experiments with added hydroquinone allowed us to estimate the internal charge transport efficiency at 6%. Anodes with thicker PMPDI films which absorbed more of the incident light showed *lower* photocurrents, likely limited therefore by exciton diffusion lengths. We can still hope to improve our overall anode efficiency by employing a dye-sensitized mesoporous semiconductor architecture, where more light can be absorbed due to the high surface area of the semiconductor, while keeping the dye thickness to a monolayer, thereby eliminating the need for lengthy exciton diffusion. Those needed studies are also in progress.

We are currently in the process of synthesizing and testing other PDI derivatives in order to further test the hypothesis that phosphonate or other ionic groups are important structural components for coupling with the inorganic catalyst; those additional PDI derivatives will also probe if device stability can be improved by the choice of especially the most oxidation resistant PDIs. Of particular interest are lifetime studies which push the limit of a more optimized device,

while also characterizing any deactivated device and system to understand its limitations (i.e., in light of the gradual drop in photocurrent we see, Figure S3.12 in the Supporting Information, which raises questions about the stability of the current PMPDI dye employed under extended photoelectrolysis conditions).

In summary, a novel perylene diimide derivative, PMPDI, was successfully synthesized and characterized. This dye is conveniently soluble in basic solutions and insoluble in neutral and acid solutions, allowing for solution-based processing. PMPDI absorbs strongly in the visible and has electronic energy levels conducive to water oxidation. We have preliminary evidence that the phosphonate groups of PMPDI may be a critical component to effectively couple the CoO_x catalyst to the organic dye. It has been confirmed that PMPDI thin films, spin-coated from solution onto ITO, can achieve photo-assisted water oxidation when coupled with photoelectrochemically deposited CoO_x catalyst. Our IPCE results confirm that photocurrents generated by the ITO/PMPDI/CoO_x electrodes originate from PMPDI absorption of light, and water oxidation has been confirmed by the direct detection of O_2, with a faradaic efficiency of 80 ± 15% under positive applied bias. Additional studies of other PDI dyes, of nanostructured versions of our device, of the stability of those second-generation devices, and of the kinetics of the photoelectrocatalysis are in progress and will be reported in due course.

3.4 Experimental Section

Materials. Perylene-3,4,9,10-tetracarboxylic dianhydride (PTCDA) (97%, Aldrich), (aminomethyl)phosphonic acid (99%, Alfa Aesar), and imidazole (99%, Acros Organics) were all used as received. N,N'-bis(1-ethylpropyl)-3,4,9,10-perylenediimide (EPPDI) was synthesized according to the literature.[47] Characterization data can be found at the end of the Supplemental

Information. One-inch-square indium tin oxide (ITO) glass slides were purchased from Delta Technologies and cleaned before use (see below). Solvents were purchased from Sigma-Aldrich or Fisher Scientific and used without further purification. Ultrapure water (18 MΩ) was used for all cleaning steps and for preparation of electrochemical solutions.

Synthesis of N,N′-bis(phosphonomethyl)-3,4,9,10-perylenediimide (PMPDI). The synthesis of PMPDI was modified from a literature procedure[28] for the N,N'-bis(phosphono*ethyl*) PDI derivative. A mixture of PTCDA (79 mg, 0.20 mmol), (aminomethyl)phosphonic acid (47 mg, 0.42 mmol), and 1.5 g of imidazole were added to a 25 mL round-bottomed flask with a magnetic stir bar. The flask was sealed with a rubber septum to prevent evaporative loss of imidazole and lowered into a hot oil bath at 130 °C (venting briefly as the flask contents warmed). After stirring for 20 min in the oil bath, the flask was removed and allowed to cool for approximately 2 min before 5 mL of a 50/50 vol% mixture of 2 M HCl/ethanol was added to precipitate a fine black solid. The solid was collected on a nylon, 0.22 μm vacuum filter and rinsed with 5 mL each of 50/50 water/ethanol, then ethanol. This product (an imidazolium salt by ^{1}H-NMR) was suspended in 10 mL DI water and dissolved by the dropwise addition of 1 M KOH (the solid began to dissolve at pH ~ 8 and was completely dissolved by pH 9.5). The solution was then vacuum-filtered to remove any unreacted PTCDA. (Note: if the solution is made too basic, the PTCDA will dissolve as well and will not be separated from the product.) The filtrate was then acidified by the dropwise addition of 2 M HCl while under rapid magnetic stirring. (Note: the product precipitates in bulk at approximately pH 5.5, forming a gel, likely as the dipotassium salt. More acidic conditions are required to remove imidazole impurities, and further stirring and dilution helps liquefy the gel before filtering.) The mixture was brought to pH ~ 1, and the precipitated product was collected by vacuum filtration. NMR of this product usually contained

trace imidazole, but can be purified by repeating the dissolving and precipitation procedure, giving a 90% yield after drying overnight in a vacuum oven at 100 °C. Elemental analysis of the product, as collected, was consistent with the mono-potassium, dihydrate of PMPDI, indicating that the product kinetically precipitates as the mono-potassium salt, which was used for subsequent studies. The fully-protonated product was also obtained by dissolving the solid in NaOH solution and leaving the solution to slowly acidify for 24 h in a desiccator saturated with HCl vapor. FT-IR (Nicolet SX-60 FT-IR spectrometer with ATR-ZnSe): 3403 cm^{-1} br m, 3067 w, 3000 w, 2948 w, 1690 s, 1650 s, 1589 s, 1575 m, 1506 w, 1485 w, 1435 m, 1402 w, 1392 m, 1363 m, 1335 m, 1301 m, 1248 m, 1186 w, 1162 w, 1106 w, 970 w, 928 br m, 861 w, 843 w, 809 w, 792 w, 733 w, 708 w. Samples for NMR (300 MHz Varian Inova) were dissolved by sonication in D_2O with half a drop of 30% NaOD (in D_2O). ^{1}H-NMR, δ (ppm): 7.85 (br, 8H, Ar); 4.16 (br, 4H, N–CH_2–P) (see Figure S3.1 in the Supporting Information). ^{31}P-NMR, δ (ppm): 12.15 ppm (see Figure S3.2 in the Supporting Information). MS (ESI/APCI in NH_4OH matrix): m/z calculated for PMPDI ($C_{26}H_{16}N_2O_{10}P_2$) = 578.03, found m/z = 577.02 $[M-H]^-$; 288.01 $[M-2H]^{2-}$. Elemental analysis of the fully-protonated product, calculated for $C_{26}H_{16}N_2O_{10}P_2$ (found): 53.99% C (51.97); 2.79% H (3.17); 4.84% N (4.80); 0% Na (0.194). The product was also analyzed by HPLC (see Figure S3.3 in the Supporting Information) and cyclic voltammetry (Figure 3.2a and Figure S3.4a in the Supporting Information).

ITO/PMPDI/CoO_x Photoanode Preparation. ITO slides were cleaned by sonication for 30 min in a Liquinox surfactant solution, rinsed with water, then sonicated for 30 min each in acetone and isopropanol solutions and allowed to dry under ambient air for at least half an hour. Before use, slides were air-plasma treated (Harrick PDC-3XG) for 15 min and moved directly into a spin coater (SCS G3P-8 Spin Coater). The phosphonate groups of PMDPI make it conveniently

soluble in water at pH ≥ 9.5 as the tetra-potassium salt. PMPDI solutions were prepared by adding 5 mg of PMPDI product (K1-PMPDI· $2H_2O$) to 1 mL of water and 2 drops of 1 M KOH, and sonicated to fully dissolve. These solutions were dripped through a 0.2 μm filter to cover the surface of a freshly cleaned one-inch square ITO substrate and spin-coated at 1000 rpm for 60 s. Dye was wiped from one edge of the slide by a wet Kimwipe in order to provide a naked ITO surface to attach copper tape as an electrical contact. These ITO/PMPDI slides were scored with a glass cutting tool and cleaved into two or three segments for further testing (typical active areas were 1–1.5 cm^2). The slides were then submerged for 30 s each in 20 mL of a 50/50 mixture of 2 M HCl/ethanol (fully protonating the PMPDI film and rendering it insoluble), distilled water, ethanol, and then blown dry under an argon stream for about a minute. Films were characterized at this point (before depositing catalyst) by UV–vis spectroscopy and cyclic voltammetry (see below). Before depositing CoO_x catalyst, a fingernail topcoat was used to cover the slide edges and any uncoated portions of the ITO surface to ensure that the only conductive surface in contact with solution was the PMPDI film. After the fingernail polish had dried, catalyst was deposited by submerging the active area of the ITO/PMPDI anode in a glass vial containing 10 mL of 0.1 M pH 7 KPi containing 1 mM $Co(NO_3)_2$, applying a potential of 700 mV vs. Ag/AgCl, and illuminating the anode for 5 min by a 65 W xenon arc lamp focused to approximately 100 mW/cm^2 intensity (measured with a Thorlabs Thermal Power Sensor model S302A). Anodes were then removed from the cobalt solution, rinsed with DI water, and used for further testing. The presence of cobalt on rinsed and dried ITO/PMPDI/CoO_x anodes was confirmed by XPS (see below, and Figure S3.7 in the Supporting Information).

Thicker PMPDI films were also prepared by drop coating two (or more) drops of the above PMPDI solutions onto cleaned ITO slides, covering with a petri dish to protect from dust, and

letting them air dry on a rotary table (Thermo Scientific Lab-Line Maxi Rotator). Such films did not evaporate evenly and created films of nonuniform thicknesses. These films were used to estimate the solid-state absorption coefficient as described in the Supporting Information, Figure S3.11. A few drop-coated films (roughly 3 times thicker than spin-coated films according to UV–vis) were tested for their photoelectrochemical performance. These films were processed and catalyst deposited under the same procedures as described above, and submitted to the same photoelectrochemical testing as described below. Resulting transients can be seen in Figure S3.10a in the Supporting Information.

ITO/EPPDI/CoO_x Photoanode Preparation. Photoanodes were prepared as described above, except spin coating was done from $CHCl_3$ solution, still at 1000 rpm for 60 s. Using the same dye concentrations as above (5 mg/mL), films spun from $CHCl_3$ were roughly 10 times the thickness of standard PMPDI films, as estimated by UV–vis. Thinner films, comparable to the thickness of spin-coated PMPDI films, were also prepared by reducing dye concentrations to 1 mg/mL. EPPDI films stayed bright-red upon submersion into KPi solutions (no change to a black phase was observed). Cobalt catalyst was deposited under the same conditions described above. XPS was performed on one of the films after catalyst deposition, showing that only trace cobalt remained (Figure S3.7b in the Supporting Information). ITO/EPPDI/CoO_x anodes were then submitted to the same photoelectrochemical testing as described below. Resulting transients can be seen in Figure S3.10b in the Supporting Information. Film thickness did not significantly alter the observed photocurrents.

XPS. Spectra were taken on a PHI 5800 XPS with Al Kα source at 350 W power, and analyzed using PHI MultiPak software. Samples were prepared by spin coating PMPDI onto ITO slides as described above. Slides were scored and broken into 3 pieces. The first was untreated

after coating, a second was submerged in 20 mL of 50/50 2 M HCl / ethanol for 60 s, then rinsed by dipping several times in DI water then ethanol, and drying for a minute under an argon stream. The third piece was treated identically to the second, then also submerged for 60 s in 0.1 M pH 7 KPi buffer and rinsed again as above. These slides were allowed to dry overnight, and then analyzed by XPS, taking both a survey scan and a high resolution scan in the region of 280 to 305 eV to calculate the C:K ratio (see Figure S3.6 in the Supporting Information). This experiment was performed 3 times and the average C:K ratios were consistent with K4-PMPDI as coated, PMPDI after acid treatment, and K2-PMPDI after KPi treatment. XPS was also taken of PMPDI and EPPDI films both before and after a standard CoO_x catalyst deposition (see Figure S3.7 in the Supporting Information).

UV–Vis. UV–vis data were collected by a Hewlett Packard 8452A diode array spectrophotometer. ITO/PMPDI slides were scored and broken into 1-cm-wide slices to fit into the sample holder and pressed against the back wall for consistent sample placement. An ITO slide, cleaned under the standard conditions (and spin coated with ~0.05 M KOH as a control for the basic dye solution) was used as the reference blank.

Cyclic Voltammetry. Electrochemical experiments were performed on a CH Instruments CHI630D potentiostat using a platinum wire counter electrode and Ag/AgCl (sat. KCl) reference electrode. The potential of the Ag/AgCl reference was confirmed to be +0.20 V vs. NHE by a 1 mM $Fe(CN)_6^{3-/4-}$ in 0.1 M HCl reference redox system.[32] Cyclic voltammetry was performed on PMPDI both dissolved in basic solution ($PMPDI^{4-}$) and as a thin film on ITO in neutral solution (K2-PMPDI). For the aqueous PMDPI experiments, a solution of ~4 mM PMPDI in 0.1 M pH 10 potassium carbonate buffer was degassed with argon before testing to avoid interference due to reduction of oxygen by reduced PMPDI or at the working electrode itself (3 mm boron-doped

diamond (CCL Diamond)). Voltammograms of K2-PMPDI films on ITO were performed in degassed 0.1 M pH 7 KPi buffer.

Photoelectrochemical Testing. All photoelectrochemical experiments were performed in a custom-made two-compartment photoelectrochemical cell, with a working compartment made from 1 × 1.5 cm quartz rectangular tubing with a working volume of 5 mL. The ITO/PMPDI/CoO_x anodes were pressed against the front wall of the cell (the glass back of the anode against the glass cell wall)and illuminated through the ITO-side with a 65 W xenon arc lamp (PTO model A 1010) powered by an OLIS XL150 adjustable power supply. The lamp was focused onto the cell through a bandpass filter (315–710 nm, Thorlabs FGS900S) to more closely simulate the AM1.5 solar spectrum, with an incident power density measured to be approximately 100 mW/cm^2, measured with a Thorlabs Thermal Power Sensor, model S302A. Photoelectrochemical experiments were recorded with the same potentiostat and electrodes as described above for cyclic voltammetry. Transient light experiments were performed by manually chopping the light source every 5 s using an opaque sheet of construction paper, while the applied potential was scanned from low to high values. Photocurrent densities tended to improve slightly upon repeating the transient experiment.

Action spectra were collected on a separate PV testing apparatus provided by Prof. C. M. Elliott's research group, which consisted of a xenon arc lamp (Oriel model 66002, 100 mW/cm^2), power supply (Oriel model 68700), monochromator (Oriel Cornerstone 130, model 7400), and a Kiethley 2400 source meter. For these experiments, a two-electrode setup was used (ITO/PMPDI/CoO_x working electrode and Pt wire counter electrode) in the same two-compartment photoelectrochemical cell described above, containing degassed 0.1 M pH 7 KPi buffer (5 mL in the working compartment, 3 mL in the auxiliary compartment). The face of the cell was pressed against an aperture, leaving an illuminated area of 0.385 cm^2. To collect the action

spectrum, the electrodes were held at short circuit while the incident light was scanned from 400 to 700 nm (≈10 nm bandwidth) in 25 nm steps, recording the steady-state current between the electrodes 15 s after each wavelength step. The incident lamp power at each wavelength step was recorded using a Thorlabs silicon standard power sensor, model S120B, in order to calculate the final IPCE values.

Oxygen Detection. Due to the relatively small photocurrents and gradual deactivation of our ITO/PMPDI/CoO_x anodes, dissolved oxygen concentration was directly detected in the KPi buffer solution instead of detecting O_2 in the headspace of the cell (consistent with this, the oxygen produced was not sufficient to generate visible bubbles). Dissolved oxygen was measured using a Clark-type electrode and meter (Microelectrodes, Inc., model M1-730A electrode and OM-4 oxygen meter), and recorded on LabView software. The Clark electrode was calibrated daily in two standard solutions of 0% (≥0.1 M Na_2SO_3)[48] and 20.9% (vortexed under ambient air) oxygen solutions—which corresponds to 0 μM and 236 μM dissolved oxygen, respectively, at 20 °C, correcting for the atmospheric pressure in Fort Collins, CO (typically between 83.2 and 85.6 kPa).[49] Because the working solution is heated by the lamp irradiation and because the Clark electrode response is temperature sensitive, the response was calibrated in both standard solutions over a temperature range of 20–30 °C (see Figure S3.13 in the Supporting Information for a typical calibration).

Water-oxidation experiments for our anodes were carried out using the same photoelectrochemical setup as described above. For these experiments, the lamp intensity was increased to ~ 300 mW/cm^2 and an applied bias of 900 mV vs. Ag/AgCl was used in order to maximize the photocurrent, and thus the resultant oxygen production, yet stay below the potential at which PMPDI films showed dark oxidative currents (see Figure S3.4b in the Supporting

Information). To avoid the difficulties of sealing the electrochemical cell from the atmosphere, we air-saturated solutions to begin with (i.e., vortexed under ambient air for at least 10 min). This way, any increase in dissolved oxygen concentration had to come from water oxidation and not from the surrounding air. The Clark electrode response in the 5 mL volume of solution in the working compartment and the temperature of solution (± 0.1 °C) were recorded both before and after a 5 min, illuminated, amperometric water-oxidation experiment. The solution was stirred only while measuring oxygen, and then only fast enough to yield a maximum electrode response. The calibration curve was used to convert the Clark electrode responses and temperatures to their corresponding oxygen concentrations. The volume of solution and change in concentration after the electrolysis was used to calculate the number of moles of oxygen produced. Finally, the current passed during the water oxidation was used to calculate the theoretical oxygen yield and the faradaic efficiency of the reaction.

It is important to note here that water oxidation and rising solution temperatures (due to high intensity illumination) resulted in solutions with dissolved oxygen concentrations above the equilibrium value. Controls were done by bubbling 100% oxygen into air-saturated solutions, creating slightly supersaturated conditions. Oxygen concentration was then monitored as a function of time and stir rate, confirming that the oxygen produced during electrolysis remained primarily in solution and did not escape to the atmosphere over the 5 min time scale of the experiments, at least to within the observed ±15% O_2-yield error bars.

REFERENCES

(1) Lewis, N. S.; Nocera, D. G. Powering the Planet: Chemical Challenges in Solar Energy Utilization. *Proc. Natl. Acad. Sci. U. S. A.* **2006**, *103*, 15729–15735.

(2) Bard, A. J.; Whitesides, G. M.; Zare, R. N.; McLafferty, F. W. Holy Grails of Chemistry. *Acc. Chem. Res.* **1995**, *28*, 91–91.

(3) Bard, A. J.; Fox, M. A. Artificial Photosynthesis: Solar Splitting of Water to Hydrogen and Oxygen. *Acc. Chem. Res.* **1995**, *28*, 141–145.

(4) Fujishima, A.; Honda, K. Electrochemical Photolysis of Water at a Semiconductor Electrode. *Nature* **1972**, *238*, 37–38.

(5) Aharon-Shalom, E.; Heller, A. Efficient p-InP (Rh-H Alloy) and p-InP (Re-H Alloy) Hydrogen Evolving Photocathodes. *J. Electrochem. Soc.* **1982**, *129*, 2865–2866.

(6) Khaselev, O.; Turner, J. A. A Monolithic Photovoltaic-Photoelectrochemical Device for Hydrogen Production Via Water Splitting. *Science* **1998**, *280*, 425–427.

(7) Licht, S.; Wang, B.; Mukerji, S.; Soga, T.; Umeno, M.; Tributsch, H. Over 18% Solar Energy Conversion to Generation of Hydrogen Fuel; Theory and Experiment for Efficient Solar Water Splitting. *Int. J. Hydrog. Energy* **2001**, *26*, 653–659.

(8) Abe, T.; Nagai, K.; Ogiwara, T.; Ogasawara, S.; Kaneko, M.; Tajiri, A.; Norimatsu, T. Wide Visible Light-Induced Dioxygen Evolution at an Organic Photoanode Coated with a Noble Metal Oxide Catalyst. *J. Electroanal. Chem.* **2006**, *587*, 127–132.

(9) Abe, T.; Nagai, K.; Kabutomori, S.; Kaneko, M.; Tajiri, A.; Norimatsu, T. An Organic Photoelectrode Working in the Water Phase: Visible-Light-Induced Dioxygen Evolution by a Perylene Derivative/Cobalt Phthalocyanine Bilayer. *Angew. Chem. Int. Ed.* **2006**, *45*, 2778–2781.

(10) Liu, G.; Chen, C.; Ji, H.; Ma, W.; Zhao, J. Photo-Electrochemical Water Splitting System with Three-Layer n-Type Organic Semiconductor Film as Photoanode under Visible Irradiation. *Sci. China Chem.* **2012**, *55*, 1953–1958.

(11) Youngblood, W. J.; Lee, S.-H. A.; Kobayashi, Y.; Hernandez-Pagan, E. A.; Hoertz, P. G.; Moore, T. A.; Moore, A. L.; Gust, D.; Mallouk, T. E. Photoassisted Overall Water Splitting in a Visible Light-Absorbing Dye-Sensitized Photoelectrochemical Cell. *J. Am. Chem. Soc.* **2009**, *131*, 926–927.

(12) Brimblecombe, R.; Koo, A.; Dismukes, G. C.; Swiegers, G. F.; Spiccia, L. Solar Driven Water Oxidation by a Bioinspired Manganese Molecular Catalyst. *J. Am. Chem. Soc.* **2010**, *132*, 2892–2894.

(13) Moore, G. F.; Blakemore, J. D.; Milor, R. L.; Hull, J. F.; Song, H.; Cai, L.; Schmuttenmaer, C. A.; Crabtree, R. H.; Brudvig, G. W. A Visible Light Water-Splitting Cell with a Photoanode Formed by Codeposition of a High-Potential Porphyrin and an Iridium Water-Oxidation Catalyst. *Energy Environ. Sci.* **2011**, *4*, 2389–2392.

(14) Zhao, Y.; Swierk, J. R.; Megiatto, J. D.; Sherman, B.; Youngblood, W. J.; Qin, D.; Lentz, D. M.; Moore, A. L.; Moore, T. A.; Gust, D.; *et al*. Improving the Efficiency of Water Splitting in Dye-Sensitized Solar Cells by Using a Biomimetic Electron Transfer Mediator. *Proc. Natl. Acad. Sci. U. S. A.* **2012**, *109*, 15612–15616.

(15) Gao, Y.; Ding, X.; Liu, J.; Wang, L.; Lu, Z.; Li, L.; Sun, L. Visible Light Driven Water Splitting in a Molecular Device with Unprecedentedly High Photocurrent Density. *J. Am. Chem. Soc.* **2013**, *135*, 4219–4222.

(16) Alibabaei, L.; Brennaman, M. K.; Norris, M. R.; Kalanyan, B.; Song, W.; Losego, M. D.; Concepcion, J. J.; Binstead, R. A.; Parsons, G. N.; Meyer, T. J. Solar Water Splitting in a Molecular Photoelectrochemical Cell. *Proc. Natl. Acad. Sci. U. S. A.* **1073**, 201319628.

(17) Bledowski, M.; Wang, L.; Ramakrishnan, A.; Bétard, A.; Khavryuchenko, O. V.; Beranek, R. Visible-Light Photooxidation of Water to Oxygen at Hybrid TiO_2–Polyheptazine Photoanodes with Photodeposited Co-Pi (CoO_x) Cocatalyst. *ChemPhysChem* **2012**, *13*, 3018–3024.

(18) Law, K. Y. Organic Photoconductive Materials: Recent Trends and Developments. *Chem. Rev.* **1993**, *93*, 449–486.

(19) Pasaogullari, N.; Icil, H.; Demuth, M. Symmetrical and Unsymmetrical Perylene Diimides: Their Synthesis, Photophysical and Electrochemical Properties. *Dyes Pigments* **2006**, *69*, 118–127.

(20) Langhals, H. Cyclic Carboxylic Imide Structures as Structure Elements of High Stability. Novel Developments in Perylene Dye Chemistry. *Heterocycles* **1995**, *40*, 477–500.

(21) Lee, S. K.; Zu, Y.; Herrmann, A.; Geerts, Y.; Müllen, K.; Bard, A. J. Electrochemistry, Spectroscopy and Electrogenerated Chemiluminescence of Perylene, Terrylene, and Quaterrylene Diimides in Aprotic Solution. *J. Am. Chem. Soc.* **1999**, *121*, 3513–3520.

(22) Gregg, B. A.; Sprague, J.; Peterson, M. W. Long-Range Singlet Energy Transfer in Perylene Bis(phenethylimide) Films. *J. Phys. Chem. B* **1997**, *101*, 5362–5369.

(23) Ferrere, S.; Zaban, A.; Gregg, B. A. Dye Sensitization of Nanocrystalline Tin Oxide by Perylene Derivatives. *J. Phys. Chem. B* **1997**, *101*, 4490–4493.

(24) Rawls, M. T.; Johnson, J.; Gregg, B. A. Coupling One Electron Photoprocesses to Multielectron Catalysts: Towards a Photoelectrocatalytic System. *J. Electroanal. Chem.* **2010**, *650*, 10–15.

(25) Kanan, M. W.; Nocera, D. G. In Situ Formation of an Oxygen-Evolving Catalyst in Neutral Water Containing Phosphate and Co^{2+}. *Science* **2008**, *321*, 1072–1075.

(26) Du, P.; Kokhan, O.; Chapman, K. W.; Chupas, P. J.; Tiede, D. M. Elucidating the Domain Structure of the Cobalt Oxide Water Splitting Catalyst by X-Ray Pair Distribution Function Analysis. *J. Am. Chem. Soc.* **2012**, *134*, 11096–11099.

(27) Zhong, D. K.; Gamelin, D. R. Photoelectrochemical Water Oxidation by Cobalt Catalyst ("Co−Pi")/α-Fe_2O_3 Composite Photoanodes: Oxygen Evolution and Resolution of a Kinetic Bottleneck. *J. Am. Chem. Soc.* **2010**, *132*, 4202–4207.

(28) Marcon, R. O.; Brochsztain, S. Characterization of Self-Assembled Thin Films of Zirconium Phosphonate/Aromatic Diimides. *Thin Solid Films* **2005**, *492*, 30–34.

(29) Rodríguez-Abreu, C.; Aubery-Torres, C.; Solans, C.; López-Quintela, A.; Tiddy, G. J. T. Characterization of Perylene Diimide Dye Self-Assemblies and Their Use As Templates for the Synthesis of Hybrid and Supermicroporous Nanotubules. *ACS Appl. Mater. Interfaces* **2011**, *3*, 4133–4141.

(30) Shin, I.-S.; Hirsch, T.; Ehrl, B.; Jang, D.-H.; Wolfbeis, O. S.; Hong, J.-I. Efficient Fluorescence "Turn-On" Sensing of Dissolved Oxygen by Electrochemical Switching. *Anal. Chem.* **2012**, *84*, 9163–9168.

(31) Gregg, B. A.; Cormier, R. A. Liquid Crystal Perylene Diimide Films Characterized by Electrochemical, Spectroelectrochemical, and Conductivity versus Potential Measurements. *J. Phys. Chem. B* **1998**, *102*, 9952–9957.

(32) Bard, A. J.; Faulkner, L. R. *Electrochemical Methods: Fundamentals and Applications*; 2nd ed.; John Wiley & Sons, Inc.: Hoboken, NJ, 2001.

(33) Gregg, B. A. Evolution of Photophysical and Photovoltaic Properties of Perylene Bis(phenethylimide) Films upon Solvent Vapor Annealing. *J. Phys. Chem.* **1996**, *100*, 852–859.

(34) Cormier, R. A.; Gregg, B. A. Self-Organization in Thin Films of Liquid Crystalline Perylene Diimides. *J. Phys. Chem. B* **1997**, *101*, 11004–11006.

(35) Cormier, R. A.; Gregg, B. A. Synthesis and Characterization of Liquid Crystalline Perylene Diimides. *Chem. Mater.* **1998**, *10*, 1309–1319.

(36) Gregg, B. A.; Kose, M. E. Reversible Switching between Molecular and Charge Transfer Phases in a Liquid Crystalline Organic Semiconductor. *Chem. Mater.* **2008**, *20*, 5235–5239.

(37) Stenzel, O. Solid State Optics. In *The Physics of Thin Film Optical Spectra: An Introduction*; Ertl, G.; Luth, H.; Mills, D. L., Eds.; Springer Series in Surface Sciences; Springer-Verlag: Berlin, 2005; Vol. 44, pp. 199–288.

(38) Kazmaier, P. M.; Hoffmann, R. A Theoretical Study of Crystallochromy. Quantum Interference Effects in the Spectra of Perylene Pigments. *J. Am. Chem. Soc.* **1994**, *116*, 9684–9691.

(39) Cardona, C. M.; Li, W.; Kaifer, A. E.; Stockdale, D.; Bazan, G. C. Electrochemical Considerations for Determining Absolute Frontier Orbital Energy Levels of Conjugated Polymers for Solar Cell Applications. *Adv. Mater.* **2011**, *23*, 2367–2371.

(40) Johansson, T.; Mammo, W.; Svensson, M.; Andersson, M. R.; Inganäs, O. Electrochemical Bandgaps of Substituted Polythiophenes. *J. Mater. Chem.* **2003**, *13*, 1316–1323.

(41) Zahn, D. R. T.; Gavrila, G. N.; Gorgoi, M. The Transport Gap of Organic Semiconductors Studied Using the Combination of Direct and Inverse Photoemission. *Chem. Phys.* **2006**, *325*, 99–112.

(42) Hains, A. W.; Liang, Z.; Woodhouse, M. A.; Gregg, B. A. Molecular Semiconductors in Organic Photovoltaic Cells. *Chem. Rev.* **2010**, *110*, 6689–6735.

(43) Park, Y.; Choong, V.; Gao, Y.; Hsieh, B. R.; Tang, C. W. Work Function of Indium Tin Oxide Transparent Conductor Measured by Photoelectron Spectroscopy. *Appl. Phys. Lett.* **1996**, *68*, 2699–2701.

(44) Steinmiller, E. M. P.; Choi, K.-S. Photochemical Deposition of Cobalt-Based Oxygen Evolving Catalyst on a Semiconductor Photoanode for Solar Oxygen Production. *Proc. Natl. Acad. Sci. U. S. A.* **2009**, *106*, 20633–20636.

(45) Salvador, P.; Gutiérrez, C. Analysis of the Transient Photocurrent-Time Behaviour of a Sintered n-$SrTiO_3$ Electrode in Water Photoelectrolysis. *J. Electroanal. Chem. Interfacial Electrochem.* **1984**, *160*, 117–130.

(46) Chen, Z.; Jaramillo, T. F.; Deutsch, T. G.; Kleiman-Shwarsctein, A.; Forman, A. J.; Gaillard, N.; Garland, R.; Takanabe, K.; Heske, C.; Sunkara, M.; *et al.* Accelerating Materials Development for Photoelectrochemical Hydrogen Production: Standards for Methods, Definitions, and Reporting Protocols. *J. Mater. Res.* **2010**, *25*, 3–16.

(47) Demmig, S.; Langhals, H. Very Soluble and Photostable Perylene Fluorescent Dyes. *Chem. Ber.* **1988**, *121*, 225–230.

(48) Falck, D. Amperometric Oxygen Electrodes. *Curr. Sep.* **1997**, *16*, 19–22.

(49) U.S. Geological Survey. Dissolved Oxygen Solubility Tables http://water.usgs.gov/software/DOTABLES/ (accessed Jun 7, 2013).

IV. SENSITIZATION OF NANOCRYSTALLINE METAL OXIDES WITH A PHOSPHONATE-FUNCTIONALIZED PERYLENE DIIMIDE: A PHOTOELECTROCHEMICAL ANODE EN ROUTE TO WATER-OXIDATION CATALYSIS[iii]

Overview

A organic thin-film composed of a perylene diimide dye (N,N´-bis(phosphonomethyl)-3,4,9,10-perylenediimide, PMPDI) with photoelectrochemically deposited cobalt oxide (CoO_x) catalyst was previously shown to photoelectrochemically oxidize water (DOI: 10.1021/am405598w). Herein, the PMPDI dye is studied for the sensitization of different nanostructured metal oxide (nano-MO_x) films in a dye-sensitized photoelectrochemical cell architecture. Dye adsorption kinetics and saturation decreases in the order TiO_2 > SnO_2 >> WO_3. Despite highest initial dye loading on TiO_2, photocurrent with hydroquinone (H_2Q) sacrificial reductant in pH 7 aqueous solution is much higher on SnO_2 films, likely due to a higher driving force for charge injection from the more positive conduction band energy of SnO_2. Dying conditions and SnO_2 film thickness have been optimized to achieve light-harvesting efficiency >99% at the λ_{max} of the dye and absorbed photon-to-current efficiency of 13% with H_2Q, a 2-fold improvement over our previous thin-film architecture. Attempts to photoelectrochemically deposit

[iii] The work described in this chapter is a continuation of the project in Chapter III, wherein a first-generation water-oxidizing photoanode was developed with an organic thin-film architecture based on a perylene diimide dye. Herein, the same dye is applied in a second-generation, dye-sensitized metal oxide architecture in an attempt to improve the light-harvesting efficiency and charge-transport efficiency relative to the first-generation device. This chapter contains a manuscript that has been prepared for submission to the journal *ACS Applied Materials & Interfaces* (Kirner, J.T.; Finke, R. G. *ACS Appl. Mater. Interfaces*, **2017**, To be submitted). Supporting Information has been compiled in Appendix II.

CoO_x as a water-oxidation catalyst resulted in lower photocurrent due to enhanced recombination between catalyst and photo-injected electrons in SnO_2, as confirmed by open-circuit photovoltage measurements. Alumina overlayers deposited by a solution-based method were shown to enhance dye loading kinetics and saturation, but always resulted in lower photocurrent due to a decreased injection efficiency. Possible future studies to enhance photoanode performance are discussed, including alterative catalyst deposition strategies or structural derivatization of the perylene dye.

4.1 Introduction

Global energy needs are growing due to an increasing global population and a more energy-intensive global economy.[1] In order to meet these energy demands while also minimizing CO_2 emissions, the use of fossil fuels as energy feedstocks must be decreased relative to carbon-neutral (and ideally, renewable) fuel sources.[1] Of the available renewable energy feedstocks, solar energy is by far the most abundant, yet one of the least-utilized.[1] However, solar energy is diffuse, making efficient collection and conversion a challenge. Additionally, the intermittency and daily fluctuation of solar energy means that the collected energy must be stored for future use, either in the form of heat, electrical energy, or chemical energy in the form of solar fuels. For this reason, artificial photosynthesis, the light-driven conversion of abundant and renewable liquid water into hydrogen and oxygen gases, has been identified as one of the "Holy Grails of Chemistry".[2,3]

An artificial photosynthesis device, or water-splitting photoelectrolysis cell (WS-PEC, see the list of abbreviations at the end of the text), requires a semiconductor for light absorption and photogenerated charge transport, and catalyst(s) for the efficient oxidation of water and reduction of protons. For practical application, a WS-PEC should be efficient, long-lived, and produce H_2 gas at a price competitive with steam reforming from natural gas.[3] Relevant to the price point,

many researchers have employed earth-abundant, organic materials as the light-collecting components of WS-PECs, the subject of our recent review article.[4] Such devices include both organic thin-film and dye-sensitized photoelectrolysis cell architectures,[4] (OTF-PECs and DS-PECs, respectively) and have employed materials including aromatic heterocycle dyes such as phthalocyanines, porphyrins, and sub-porphyrins;[5–12] perylenes;[5,6,13–16] all-organic Donor–Acceptor type dyes;[17,18] as well as organic polymers and fullerenes.[8,13,19–22]

Previously, our group developed a water-oxidation photoanode based on an organic thin-film composed of a novel perylene diimide (PDI) dye with co-deposited CoO_x water oxidation catalyst (WOCatalyst).[14] The dye, N,N´-bis(phosphonomethyl)-3,4,9,10-perylenediimide (PMPDI, Fig. 4.1), incorporates phosphonate groups in an attempt to help couple the organic dye to the inorganic CoO_x catalyst. We previously found that the device efficiency was limited by low light absorption efficiency (only 12% of incident light was absorbed by the thin film at the dye's λ_{max}) and significant charge carrier recombination (only 6% charge transport efficiency).[14] We hypothesized that both of these limitations might be improved through the use of a nanostructured device architecture such a DS-PEC. There have been many examples of water-oxidizing DS-PEC systems in the literature, which have been summarized in several review articles.[4,23–29]

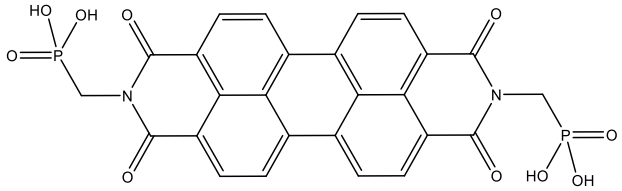

Figure 4.1 Structure of N,N´-bis(phosphonomethyl)-3,4,9,10-perylenediimide (PMPDI).

Perylene dyes have been studied as light-harvesting materials in many systems aimed towards light-driven water splitting, including homogeneous (dissolved or suspended) photocatalytic systems,[30–38] OTF-PEC systems,[5,6,13,14,39–41] and DS-PEC systems.[15,16,42–45] Of the

handful of DS-PEC systems,[15,16,42–45] successful water oxidation had remained elusive until two recently published systems.[15,16] Specifically, a 2015 study by Ronconi *et al.*[15] reported a water-oxidizing DS-PEC composed of a nanostructured WO_3 film sensitized with a cationic PDI dye and co-loaded with IrO_2 nanoparticle WOCatalyst. In pH 3 buffer and ~1 sun illumination, WO_3/PDI/IrO_2 photocurrent reached ~70 μA/cm² (approximately a 4-fold enhancement relative to WO_3/PDI without catalyst), though water oxidation was not confirmed by the direct detection of O_2 product.

A second system by Kamire *et al*.[16] was composed of nanostructured TiO_2 sensitized with a perylene monoimide (PMI) dye. The TiO_2/PMI film was subsequently treated by atomic layer deposition (ALD) to partially encapsulate the dye with an electronically insulating Al_2O_3 overlayer. WOCatalyst (either a dimeric IrIr catalyst or a monomeric Ir catalyst with a phenyl spacer and silatrane anchor group) was subsequently loaded atop the Al_2O_3 layer.[16] Kamire *et al.* found that the Al_2O_3 overlayer served to enhance the stability of the PMI dye on the surface, and also served to decrease the rate of recombination between photo-injected electrons in the TiO_2 conduction band and oxidized catalyst at the surface or oxidizable species in solution.[16] Steady-state photocurrent for TiO_2/PMI/Al_2O_3/Ir anodes in aqueous electrolyte with 1-sun illumination reached as high as ~15 μA/cm², though faradaic efficiencies for O_2 production were low, ~20%.[16]

Herein we report an exploratory study on the dye-sensitization of several nanoparticle metal oxide (MO_x) films with our precedented[14] PMPDI dye. While nano-TiO_2 is the most common substrate for DS-PEC studies,[4,23–29]examples exist where perylene dyes do not have sufficient LUMO energies (lowest unoccupied molecular orbital) to photo-inject an electron into the TiO_2 conduction band.[43,45] Furthermore, transient absorption spectroscopy studies of perylene dyes on various MO_x films have found different rates for electron injection and recombination

depending on the identity of the MO_x,[15,45] including TiO_2, SnO_2, and WO_3. Therefore, we chose to broaden our initial studies to include these three MO_x materials. We report on the preparation and characterization of TiO_2, SnO_2, and WO_3 nanostructured films. We then study the sensitization of these films with PMPDI dye and test photocurrent in the presence of sacrificial reductant. Overall, we find that: (i) the SnO_2 substrate shows the most promising results with our PMPDI dye; (ii) optimization of dying conditions and SnO_2 film thickness allowed for >99% light-harvesting efficiency at the λ_{max} of PMPDI; (iii) absorbed photon-to-current efficiency (APCE) measured for this DS-PEC architecture and sacrificial reductant are superior to our previous OTF-PEC architecture; (iv) employing photoelectrochemical deposition of CoO_x as WOCatalyst results in decreased photocurrent, contrary to results for our previous architecture, and for reasons which will be described. This last finding illustrates the difficulty of coupling the catalyst to the dye while also preventing recombination, and we list several possible pathways for future studies to improve efficiency and achieve water oxidation.

4.2 Experimental Section

Materials. The following starting materials and solvents were used as received: Perylene-3,4,9,10-tetracarboxylic dianhydride (PTCDA) (Aldrich, 97%); (aminomethyl)phosphonic acid (Alfa Aesar, 99%); imidazole (Acros Organics, 99%); formamide (certified ACS grade, Fisher); $Co(NO_3)_2 \cdot 6H_2O$ (Fluka, >99%); hydroquinone (Aldrich, >99%). Buffer solutions were prepared from water (Barnstead NANOpure ultrapure water system, 18 MΩ), KH_2PO_4 (Fisher, Certified ACS grade, 99.3%, 0.0005% Fe); KOH (Fisher, Certified ACS grade, 88.5%, 11.5% water, 0.00028% Fe, 0.0008% Ni).

Synthesis of N,N′-bis(phosphonomethyl)-3,4,9,10-perylenediimide (PMPDI). PMPDI was prepared as detailed in our previous publication.[14] Briefly, the starting materials PTCDA and (aminomethyl)phosphonic acid were stirred together in molten imidazole at 130 °C for 20 min, followed by precipitation of the product by the addition of 2 M HCl/ethanol. The product was purified from PTCDA starting material by dissolving the product with aqueous KOH, filtering, then slowly acidifying with HCl to re-precipitate the product and dissolve residual imidazolium, collecting the product by filtration. This process was repeated twice to yield the di-potassium salt of PMPDI. Finally, the fully-protonated form of PMPDI was obtained by dissolving the solid in aqueous NaOH solution and leaving the solution to slowly acidify for 24 h in a desiccator saturated with HCl vapor. The final product was collected by filtration. Characterization data are provided in our previous publication.[14]

Preparation and Characterization of MO_x Sintered Nanoparticle Films. Experimental details for the preparation and characterization of nano-TiO_2, SnO_2, and WO_3 films are provided in Sections S4.2 and S4.3 of the Supporting Information. Briefly, nano-MO_x pastes were either purchased or prepared in-house, doctor bladed onto fluorene-doped tin oxide coated glass (FTO) between Scotch tape spacers (1–4 layers, where stated, to vary the resulting film thickness), and the resulting paste films were calcined to form the sintered, mesoporous films. Paste formulations may be adjusted in future studies for the convenient preparation of a given thickness by 1-layer of Scotch tape. Where stated, alumina overlayers were also deposited on MO_x films by a solution-based method,[46,47] prior to dye loading (see Sec. S4.7c in the Supporting Information for experimental and characterization details).

Dying of MO_x Films. Preliminary dying experiments were done by placing MO_x films (approximately 1.2×1.2 cm films on 1.2×2.5 cm FTO) in a covered petri dish filled with enough

dye solution to cover the entire film surface with several millimeters of solution. Dye solutions usually consisted of 3 mg of PMPDI (fully protonated form) in 10 mL of formamide (sonicated to dissolve, saturated, <0.5 mM PMPDI). Dying films were stored in a dark drawer for ≥18 h. After dying, films were soaked in fresh formamide for 1 min (to remove any weakly adsorbed dye and residual dye solution on the pores of the film), soaked in water for 1 min (to rinse away formamide), and were then allowed to air-dry. Note, no effort was made to exclude water from the film surface before dying (as is generally done for DSSC preparation, by heating the films to ≥100 °C immediately before submerging in dye solution) because the anodes are to be tested in water solutions anyway. UV–vis spectra of dyed films were collected using a a Hewlett Packard 8452A diode array spectrophotometer, illuminated from the substrate side. Spectra of bare MO_x films were measured and subtracted from the dyed films to give the absorbance by the dye alone. Figure 4.2 below shows UV–vis spectra of dyed MO_x films (each prepared using 1 layer of Scotch tape spacer) as well as the time-dependent dying kinetics. Subsequently, dying conditions were optimized for SnO_2 by varying the dying solvent and solution temperature (Sec. S4.7 of the Supporting Information).

Photoelectrochemical Testing of Dyed MO_x Films. All photoelectrochemical experiments were performed in a custom-made two-compartment photoelectrochemical cell with a working compartment made from 1 × 1.5 cm^2 Pyrex rectangular tubing with a working volume of ~5 mL and separated from the auxiliary compartment by a medium porosity glass frit. Experiments were controlled by a CH Instruments CHI630D potentiostat, using a platinum wire counter electrode (in the auxiliary compartment) and Ag/AgCl (3 M NaCl, +0.215 V vs NHE) reference electrode (in the working compartment, within several millimeters of the MO_x/PMPDI surface).

For testing, the FTO/MO_x/PMPDI(/CoO_x, see below) anodes were clamped against the front wall of the cell with the working electrode alligator clip (the glass back of the anode against the glass cell wall) and the cell was filled with electrolyte solution (pH 7, 0.1 M KPi aqueous buffer) to cover the active area of the film. The anode was illuminated through the substrate side by a 65 W xenon arc lamp (PTO model A 1010) powered by an OLIS XL150 adjustable power supply. The lamp was focused onto the cell through a bandpass filter (315−710 nm, Thorlabs KG3, FGS900S) and UV filter (400 nm long-pass, Thorlabs FGL400S), and the power density was adjusted to closely match the visible region of the standard AM 1.5 G spectrum (see the Sec. S4.5 of the Supporting Information for additional details) according to a Thorlabs Thermal Power Sensor, model S302A. For transient experiments, the light was chopped with black cardboard at the stated time interval.

Oxygen quantification in solution was done by a Generator–Collector (G–C) method[48,49], with details and results described in Sec. S4.8 of the Supporting Information. IPCE measurement details and results are described in Sec. S4.9 of the Supporting Information. Open-circuit photovoltage (V_{oc}) measurements were performed in a 3-electrode configuration. Following a current transient experiment such as that shown in Fig. 4.5c, the cell was allowed to short-circuit in the dark for 60 s to depopulate electrons from SnO_2 sub-bandgap states. The V_{oc} was measured (vs the Ag/AgCl reference) for ≥10 s in the dark until stabilized, followed by exposed to white light illumination (same as above, approximating 1-sun irradiance in the visible wavelength range). The measurement was continued until a steady-state V_{oc} was reached (typically within 90 s). We note that the steady-state V_{oc} of our anodes in the dark were significantly negative of the E^0 for the O_2/H_2O couple (+0.61 V vs Ag/AgCl, 3 M NaCl), consistent with a previous observation by the Mallouk group.[50] This suggests that the SnO_2 electrode is not at equilibrium with the O_2/H_2O

couple, and instead its resting potential is likely determined by dark redox processes such as O_2 reduction or SnO_2 trap states.[50]

Photoelectrochemical Deposition of CoO_x. SnO_2/PMPDI anodes were submerged in pH 7, 0.1 M potassium phosphate buffer (KPi) containing 0.5 mM $Co(NO_3)_2$. Anodes were biased at +0.2 V vs Ag/AgCl and illuminated with visible light for 3 min. After the deposition, anodes were soaked in water for ≤ 1 min to remove any free Co(II) and copiously rinsed with water.

4.3 Results And Discussion

Preparation and Characterization of MO_x Nanoparticle Films. Nanostructure MO_x films have been widely used in the DSSC and DS-PEC literature, and so a variety of nanoparticle paste formulations and film preparation procedures exist. A detailed discussion on our selection of MO_x film preparation procedures can be found in Sec. S4.1 of the Supporting Information, followed by experimental details and characterization data in Sections S4.2 and S4.3, respectively. Briefly, a commercial TiO_2 nanoparticle paste was purchased, WO_3 nanoparticles and paste were prepared by a literature method[51] (with poor reproducibility), and a commercial SnO_2 nanoparticle powder was purchased and formulated into a paste. Nanoparticle pastes were subsequently doctor bladed onto fluorine-doped tin oxide (FTO)-coated glass between Scotch tape spacer(s), and subsequently calcined to form mesoporous, sintered films. Characterization data for the as-prepared MO_x films are summarized in Table 4.1.

Table 4.1 Characterization data for sintered MO_x nanoparticle films.

Characteristic, unit (method)	TiO_2	SnO_2	WO_3
Particle diameter, nm (reported[a])	15–20	18 (BET)	50–100 (SEM)
Particle diameter, nm (SEM)	18 ± 3	16 ± 5	52 ± 13
Particle diameter, nm (PXRD)	15	17	33
Film crystal system (PXRD)	tetragonal	tetragonal	monoclinic
Film thickness, μm (profilometry)	5.5 ± 0.3	2.5 ± 0.2	0.75 ± 0.05
E_{CB}, V vs Ag/AgCl (photoelectrochemistry)	−0.51 ± 0.01	−0.16 ± 0.01	−0.035 ± 0.001

[a] Particle size as reported by manufacturer or literature preparation method.

The TiO_2 and SnO_2 paste formulations produced optically transparent films, whereas the WO_3 paste formulation[51] was found to be irreproducible until an experimental typographical error was confirmed (see Sec. S4.2c of the Supporting Information). Even with the error corrected, the resulting WO_3 films were usually optically opaque due to light scattering from micrometer-scale cracks in the film (see Fig. S4.1 of the Supporting Information). Powder X-ray diffraction (XRD) was used to confirm that MO_x particles were crystalline after calcination. Scherrer analysis[52] of the most intense diffraction peaks allowed for estimation of the average crystallite size, which was compared to average particle sizes as determined from SEM images of the films.

The good agreement between SEM and XRD particle sizes for both TiO_2 and SnO_2 suggests monocrystalline particles. For WO_3 the average particle diameters were 52 and 33 nm by SEM and XRD, respectively, which could indicate some polycrystallinity of the WO_3 particles. The measured particle sizes found for the sintered MO_x films were consistent with the respective starting material particle sizes reported by the manufacturer (TiO_2 and SnO_2) or the literature[51] (WO_3), indicating that particles did not grow significantly during calcination. It would be ideal to obtain WO_3 films with smaller average sizes that are comparable to TiO_2 and SnO_2 (~20 nm), so that particle size would not be a variable when comparing DS-PEC performance. However, the surface chemistry of WO_3 quickly eliminated the material from our consideration (see below). Therefore, alternative synthetic procedures for WO_3 nanoparticles,[53] as well as alternative, more reproducible, and more stable paste formulations are of interest for future research, but were not pursued as part of the present study.

Film thicknesses were measured by optical profilometry, and are reported in Table 4.1 for each film prepared with one layer of Scotch tape as spacer. Film thicknesses varied significantly between the three different MO_x systems, most likely due to the differences in paste formulations,

such as different molecular weights and wt% of the different metal oxides, and different identities and wt% of paste-thickening and stabilizer material. For initial studies herein, film thicknesses were varied when necessary by using multiple layers of Scotch tape spacer ("1-Scotch" film, "2-Scotch" film, etc.).

Also included in Table 4.1, the electrochemical energy of the conduction band edge (E_{CB}) for each MO_x film was estimated by an electrochemical photocurrent onset method[54] (Sec. S4.3d of the Supporting Information). For comparison, the HOMO and LUMO of PMPDI were estimated by cyclic voltammetry and visible absorption and fluorescence spectroscopy (Sec. S4.4 of the Supporting Information). This allows for the preparation of an approximate energy diagram for the DS-PEC systems under study (Fig. 4.2), which reveals that the thermodynamic driving force for electron injection from the LUMO of photo-excited dye, PMPDI*, into the CB of the specific MO_x increases in the order $TiO_2 < SnO_2 < WO_3$. Given that injection is expected to occur in the Marcus normal region[56] where the rate increases with increasing driving force, we therefore expect increasing rates (and overall yield) of injection in the order $TiO_2 < SnO_2 < WO_3$. This predicted

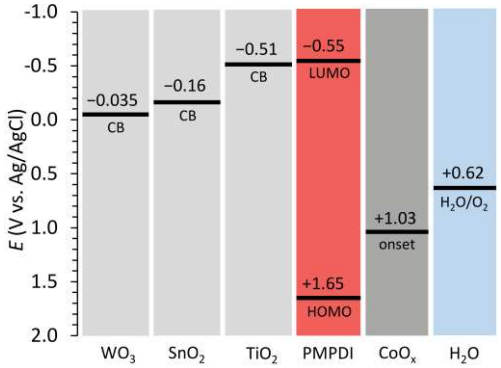

Figure 4.2 Estimated energy diagram for the MO_x/PMPDI/CoOx system. Values are given vs Ag/AgCl for the components in solution at pH 7. The energies of the MO_x conduction band edges (E_{CB}) were estimated herein (Sec. S4.3d, Fig. S4.7). Energy levels of PMPDI are discussed and estimated in Sec. S4.4a and Fig. S4.8 of the Supporting Information. The catalytic onset of water oxidation by CoO_x on an ITO electrode is 1.03 V vs. Ag/AgCl in pH 7 buffer,[55] and the thermodynamic potential for water oxidation at pH 7 is 0.62 V vs Ag/AgCl.

trend was previously observed by for a perylene derivative by Ronconi *et al.*[15] using transient absorption spectroscopy, though they did not measure the MO_x conduction band energies.

MO_x Sensitization with PMPDI. Preliminary studies for the dying of MO_x films with PMPDI were done using formamide dye solutions because the visible absorbance spectrum of PMPDI in that solvent showed vibronic structure indicative of molecularly dissolved dye instead of dissolved aggregates[57–59] (see Fig. S4.8b for example). To track dye loading over time, MO_x films were removed from dye solution at varying time intervals and rinsed, a UV–vis absorbance spectrum was collected, and the film was returned to solution to continue dying. Absorbance spectra from different MO_x films (normalized for film thickness) are shown in Fig. 4.3a, and normalized absorbance is plotted vs time in Fig. 4.3b. Dye adsorption onto TiO_2 was kinetically fastest, and also reached the highest dye saturation level (inset photo, Fig. 4.3a) after ~5 days. With saturated dye loading, the absorptance (1 – Transmittance) of PMPDI on 1-Scotch TiO_2 reached >99% at the λ_{max} of 490 nm. For comparison, the kinetics of dye adsorption on SnO_2 were much slower, taking ~3 weeks to reach a significantly lower saturation level, which is clearly not

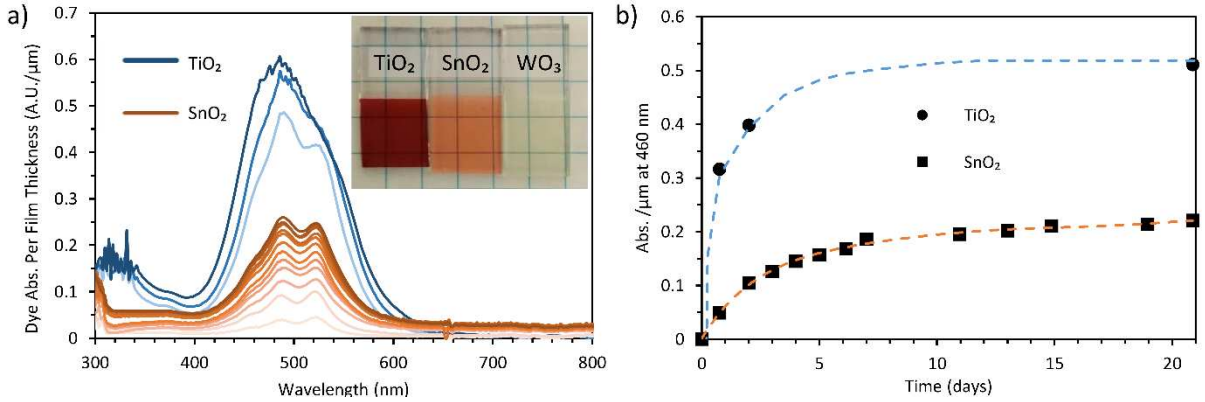

Figure 4.3 Dye adsorption kinetics on various MO_x films on FTO. (a) UV–vis spectra of dying TiO_2 (blue) and SnO_2 (orange) films over time (light to dark), normalized by average film thickness according to Table 4.1. Films were dyed from 0.5 mM PMPDI in formamide. Spectra correspond to absorption by PMPDI only, as spectra of bare MO_x films have been subtracted out. The inset provides photographs of MO_x films after 3 weeks of dying. Note that WO_3 had no appreciable dye absorbance. (b) Dye absorbance at 460 nm, normalized by average film thickness on TiO_2 (●) and SnO_2 (■) over time. This wavelength was chosen because it is relatively insensitive to dye aggregation.[57,58] Dashed lines are provided to guide the eye.

convenient for preparation and study. At saturation, the absorptance of PMPDI on 1-Scotch SnO_2 reached only 76% at the λ_{max} of 490 nm.

Similar behavior of significantly lower dye loading on nano-SnO_2 than TiO_2 was previously reported by Kay and Grätzel,[60] using the common Ru-based dye, N719. They rationalized this behavior based on the different isoelectric points (IEPs) of the MO_x (that is, the pH at which the net surface charge of the oxide is zero). The IEP of TiO_2 (anatase) is generally 6–7, whereas that of SnO_2 (cassiterite) is 4–5.[61–63] Hence, the SnO_2 surface is more acidic than TiO_2, and therefore the interaction between the SnO_2 surface and acidic dye anchor groups such as carboxylates or phosphonates is expected to be weaker than for TiO_2. An alternative/complementary hypothesis for the lower dye loading on SnO_2 is a lower internal surface area[64] relative to TiO_2, as suggested by the higher degree of particle aggregation observed by SEM for SnO_2 films relative to TiO_2 films (Fig. S4.4). Consistently, WO_3 has the lowest IEP[61] of <1 (most acidic surface), and also likely a lower film internal surface area due to the larger particle size (Fig. S4.4). Therefore, it is not surprising that *no detectable PMPDI* (with its acidic anchor groups) was adsorbed onto WO_3, whereas the *cationic* perylene derivative reported previously by Ronconi *et al.*[15] was successfully adsorbed on WO_3 (albeit, interestingly, with slower kinetics than on TiO_2 and SnO_2).

Photocurrent of MO_x/PMPDI films. The photoelectrochemical performance of the dyed TiO_2 and SnO_2 films were studied in pH 7 buffer, using a Xe arc lamp calibrated to closely match the irradiance spectrum of the Air Mass (AM) 1.5 standard[65] in the visible region (see Sec. S4.5 in the Supporting Information for details). For such conditions, low photocurrent is expected because no water oxidation catalyst has been added. The water-oxidation reaction requires two water molecules and the removal of four electrons to generate one O_2 molecule ($H_2O \rightarrow O_2 + 4H^+ +$

$4e^-$). By contrast, light absorption by a dye molecule followed by rapid injection of the excited electron into the MO_x conduction band only generates one hole (h^+) at the electrolyte interface per dye molecule per photon. With no catalyst to accumulate the multiple holes required for an overall water oxidation reaction, it is likely that the majority of photo-generated holes on the dye molecules are lost to recombination before they can participate in the multiple-electron reaction.

In order to gauge the relative performance of photoelectrodes before catalyst is deposited, it is common to add a sacrificial reductant to solution, one whose oxidation is thermodynamically and kinetically more facile than that of water. Examples of sacrificial reductants used in related studies include ferrocyanide,[66] triethanolamine,[67] sulfite,[22] isopropanol,[68] and hydroquinone.[14,18] For our studies, we chose to use hydroquinone (H_2Q) because its oxidation to benzoquinone involves $2e^-$ and $2H^+$, arguably making it a closer model for the water oxidation reaction ($4e^-$, $4H^+$). The standard reduction potential of H_2Q[69] is +0.7 V vs NHE at pH 0 (+0.076 V vs Ag/AgCl, pH 7).

Initial controls with SnO_2/PMPDI showed that photocurrent is saturated well before a concentration of 20 mM H_2Q, and by an applied potential of +0.2 V vs Ag/AgCl (see Fig. S4.10). It is prudent to note that "current doubling" can occur with H_2Q sacrificial reductant,[69] wherein the initial (presumably outer-sphere) photo-oxidation generates a more-easily oxidized intermediate that may be capable of a subsequently (outer sphere) electron transfer to the semiconductor conduction band before diffusing away from the surface, generating a net $2e^-$ per photon. This effect is dependent on semiconductor band energies and pH.[69] While we have not been able to confirm if current doubling occurs from H_2Q in our system, it was previously found not to occur at TiO_2 photoanodes.[70] We note that current doubling would not be analogous to the

inner-sphere, catalyzed water-oxidation reaction, which requires at least 4 photons per $4e^-$ catalytic turnover.[71]

Figure 4.4 shows the photocurrent density (J) of dyed TiO_2 and SnO_2 films (films prepared with 1-Scotch spacer and dyed 3 weeks from formamide solution as shown in Fig. 4.3) in pH 7 potassium phosphate (KPi) buffer, using 30 s transients white light illumination. Anodic current (with a negative sign by the American convention) has been plotted upwards to accentuate photocurrent. Figure S4.11 of the Supporting Information includes control experiments showing photocurrent density on bare (undyed) TiO_2 and SnO_2 films with and without H_2Q, as well as photocurrent for dyed films without dark currents subtracted. Figure S4.12 also shows current density transients as a function of scanned potential (J–V transients) for dyed and undyed TiO_2 and SnO_2 films, both with and without H_2Q.

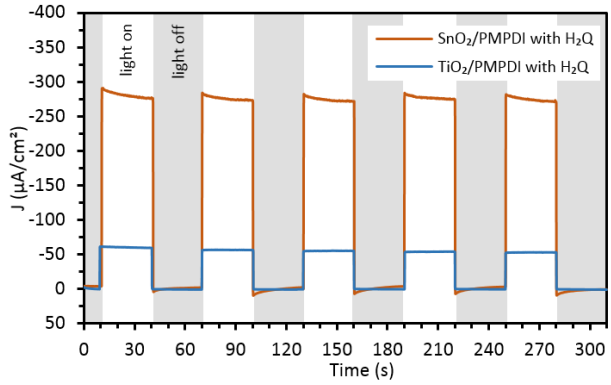

Figure 4.4 Anodic photocurrent density-time (J–t) traces with 30 s light transients for TiO_2/PMPDI (blue) and SnO_2/PMPDI (orange) with 20 mM H_2Q in pH 7, 0.1 M KPi buffer and held at +0.2 V vs Ag/AgCl. Illumination was provided with a Xe arc lamp calibrated to approximate the AM1.5 visible spectrum. Dark currents were subtracted, which were ~25 μA/cm² for TiO_2/PMPDI and ~150 μA/cm² for SnO_2/PMPDI (see Fig. S4.11 of the Supporting Information).

In the presence of H_2Q, TiO_2/PMPDI and SnO_2/PMPDI anodes showed photocurrent densities of ~55 and ~270 μA/cm², respectively, which were relatively stable during the 5 min test. Importantly, despite the much higher dye loading on TiO_2 compared to SnO_2 (Fig. 4.3),

photocurrent was nearly 5-fold higher for SnO_2/PMPDI. This is consistent with a significantly lower quantum yield for charge injection from excited PMPDI into the conduction band of TiO_2 than SnO_2, as predicted from the low driving force for this process (Fig. 4.2). With no added H_2Q, TiO_2/PMPDI and SnO_2/PMPDI anodes still exhibited photocurrent densities of <1 and <10 μA/cm², respectively, and currents from both anodes decayed by about 40% within the first 5 min of transients (see Fig. S4.11c). Controls with bare (undyed) TiO_2 and SnO_2 under the same conditions yielded photocurrent of ~0.3 and 0.2 μA/cm², respectively (Fig. S4.11a). Given the inability of PMPDI to adsorb to WO_3 and the preliminary photocurrent results for dyed TiO_2 and SnO_2, we chose the SnO_2 films for subsequent optimization studies.

Optimization of SnO_2/PMPDI Anodes.

Dying Solvent and SnO_2 Film Thickness. In an attempt to improve PMPDI dye adsorption kinetics and saturation on SnO_2 films, alternative solvents and higher temperatures were tested (see Sec, 4.7a of the Supporting Information for details). It was found that dying kinetics were faster from water and ethylene glycol dye solutions than from formamide, and that increasing the dying temperature to 90 °C allowed for dye saturation within 24 h, a clear improvement over the 3 weeks required in Fig. 4.3 (notably, freshly-dissolved PMPD (acid form) in water was pH ~4, which may result in a positively-charged SnO_2 surface to attract the negatively charged phosphonate groups of PMPDI). Photoelectrochemical measurements indicate that the steady-state photocurrent is strongly correlated to the integrated absorptance of PMPDI on SnO_2 (that is, higher dye loading results in a corresponding higher photocurrent, see Fig. S4.14).

Interestingly, when dye loading was kept low (by shorter dying times), the visible absorbance spectra of PMPDI adsorbed on SnO_2 films from ethylene glycol solutions exhibited vibronic structure suggesting monomeric, non-aggregated dye, [57–59] while spectra of PMPDI

adsorbed from water exhibited vibronic structure suggesting that the dye was at least an aggregated dimer on the surface[57–59] (see Fig. S4.14). Dye aggregation in DSSCs and DS-PECs often results in lower photovoltaic performance due to non-radiative relaxation pathways that compete with electron injection into the conduction band of the MO_x substrate.[16,45,72–74] Consistently, SnO_2/PMPDI films dyed from ethylene glycol exhibited higher photocurrent than those dyed from water with comparable, low dye loading (Fig. S4.14d). However, the effect was less pronounced at higher dye loadings (where surface aggregation was comparable for both solvents). Given that ethylene glycol can likely co-adsorb to the SnO_2 surface, we chose to complete all subsequent studies with water dying solvent to eliminate that variable.

Subsequently, we studied the effect of increasing the SnO_2 film thickness in order to maximize the light absorptance by PMPDI (see Sec. S4.7b for details). Film thicknesses were varied by depositing multiple layers of nano-SnO_2 paste onto FTO before calcination. Upon dying the films, it was found that light absorptance and photocurrent were saturated for SnO_2 films ≥6 μm thick, and that light absorptance and photocurrent were strongly correlated (Fig. S4.15). SnO_2 films with a thickness of ~6 μm could be reproducibly prepared by doctor blading a single layer of nano-SnO_2 paste between two thicknesses of Scotch tape. Therefore, optimized SnO_2/PMPDI films were prepared from "2-Scotch" SnO_2 films dyed from PMPDI in water at 90 °C for 24 h.

Alumina Overlayer Attempts. Several studies have shown that recombination is often faster for dye-sensitized nano-SnO_2 than TiO_2,[75,76] due to faster electron diffusion in SnO_2 and to the more positive conduction band resulting in a lower driving force for recombination (occurring in the Marcus inverted region).[56] Kay and Grätzel previously demonstrated[60] that the deposition of a thin shell (overlayer) of insulating metal oxide such as alumina, Al_2O_3, onto the surface of nano-SnO_2 films could significantly enhance dye loading on those films because of the more basic

surface (higher IEP).[60] When assembled in DSSCs, the resulting films also achieved up to a >4-fold enhancement in efficiency, consistent with the introduction of an electron tunneling barrier by the insulating oxide resulting in significantly reduced the rates of recombination.[60] It was subsequently confirmed that even a single layer of Al_2O_3 on SnO_2 by atomic layer deposition (ALD) could increase the lifetime of injected electrons by 2 orders of magnitude, attributable primarily to the passivation of SnO_2 surface states which can act as recombination centers.[77] However, it has also been shown that Al_2O_3 overlayers can significantly decrease the rate of photo-injection from excited dye, especially as the overlayer thickness increases, again due to the introduction of a thicker electron-tunneling barrier.[78]

Hence, it was of interest to study the effect of Al_2O_3 overlayers on our own system. We chose to prepare overlayers by a convenient solution-based method originally developed by Ichinose *et al.*,[46] involving the reaction of the SnO_2 surface with dissolved aluminum alkoxide in solution, followed by hydrolysis and calcination to produce the Al_2O_3 overlayer. Because the chemical reaction requires the availability of surface hydroxyl groups, this method is expected to deposit a monolayer or less of Al_2O_3 after one cycle of reaction.[46] The experimental details and results of our Al_2O_3 overlayer experiments are provided in Sec. S4.7c of the Supporting Information. Briefly, one cycle of reaction of nano-SnO_2 and WO_3 films with aluminum(III) isopropoxide successfully altered the surfaces without changing their optical properties. Successful surface alteration was evident by the significantly faster dying kinetics and higher saturation of PMPDI loading on both SnO_2 and WO_3 (Fig. S4.17).

Contrary to previous studies,[60,77] we did not observe any performance enhancement after one layer of Al_2O_3. Instead, the photocurrent from MO_x/Al_2O_3/PMPDI films was significantly lower than MO_x/PMPDI films without alumina, suggesting that the effect of increasing the

tunneling barrier and hindering injection yield counteracts the benefit of enhanced dye loading. We propose that our PMPDI dye may be more affected by the alumina tunneling barrier than previous systems[60,77] because of an already low injection efficiency, which can be expected due to dye aggregation[16,45,72–74] or due to poor electronic coupling between the perylene core and SnO_2 as a result of the non-conjugated phosphonomethyl anchor group.[78,79] Therefore, future studies of interest include strategies to reduce the aggregation of PMPDI on the SnO_2 surface, or structural derivatization of the dye to include conjugated and short linker groups between the perylene core and the anchor group.

Characterization data for a representative optimized SnO_2/PMPDI anode are provided in Fig. 4.5. Figure 4.5a shows the absorbance spectrum of PMPDI loaded on a 2-Scotch SnO_2 film from 90 °C water for 24h (the spectrum from a bare SnO_2 film on ITO has been subtracted). The inset displays the spectrum converted to absorptance. Notably, PMPDI reaches an absorptance of 99% at the λ_{max} of 490 nm, and absorbs strongly over a broad portion of the visible spectrum. The *integrated* absorptance of PMPDI in the visible wavelength range (400–700 nm, Fig. 4.5a inset) is 61%. Figure 4.5b shows the photocurrent transients for this SnO_2/PMPDI anode held at +0.2 V vs Ag/AgCl in pH 7 buffer with 20 mM H_2Q sacrificial reductant. Again, anodic (–) currents are plotted upwards for clarity, and dark currents of approx. −130 μA/cm² have been subtracted. Steady-state photocurrent reached ~1,100 μA/cm², representing a 4-fold enhancement over the unoptimized SnO_2/PMPDI film shown in Fig. 4.4. Photocurrent gradually decayed during each light transient, which is likely related to mass transport of H_2Q (the solution was not stirred), as photocurrent recovered after each dark transient. This demonstrates relatively good stability for the SnO_2/PMPDI anode, at least over the course of the 5 min experiment in the presence of H_2Q sacrificial reductant.

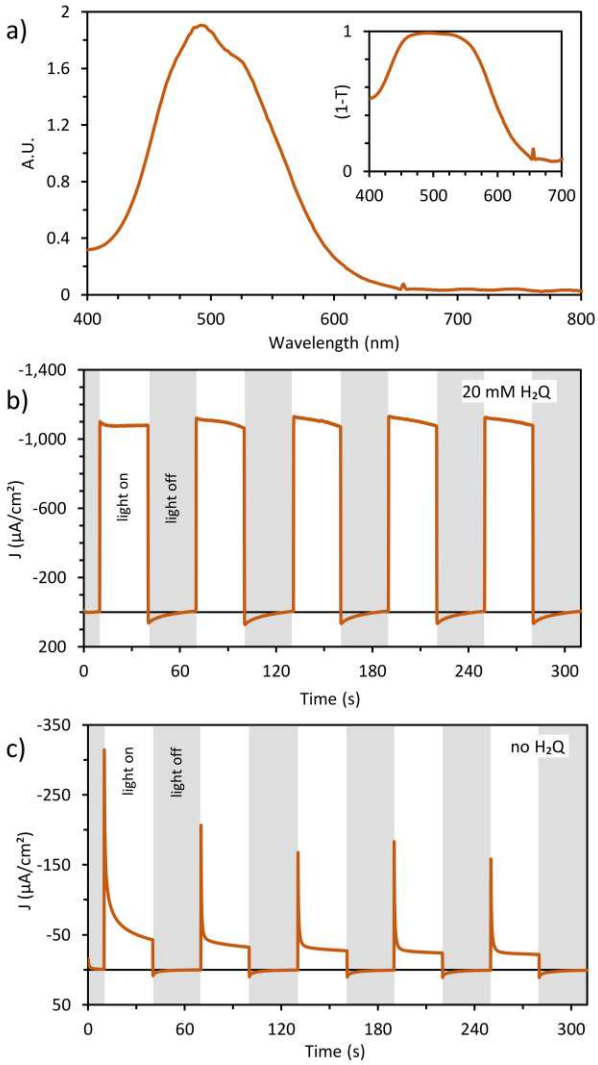

Figure 4.5 Characterization of optimized SnO_2/PMPDI anodes (6 μm thick SnO_2, dyed 24h from 0.5 mM PMPDI in 90 °C water). (a) UV–vis absorbance spectrum of PMPDI on SnO_2 (absorbance of bare SnO_2 film subtracted). The inset shows the spectrum converted to absorptance (1−T). (b) *J–t* transients in the presence of 20 mM H_2Q sacrificial reductant, with background dark currents. (c) *J–t* transients in the absence of mM H_2Q, no background subtraction. *J–t* transients were performed at +0.2 V vs Ag/AgCl in pH 7, 0.1 M KPi buffer with 15 s transient illumination by a Xe arc lamp approximating the AM1.5 visible spectrum.

In the absence of sacrificial reductant, SnO_2/PMPDI anodes in pH 7 buffer still exhibit photocurrent (Fig. 4.5c), even before any WOCatalyst has been added. Upon illumination, sharp anodic current spikes appear, then quickly decay over the course of seconds towards a steady-state value. Pronounced photocurrent spikes are absent at higher applied potentials (see Fig. S4.12,

Fig.4.7 below). Our current best hypothesis for the cause of the current spikes are SnO_2 surface states that act as recombination centers (see Sec. S4.6a of the Supporting Information), which have previously been proposed for SnO_2[77] and TiO_2.[80–83] Figure 4.5c also shows that in the absence of H_2Q, steady-state photocurrent from SnO_2/PMPDI anodes decays by ~50% over the course of the 5 min *J–t* experiment, falling from ~40 to 20 μA/cm². Such photocurrent decay could potentially result from oxidative instability of PMPDI in the absence of sacrificial reductant. However, an alternative hypothesis from the literature is proton intercalation.[84] The Mallouk group recently showed evidence that proton intercalation into nano-TiO_2 in DS-PECs occurs within the first few minutes of testing, resulting in long-lived electron traps near the TiO_2 surface that subsequently enhance recombination by back-electron transfer to surface-bound oxidized dye molecules.[84,85] We propose that the same process could be happening in our SnO_2-based anodes, thereby responsible for the observed potential-dependent current spikes and gradual photocurrent decay.

We note that the chemical reaction giving rise to photocurrent from SnO_2/PMPDI anodes in the absence of H_2Q or WOCatalyst (Fig. 4.5c) is unknown, though similar transient photocurrent shapes and magnitudes (tens of μA/cm²) have been reported for many other DS-PEC systems that employ organic sensitizers, also before addition of WOCatalyst.[7,9–11,16,17,19,86,87] Given that recent reports of photocatalytic systems (suspended colloids with sacrificial reductant) composed of nanostructured perylene derivatives can generate oxygen even before decoration with a WOCatalyst,[35,36,38] water oxidation by PMPDI is one hypothesis for the photocurrent observed in Fig. 4.5c. Alternative hypotheses include degradative oxidation of PMPDI, or the oxidation of trace buffer impurities.

Preliminary Oxygen Detection Experiments. In order to probe the origin of photocurrent observed for SnO_2/PMPDI anodes in pH 7 buffer in the absence of sacrificial reductant and before

the deposition of WOCatalyst (Fig. 4.5c), we chose to follow the dissolved oxygen concentration in solution during photolysis experiments. Given the low magnitude and gradual decay of photocurrent, we were unable to detect any change in dissolved oxygen concentration within the 15% experimental error when using our previous method of a Clark electrode.[14] Subsequently, we chose to try a Generator–Collector (G–C) method for oxygen quantification, which was originally used by the Mallouk group[48] and subsequently adapted by the Meyer group.[49] This method involves the use of a planar Collector electrode (Pt[48] or FTO[49]) spaced a short distance from the oxygen-generating photoanode, and poised at a potential sufficiently negative to reduce O_2 that diffuses through solution from the Generator to the Collector. Oxygen-collection efficiencies as high as 96% have been reported for this G–C method,[50] illustrating the high sensitivity of this electrochemical technique. We note that the lack of an oxygen-selective membrane between the Generator and Collector allows for the possible detection of species other than oxygen, though potential-varying controls can improve confidence that O_2 is the product being detected.[49]

Experimental details and data for oxygen detection by the G–C method are provided in Sec. S4.8 of the Supporting Information. Our experiments for SnO_2/PMPDI anodes yielded average faradaic efficiency for O_2 (or possibly other reducible products) of $\mathbf{1 \pm 2\%}$. This means that, within experimental error, practically none of the photocurrent observed at SnO_2/PMPDI anodes can be attributable to O_2 evolution. The next most likely hypothesis for the origin of photocurrent is PMPDI degradation, given the gradual decay of photocurrent (Fig. 4.5c). Therefore, UV–vis and film dimension data were used to estimate the amount of dye contained in SnO_2/PMPDI films (Sec. S4.8a of the Supporting Information). In summary, 1.4-times more charge was passed during 10 min of photolysis than the approximate number of PMPDI molecules on the SnO_2 film, and photocurrent remained stable beyond this time. Meanwhile, the UV–vis

absorbance spectra of the film before and after photolysis indicates only 12% loss of PMPDI. This indicates that the majority of photocurrent cannot be attributed to decomposition of PMPDI, nor to O_2 production by water oxidation. Therefore, the last remaining hypotheses for the origin of photocurrent is the oxidation of water to H_2O_2 or the oxidation of solution impurity species (for example, Cl^- leached from the reference electrode or the parts per million trace metals in the buffer).

IPCE of SnO_2/PMPDI. In order to further probe the origin of photocurrent from SnO_2/PMPDI anodes without catalyst, we collected photocurrent action spectra (photocurrent vs monochromatic illumination wavelength) and calculated the incident-photon-to-current efficiency (IPCE, see Sec. S4.9 of the Supporting Information). The IPCE spectrum for optimized SnO_2/PMPDI anodes in the presence of 20 mM H_2Q is shown in Fig. 4.6. Notably, the IPCE spectrum with H_2Q is a good match for the absorptance spectrum of PMPDI. Deviation at 400 nm may indicate photocurrent contribution by direct light absorption by SnO_2.

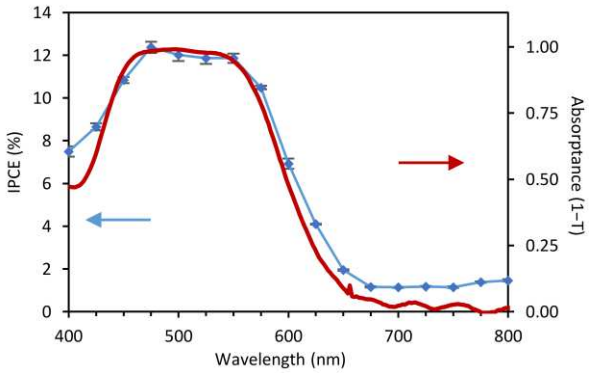

Figure 4.6 IPCE spectrum of optimized SnO_2/PMDDI anodes in pH 7, 0.1 M KPi buffer with 20 mM H_2Q (blue trace) compared to the absorptance (1−T) spectrum of the PMPDI (absorptance from bare SnO_2 was subtracted).

To aid in interpretation of the IPCE spectra, we note that the factors which contribute to the IPCE of DS-PECs are:[29]

$$\mathrm{IPCE}(\lambda) = \mathrm{LHE}(\lambda) \times \eta_{\mathrm{inj}} \times \eta_{\mathrm{col}} \tag{4.1}$$

where LHE is the wavelength-dependent light-harvesting efficiency (absorptance spectrum), η_{inj} is the injection efficiency (the fraction of excited dye that injects an electron into the MO_x before relaxation), and η_{col} is the charge collection efficiency (the fraction of injected electrons that are collected through the circuit, counteracted by recombination reactions such as back-electron transfer to oxidized dye at the surface or reduction of species in solution).[29] Dividing out the LHE (the measured absorptance spectrum), we can estimate the *absorbed* photon-to-current efficiency (APCE), which is therefore a combination of η_{inj} and η_{col}:

$$\text{APCE} = \frac{\text{IPCE}}{\text{LHE}} = \eta_{\text{inj}} \times \eta_{\text{col}} \tag{4.2}$$

This calculation for our SnO_2/PMPDI anodes in the presence of H_2Q yields an average APCE of 13 ± 2%. For comparison, the same testing conditions for our previous, organic-thin-film PEC system[14] (ITO/PMPDI/CoO_x) achieved APCE of only 6 ± 2% in the presence of H_2Q. Therefore, we can conclude that the DS-PEC architecture in the present study has not only improved the light-harvesting efficiency relative to the previous OTF architecture, but also the APCE, even before depositing catalyst.

We note that the IPCE spectra for SnO_2/PMPDI anodes in the absence of H_2Q are less of a match for the absorptance spectrum (Fig. S4.23) and are not well understood, especially because the precise oxidation reaction responsible for photocurrent is unknown. We note that by eq. 4.2, the APCE is limited by η_{inj} and η_{col}. While we have not yet measured η_{inj} for our SnO_2/PMPDI system (by transient absorption spectroscopy, for example) we predict that it is likely the major limiting factor to the APCE, given the dye aggregation[16,45,72–74] and poor electronic coupling through the phosphonomethyl anchor group.[78,79] As described above, future studies may improve η_{inj} by using strategies to reduce dye aggregation, or by structural derivatization of PMPDI.

Photoelectrochemical CoO_x Deposition. As the ultimate goal of our DS-PEC is light-driven water oxidation, we next studied the effect of loading our optimized SnO_2/PMPDI anodes with CoO_x WOCatalyst, following the same photoelectrochemical method used in our prior system.[14] We hoped that the two phosphonate groups of PMPDI (Fig. 4.1) would allow the dye to anchor to SnO_2 by one group, leaving the second extending towards solution to provide a binding group to heterogeneous CoO_x clusters (Scheme 4.1A). This picture is also promising given recent literature examples where anchoring molecular WOCatalysts to the MO_x surface through spacer groups can decrease the rate of recombination between the catalyst and conduction band electrons.[16,88] Note that, based on compiled pK_a values for a variety of phosphonates,[89] an educated guess for the pK_a values of PMPDI are 1.8, 2.3, 7.7, and 8.2. If the values are unchanged upon adsorption to SnO_2, we would predict that in pH 7 buffer, the majority of the free phosphonate groups of PMPDI will be in the $–PO_3H^–$ form with a smaller fraction in the $–PO_3^{2–}$ form, and therefore capable of coulombically attracting Co(II) in solution.

Scheme 4.1. (A) Proposed ideal binding modes of PMPDI and CoO_x WOCatalyst. (B) More likely binding modes of PMPDI and deposited CoO_x WOCatalyst as prepared herein. Green arrows indicate the desirable charge transfer reactions for water oxidation, red arrows indicate undesirable charge recombination reactions, and blue arrows indicate electron diffusion within SnO_2.

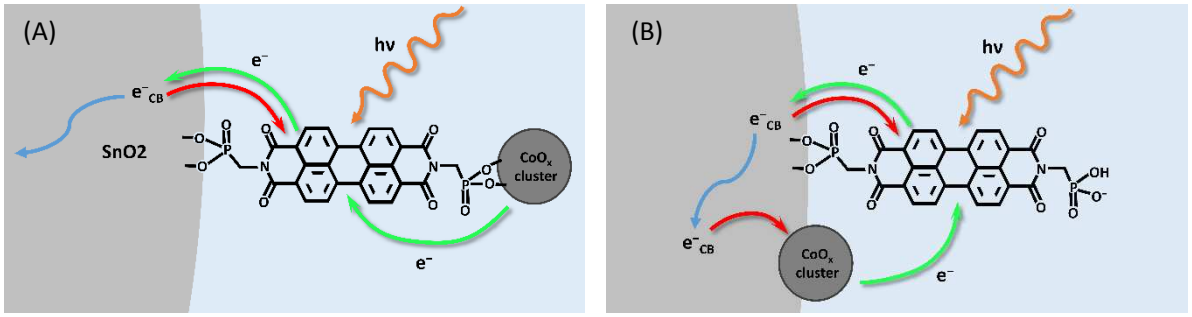

To deposit catalyst, SnO_2/PMPDI anodes were submerged in pH 7 KPi buffer containing 0.5 mM $Co(NO_3)_2$, poised at +0.2 V vs Ag/AgCl (a potential too negative to oxidize Co(II), but sufficiently positive of the SnO_2 E_{CB} to collect photo-injected electrons) and illuminated with

visible light for ≥3 min. Theoretically, after injecting a photo-excited electron, oxidized PMPDI will accept an electron from Co(II) in solution. The oxidized Co(III) can then precipitate onto the electrode, and subsequent oxidation reactions can grow the heterogeneous CoO_x WOCatalyst. After the photo-deposition, anodes were copiously rinsed with water and subsequently tested by *J*–*V* photocurrent transients in pH 7 KPi. Results are shown in Fig. 4.7.

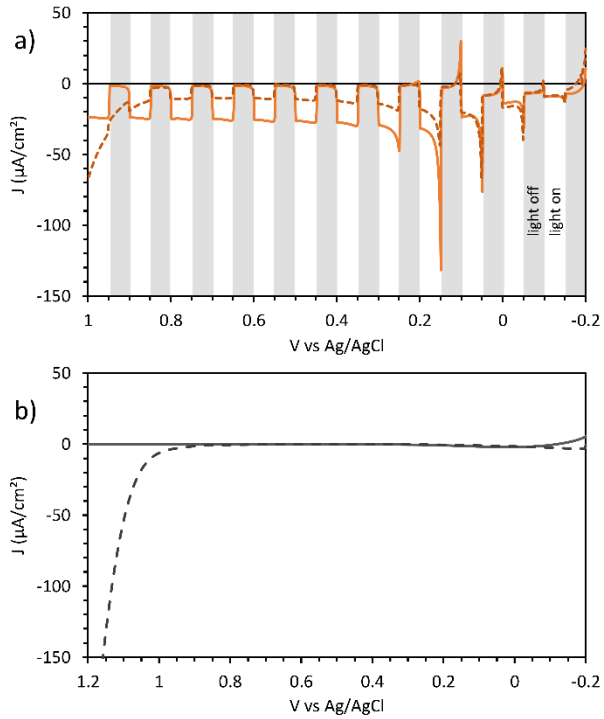

Figure 4.7 Linear sweep voltammograms (a) with transient illumination for an SnO_2/PMPDI anode before (solid line) and after (dashed line) photoelectrochemical deposition of CoO_x, and (b) in the dark using a bare (undyed) nano-SnO_2 anode before (solid line) and after (dashed line) soaking in a pH 7 KPi solution containing 0.5 mM $Co(NO_3)_2$. Voltammograms were recorded in pH 7, 0.1 M KPi buffer using a 10 mV/s scan rate and 5 s white light transients where indicated.

The onset of a catalytic anodic current at approx. +0.9 V vs Ag/AgCl is evidence that Co was successfully deposited on the film (Fig. 4.7a, dashed line). Unfortunately, steady-state photocurrent between +0.2 and +0.9 V vs Ag/AgCl is not enhanced after catalyst deposition, but actually *decreases* by a factor of 2–3. Furthermore, the presence of CoO_x does not significantly enhance the faradaic efficiency for oxygen production as measured by the G–C method (3 ± 5%).

This was surprising, given that photoelectrochemical deposition of CoO_x has previously been used by the Beranek group to enhance photocurrent from their water-oxidizing DS-PEC based on nano-TiO_2 decorated with poly(heptazine) light-harvesting polymer.[19] Given that the IEP for SnO_2 is the range of 4–5,[61–63] we expect the surface to be negatively charged in pH 7 buffer, and therefore it will coulombically attract cationic Co(II) ions in solution. As a control, a naked nano-SnO_2 film was soaked for 1 min in pH 7 KPi buffer, and linear sweep voltammetry was performed in the dark, revealing minimal current in the range of −0.1 to 1.2 V vs Ag/AgCl (Fig. 4.7b, solid trace). Subsequently, the film was soaked for 1 min in the dark in buffer with 0.5 mM $Co(NO_3)_2$, then soaked for 1 min in nanopure water and thoroughly rinsed to remove any Co(II) that was not strongly adsorbed. Subsequent voltammetry of this film (Fig. 4.7b, dashed trace) shows significant catalytic anodic current at potentials positive of +0.9 V vs Ag/AgCl, confirming that Co is retained on the SnO_2 surface without the need for photoelectrochemical oxidation.

Therefore, it follows that when we try to photoelectrochemically deposit CoO_x, the majority actually ends up directly on the SnO_2 surface, where it can easily scavenge photo-injected electrons from SnO_2 (Scheme 4.1B). Indeed, the Mallouk group previously studied a DS-PEC using a nanoparticle IrO_2 WOCatalyst loaded directly on the TiO_2 surface, which was shown to dominate recombination under those conditions.[50] The successful use of photoelectrochemical CoO_x deposition by the Beranek group[19] to enhance photocurrent may have been due to more complete surface coverage of their nano-TiO_2 film with poly(heptazine), preventing direct recombination between the TiO_2 conduction band electrons and CoO_x, or alternatively due to the higher IEP of TiO_2, possibly rendering the TiO_2 surface less negative at pH 7 during deposition.

Open-Circuit Photovoltage Measurements. To provide additional evidence that Co on the SnO_2 surface acts as a recombination center, we chose to study the open-circuit photovoltage

(V_{oc}) of our DS-PEC anodes. The V_{oc} of a DS-PEC is the difference between the quasi-Fermi energy of electrons in the nano-MO_x substrate, $E_{F,n}$, and the electrochemical potential, E^0, of the redox couple in solution[50,56] (the O_2/H_2O couple for DS-PEC anodes), as shown in Fig. 4.8a. Under illumination, the $E_{F,n}$ is kinetically determined by the relative rates of electron injection from photo-excited dye and all recombination reactions which depopulate the MO_x states.[56] By the modified diode equation:[56]

$$V_{oc} \propto \frac{k_B T}{e} \ln\left(\frac{\text{Rate}_{\text{charge in}}}{\text{Rate}_{\text{charge out}}}\right) \tag{4.3}$$

where k_B is the Boltzmann constant (eV/K), T is the temperature (K), and e is the elementary charge. Based on this relation, at 25 °C, every order of magnitude change in the ratio of injection relative to recombination causes a change of 59 mV in V_{oc}.

The results of our V_{oc} measurements are illustrated in Fig. 4.8b. The average V_{oc} measured for SnO_2/PMPDI anodes was 0.00 ± 0.02 V vs Ag/AgCl. After photoelectrochemical deposition of Co, SnO_2/PMPDI/CoO_x anodes exhibited an average photovoltage of +0.05 ± 0.02 V vs Ag/AgCl. We do not expect the deposition of CoO_x to significantly alter the rate of electron injection from excited PMPDI. Therefore, we can attribute the +50 mV shift in average V_{oc} after Co deposition to a 7-fold enhancement in the rate of recombination. We also tested the V_{oc} of SnO_2/Al_2O_3/PMPDI anodes, yielding an average of −0.07± 0.03 V vs Ag/AgCl. As described above, the Al_2O_3 tunneling barrier is expected to decrease the rates of all electron transfer processes at the interface, including both injection and recombination. Therefore, the −70 mV shift in V_{oc} of SnO_2/Al_2O_3/PMPDI anodes relative to SnO_2/PMPDI anodes suggests a 15-fold *decrease* in the rates of recombination relative to injection (though injection rate was also clearly decreased, given the reduced photocurrent, Sec. S4.7c).

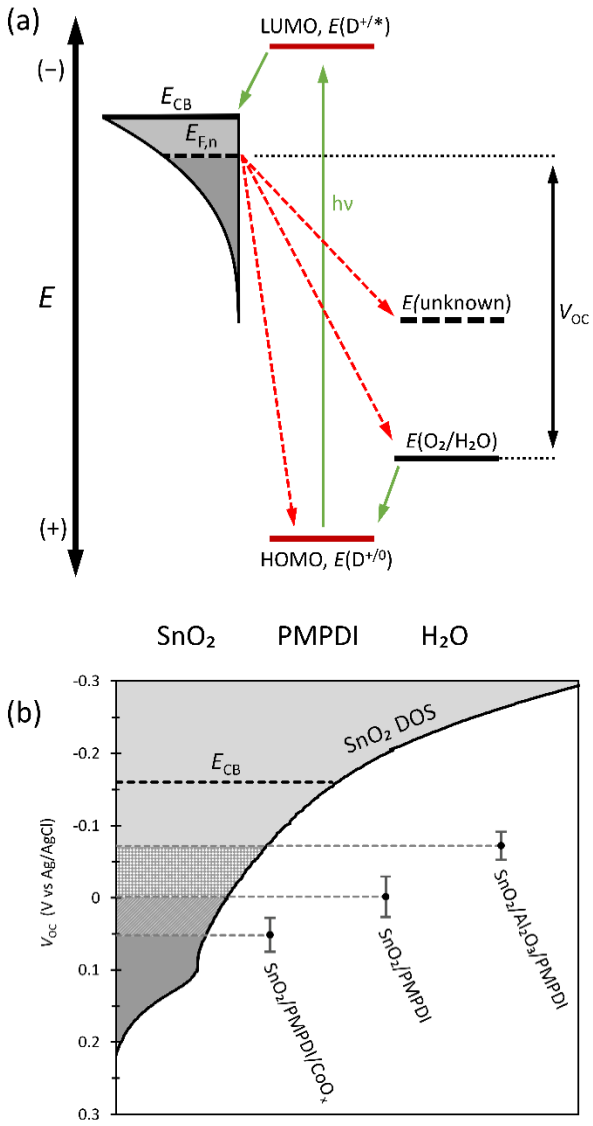

Figure 4.8 (a) Schematic diagram of the SnO_2/PMPDI DS-PEC studied herein. Green arrows indicate favorable charge transfer processes, while red arrows indicate unfavorable charge transfer processes. The theoretical V_{OC} of the photoanode is the difference between the thermodynamic potential for water oxidation ($E^0(O_2/H_2O)$) and the quasi-Fermi energy of electrons ($E_{F,n}$) (that is, the occupancy of SnO_2 sub-band gap states). The $E_{F,n}$ therefore depends on the relative rates SnO_2 state population (electron injection from excited PMPDI) and depopulation (all recombination reactions, including back-electron-transfer to the oxidized dye, reduction of O_2 or water oxidation intermediates, or any redox active impurities in the electrolyte). (b) Average V_{oc} values measured herein for several different cell configurations, overlayed with the SnO_2 density of states estimated by linear sweep voltammetry (Fig. S4.13). Error bars indicate the experimental standard deviation.

Insights for an Improved Device by Rational Placement of CoO_x. The above results provide clear direction for future experiments that may allow for the rational placement of CoO_x WOCatalyst, that is, as shown in Scheme 4.1A as opposed to 4.1B. First, we have already begun survey experiments to photoelectrochemically deposit CoO_x over a range of lower pH. Ideally, a range will be found where the SnO_2 surface is positively charged to *repel* Co(II), while the free phosphonate of adsorbed PMPDI remains negatively charged to *attract* Co(II). Alternatively, we are studying the effect of loading the SnO_2/PMPDI anode with pre-formed Co_3O_4 nanoparticles.[90] Initial results are similar to photo-deposited CoO_x, where the deposition of Co_3O_4 nanoparticles results in decreased photocurrent, like as a result of enhanced recombination from any Co_3O_4 nanoparticles loaded directly on the SnO_2 surface. Therefore, controlling the SnO_2 surface charge by pH surveys will be important for these studies as well. We will also study a precedented methods of decorating the catalyst nanoparticles with long anchor groups[91] or with dye molecules,[92] allowing for their attachment to the MO_x surface but retaining spatial separation to reduce the rate of recombination.

Alternatively, additional studies of Al_2O_3 overlayers may be of interest, but where deposition is attempted *after* dye loading but *before* catalyst loading, as recently done by Kamire *et al*.[16] by atomic layer deposition, which is expected to result in a more uniform overlayer film[93] than the solution-based methods employed in this study. This strategy of overlayer deposition *after* dye loading should not significantly decrease the injection efficiency from PMPDI, but still provide a tunneling barrier for subsequently deposited CoO_x catalyst. Finally, and as described above, we may explore methods to enhance the efficiency of charge injection, perhaps by using co-adsorbers to decrease dye aggregation, or by synthetically altering the dye structure to include conjugated anchor groups.

4.4 Conclusions

Our previous study[14] of a phosphonomethyl-substituted perylene diimide, PMPDI, used in an organic thin-film photoelectrochemical cell, confirmed that ITO/PMPDI/CoO_x anodes are capable of light-assisted water oxidation, but suffered from low light-harvesting efficiency and low charge-transport efficiency (pronounced recombination).[14] In the present study, we applied that same PMPDI dye in an alternative DS-PEC architectures. We first prepared nano-MO_x films of TiO_2, SnO_2, and WO_3 from commercial starting materials, or by literature methods, and characterized the films by a variety of physical methods. We found that the kinetics and saturation of PMPDI adsorption onto the surface of nano-MO_x films decreased in the order TiO_2 > SnO_2 > WO_3, consistent with the decreasing isoelectric points (increasing acidity of the MO_x surfaces) in that order. In fact, the acidic phosphonate anchor groups of PMPDI were not able to bind to the highly acidic WO_3 surface at all.

The loading of PMPDI onto TiO_2 proved more facile than onto SnO_2. However, photocurrent measured in the presence of hydroquinone sacrificial reductant are much lower on TiO_2 than on SnO_2, consistent with poor injection efficiency from the LUMO of PMPDI into the more negative conduction band of TiO_2. Hence, SnO_2 was chosen for optimization studies. SnO_2 film thickness and dying conditions were optimized to achieve >99% light-harvesting efficiency at the λ_{max} of PMPDI on ~6 μm-thick films. Photocurrent of ~1,100 μA/cm² is typical for optimized SnO_2/PMPDI films in pH 7 buffer in the presence of hydroquinone.

In the absence of hydroquinone and before depositing a water-oxidation catalyst, SnO_2/PMPDI anodes still exhibit photocurrent that decays from ~40 to 20 μA/cm² over 5 min. However, O_2 detection experiments by a Generator–Collector method revealed that such currents do not originate from water oxidation. Furthermore, an approximation of the dye concentration on

SnO_2 indicates that a significant portion of photolysis current cannot correspond to degradative oxidation of PMPDI. All attempts to load CoO_x water-oxidation catalyst by photoelectrochemical deposition from $Co(NO_3)_2$ have resulted in decreased photocurrent. Controls and open-circuit photovoltage measurements are consistent with enhanced recombination in the presence of CoO_x, due to catalyst adsorbed directly to the SnO_2 surface intercepting conduction band electrons. Although our goal of a water-oxidizing SnO_2/PMPDI/CoO_x DS-PEC has yet to be realized, the present studies have yielded several readily testable hypotheses for the rational preparation of a successful device. Additional studies of a now third-generation device are now under way.

REFERENCES

(1) Lewis, N. S.; Nocera, D. G. Powering the Planet: Chemical Challenges in Solar Energy Utilization. *Proc. Natl. Acad. Sci. U. S. A.* **2006**, *103*, 15729–15735.

(2) Bard, A. J.; Whitesides, G. M.; Zare, R. N.; McLafferty, F. W. Holy Grails of Chemistry. *Acc. Chem. Res.* **1995**, *28*, 91–91.

(3) Bard, A. J.; Fox, M. A. Artificial Photosynthesis: Solar Splitting of Water to Hydrogen and Oxygen. *Acc. Chem. Res.* **1995**, *28*, 141–145.

(4) Kirner, J. T.; Finke, R. G. Water-Oxidation Photoanodes Using Organic Light-Harvesting Materials: A Review. **2017**, *Submitted to Energy and Environmental Science*, *Feb 2017*.

(5) Abe, T.; Nagai, K.; Kabutomori, S.; Kaneko, M.; Tajiri, A.; Norimatsu, T. An Organic Photoelectrode Working in the Water Phase: Visible-Light-Induced Dioxygen Evolution by a Perylene Derivative/Cobalt Phthalocyanine Bilayer. *Angew. Chem. Int. Ed.* **2006**, *45*, 2778–2781.

(6) Abe, T.; Nagai, K.; Ogiwara, T.; Ogasawara, S.; Kaneko, M.; Tajiri, A.; Norimatsu, T. Wide Visible Light-Induced Dioxygen Evolution at an Organic Photoanode Coated with a Noble Metal Oxide Catalyst. *J. Electroanal. Chem.* **2006**, *587*, 127–132.

(7) Moore, G. F.; Blakemore, J. D.; Milot, R. L.; Hull, J. F.; Song, H.; Cai, L.; Schmuttenmaer, C. A.; Crabtree, R. H.; Brudvig, G. W. A Visible Light Water-Splitting Cell with a Photoanode Formed by Codeposition of a High-Potential Porphyrin and an Iridium Water-Oxidation Catalyst. *Energy Environ. Sci.* **2011**, *4*, 2389–2392.

(8) Chen, J.; Wagner, P.; Tong, L.; Wallace, G. G.; Officer, D. L.; Swiegers, G. F. A Porphyrin-Doped Polymer Catalyzes Selective, Light-Assisted Water Oxidation in Seawater. *Angew. Chem.* **2012**, *124*, 1943–1946.

(9) Swierk, J. R.; Méndez-Hernández, D. D.; McCool, N. S.; Liddell, P.; Terazono, Y.; Pahk, I.; Tomlin, J. J.; Oster, N. V.; Moore, T. A.; Moore, A. L.; *et al.* Metal-Free Organic Sensitizers for Use in Water-Splitting Dye-Sensitized Photoelectrochemical Cells. *Proc. Natl. Acad. Sci.* **2015**, *112*, 1681–1686.

(10) Yamamoto, M.; Wang, L.; Li, F.; Fukushima, T.; Tanaka, K.; Sun, L.; Imahori, H. Visible Light-Driven Water Oxidation Using a Covalently-Linked Molecular Catalyst–Sensitizer Dyad Assembled on a TiO_2 Electrode. *Chem. Sci.* **2016**, *7*, 1430–1439.

(11) Yamamoto, M.; Nishizawa, Y.; Chábera, P.; Li, F.; Pascher, T.; Sundström, V.; Sun, L.; Imahori, H. Visible Light-Driven Water Oxidation with a Subporphyrin Sensitizer and a Water Oxidation Catalyst. *Chem. Commun.* **2016**, *52*, 13702–13705.

(12) Cheng, Y.; Memar, A.; Saunders, M.; Pan, J.; Liu, C.; Gale, J. D.; Demichelis, R.; Shen, P. K.; Jiang, S. P. Dye Functionalized Carbon Nanotubes for Photoelectrochemical Water Splitting – Role of Inner Tubes. *J. Mater. Chem. A* **2016**, *4*, 2473–2483.

(13) Liu, G.; Chen, C.; Ji, H.; Ma, W.; Zhao, J. Photo-Electrochemical Water Splitting System with Three-Layer n-Type Organic Semiconductor Film as Photoanode under Visible Irradiation. *Sci. China Chem.* **2012**, *55*, 1953–1958.

(14) Kirner, J. T.; Stracke, J. J.; Gregg, B. A.; Finke, R. G. Visible-Light-Assisted Photoelectrochemical Water Oxidation by Thin Films of a Phosphonate-Functionalized Perylene Diimide Plus CoO_x Cocatalyst. *ACS Appl. Mater. Interfaces* **2014**, *6*, 13367–13377. http://pubs.acs.org/doi/abs/10.1021/am405598w.

(15) Ronconi, F.; Syrgiannis, Z.; Bonasera, A.; Prato, M.; Argazzi, R.; Caramori, S.; Cristino, V.; Bignozzi, C. A. Modification of Nanocrystalline WO_3 with a Dicationic Perylene Bisimide: Applications to Molecular Level Solar Water Splitting. *J. Am. Chem. Soc.* **2015**, *137*, 4630–4633.

(16) Kamire, R. J.; Materna, K. L.; Hoffeditz, W. L.; Phelan, B. T.; Thomsen, J. M.; Farha, O. K.; Hupp, J. T.; Brudvig, G. W.; Wasielewski, M. R. Photodriven Oxidation of Surface-Bound Iridium-Based Molecular Water-Oxidation Catalysts on Perylene-3,4-Dicarboximide-Sensitized TiO_2 Electrodes Protected by an Al_2O_3 Layer. *J. Phys. Chem. C* **2017**, *121*, 3752–3764.

(17) Li, F.; Fan, K.; Xu, B.; Gabrielsson, E.; Daniel, Q.; Li, L.; Sun, L. An Organic Dye-Sensitized Tandem Photoelectrochemical Cell for Light Driven Water Splitting. *J. Am. Chem. Soc.* **2015**.

(18) Wee, K.-R.; Sherman, B. D.; Brennaman, M. K.; Sheridan, M. V.; Nayak, A.; Alibabaei, L.; Meyer, T. J. An Aqueous, Organic Dye Derivatized SnO_2/TiO_2 Core/Shell Photoanode. *J. Mater. Chem. A* **2016**, *4*, 2969–2975.

(19) Bledowski, M.; Wang, L.; Ramakrishnan, A.; Bétard, A.; Khavryuchenko, O. V.; Beranek, R. Visible-Light Photooxidation of Water to Oxygen at Hybrid TiO_2–Polyheptazine Photoanodes with Photodeposited Co-Pi (CoO_x) Cocatalyst. *ChemPhysChem* **2012**, *13*, 3018–3024.

(20) Wang, Z.; Xiao, P.; Qiao, L.; Meng, X.; Zhang, Y.; Li, X.; Yang, F. Polypyrrole Sensitized ZnO Nanorod Arrays for Efficient Photo-Electrochemical Splitting of Water. *Phys. B Condens. Matter* **2013**, *419*, 51–56.

(21) Gustafson, M. P.; Clark, N.; Winther-Jensen, B.; MacFarlane, D. R. Organic Photovoltaic Structures as Photo-Active Electrodes. *Electrochimica Acta* **2014**, *140*, 309–313.

(22) Bornoz, P.; Prevot, M. S.; Yu, X.; Guijarro, N.; Sivula, K. Direct Light-Driven Water Oxidation by a Ladder-Type Conjugated Polymer Photoanode. *J. Am. Chem. Soc.* **2015**.

(23) Caramori, S.; Cristino, V.; Meda, L.; Argazzi, R.; Bignozzi, C. A. Hydrogen Production with Nanostructured and Sensitized Metal Oxides. *Top. Curr. Chem.* **2011**, *303*, 39–94.

(24) Young, K. J.; Martini, L. A.; Milot, R. L.; Snoeberger, R. C.; Batista, V. S.; Schmuttenmaer, C. A.; Crabtree, R. H.; Brudvig, G. W. Light-Driven Water Oxidation for Solar Fuels. *Coord. Chem. Rev.* **2012**, *256*, 2503–2520.

(25) Alibabaei, L.; Luo, H.; House, R. L.; Hoertz, P. G.; Lopez, R.; Meyer, T. J. Applications of Metal Oxide Materials in Dye Sensitized Photoelectrosynthesis Cells for Making Solar Fuels: Let the Molecules Do the Work. *J. Mater. Chem. A* **2013**, *1*, 4133–4145.

(26) Swierk, J. R.; Mallouk, T. E. Design and Development of Photoanodes for Water-Splitting Dye-Sensitized Photoelectrochemical Cells. *Chem. Soc. Rev.* **2013**, *42*, 2357–2387.

(27) Ashford, D. L.; Gish, M. K.; Vannucci, A. K.; Brennaman, M. K.; Templeton, J. L.; Papanikolas, J. M.; Meyer, T. J. Molecular Chromophore–Catalyst Assemblies for Solar Fuel Applications. *Chem. Rev.* **2015**, *115*, 13006–13049.

(28) Yu, Z.; Li, F.; Sun, L. Recent Advances in Dye-Sensitized Photoelectrochemical Cells for Solar Hydrogen Production Based on Molecular Components. *Energy Environ. Sci.* **2015**, *8*, 760–775.

(29) Yamamoto, M.; Tanaka, K. Artificial Molecular Photosynthetic Systems: Towards Efficient Photoelectrochemical Water Oxidation. *ChemPlusChem* **2016**, *81*, 1028–1044.

(30) Vagnini, M. T.; Smeigh, A. L.; Blakemore, J. D.; Eaton, S. W.; Schley, N. D.; D'Souza, F.; Crabtree, R. H.; Brudvig, G. W.; Co, D. T.; Wasielewski, M. R. Ultrafast Photodriven Intramolecular Electron Transfer from an Iridium-Based Water-Oxidation Catalyst to Perylene Diimide Derivatives. *Proc. Natl. Acad. Sci. U. S. A.* **2012**, *109*, 15651–15656.

(31) Chen, S.; Jacobs, D. L.; Xu, J.; Li, Y.; Wang, C.; Zang, L. 1D Nanofiber Composites of Perylene Diimides for Visible-Light-Driven Hydrogen Evolution from Water. *RSC Adv.* **2014**, *4*, 48486–48491.

(32) Kunz, V.; Stepanenko, V.; Würthner, F. Embedding of a Ruthenium(II) Water Oxidation Catalyst into Nanofibers via Self-Assembly. *Chem. Commun.* **2014**, *51*, 290–293.

(33) Weingarten, A. S.; Kazantsev, R. V.; Palmer, L. C.; McClendon, M.; Koltonow, A. R.; Samuel, A. P. S.; Kiebala, D. J.; Wasielewski, M. R.; Stupp, S. I. Self-Assembling Hydrogel Scaffolds for Photocatalytic Hydrogen Production. *Nat. Chem.* **2014**, *6*, 964–970.

(34) Chen, S.; Wang, C.; Bunes, B. R.; Li, Y.; Wang, C.; Zang, L. Enhancement of Visible-Light-Driven Photocatalytic H_2 Evolution from Water over g-C_3N_4 through Combination with Perylene Diimide Aggregates. *Appl. Catal. Gen.* **2015**, *498*, 63–68.

(35) Li, J.-X.; Li, Z.-J.; Ye, C.; Li, X.-B.; Zhan, F.; Fan, X.-B.; Li, J.; Chen, B.; Tao, Y.; Tung, C.-H.; *et al.* Visible Light-Induced Photochemical Oxygen Evolution from Water by 3,4,9,10-Perylenetetracarboxylic Dianhydride Nanorods as an N-Type Organic Semiconductor. *Catal. Sci. Technol.* **2016**, *6*, 672–676.

(36) Liu, D.; Wang, J.; Bai, X.; Zong, R.; Zhu, Y. Self-Assembled PDINH Supramolecular System for Photocatalysis under Visible Light. *Adv. Mater.* **2016**, *28*, 7284–7290.

(37) Sun, T.; Song, J.; Jia, J.; Li, X.; Sun, X. Real Roles of Perylenetetracarboxylic Diimide for Enhancing Photocatalytic H_2-Production. *Nano Energy* **2016**, *26*, 83–89.

(38) Wang, J.; Shi, W.; Liu, D.; Zhang, Z.; Zhu, Y.; Wang, D. Supramolecular Organic Nanofibers with Highly Efficient and Stable Visible Light Photooxidation Performance. *Appl. Catal. B Environ.* **2017**, *202*, 289–297.

(39) Rawls, M. T.; Johnson, J.; Gregg, B. A. Coupling One Electron Photoprocesses to Multielectron Catalysts: Towards a Photoelectrocatalytic System. *J. Electroanal. Chem.* **2010**, *650*, 10–15.

(40) Abe, T.; Chiba, J.; Ishidoya, M.; Nagai, K. Organophotocatalysis System of p/n Bilayers for Wide Visible-Light-Induced Molecular Hydrogen Evolution. *RSC Adv.* **2012**, *2*, 7992–7996.

(41) Balapanuru, J.; Chiu, G.; Su, C.; Zhou, N.; Hai, Z.; Xu, Q.; Loh, K. P. Photoactive PDI–Cobalt Complex Immobilized on Reduced Graphene Oxide for Photoelectrochemical Water Splitting. *ACS Appl. Mater. Interfaces* **2015**, *7*, 880–886.

(42) Ferrere, S.; Zaban, A.; Gregg, B. A. Dye Sensitization of Nanocrystalline Tin Oxide by Perylene Derivatives. *J. Phys. Chem. B* **1997**, *101*, 4490–4493.

(43) Brennaman, M. K.; Norris, M. R.; Gish, M. K.; Grumstrup, E. M.; Alibabaei, L.; Ashford, D. L.; Lapides, A. M.; Papanikolas, J. M.; Templeton, J. L.; Meyer, T. J. Ultrafast, Light-Induced Electron Transfer in a Perylene Diimide Chromophore-Donor Assembly on TiO_2. *J. Phys. Chem. Lett.* **2015**, *6*, 4736–4742.

(44) Chen, H.-C.; Williams, R. M.; Reek, J. N. H.; Brouwer, A. M. Robust Benzo[ghi]perylenetriimide Dye-Sensitized Electrodes in Air-Saturated Aqueous Buffer Solution. *Chem. - Eur. J.* **2016**, *22*, 5489–5493.

(45) Lindquist, R. J.; Phelan, B. T.; Reynal, A.; Margulies, E. A.; Shoer, L. E.; Durrant, J. R.; Wasielewski, M. R. Strongly Oxidizing Perylene-3,4-Dicarboximides for Use in Water Oxidation Photoelectrochemical Cells. *J. Mater. Chem. A* **2016**, *4*, 2880–2893.

(46) Ichinose, I.; Senzu, H.; Kunitake, T. Stepwise Adsorption of Metal Alkoxides on Hydrolyzed Surfaces : A Surface Sol-Gel Process. *Chem. Lett.* **1996**, *25*, 831–832.

(47) Liberatore, M.; Burtone, L.; Brown, T. M.; Reale, A.; Carlo, A. D.; Decker, F.; Caramori, S.; Bignozzi, C. A. On the Effect of Al_2O_3 Blocking Layer on the Performance of Dye Solar Cells with Cobalt Based Electrolytes. *Appl. Phys. Lett.* **2009**, *94*, 173113.

(48) Zhao, Y.; Swierk, J. R.; Megiatto, J. D.; Sherman, B.; Youngblood, W. J.; Qin, D.; Lentz, D. M.; Moore, A. L.; Moore, T. A.; Gust, D.; *et al.* Improving the Efficiency of Water Splitting in Dye-Sensitized Solar Cells by Using a Biomimetic Electron Transfer Mediator. *Proc. Natl. Acad. Sci. U. S. A.* **2012**, *109*, 15612–15616.

(49) Ashford, D. L.; Sherman, B. D.; Binstead, R. A.; Templeton, J. L.; Meyer, T. J. Electro-assembly of a Chromophore–Catalyst Bilayer for Water Oxidation and Photocatalytic Water Splitting. *Angew. Chem.* **2015**, *127*, 4860–4863.

(50) Swierk, J. R.; McCool, N. S.; Saunders, T. P.; Barber, G. D.; Strayer, M. E.; Vargas-Barbosa, N. M.; Mallouk, T. E. Photovoltage Effects of Sintered IrO_2 Nanoparticle Catalysts in Water-Splitting Dye-Sensitized Photoelectrochemical Cells. *J. Phys. Chem. C* **2014**, *118*, 17046–17053.

(51) Meda, L.; Tozzola, G.; Tacca, A.; Marra, G.; Caramori, S.; Cristino, V.; Bignozzi, C. A. Photo-Electrochemical Properties of Nanostructured WO_3 Prepared with Different Organic Dispersing Agents. *Sol. Energy Mater. Sol. Cells* **2010**, *94*, 788–796.

(52) Scherrer, P. Bestimmung der Größe und der inneren Struktur von Kolloidteilchen mittels Röntgenstrahlen. *Nachrichten Von Ges. Wiss. Zu Gött. Math.-Phys. Kl.* **1918**, *1918*, 98–100.

(53) Santato, C.; Odziemkowski, M.; Ulmann, M.; Augustynski, J. Crystallographically Oriented Mesoporous WO_3 Films: Synthesis, Characterization, and Applications. *J. Am. Chem. Soc.* **2001**, *123*, 10639–10649.

(54) Beranek, R. (Photo)electrochemical Methods for the Determination of the Band Edge Positions of TiO_2-Based Nanomaterials. *Adv. Phys. Chem.* **2011**, *2011*, 1–20.

(55) Ardo, S.; Meyer, G. J. Photodriven Heterogeneous Charge Transfer with Transition-Metal Compounds Anchored to TiO_2 Semiconductor Surfaces. *Chem. Soc. Rev.* **2009**, *38*, 115–164.

(56) Kanan, M. W.; Nocera, D. G. In Situ Formation of an Oxygen-Evolving Catalyst in Neutral Water Containing Phosphate and Co^{2+}. *Science* **2008**, *321*, 1072–1075.

(57) Ford, W. E. Photochemistry of 3,4,9,10-Perylenetetracarboxylic Dianhydride Dyes: Visible Absorption and Fluorescence of the Di(glycyl)imide Derivative Monomer and Dimer in Basic Aqueous Solutions. *J. Photochem.* **1987**, *37*, 189–204.

(58) Chen, Z.; Stepanenko, V.; Dehm, V.; Prins, P.; Siebbeles, L. D. A.; Seibt, J.; Marquetand, P.; Engel, V.; Würthner, F. Photoluminescence and Conductivity of Self-Assembled $\pi-\pi$ Stacks of Perylene Bisimide Dyes. *Chem. – Eur. J.* **2007**, *13*, 436–449.

(59) Gallaher, J. K.; Aitken, E. J.; Keyzers, R. A.; Hodgkiss, J. M. Controlled Aggregation of Peptide-Substituted Perylene-Bisimides. *Chem. Commun.* **2012**, *48*, 7961–7963.

(60) Kay, A.; Grätzel, M. Dye-Sensitized Core−Shell Nanocrystals: Improved Efficiency of Mesoporous Tin Oxide Electrodes Coated with a Thin Layer of an Insulating Oxide. *Chem. Mater.* **2002**, *14*, 2930–2935.

(61) Parks, G. A. The Isoelectric Points of Solid Oxides, Solid Hydroxides, and Aqueous Hydroxo Complex Systems. *Chem. Rev.* **1965**, *65*, 177–198.

(62) Kosmulski, M. The pH-Dependent Surface Charging and the Points of Zero Charge. *J. Colloid Interface Sci.* **2002**, *253*, 77–87.

(63) Kosmulski, M. pH-Dependent Surface Charging and Points of Zero Charge II. Update. *J. Colloid Interface Sci.* **2004**, *275*, 214–224.

(64) Fukai, Y.; Kondo, Y.; Mori, S.; Suzuki, E. Highly Efficient Dye-Sensitized SnO_2 Solar Cells Having Sufficient Electron Diffusion Length. *Electrochem. Commun.* **2007**, *9*, 1439–1443.

(65) Reference Solar Spectral Irradiance: Air Mass 1.5 http://rredc.nrel.gov/solar/spectra/am1.5/ (accessed Dec 8, 2016).

(66) Abe, T.; Nagai, K.; Matsukawa, T.; Tajiri, A.; Norimatsu, T. Photoelectrode Characteristics of an Organic Bilayer in Water Phase Containing a Redox Molecule. *J. Solid State Electrochem.* **2007**, *11*, 303–309.

(67) Lee, J.; Kwak, J.; Ko, K. C.; Park, J. H.; Ko, J. H.; Park, N.; Kim, E.; Ryu, D. H.; Ahn, T. K.; Lee, J. Y.; *et al.* Phenothiazine-Based Organic Dyes with Two Anchoring Groups on TiO_2 for Highly Efficient Visible Light-Induced Water Splitting. *Chem. Commun.* **2012**, *48*, 11431–11433.

(68) Durrell, A. C.; Li, G.; Koepf, M.; Young, K. J.; Negre, C. F. A.; Allen, L. J.; McNamara, W. R.; Song, H.; Batista, V. S.; Crabtree, R. H.; *et al.* Photoelectrochemical Oxidation of a Turn-on Fluorescent Probe Mediated by a Surface Mn^{II} Catalyst Covalently Attached to TiO_2 Nanoparticles. *J. Catal.* **2014**, *310*, 37–44.

(69) Memming, R.; Möllers, F. Two-Step Redox Processes with Quinones at Semiconductor Electrodes. *Berichte Bunsenges. Für Phys. Chem.* **1972**, *76*, 609–616.

(70) Frank, S. N.; Bard, A. J. Semiconductor Electrodes. 12. Photoassisted Oxidations and Photoelectrosynthesis at Polycrystalline Titanium Dioxide Electrodes. *J. Am. Chem. Soc.* **1977**, *99*, 4667–4675.

(71) Walter, M. G.; Warren, E. L.; McKone, J. R.; Boettcher, S. W.; Mi, Q.; Santori, E. A.; Lewis, N. S. Solar Water Splitting Cells. *Chem. Rev.* **2010**, *110*, 6446–6473.

(72) Mishra, A.; Fischer, M. K. R.; Bäuerle, P. Metal-Free Organic Dyes for Dye-Sensitized Solar Cells: From Structure: Property Relationships to Design Rules. *Angew. Chem. Int. Ed.* **2009**, *48*, 2474–2499.

(73) Hagfeldt, A.; Boschloo, G.; Sun, L.; Kloo, L.; Pettersson, H. Dye-Sensitized Solar Cells. *Chem. Rev.* **2010**, *110*, 6595–6663.

(74) Giribabu, L.; Kanaparthi, R. K.; Velkannan, V. Molecular Engineering of Sensitizers for Dye-Sensitized Solar Cell Applications. *Chem. Rec.* **2012**, *12*, 306–328.

(75) Green, A. N. M.; Palomares, E.; Haque, S. A.; Kroon, J. M.; Durrant, J. R. Charge Transport versus Recombination in Dye-Sensitized Solar Cells Employing Nanocrystalline TiO_2 and SnO_2 Films. *J. Phys. Chem. B* **2005**, *109*, 12525–12533.

(76) Knauf, R. R.; Brennaman, M. K.; Alibabaei, L.; Norris, M. R.; Dempsey, J. L. Revealing the Relationship Between Semiconductor Electronic Structure and Electron Transfer Dynamics at Metal Oxide–Chromophore Interfaces. *J. Phys. Chem. C* **2013**, *117*, 25259–25268.

(77) Prasittichai, C.; Hupp, J. T. Surface Modification of SnO_2 Photoelectrodes in Dye-Sensitized Solar Cells: Significant Improvements in Photovoltage via Al_2O_3 Atomic Layer Deposition. *J. Phys. Chem. Lett.* **2010**, *1*, 1611–1615.

(78) Guo, J.; She, C.; Lian, T. Effect of Insulating Oxide Overlayers on Electron Injection Dynamics in Dye-Sensitized Nanocrystalline Thin Films. *J. Phys. Chem. C* **2007**, *111*, 8979–8987.

(79) Asbury, J. B.; Hao, E.; Wang, Y.; Lian, T. Bridge Length-Dependent Ultrafast Electron Transfer from Re Polypyridyl Complexes to Nanocrystalline TiO_2 Thin Films Studied by Femtosecond Infrared Spectroscopy. *J. Phys. Chem. B* **2000**, *104*, 11957–11964.

(80) Vandermolen, J.; Gomes, W. P.; Cardon, F. Investigation on the Kinetics of Electroreduction Processes at Dark TiO_2 and $SrTiO_3$ Single Crystal Semiconductor Electrodes. *J. Electrochem. Soc.* **1980**, *127*, 324–328.

(81) Salvador, P.; Gutiérrez, C. Mechanisms of Charge Transfer at the Semiconductor-Electrolyte Interface I. Kinetics of Electroreduction at Dark of $Fe(CN)_6^{3-}$ and $IrCl_6^{2-}$ in Aqueous Solution on a Sintered Nb-doped n-$SrTiO_3$ Electrode: Influence of pH. *J. Electrochem. Soc.* **1984**, *131*, 326–336.

(82) Bisquert, J.; Zaban, A.; Salvador, P. Analysis of the Mechanisms of Electron Recombination in Nanoporous TiO_2 Dye-Sensitized Solar Cells. Nonequilibrium Steady-State Statistics and Interfacial Electron Transfer via Surface States. *J. Phys. Chem. B* **2002**, *106*, 8774–8782.

(83) Ondersma, J. W.; Hamann, T. W. Measurements and Modeling of Recombination from Nanoparticle TiO_2 Electrodes. *J. Am. Chem. Soc.* **2011**, *133*, 8264–8271.

(84) McCool, N. S.; Swierk, J. R.; Nemes, C. T.; Saunders, T. P.; Schmuttenmaer, C. A.; Mallouk, T. E. Proton-Induced Trap States, Injection and Recombination Dynamics in Water-Splitting Dye-Sensitized Photoelectrochemical Cells. *ACS Appl. Mater. Interfaces* **2016**, *8*, 16727–16735.

(85) Swierk, J. R.; McCool, N. S.; Saunders, T. P.; Barber, G. D.; Mallouk, T. E. Effects of Electron Trapping and Protonation on the Efficiency of Water-Splitting Dye-Sensitized Solar Cells. *J. Am. Chem. Soc.* **2014**, *136*, 10974–10982.

(86) Bledowski, M.; Wang, L.; Ramakrishnan, A.; Khavryuchenko, O. V.; Khavryuchenko, V. D.; Ricci, P. C.; Strunk, J.; Cremer, T.; Kolbeck, C.; Beranek, R. Visible-Light Photocurrent Response of TiO_2–Polyheptazine Hybrids: Evidence for Interfacial Charge-Transfer Absorption. *Phys. Chem. Chem. Phys.* **2011**, *13*, 21511–21519.

(87) Poddutoori, P. K.; Thomsen, J. M.; Milot, R. L.; Sheehan, S. W.; Negre, C. F. A.; Garapati, V. K. R.; Schmuttenmaer, C. A.; Batista, V. S.; Brudvig, G. W.; van der Est, A. Interfacial Electron Transfer in Photoanodes Based on phosphorus(V) Porphyrin Sensitizers Co-Deposited on SnO_2 with the Ir(III)Cp* Water Oxidation Precatalyst. *J. Mater. Chem. A* **2015**, *3*, 3868–3879.

(88) Gao, Y.; Zhang, L.; Ding, X.; Sun, L. Artificial Photosynthesis – Functional Devices for Light Driven Water Splitting with Photoactive Anodes Based on Molecular Catalysts. *Phys. Chem. Chem. Phys.* **2014**, *16*, 12008–12013.

(89) Jencks, W. P.; Regenstein, J. Ionization Constants of Acids and Bases. In *Handbook of Biochemistry and Molecular Biology*; Lundblad, R. L.; Macdonald, F., Eds.; Taylor & Francis Group, LLC: New York, 2010; pp. 305–351.

(90) Grzelczak, M.; Zhang, J.; Pfrommer, J.; Hartmann, J.; Driess, M.; Antonietti, M.; Wang, X. Electro- and Photochemical Water Oxidation on Ligand-Free Co_3O_4 Nanoparticles with Tunable Sizes. *ACS Catal.* **2013**, *3*, 383–388.

(91) Wei, P.; Hu, B.; Zhou, L.; Su, T.; Na, Y. New Strategy to Incorporate Nano-Particle Sized Water Oxidation Catalyst into Dye-Sensitized Photoelectrochemical Cell for Water Splitting. *J. Energy Chem.* **2016**, *25*, 345–348.

(92) Youngblood, W. J.; Lee, S.-H. A.; Kobayashi, Y.; Hernandez-Pagan, E. A.; Hoertz, P. G.; Moore, T. A.; Moore, A. L.; Gust, D.; Mallouk, T. E. Photoassisted Overall Water Splitting in a Visible Light-Absorbing Dye-Sensitized Photoelectrochemical Cell. *J. Am. Chem. Soc.* **2009**, *131*, 926–927.

(93) van Delft, J. A.; Garcia-Alonso, D.; Kessels, W. M. M. Atomic Layer Deposition for Photovoltaics: Applications and Prospects for Solar Cell Manufacturing. *Semicond. Sci. Technol.* **2012**, *27*, 074002.

V. ARE HIGH-POTENTIAL COBALT TRIS(BIPYRIDYL) COMPLEXES SUFFICIENTLY STABLE TO BE EFFICIENT MEDIATORS IN DYE-SENSITIZED SOLAR CELLS? SYNTHESIS, CHARACTERIZATION, AND STABILITY TESTS[iv]

Overview

We report the synthesis of three new, high-oxidation-potential cobalt complexes. The ligand lability of cobalt complexes, especially those of higher redox potential, has been scantly addressed in the current literature on the use of these complexes in dye-sensitized solar cells (DSSCs). In characterizing our high-potential complexes, multiple pieces of evidence reveal a trend of decreasing complex stability with increasing redox potential. These include the appearance of multiple waves in the cyclic voltammetry, a color change upon addition of 4-*tert*-butylpyridine indicating the formation of a new species, direct NMR evidence of free dissociated ligand in acetonitrile solution, and potential-independent DSSC recombination currents paralleling the stability trends as determined by NMR. We take advantage of a simple quantitative NMR experiment to determine the approximate ligand-binding equilibrium (stability) constants of our complexes in acetonitrile at room temperature. With the above information, we

[iv] This chapter describes work done on a secondary project from the previous Chapters II–IV, concerned with the study of dye-sensitized solar cells for solar energy capture and its conversion into *electrical energy* rather than its storage in the chemical bonds of solar fuels. The work was done under the advisorship of Prof. C. Michael Elliott. This chapter includes the complete published manuscript (Kirner, J. T.; Elliott, C. M. *J. Phys. Chem. C* **2015**, *119*, 17502-17514. http://pubs.acs.org/doi/full/10.1021/acs.jpcc.5b02513.) which was completed after the untimely death of Prof. Elliott in July of 2014. This article is reproduced with permission, and only minor changes have been made to meet dissertation formatting requirements. For example, table and figure numbers have been changed to indicate that they are specific to this chapter, and Supporting Information have been moved to Appendix III.

propose alternative, clathrochelating ligand structures for the future study of high potential cobalt mediators for application in DSSCs.

5.1 Introduction

Since their inception in 1985, dye-sensitized solar cells (DSSCs) have been identified as a promising alternative technology for solar energy conversion when compared to conventional, inorganic, solid-state devices.[1] This promise stems from the DSSC's potential for cheap commercialization while still achieving relatively high conversion efficiencies.[2,3] To date, a large proportion of DSSC research has focused on the relationships between the structure of the dye employed and the corresponding charge-transfer reactions and overall cell performance.[4–7] Such studies have led to a strong understanding of dye-related processes and the engineering of dye molecules to gradually improve the efficiencies of DSSCs, reaching absorbed photon-to-current conversion efficiencies of nearly 100%. To continue optimizing DSSCs, it has become evident that research needs to focus on other aspects of the DSSC,[8–11] one important example being the need to study alternative redox mediators for regeneration of the oxidized dye.

Traditional DSSCs have almost exclusively employed iodide/triiodide as the redox couple. The success of I^-/I_3^- has been attributed to its fast dye regeneration kinetics,[4] combined with its slow recombination reaction with TiO_2 conduction band electrons.[12] However, I^-/I_3^- possesses a number of unfavorable qualities. Arguably the most significant of these is that its redox potential (+0.11 V vs saturated sodium calomel electrode, SSCE)[4] is not ideally positioned for many sensitizers, leading to a significant loss in the maximum open-circuit potential (V_{oc}) and a corresponding loss in the maximum overall efficiency of the cell. In 2001, researchers found that cobalt complexes could exhibit DSSC operating kinetics that were comparable to those of I^-/I_3^-.[13]

Since that time, many new cobalt complexes have been successfully employed as DSSC mediators, with several examples summarized in a recent review by Hamann.[10] Notably, the current top-performing DSSC uses the $[Co(bpy)_3]^{2+/3+}$redox couple as the dye-regenerating mediator.[14]

Cobalt complexes are particularly promising mediator alternatives for several reasons. They tend to be less colored than iodide solutions, and therefore compete less with the dye for visible light absorption. Unlike I^-/I_3^-, cobalt complexes are nonvolatile and noncorrosive to metal cathodes. Perhaps most interesting to chemists is the fact that cobalt mediators have synthetically tunable redox potentials, which makes them particularly promising for fundamental structure/function studies. It is in the interest of the DSSC community to have a library of available cobalt complexes with varying redox potentials. For example, when researching novel dyes or semiconductors, one could select a mediator with optimal driving force for dye regeneration based on the dye's redox potential.[15] Mediators with more positive redox potentials relative to I^-/I_3^- are of particular interest in maximizing the V_{oc} of DSSCs.

Herein, we report three new cobalt complexes, shown in Figure 5.1, employing ligands with multiple electron-withdrawing groups in order to positively shift the redox potentials of the complexes. While cobalt complexes containing ligands with ester and amide groups have been

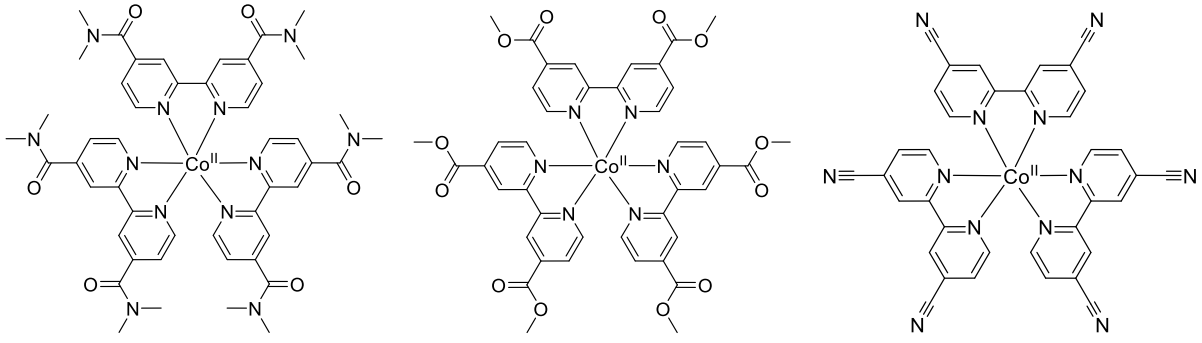

Figure 5.1 Structures of the three new cobalt mediator complexes studied (from left to right): $[Co(dma\text{-}bpy)_3]^{2+}$, $[Co(me\text{-}bpy)_3]^{2+}$, and $[Co(cn\text{-}bpy)_3]^{2+}$ (dma-bpy = 2,2'-bipyridine-4,4'-bis(N,N-dimethylcarboxamide), me-bpy = 2,2'-bipyridine-4,4'-bis(methylester), cn-bpy = 2,2'-bipyridine-4,4'-dicarbonitrile).

previously studied,[16] we targeted these ligands with shorter alkyl groups with the goal of minimizing the impact of mass transport-limited photocurrent.[17]

It is important to note that, when employing ligands with strong electron withdrawing groups, the complex stability may be expected to decrease; withdrawing electron density from the lone pair of electrons on the bipyridine nitrogen atoms is expected to make the ligand a weaker σ-donor (Lewis base), and possibly more labile. However, the electron-withdrawing groups could also make the ligands stronger π-acceptors, so the effects on the complexes' stabilities are not easily predictable. In short, while it is desirable to study high-potential cobalt mediator complexes, it is equally important to test their stabilities. Hence, herein we both prepare and characterize three new high-potential cobalt complexes, determine approximate stability constants by a straightforward, semiquantitative NMR experiment, and relate dark current trends observed in assembled DSSCs to mediator complex instability.

5.2 Experimental Section

Materials. The following chemicals were used as received: acetonitrile (EMD, OmniSolv grade), 28–30% ammonium hydroxide solution (Mallinckrodt Chemicals, ACS grade), γ-butyrolactone (Aldrich, 99+%), dichloromethane (Fisher, HPLC grade), chloroform (Fisher, HPLC grade), ethanol (Pharmco-Aaper, ACS grade), isopropanol (Fisher, HPLC grade), methanol (Fisher, HPLC grade), *tert*-butanol (Fisher, Certified grade), phosphorus oxychloride (Baker & Adamson, 99+%), thionyl chloride (Sigma-Aldrich, ≥99%), 4-*tert*-butylpyridine (Aldrich, 99%), cobalt(II) perchlorate hexahydrate (Frederick Smith Chemical Company, 99+%), Z907 sensitizer dye (Solaronix Ruthenizer 520-DN), RK1 organic sensitizer dye (Solaronix Sensidizer RK1),

silica gel (Sigma-Aldrich, 200–400 mesh, 60 Å), and aluminum oxide (Sigma-Aldrich, activated, basic, Brockmann I, standard grade, ~150 mesh, 58 Å).

2,2'-Bipyridine-4,4'-dicarboxylic acid[18] and 2,2'-bipyridine-4,4'-bis(methyl ester)[19] were prepared according to published procedures. *N*,*N*-Dimethylformamide (DMF, EMD Millipore, OmniSolv grade) was dried before use (where stated) following published procedures.[20] Specifically, 100 mL of DMF was dried overnight over 5 g of 4 Å molecular sieves (5% w/v). The DMF was decanted into a 250 mL round bottomed flask with magnetic stir bar, and 5 g of phosphorus pentoxide (Fisher, 99.1%) was added (5% w/v). The solution was stirred while heating, then vacuum distilled (mechanical pump, low heat) onto anhydrous potassium carbonate (Fisher, 99.5%), then decanted into an oven-dried Erlenmeyer flask with 4 Å molecular sieves, and finally sealed with a rubber septum for storage before use. Lithium perchlorate (Aldrich, 95+%) was dried overnight in a vacuum oven (100 °C, 25 in. Hg vacuum) and stored in a desiccator until use. Nitrosonium tetrafluoroborate (Acros Organics, 97%) was sealed with Parafilm and stored in a refrigerator until use. Anhydrous ethyl ether (EMD Millipore, ACS grade) was stored in a refrigerator until use.

Analytical Methods. Cyclic voltammetry data was performed on a CHI-750D bipotentiostat. Solutions of each cobalt complex (1.0 mM) were prepared in acetonitrile containing 100 mM $LiClO_4$. Testing was performed on 1.0 mL of each solution in a 1 dram shell vial, using a gold working electrode (0.0314 cm^2), saturated sodium calomel reference electrode (SSCE), and platinum wire counter electrode. The SSCE electrode potential was confirmed to be +0.24 V vs NHE by a separate ferrocene reference solution in the same electrolyte. Before testing each solution, the working electrode was polished with a DI water slurry of alumina polishing powder (0.3 μm), rinsed with DI water, cleaned by sonication in ethanol for 30 s, and allowed to air-dry.

For voltammograms run in the presence of 4-*tert*-butylpyridine (TBP), one drop of TBP (~9.7 mg) was added to the 1.0 mL of solution by glass pipet (~70 mM, large excess).

Infrared spectra were obtained for solid powder samples using a Thermo Scientific Nicolet 380 FT-IR spectrometer with attenuated total reflectance mode through a ZnSe crystal. Thermogravimetric analysis was performed on a TA Instruments TGA 2950 thermogravimetric analyzer. Elemental analysis was performed by Galbraith Laboratories by combustion. UV–vis and quantitative NMR experiments are described in detail in the Supporting Information (SI).

Synthesis of 2,2'-Bipyridine-4,4'-dicarboxylic Acid Chloride. The desired amount (see below) of 2,2'-bipyridine-4,4'-dicarboxylic acid and a magnetic stir bar were added to a 25 mL round-bottomed flask, followed by an excess (67 equiv) of thionyl chloride. The flask was fit with a condenser and the stirring mixture was brought to reflux for 2 days until no solid was visible and the solution was translucent yellow. Remaining thionyl chloride was removed by vacuum distillation (mechanical pump), leaving a pale yellow solid. The flask was sealed with a rubber septum and flushed with N_2 gas (first passing through a drying tube filled with Drierite desiccant) for 15 min using a gas inlet and a vent needle, before using the product for subsequent reactions.

Synthesis of 2,2'-Bipyridine-4,4'-bis(N,N-dimethylcarboxamide) (dma-bpy). A two-step synthesis was employed, starting with conversion of 2,2'-bipyridine-4,4'-dicarboxylic acid to the dicarboxylic acid chloride, followed by reflux in distilled and dried DMF (taking advantage of DMF's known decomposition to generate dimethylamine[21]). As described above, 500 mg (2.05 mmol) of 2,2'-bipyridine-4,4'-dicarboxylic acid was converted to the acid chloride, isolated by vacuum distillation, and stored in a flask sealed with a rubber septum under N_2. Distilled and dried DMF (3 mL) was added by syringe through the rubber septum, and the solution turned bright red. The septum was replaced with a condenser, and the mixture was brought to reflux for 6 h. After

cooling, DMF was removed by vacuum distillation (mechanical pump), leaving a light brown solid. The crude product was dissolved in dichloromethane and purified by silica column, using ~25 g of silica per ~1 g of product to be purified and eluting with 100% dichloromethane. The first band (yellow/tan) was collected, evaporated to dryness by rotary evaporation to yield a light brown solid, and dried overnight in a vacuum oven (100 °C, 25 in. Hg vacuum). The product yield was 511 mg of light beige powder, 84% yield.

^{1}H NMR (300 MHz, $CDCl_3$) δ ppm: 3.01 (s, 6H, 2×CH_3); 3.16 (s, 6H, 2×CH_3); 7.37 (dd, 2H, 2×H5); 8.44 (s, 2H, 2×H3); 8.75 (d, 2H, 2×H6). FT-IR (solid powder): 3068 w; 3053 w; 3020 w; 2960 w; 2931 w; 1629 s; 1589 w; 1547 m; 1499 m; 1447 m; 1400 s; 1356 m; 1261 m; 1241 w; 1215 m; 1091 m; 1062 m; 986 w; 933 m; 874 s; 763 m; 741 m; 727 m.

Synthesis of 2,2'-Bipyridine-4,4'-dicarboxamide. As described above, 500 mg (2.05 mmol) of 2,2'-bipyridine-4,4'-dicarboxylic acid was converted to the acid chloride, isolated by vacuum distillation, and stored in a flask sealed with a rubber septum under N_2. Chloroform was dried by passing through a column of activated aluminum oxide (~10 g) and added by syringe (~5 mL) through the septum to dissolve the acid chloride. A small beaker containing 10 mL of concentrated aqueous ammonia solution (28%) was cooled on an ice water bath and stirred to vortex with a magnetic stir bar. The acid chloride solution was added by syringe to the vortexing ammonia solution at a rate of 2–3 drops per second, which immediately fumed and precipitated a white solid. The mixture was transferred to a 20 mL vial and centrifuged, and the solution was decanted away. Carboxylic acid byproduct was removed by washing the solid with additional aqueous ammonia (3×10 mL) and once with isopropanol (10 mL); the vial was shaken for several minutes, centrifuged, and the liquid was decanted each time. The solid was dried by rotary evaporation, at which point it turned bright pink (possibly due to the presence of an iron impurity).

The solid was purified by dissolving in a minimum of hot DMF and collecting the fine white solid from the cooled solution by vacuum filtration. The DMF precipitation also served to make the product much more finely powdered, proving beneficial in the next step of the synthesis. The average yield of purified product was 56%.

FT-IR (solid powder): 3300 m, br; 3129 m, br; 1678 s; 1631 m; 1601 m; 1549 m; 1433 w; 1412 s; 1365 w; 1269 w; 1246 w; 1165 w; 1138 m; 1102 m; 1075 w; 998 w; 928 w, 857 s; 807 w.

Synthesis of 2,2'-Bipyridine-4,4'-dicarbonitrile (cn-bpy). A literature procedure for this molecule was followed,[22] though additional workup details[23] were required in order to isolate the desired product. To a single-neck, 10 mL round-bottomed flask was added 265 mg (1.09 mmol) of 2,2'-bipyridine-4,4'-dicarboxamide as a fine white powder and 10 mL (100 equiv) of $POCl_3$. The flask was fit with a condenser and drying tube (filled with anhydrous calcium sulfate desiccant), submerged in a sonicating water bath up to the neck of the flask, and the bath was covered by aluminum foil to slow evaporation. The mixture was left sonicating until all the solid had visibly dissolved and the solution was a translucent dark red, taking anywhere from 18 to 48 h (depending on the water bath temperature, which ranged from room temperature to as high as 70 °C when covered with aluminum foil, and depending on how finely powdered the amide starting material was). A magnetic stir bar was added and excess $POCl_3$ was removed by vacuum distillation (mechanical pump) down to ~1 mL of solution. The stirring solution was cooled on an ice bath and quenched by adding small pieces of crushed ice (from nanopure water) until no more bubbling occurred upon ice addition. Still on the ice bath, aqueous ammonia solution (28%) was added dropwise until a pH of 7 or 8 was reached according to universal pH paper. During neutralization, an orange precipitate formed. The solution was extracted with chloroform (10 mL portions) until no more fluorescent material was evident in the chloroform by TLC/UV light. The

combined organic phase was concentrated by rotary evaporation and purified by silica column, using ~25 g of silica per ~1 g of product to be purified. The product was eluted with 100% chloroform, collecting the first light-yellow band. The eluent was dried by rotary evaporation, leaving a fluffy white powder, and additionally dried overnight in a vacuum oven on low heat (~70 °C, 25 in. Hg vacuum), as the product can sublime.[22] Yields averaged 71%.

^{1}H NMR (300 MHz, $CDCl_3$) δ ppm: 7.62 (d, 2H, 2×H5); 8.74 (s, 2H, 2×H3); 8.89 (d, 2H, 2×H6). FT-IR (solid powder): 3096 w; 3072 w, 3014 w; 2245 w; 2237 w; 1587 m; 1547 m; 1457 m; 1367 m; 1319 w; 1252 w; 1230 w; 1199 w; 1101 m; 1070 w; 989 m; 920 w, 854 s; 796 m; 754 w.

Synthesis of $[Co(L)_3](ClO_4)_2$ Complexes. The complexes shown in Figure 5.1 were all prepared using the same procedure. Briefly, 3.3 equiv of the respective ligand were dissolved in a minimum of hot methanol. When all ligand was dissolved, 1 equiv of cobalt(II) perchlorate hexahydrate was added, and the mixture was refluxed for 2 h. After cooling, solutions were concentrated by ~80% by rotary evaporation, and diethyl ether was added to help precipitate the light-yellow solid product. The yellow products were collected by vacuum filtration, rinsed with excess diethyl ether, and dried overnight in a vacuum oven (100 °C, 25 in. Hg vacuum). In the case of the $[Co(dma\text{-}bpy)_3](ClO_4)_2$ product, the yellow solid began to form an oil as it dried on the vacuum filter. This oil was dissolved in acetonitrile and transferred to a vial, and then evaporated to dryness by rotary evaporator before drying overnight in a vacuum oven. The fully dried product was a solid.

Thermogravimetric analysis was performed on all complexes (stored in closed vials on the benchtop), and each showed small percentage mass losses (3.2% or less) at temperatures below 150 °C, consistent with weakly hydrated complexes. Complexes were sent to Galbraith

Laboratories for elemental analysis. Analyses are consistent with dihydrates. Complexes were subsequently redried by vacuum oven and stored in a desiccator until use.

Elemental analysis (%) calculated for $[Co(dma\text{-}bpy)_3](ClO_4)_2 \cdot 2H_2O$, $C_{48}H_{58}Cl_2CoN_{12}O_{16}$ (1187.28): C 48.49, H 4.92, N 14.14; found: C 48.70, H 5.03, N 14.31. Calculated for $[Co(me\text{-}bpy)_3](ClO_4)_2 \cdot 2H_2O$, $C_{42}H_{40}Cl_2CoN_6O_{22}$ (1110.09): C 45.42, H 3.63, N 7.57; found: C 45.30, H 3.73, N 7.69. Calculated for $[Co(cn\text{-}bpy)_3](ClO_4)_2 \cdot 2H_2O$, $C_{36}H_{22}Cl_2CoN_{12}O_{10}$ (912.48): C 47.39, H 2.43, N 18.42; found: C 47.69, H 2.69, N 18.56. Note that the elemental analyses indicate that, for each cobalt complex, the ligands are present in the expected 3:1 ligand-to-cobalt ratio. NMR and UV–vis characterizations of the complexes are included in the SI.

DSSC Dark Current Testing. Experimental conditions were chosen to closely mimic a previous recombination study.[24] Cobalt mediator solutions were prepared with 40 mM $[Co(L)_3](ClO_4)_2$ and 100 mM $LiClO_4$ in γ-butyrolactone (gBL) solvent. During preparation, a measured amount of a stock solution of $NOBF_4$ (~0.2 M in gBL) was added in order to oxidize half of the mediator to Co^{3+}. Gold cathodes and TiO_2 anodes were prepared as described in a previous publication.[25] Briefly, cathodes were thermally evaporated gold-on-chromium-on-FTO. The photoanode consisted of a compact TiO_2 under-layer on fluorine-doped tin oxide coated glass (FTO, TEC 15, Hartford Glass) beneath a mesoporous TiO_2 layer. The compact layer was prepared by spin coating a TiO_2 sol onto an FTO slide. On top of this, a commercial TiO_2 slurry (T-37 nanoxide, Solaronix) was doctor-bladed into the gap between two pieces of Scotch tape. The tape was removed and the TiO_2 was sintered in air in a furnace gradually stepped to 500 °C and held for 60 min. This procedure generally produces TiO_2 films that are ~2.5 μm thick.[25] The anodes were slowly cooled to 150 °C and placed directly in a solution of Z907 sensitizer (0.3 mM in 1:1 CH_3CN–*t*-BuOH) or RK1 sensitizer (0.2 mM in absolute ethanol), where they soaked in the dark

for ≥48 h. Anodes were removed from dye solution, rinsed clean with ethanol and acetonitrile, and dabbed dry with a Kimwipe before use.

Sensitized anodes were "pretreated" by soaking in the dark for at least 15 min in gBL solution containing 100 mM $LiClO_4$, rinsed with acetonitrile, patted dry with a Kimwipe, and allowed to further air-dry until cell assembly. The pretreatment solutions containing RK1-sensitized anodes became orange, likely dissolving aggregated dye which was not specifically anchored to the TiO_2 surface. When dark current tests were to be run with added TBP, the dyed anodes were pretreated overnight in gBL containing 100 mM $LiClO_4$ and 200 mM TBP, in order to avoid time-dependent effects which could result from slow TBP adsorption.[26] A 25 μm Kapton spacer was prepared by using a leather hole puncher to cut a 0.503 cm^2 circle out of a square Kapton strip, allowing a defined area for the experiment. Electrodes were arranged in a sandwich configuration, with the photoanode clamped against the cathode with small binder clips, separated by the Kapton spacer. The mediator solution of choice was introduced (10 μL) via an auto pipet with disposable plastic tip through one of two 1 mm holes drilled in the cathode. Holes were not sealed during testing, made possible by the low vapor pressure of the gBL solvent.

Dark currents were run using a CHI-750D bipotentiostat in a two-electrode configuration (working lead clipped to the TiO_2 anode, auxiliary lead attached to the gold cathode, and reference lead clipped to the auxiliary lead). The cell was kept in the dark during testing. Data was collected by linear sweep voltammetry, scanning from +0.1 to −1.0 V vs. the cathode, with a scan rate of 50 mV/s. After testing, cells were disassembled and each component was rinsed with acetonitrile and dabbed dry with a Kimwipe. The cell was then reassembled and the next mediator solution was introduced for testing. Each respective mediator solution was tested three times on three different anodes, and the dark currents averaged to yield Figure 5.5 (see below). Very little variation

occurred between trials of the same mediator solution, and dark currents were not dependent on the order of mediator testing.

For experiments shown in Figure 5.7 (see below), anodes included bare FTO, FTO/dense layer TiO_2, FTO/dense layer/mesoporous TiO_2, and FTO/dense layer/mesoporous TiO_2/Z907. These anodes were prepared as above, but stopping at the appropriate step. FTO and FTO/dense layer TiO_2 anodes were also annealed in air to 500 °C for 60 min and cooled to 150 °C before being placed in pretreatment solution.

5.3 Results And Discussion

Synthesis of New Ligands and Cobalt Complexes. Detailed procedures for the syntheses of ligands are provided in the Experimental Section above, and a discussion of the selected synthetic strategies for dma-bpy and cn-bpy ligands are provided in the SI. Once the ligands were in hand, cobalt complexes were synthesized by the typical procedure:[16] 3.3 equiv of ligand were dissolved in a minimal amount of hot methanol, followed by 1 equiv of $Co(ClO_4)_2$, and the solution was refluxed for 2 h. Usually, solutions turned yellow immediately upon addition of cobalt, indicating the formation of the complex. Interestingly, the cn-bpy solution remained the light pink shade of $Co(ClO_4)_2$ throughout the reflux, indicating that the cn-bpy ligand competed poorly to coordinate with the metal at these high temperatures. After reflux, solutions were concentrated by rotary evaporation and diethyl ether was added to help precipitate the product. It was not until this concentration step that the $[Co(cn\text{-}bpy)_3]^{2+}$ solution began to precipitate a white solid (likely uncoordinated ligand), which then spontaneously turned yellow as concentration progressed. Solids were collected by vacuum filtration, washed with diethyl ether, dried overnight in a vacuum oven, and stored in sealed vials under ambient conditions before analysis. Elemental analyses of

each complex were consistent with $[Co(L)_3](ClO_4)_2 \cdot 2H_2O$ within ±0.3 atomic percent. Thermogravimetric analysis of the complexes was also consistent with 1–2 waters of hydration, as indicated by small percentage mass losses at temperatures below 150 °C. Complexes were subsequently redried in a vacuum oven and stored in a desiccator until used.

Cyclic Voltammetry of Cobalt Complexes. Each complex was characterized by cyclic voltammetry. A previous study found that the electron-transfer kinetics of many cobalt tris(bipyridyl) derivatives can by very dependent on the electrode material; the most reversible behavior was observed on gold and glassy carbon, while non-reversible behavior was observed on platinum.[16] Cyclic voltammograms (CVs) of our new complexes on gold electrodes are shown in Figure 5.2, and electrochemical data are summarized in Table 5.1.

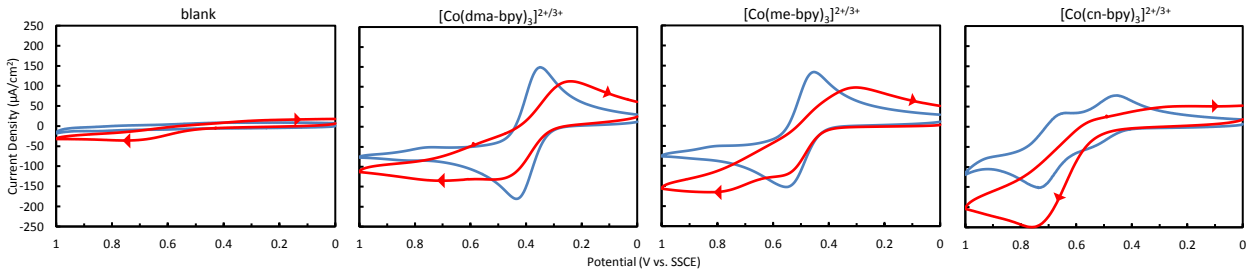

Figure 5.2 Cyclic voltammograms of the prepared cobalt complexes (1 mM) in acetonitrile with 100 mM $LiClO_4$ supporting electrolyte (blue curves) and with added 1 drop (~70 mM, large excess) of 4-*tert*-butylpyridine (TBP) to the solution. Working electrodes were polished gold, SSCE reference, platinum wire counter electrode, and 50 mV/s scan rate.

Table 5.1 Electrochemical Properties of Cobalt Complexes in Acetonitrile Electrolyte on Various Electrode Materials.

	gold		glassy carbon		platinum	
solution	$E_{1/2}$ (mV)[a]	ΔE_p (mV)	$E_{1/2}$ (mV)[a]	ΔE_p (mV)	$E_{1/2}$ (mV)[a]	ΔE_p (mV)
$[Co(dma\text{-}bpy)_3]^{2+/3+}$	392	84	374	133	374	148
$[Co(dma\text{-}bpy)_3]^{2+/3+}$ + TBP	381	279	409	382	ND[b]	ND[b]
$[Co(me\text{-}bpy)_3]^{2+/3+}$	503	101	515	159	561	349
$[Co(me\text{-}bpy)_3]^{2+/3+}$ + TBP	440	270	534	432	ND[b]	ND[b]
$[Co(cn\text{-}bpy)_3]^{2+/3+}$	688	93	800	265	ND[b]	ND[b]
$[Co(cn\text{-}bpy)_3]^{2+/3+}$ + TBP	479	568	ND[b]	ND[b]	ND[b]	ND[b]
[c]$[Co(bpy)_3]^{2+/3+}$	220	60	223	86	223	60
[d]$[Co(bpy)_3]^{2+/3+}$ + TBP	ND[b]	>650				

[a] vs SSCE. [b] Peak(s) not discernible. [c]Adjusted from previous publication[16], scan rate = 200 mV/s. [d]From previous publication.[27]

In the present study the most reversible behavior, as indicated by the peak separation, ΔE_p, was found on gold electrodes. From the $E_{1/2}$ values of each complex, it is evident that the electron withdrawing nature of the ligands increases in the order dma-bpy < me-bpy < cn-bpy. It is also important to point out that the $[Co(cn\text{-}bpy)_3](ClO_4)_2$ complex exhibited two electron-transfer waves in acetonitrile; the first at $E_{1/2} \approx 500$ mV and the second at 688 mV vs SSCE. The appearance of two waves suggests the presence of two different electroactive species in solution. As discussed in the Introduction section, ligand dissociation and resultant complex instability may be expected to increase as the electron withdrawing nature of its functional groups increases. Therefore, it is not surprising that $[Co(cn\text{-}bpy)_3](ClO_4)_2$ showed evidence of two species by cyclic voltammetry. The most likely identity of the second species, then, is $[Co(cn\text{-}bpy)_2(CH_3CN)_2]^{n+}$, resulting from the loss of a cn-bpy ligand and replacement by the mildly coordinating acetonitrile solvent.[28]

Effects of Added 4-Tert-butypyridine. A common additive in DSSCs electrolyte solutions is 4-*tert*-butylpyridine (TBP), which has been found to improve DSSC performance by providing a barrier to recombination between the mediator and electrons in the TiO_2, and by negatively shifting the energy of electrons in the conduction band.[29] Because *tert*-butyl groups are electron donating, it is expected that TBP should be a stronger σ-donor than the bipyridine ligands studied here, though it lacks the chelate effect of the bidentate bipyridine ligands. It was of interest, therefore, to study the effect that TBP might have on the stability of these high-potential cobalt complexes. To probe this effect, one drop of TBP was added to each solution, and CVs were repeated. We note that this addition results in a large, ~70-fold molar excess of TBP relative to the cobalt complex, which should accentuate any potential stability issues.

It can be seen from Figure 5.2 and the data in Table 5.1 that the addition of TBP to solution greatly reduces the reversibility of electrochemistry on all the electrode materials tested. The

literature explanation for this decreased reversibility is that TBP adsorbs onto the surface of the electrode, increasing the resistance to charge transfer (decreasing electronic coupling) between the electrode surface and the mediator complex, likely due to the steric bulk of the *tert*-butyl group.[27] While we have previously shown that modifying gold cathode surfaces with sulfide ions can result in much more Nernstian voltammetry for cobalt complexes in the presence of TBP,[27] a more pronounced redox wave due to TBP also appears with an $E_{1/2}$ of about 0.55 V vs SSCE. Such a redox wave would overlap with the redox chemistry of the more positive-potential cobalt complexes in this study.

As shown by Figure 5.2, the effect of added TBP was qualitatively the same on the electrochemistry of both the $[Co(dma\text{-}bpy)_3](ClO_4)_2$ and $[Co(me\text{-}bpy)_3](ClO_4)_2$ complexes but differed for $[Co(cn\text{-}bpy)_3](ClO_4)_2$. We note that the CV of $[Co(bpy)_3](ClO_4)_2$ on a gold electrode with and without TBP has been published previously and was qualitatively similar to those shown for $[Co(dma\text{-}bpy)_3](ClO_4)_2$ and $[Co(me\text{-}bpy)_3](ClO_4)_2$ in Figure 5.2.[27] The voltammetry of $[Co(cn\text{-}bpy)_3](ClO_4)_2$ with TBP became almost completely irreversible, showing barely any cathodic wave on the reverse sweep. This observation indicates that something fundamentally different is occurring in the $[Co(cn\text{-}bpy)_3](ClO_4)_2$ + TBP solutions; that is, increased resistance to electron transfer is not the only effect of TBP in this case.

Cobalt complex solutions were characterized by UV–vis spectroscopy, both before and after adding TBP, and again after performing cyclic voltammetry (see Figures S5.1 and S5.2 in the SI). All solutions initially had a pale-yellow hue. For $[Co(bpy)_3](ClO_4)_2$, $[Co(dma\text{-}bpy)_3](ClO_4)_2$, and $[Co(me\text{-}bpy)_3](ClO_4)_2$ complex solutions, the absorption spectra remained unchanged after adding TBP and performing CVs. By contrast, $[Co(cn\text{-}bpy)_3](ClO_4)_2$ solutions changed to bright green after adding TBP and performing CVs, providing evidence for the formation of a new

species. Absorption spectra and a discussion of this color change can be found in the SI (Figure S5.2). After several controls and review of literature spectra, we conclude that the color change is likely caused by the formation of a small percentage of a bright blue, $Co(TBP)_2Cl_2$ byproduct, following dissociation of labile cn-bpy ligands, and with the chloride ions originating from the SSCE reference electrode (see the discussion in the SI). We note that this byproduct would not form under DSSC conditions due to the lack of chloride ion and merely served as a fortuitous, early indication of complex instability.

While acetonitrile is one of the most common electrolyte solvents in DSSC studies due to its low viscosity and high dielectric constant,[4] it is a relatively strongly coordinating solvent[28] and is therefore not the most ideal solvent for potentially labile cobalt complexes. Therefore, electrochemistry of $[Co(cn\text{-}bpy)_3](ClO_4)_2$ was also tested in two less-coordinating solvents: nitromethane and γ-butyrolactone (gBL). Note that gBL is the solvent of choice in the authors' research group for DSSC studies due to its very low volatility, thereby eliminating the need to run experiments on sealed cells. The resulting CVs with alternative solvents are shown in Figure 5.3.

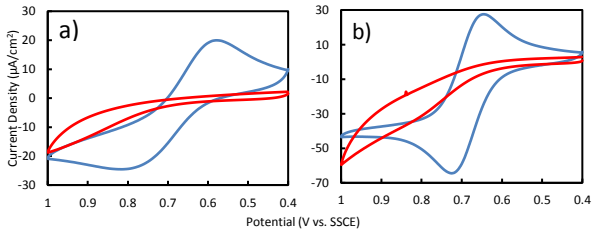

Figure 5.3 Cyclic voltammograms of 1 mM $[Co(cn\text{-}bpy)_3](ClO_4)_2$ in (a) gBL and (b) nitromethane with 200 mM $LiClO_4$ supporting electrolyte (blue curves) and with added 1 drop (large molar excess) of TBP to the solution (red curves). Working electrodes were polished gold, SSCE reference, platinum wire counter electrode, and 10 mV/s scan rate.

For $[Co(cn\text{-}bpy)_3](ClO_4)_2$ in gBL, $E_{1/2}$ = 697 mV and ΔE_p = 240 mV. In nitromethane, $E_{1/2}$ = 685 mV and ΔE_p = 80 mV vs SSCE. Notable in both these voltammograms is that only one wave is present as opposed to the two waves observed in acetonitrile (Figure 5.2), meaning there is no electrochemical evidence for complex instability in these less-coordinating solvents. However,

when 1 drop of TBP is added, the electrochemistry becomes completely irreversible, just as in acetonitrile (Figure 5.2). Similar to the acetonitrile case, $[Co(cn\text{-}bpy)_3](ClO_4)_2$ in gBL also turned bright green after addition of 1 drop of TBP and performing CVs. The nitromethane solution for electrochemistry did not turn green upon adding TBP, but a translucent precipitate formed. It is noteworthy that the complex was already at its very limit of solubility even at 1 mM concentration in the nitromethane electrolyte solution. Despite the lack of a color change, the CV in Figure 5.3b still seems to indicate that the complex is unstable in the presence of TBP in nitromethane at room temperature.

NMR Determination of Stability Constants. In light of the above results, it became of interest to determine, at least semiquantitatively, the stabilities of our cobalt complexes. A simple metric would then be to measure the stoichiometric ligand-binding equilibrium constants, *K* (also referred to as stability constants or formation constants), between a metal ion and its ligands in solution. The sequential equilibrium constants of ligand (L) coordinating to a metal cation (M) as classically defined are given below:[30]

$$\mathrm{M} + \mathrm{L} \rightleftharpoons \mathrm{ML}, \; K_1 = \frac{[ML]}{[M][L]} \tag{5.1}$$

$$\mathrm{ML} + \mathrm{L} \rightleftharpoons \mathrm{ML_2}, \; K_2 = \frac{[ML_2]}{[ML][L]} \tag{5.2}$$

$$\mathrm{ML_2} + \mathrm{L} \rightleftharpoons \mathrm{ML_3}, \; K_3 = \frac{[ML_3]}{[ML_2][L]} \tag{5.3}$$

It has been found, for cobalt (II) complexes with 2,2'-bipyridine and 1,10-phenantholine ligands in water, that the above equilibrium constants decrease in the expected order $K_1 > K_2 > K_3$.[31] If it is assumed that, upon dissolution, CoL_3 complexes equilibrate only into species present in eq 5.3 (this assumption was clearly not valid for the case of $[Co(cn\text{-}bpy)_3](ClO_4)_2$, see the discussion in the SI), and if the equilibrium concentrations of two of the three chemical species in eq 5.3 can be

determined, then an approximate K_3 value can be calculated for that complex. Due to the ubiquity of NMR instruments in chemistry departments and the simplicity of NMR experiments, we chose this technique as a facile and quick method which can be used for probing the stability of new cobalt mediator complexes for DSSC applications.

Cobalt(III) tris(bipyridyl) complexes are low spin and diamagnetic, so NMR of the complexes should be straightforward. However, the Co^{3+} species of the redox couple is expected to be much less labile than the high spin Co^{2+} and is therefore not the correct species to study if stability is a concern. Brisig et al. have previously shown that Co^{2+} complexes can often be studied by NMR despite being paramagnetic.[32] The ^1H signals of the coordinated bipyridine ligands are broadened and shifted significantly downfield of the typical aromatic range due to the paramagnetic cobalt center. Fortunately, this leaves the aromatic region uncluttered, and the ^1H signals of any dissociated free ligand can be easily detected. NMR spectra of our new cobalt(II) complexes, as well as $[Co(bpy)_3](ClO_4)_2$ as a control, are provided in Figure S5.3 in the SI.

In order to quantify the amount of free, dissociated bpy ligand from each complex, individual samples were prepared in d_3-acetonitrile with a known starting concentration of each of our new, high-potential cobalt complexes, as well as $[Co(bpy)_3](ClO_4)_2$. Once dissolved and equilibrated, any detectable free ligand was quantified against a benzene internal standard. In addition, each sample was diluted at least twice with d_3-acetonitrile, allowing for multiple K_3 calculations and averaging of the K_3 for each sample. Details of the experiments and calculations are provided in the SI, and results are provided in Table 5.2.

Table 5.2 Stability Constants for $[Co(L)_3](ClO_4)_2$ Complexes in d_3-Acetonitrile Calculated by Quantitative NMR Experiments.

complex	K_3 (std dev)	$E_{1/2}$ (mV vs SSCE)
$[Co(bpy)_3]^{2+}$	4.6 (0.7) $\times 10^5$	220
$[Co(dma\text{-}bpy)_3]^{2+}$	8 (3) $\times 10^6$	392
$[Co(me\text{-}bpy)_3]^{2+}$	9.2 (0.5) $\times 10^3$	503
$[Co(cn\text{-}bpy)_3]^{2+}$	2 (1) $\times 10^2$	688

As further detailed in the SI, the NMR spectra showed that trace amounts (≤ 1%) of some of the complexes had been oxidized to Co^{3+}. We note that no oxidized complex was evident in the $[Co(cn\text{-}bpy)_3](ClO_4)_2$ sample, which has the most positive redox potential, and therefore the lowest driving force for oxidation relative to the other three complexes studied. As samples were diluted, the detected percentage of Co^{3+} complex impurity remained essentially unchanged, while the percent dissociated ligand increased. This observation provides additional evidence that the detected free ligand in each sample originated from an equilibrium process, not simply from residual, uncoordinated ligand impurity. Also, recall that the elemental analysis of each sample was consistent with the ligands being present in the expected 3:1 ligand-to-cobalt ratio.

The results summarized in Table 5.2 show (i) that the K_3 stability constants estimated for the new cobalt complexes studied herein vary by several orders of magnitude and (ii) that the trend in K_3 stability constants decrease as redox potentials increase. We note that the K_3 stability constants calculated in this study are likely underestimates, due to our simplifying assumption that the equilibria reactions in eqs 5.1 and 5.2 did not contribute to the detected equilibrium concentration of dissociated ligand. In fact, the breakdown in this assumption is likely what led to the significant 50% uncertainty in the K_3 values calculated for the least stable complex, $[Co(cn\text{-}bpy)_3](ClO_4)_2$. By contrast, the nearly 40% uncertainty in the measured K_3 values for the most stable complex, $[Co(dma\text{-}bpy)_3](ClO_4)_2$, illustrates the difficulty of measuring such high equilibrium constants by NMR.

The $[Co(bpy)_3](ClO_4)_2$ complex was also included as a control. While $[Co(bpy)_3](ClO_4)_2$ has the most negative redox potential of the complexes studied, it did not show the largest equilibrium constant. For comparison, a previous study of $[Co(bpy)_3]^{2+}$ in aqueous 0.1 M KCl found a $\log(K_3)$ value of 4.80 (K_3 of 6.3×10^4), as determined by a more sensitive liquid–liquid

partition technique.[31] Our calculated K_3 value of $(4.6\pm0.7)\times10^5$ is significantly larger, which is not necessarily unexpected. The stabilities of complexes will, of course, vary by solvent as already shown above for our $[Co(cn\text{-}bpy)_3](ClO_4)_2$ complex based on the different electrochemical results in acetonitrile vs gBL or nitromethane (Figures 5.2 and 5.3, respectively). In fact, the overall stability constant, β_3 ($\beta_3 = K_1K_2K_3$), for $[Co(bpy)_3]^{2+}$ has also been found to be over 10^{20} higher in water-saturated dichloromethane than in water solution.[33]

Under the conditions of our NMR study, we found that the approximate percent Co^{2+} complex that had dissociated a ligand ranged from less than 1% for $[Co(bpy)_3](ClO_4)_2$ and $[Co(dma\text{-}bpy)_3](ClO_4)_2$ up to more than 100% for $[Co(cn\text{-}bpy)_3](ClO_4)_2$ (that is, some proportion of $[Co(cn\text{-}bpy)_3](ClO_4)_2$ dissociated more than one cn-bpy ligand, see Table S5.2 in the SI). As an additional control, NMR spectra were taken for each complex in d_3-acetonitrile with added TBP (1.5 mol equiv vs cobalt). Though the concentrations of free bpy ligand were not quantified in these experiments, the free bpy signals increased upon TBP addition for all three of our new complexes, indicating that TBP shifts the equilibrium toward more bpy ligand dissociation.[34] Restated, *the TBP additive reduces the stability of cobalt(II) tris(bipyridyl) complexes.*

DSSC Dark Current (Recombination) Measurements. The precise effect that mediator complex instability would have on DSSC operation is difficult to predict but would likely depend on the extent to which ligand substitution occurs, and the ultimate speciation of the new complex formed. It was expected that the easiest metric to test a possible effect would be dark current measurements. Dark currents gauge the extent of recombination between electrochemically generated electrons in the TiO_2 and the oxidized form of the mediator complex in the electrolyte solution. Therefore, each of the new cobalt complexes were used to prepare DSSC mediator solutions.

While it would be ideal to compare dark currents from mediator solutions in acetonitrile solvent so that the results could be directly related to the K_3 constants calculated by NMR, the $[Co(cn\text{-}bpy)_3](ClO_4)_2$ complex is only soluble up to 5 mM in acetonitrile and gradually precipitates after being oxidized to Co^{3+} by $NOBF_4$. Hence, mediator solutions were prepared in gBL solvent, where $[Co(cn\text{-}bpy)_3]^{3+}$ remains soluble up to at least 20 mM. Mediator solutions contained 100 mM $LiClO_4$ and 40 mM $[Co(L)_3](ClO_4)_2$, half of which was oxidized to Co^{3+} using a stock solution of $NOBF_4$. Again, the choice of gBL solvent also has the advantage of a very low vapor pressure, so that DSSC tests can be performed without the complication of sealing the cell to avoid evaporation of the electrolyte solvent. Although the *magnitudes* of the stability constants are expected to be different in gBL and acetonitrile solvents, the qualitative stability *trend* is expected to hold. That is, the complex stabilities are expected to decrease as their respective $E_{1/2}$ values increase.

To mimic a typical DSSC cell, mesoporous TiO_2 anodes (with a dense TiO_2 blocking layer to prevent recombination between the mediator and FTO support) were dyed with a common ruthenium DSSC sensitizer, Z907, shown in Figure 5.4. This sensitizer was originally designed to improve the stability of DSSCs by adding hydrophobic nonyl groups which repel trace water impurity.[35] It has been found that these groups can also act as a steric barrier to recombination between cobalt mediator complexes and TiO_2 electrons.[36] Cells were assembled in a sandwich configuration with a gold cathode and a 25 μm Kapton spacer, and dark currents were measured using linear sweep voltammetry.

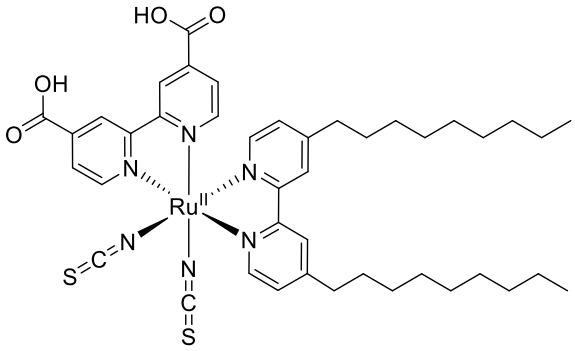

Figure 5.4 Structure of the common Z907 DSSC sensitizer.[35]

Note that in dark current experiments, potential is applied to the anode (E_{appl}) relative to the potential of the cathode. The potential of the cathode in a DSSC has been shown to be pinned at the redox potential of the electrolyte[37] (in this case, the $E_{1/2}$ of each complex as reported in Table 5.1 on gold electrodes) and which will be different for each respective mediator complex. In order to compare recombination across different mediators, it is necessary to plot dark currents relative to the electrochemical potential of electrons in the TiO_2, or the quasi-Fermi level (E_F), rather than E_{appl}. This simple conversion is shown by eq 5.4:

$$E_F = E_{appl} + E_{1/2,redox} \tag{5.4}$$

Averaged dark currents for each mediator solution on three different dyed TiO_2 anodes are shown in Figure 5.5.

For the new, high-potential cobalt complexes, recombination currents are highest for $[Co(cn\text{-}bpy)_3](ClO_4)_2$ mediator solutions, followed by $[Co(me\text{-}bpy)_3](ClO_4)_2$ and then $[Co(dma\text{-}bpy)_3](ClO_4)_2$. As for the $[Co(bpy)_3](ClO_4)_2$ control, the dark current onsets at the most negative potential, consistent with its more negative redox potential. However, as potential is scanned in the negative direction, the current magnitude increases more rapidly for $[Co(bpy)_3](ClO_4)_2$ than for the other three complexes. This result is expected because the lack of additional functional groups on the ligands means that $[Co(bpy)_3](ClO_4)_2$ should have the fastest

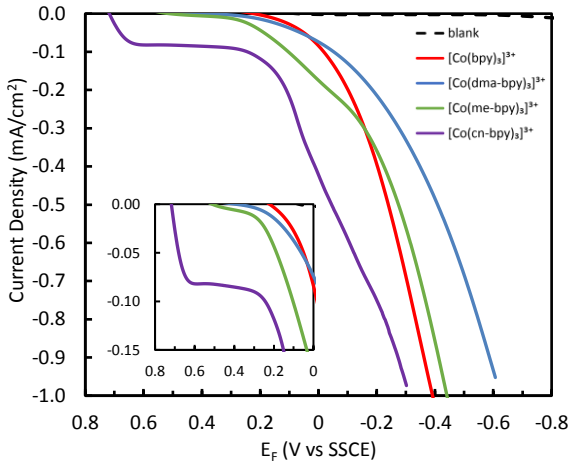

Figure 5.5 Dark current densities vs TiO_2 quasi-Fermi level for cobalt mediator solutions on TiO_2 anodes (with dense TiO_2 under-layer) sensitized with Z907 dye. Mediator solutions contained 40 mM $[Co(L)_3](ClO_4)_2$, half of which was oxidized to Co^{3+} with a stock solution of $NOBF_4$, and 100 mM $LiClO_4$ in gBL solvent. Dark current curves are each an average of three trials with three different anodes. Also shown is the dark current measured with blank electrolyte (100 mM $LiClO_4$ in gBL), which was not corrected by eq 5.4. The inset is zoomed in on the region of potential-independent current.

mass transport through the electrolyte solution, and the least intrinsic barrier to recombination at the TiO_2 surface.

The dark current for the $[Co(cn\text{-}bpy)_3](ClO_4)_2$ complex shows an unexpected feature. When scanning from positive to negative potentials, the recombination current immediately increases and then quickly plateaus to a (nearly) potential-independent value. Once an E_F of about 0.2 V vs SSCE is reached, current again increases rapidly, as was observed for the other three mediator complexes at the same potential. From the inset of Figure 5.5, it can be seen that $[Co(me\text{-}bpy)_3](ClO_4)_2$ also exhibits some nearly potential-independent current but at a much lower magnitude (consistent with the higher stability constant for that complex). Another peculiar feature of the dark currents for $[Co(cn\text{-}bpy)_3](ClO_4)_2$ and $[Co(me\text{-}bpy)_3](ClO_4)_2$ are "bumps" in the currents centered at about 0.0 V vs SSCE. This feature is not present for $[Co(dma\text{-}bpy)_3](ClO_4)_2$ or $[Co(bpy)_3](ClO_4)_2$, which show a more typical exponential looking increase in current as the potential is scanned in the negative direction.

A previous publication by Feldt et al. studied 13 different cobalt complex mediators with varying redox potentials.[15] Dark current measurements were performed for each of those complexes (viewable in the SI of that study)[15] and potential-independent recombination currents such as those seen in Figure 5.5 were not observed for *any* of those mediators.[38] However, some of the mediators *did* exhibit a similar "bump" in the current curve at similar adjusted potentials.

Recombination Modeling. In order to better understand the above dark current results, we chose to model expected recombination rates for the different cobalt complex mediators. Heterogeneous electron transfer at semiconductor electrodes can be modeled by Marcus–Gerischer theory, which is based on overlap between the electronic density of states of the electrode and those of the dissolved reactant in solution.[39] This model was used to estimate relative recombination rates for each of the cobalt complexes in this study, with the important assumption that the mediator complexes are 100% stable and that the complexes only weakly interact with the semiconductor surface (that is, there is not significant overlap between the electronic wave functions of the cobalt complexes and the TiO_2 surface).[39] Therefore, recombination features not present in the modeled current can potentially be attributed to complex instability, specifically to some unknown redox species originating from the dissociation of one or more of the original bipyridine ligands. Details for the recombination modeling are provided in the SI, and results are provided in Figure 5.6.

From the density of states diagram shown in Figure 5.6a, it is clear that the model predicts that recombination between TiO_2 electronic states and mediator acceptor states (Co^{3+}) should increase as the redox potentials of the mediators grow more positive, caused by improved overlap of the densities of states. In other words, recombination is expected to be in the Marcus normal

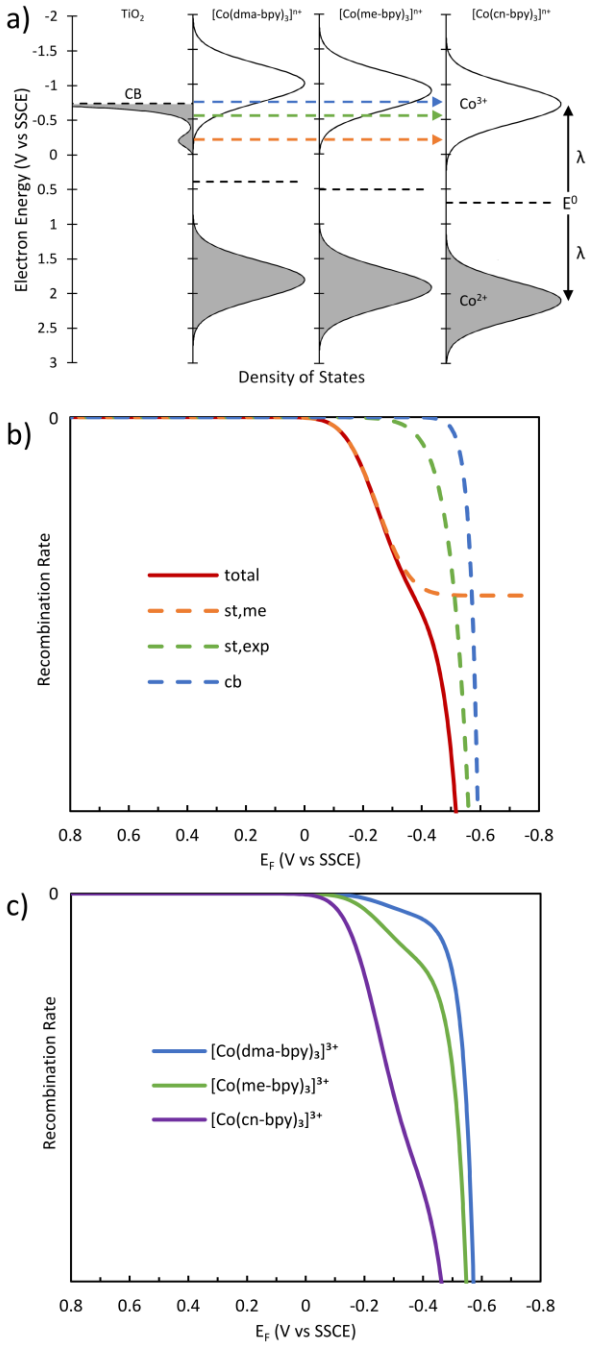

Figure 5.6. Recombination modeled using Marcus–Gerischer theory: (a) overlap of electronic states with indicated isoenergetic electron transfer from TiO_2 monoenergetic trap states (dashed orange line), exponential distribution of trap states (dashed green line), and from the conduction band (dashed blue line); (b) total modeled recombination rate vs TiO_2 Fermi energy for $[Co(cn\text{-}bpy)_3]^{3+}$, also showing individual contributing currents from electrons originating in different TiO_2 states; (c) modeled total recombination rates vs TiO_2 Fermi energy for each of the new cobalt complexes in this study.

region. This is consistent with our experimentally observed dark currents (Figure 5.5). Figure 5.6b shows that the recombination model can resolve individual contributing currents for electrons originating in different TiO_2 states. These states include free conduction band electrons, as well as localized electrons in an exponential distribution of trap states[40] and "monoenergetic" trap states.[24,41,42]

Figure 5.6c shows the calculated total recombination rates vs TiO_2 quasi-Fermi energy for each of the new cobalt mediators in this study. The $[Co(bpy)_3]^{3+}$ control was omitted from this figure for the following reason: the recombination model assumes an equal electron-transfer rate constant between each of the complexes and the TiO_2 surface. As described in the text above, the lack of additional functional groups on the ligands of $[Co(bpy)_3]^{3+}$ means that it should have the least intrinsic barrier to recombination at the TiO_2 surface, likely leading to the higher dark current slope observed for this complex in Figure 5.5. Rather than arbitrarily adjusting the electron transfer rate constant in the model for $[Co(bpy)_3]^{3+}$, the complex was omitted.

Note that the qualitative shapes of the modeled recombination currents in Figure 5.6c match relatively well with the observed recombination currents in Figure 5.5 at more negative potentials. Specifically, the "bump" observed in the current curves for $[Co(cn\text{-}bpy)_3](ClO_4)_2$ and $[Co(me\text{-}bpy)_3](ClO_4)_2$ mediator solutions can be attributed to recombination originating from monoenergetic trap states in the TiO_2, as shown in Figure 5.6b. Importantly, the modeled recombination currents (calculated assuming stable mediators which only weakly interact with the TiO_2 surface) could *not* account for the potential-independent currents observed for $[Co(cn\text{-}bpy)_3](ClO_4)_2$ and $[Co(me\text{-}bpy)_3](ClO_4)_2$ solutions at more positive potentials. Therefore, the hypothesis that these currents could be caused by complex instability is still plausible.

Additional Discussion on Potential-Independent Recombination Currents. According to previous literature, potential-independent recombination currents (also described as *saturation* recombination current) are expected for recombination from fully occupied deep trap states.[39,43–45] When the rate of recombination from these trap states is slower than the rate of detrapping to the conduction band, their occupancy can be calculated as a function of the Fermi energy by Fermi–Dirac statistics[45] (we note that this condition is made more likely on dyed anodes, because the steric bulk of the dye reduces the rate of recombination). Under this condition, the trap states would be fully occupied when the Fermi energy reached about $4k_BT$ above the potential of the trap states (about 100 meV at room temperature), and a saturation current would result.

Indeed, the recombination currents modeled in this study show that a saturation current is expected for recombination from the monoenergetic trap states of TiO_2 (dashed orange curve of Figure 5.6b). Potential-independent currents have also been experimentally observed for dark currents between a sintered, Nb-doped $SrTiO_3$ electrode and ferricyanide redox mediator in basic buffered water solutions.[44] However, recombination from deep trap states alone cannot explain the saturation currents observed for $[Co(cn\text{-}bpy)_3](ClO_4)_2$ at potentials as high as +0.6 V vs SSCE (Figure 5.5). This would require the existence of additional states in Figure 5.6a; both electronic states for $[Co(cn\text{-}bpy)_3]^{3+}$ in solution at more positive potentials, and the existence of monoenergetic trap states in the TiO_2 as high as +0.7 V vs SSCE, in order for the states to be fully occupied by +0.6 V to give rise to a saturation current. There is no evidence for such positive TiO_2 trap states, either in this study or in the literature.

An alternative hypothesis for the origin of the potential-independent recombination current could be the presence of some redox-active impurity. As a control, cyclic voltammograms were performed for each mediator complex in gBL electrolyte, scanning the full potential range of the

dark current experiments (Figure S5.10, SI), that is, scanning as far negative as the TiO_2 conduction band, approximately −0.75 V vs SSCE. As the complexes' potentials grow more positive, a second redox wave begins to occur within the solvent window at more negative potentials, consistent with the $Co^{1+/2+}$ couple. In the case of $[Co(cn\text{-}bpy)_3](ClO_4)_2$, a $Co^{1+/2+}$ wave occurred with an $E_{1/2}$ of −0.35 V vs SSCE, and a second, less reversible wave was present with an $E_{1/2}$ of approximately −0.58 V vs SSCE. This set of two waves for the $Co^{1+/2+}$ couple in gBL is very similar to the voltammogram shown for the $Co^{2+/3+}$ couple in acetonitrile (Figure 5.2). As discussed in the SI, this result is consistent with enhanced complex stability in gBL relative to acetonitrile, but still dissociating a cn-bpy ligand after reduction of the complex. Moreover, if a redox-active impurity were responsible for the unusual dark current behavior observed for $[Co(cn\text{-}bpy)_3](ClO_4)_2$, we would expect to see its redox activity by CV at potentials as positive as +0.6 V vs SSCE, in order to give rise to the observed potential-independent dark current of Figure 5.5. As an aside, an important insight gained from Figure S5.10 in the SI is that, for high-redox-potential cobalt complex mediators, reduction of Co^{2+} to Co^{1+} by conduction band electrons could potentially contribute to recombination currents.

Another alternative hypothesis for the origin of the potential-independent recombination current could be direct recombination between Co^{3+} complex and electrons in the FTO substrate beneath the TiO_2 film. This is unlikely due to the use of a dense TiO_2 blocking layer between the FTO and the mesoporous TiO_2 film. Regardless, controls were performed to eliminate FTO recombination as a possibility. Figure 5.7 shows recombination currents for cells containing $[Co(cn\text{-}bpy)_3](ClO_4)_2$ mediator on different anodes, including bare FTO, FTO/dense layer TiO_2, FTO/dense layer/mesoporous TiO_2, and FTO/dense layer/mesoporous TiO_2/Z907 sensitizer.

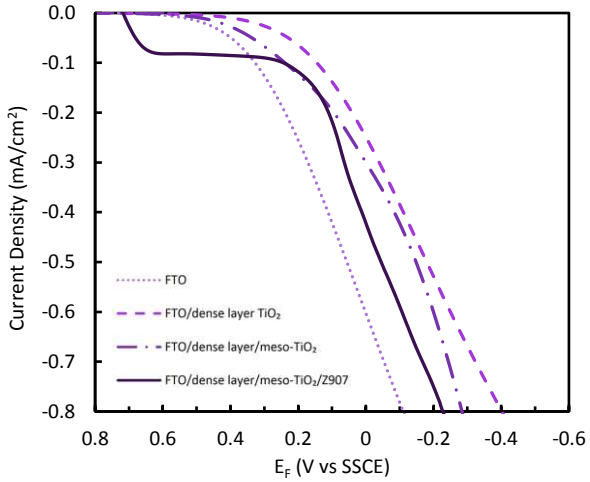

Figure 5.7 Dark current densities on various anodes vs anode quasi-Fermi level for 40 mM $[Co(cn\text{-}bpy)_3](ClO_4)_2$, half of which was oxidized to Co^{3+} with a stock solution of $NOBF_4$, and 100 mM $LiClO_4$ in gBL solvent.

Compared to bare FTO anodes, recombination currents were roughly halved with a TiO_2 dense layer, which is much less conductive. Currents were slightly higher on FTO/dense layer/mesoporous TiO_2 anodes due to the higher surface area of the mesoporous TiO_2. Unexpectedly, currents were slightly higher again on anodes dyed with Z907 sensitizer, despite its known steric blocking effect. The opposite was seen for cells containing $[Co(dma\text{-}bpy)_3](ClO_4)_2$ and $[Co(me\text{-}bpy)_3](ClO_4)_2$ mediator solutions; recombination was lower, as expected, on dyed anodes compared to undyed anodes. Most notably, the potential-independent recombination current observed for $[Co(cn\text{-}bpy)_3](ClO_4)_2$ and $[Co(me\text{-}bpy)_3](ClO_4)_2$ mediators was *only* present on dyed anodes, implying that the potential-independent current is caused by some interaction between a redox species and the Z907 sensitizer.

A third alternative hypothesis for the origin of the potential-independent recombination current could be adsorption of the mediator to the TiO_2 surface, whereby the rate of recombination could be limited by the rate of either adsorption or desorption of the mediator. Indeed, carboxylic acid derivatives such as esters and amides have been used as sensitizer anchor groups.[4] Transition metal cyanides have also been shown to adsorb to TiO_2 through ambidentate cyano ligands,[46] so it

seems reasonable to expect that cn-bpy could also adsorb. However, Figure 5.7 also rules out this hypothesis; if the potential-independent recombination current were caused by mediator adsorption, we would expect to see the feature on undyed anodes as well, which was not observed.

In order to test dark currents under cell conditions that more closely mimic a typical DSSC, cells were also run with added 200 mM TBP (a typical concentration for DSSC mediator solutions). Interestingly, after adding TBP to the $[Co(cn\text{-}bpy)_3](ClO_4)_2$ solution, an unidentified precipitate began to gradually form as fine needles. Dark current measurements were repeatedly taken from this mediator solution over time (Figure S5.11, SI). The resulting potential-independent recombination current decreased over time, coinciding with precipitate formation, which indicates that the saturation current is proportional to the concentration of some redox species related to the original mediator in solution. An additional dark current experiment without TBP showed that the saturation current is also independent of scan rate (see Figure S5.12, SI). Both of these results are consistent with a diffusion-limited current (i_l) of some species in solution:[47]

$$i_l = nFAmC^* \tag{5.5}$$

where n is the stoichiometric number of electrons involved in the electrode reaction, F is the Faraday constant, A is the area of the electrode, m is the mass transfer coefficient of the reacting species, and C^* is the bulk concentration of the reacting species.

As our remaining hypothesis, we propose that the reacting species giving rise to the saturation recombination current is some mediator complex species that has lost a bipyridine ligand, that is present in low concentration as determined by the stability constant of the complex, and that interacts with the Z907 dye as required by the results in Figure 5.7. An illustration of a possible interaction is shown in Figure 5.8. Indeed, a previous study by Mosconi et al. performed molecular dynamics simulations which suggested that an associated complex can form between

TiO_2-adsorbed ruthenium based dyes (including Z907) and a $[Co(bpy)_3]^{3+}$ mediator.[48] A positive binding energy was calculated for the associated complex formed between $[Co(bpy)_3]^{3+}$ and Z907 dye, even when the dye carried no formal charge (fully protonated carboxylate anchor groups) due to a partial negative Mulliken charge calculated for the sulfur atoms of the thiocyanate groups.[48] Such an interaction would bring the mediator close to the TiO_2 surface, which should enhance electronic coupling and therefore recombination. We assume that the loss of a bpy ligand would only enhance this interaction.

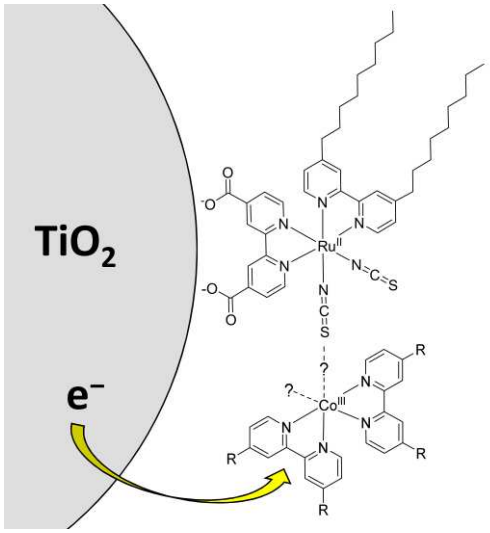

Figure 5.8 Proposed interaction between a labile cobalt complex mediator and Z907 sensitizer, forming a bridged complex via the dye's NCS^- ligands. Such an associated complex could be responsible for observed potential-independent dark currents.

In the above study by Mosconi et al, molecular dynamic simulations were also performed to probe the interaction between $[Co(bpy)_3]^{3+}$ mediator and several fully organic dyes which have achieved high-efficiency DSSCs. Interestingly, nearly zero binding energy was calculated for the associated complexes between $[Co(bpy)_3]^{3+}$ and the neutral organic dyes, in contrast to the neutral Z907 dye.[48] In a subsequent study by Liu et al., the calculated resistance to recombination between $[Co(bpy)_3]^{3+}$ and TiO_2 electrons was found to be 10–100 times lower for Z907-dyed anodes when compared to those dyed with the fully organic Y123 dye, one of the top-performing DSSC

sensitizers at the time.[49] Therefore, it was of interest to test the dark currents of our $[Co(cn\text{-}bpy)_3](ClO_4)_2$ mediator on anodes dyed with an organic dye.

For this purpose, we chose a commercially available donor–acceptor-type organic dye, RK1, which is structurally similar to Y123. The dark currents observed on RK1-sensitized anodes are provided in Figure S5.13, SI, along with the structure of RK1. Interestingly, a nearly potential-independent recombination current was still observed, though its magnitude was roughly one-third that of Z907-sensitized anodes. The magnitude difference could be explained by differences in dye coverage and packing, different steric effects of the dyes, differences in the ability to attenuate the electronic coupling between the mediator and TiO_2, or differences in the dyes' abilities to bind with the Co^{3+} complexes near the TiO_2 surface.[49] It may be possible that unstable mediator could interact with the nitrile group of RK1 similarly to the SCN^- of Z907 as shown in Figure 5.8.

Discussion and Implications of Cobalt Complex Mediator Instability on DSSC Performance. The precise effect that mediator complex instability should have on overall DSSC performance is difficult to predict, but would certainly depend on the extent to which ligand substitution occurs, and the ultimate speciation of the new complex formed. Other ligands in solution which could replace the lost bipyridyl ligand include CH_3CN solvent (if used), TBP additive, or possibly trace H_2O or NCS^- (the NCS^- ligand may be present in very small concentrations in DSSCs which employ the archetypal heteroleptic $RuL_2(NCS)_2$-type dyes, as a rare decomposition product of the excited dye).[4] Of these ligands, the relative coordinating abilities are expected to decrease in the order TBP ≈ NCS^- > H_2O > CH_3CN,[28] and the most abundant ligands are CH_3CN and TBP (a typical TBP concentration in DSSC mediator solutions is 200 mM). Therefore, TBP seems the most likely candidate to replace a dissociated bipyridyl ligand in a typical DSSC cobalt mediator solution.

If, in DSSCs mediated by cobalt tris(bipyridyl) complexes, TBP additive replaces bipyridyl ligands to some extent, we can predict some possible effects. For example, a $[Co(L)_2(TBP)_2]^{n+}$ species would likely have a more negative redox potential than its $[Co(L)_3]^{n+}$ parent complex, due to the electron-donating nature of the *tert*-butyl group. If this species formed to a large enough extent, it could negatively shift the redox potential of the electrolyte. This would have the effect of *reducing* the V_{oc} and, therefore, the overall efficiency of the cell. In addition, a $[Co(L)_2(TBP)_2]^{n+}$ species might have higher charge transfer resistance with the cathode, the sensitizer, and/or the TiO_2; electron transfer for $[Co(t\text{-Bu-bpy})_3]^{2+/3+}$ (*t*-Bu-bpy = 4,4'-di-*tert*-butylbipyridine) has been found to be significantly nonadiabatic.[50]

A recent study tested the 2000 h photostability of DSSCs with Z907 dye and acetonitrile electrolyte containing $[Co(bpy)_3]^{2+/3+}$ mediator and TBP additive.[51] The efficiency of these cells deceased by 34% over the course of the study. Some of the loss in efficiency was attributed to increases in both the counter electrode charge transfer resistance and Nernst diffusion resistance over time.[51] Interestingly, the gradual decomposition of $[Co(bpy)_3]^{2+/3+}$ to some species such as $[Co(bpy)_2(TBP)_2]^{2+/3+}$ could contribute to both higher charge transfer resistance at the cathode and higher diffusion resistance due to the bulk that the *tert*-butyl groups would add to the complex. However, considering the high K_3 constant we found for $[Co(bpy)_3](ClO_4)_2$, it seems unlikely that the ligand substitution would occur to such an extent as to account for *all* the drop in efficiency.

Preliminary DSSC Testing of New Cobalt Complex Mediators. In order to probe the performance of our new, high-redox-potential cobalt mediators, DSSC cells were characterized employing each of the mediators in gBL solution with Z907-sensitized anodes. While these cells were highly unoptimized, results are useful for comparison of the performance of the new mediators relative to a $[Co(bpy)_3](ClO_4)_2$ control, to determine if further testing of the new

mediators is warranted. The new $[Co(cn\text{-}bpy)_3](ClO_4)_2$ complex was not tested in a DSSC due to its much lower solubility and gradual precipitation upon addition of TBP. Experimental details for DSSC testing are provided in the SI, as well as testing results in Figure S5.14 and Table S5.5, along with a detailed discussion.

Neither $[Co(dma\text{-}bpy)_3](ClO_4)_2$ nor $[Co(me\text{-}bpy)_3](ClO_4)_2$ mediators resulted in improved overall efficiency relative to $[Co(bpy)_3](ClO_4)_2$, owing to significantly lower photocurrents. Both new complexes did, however, achieve higher V_{oc} values than $[Co(bpy)_3](ClO_4)_2$ mediator. Perhaps most promising, the $[Co(dma\text{-}bpy)_3](ClO_4)_2$ complex has a redox potential that is 172 mV more positive than that of $[Co(bpy)_3](ClO_4)_2$, and was able to achieve a V_{oc} that was 135 mV greater. Open-circuit voltage decay (OCVD) measurements allowed for the calculation of TiO_2 electron lifetimes, which are limited by recombination with the oxidized mediator. Electron lifetimes were higher for $[Co(dma\text{-}bpy)_3](ClO_4)_2$ mediator than for $[Co(bpy)_3](ClO_4)_2$ at most electron energies, indicating slower overall recombination. By contrast, electron lifetimes with $[Co(me\text{-}bpy)_3](ClO_4)_2$ mediator were equal or smaller at all electron energies, likely owing to a significant saturation dark current observed for this complex, which we hypothesize is caused by complex instability.

Results of current transient experiments indicate that the short-circuit current (J_{sc}) is limited by mass transport of the mediator complexes in all cases, though this limitation is more severe for the larger $[Co(dma\text{-}bpy)_3](ClO_4)_2$ and $[Co(me\text{-}bpy)_3](ClO_4)_2$ complexes. Finally, incident photon-to-current efficiency (IPCE) values for $[Co(dma\text{-}bpy)_3](ClO_4)_2$ and $[Co(me\text{-}bpy)_3](ClO_4)_2$ mediators were roughly one-half and one-tenth those found for $[Co(bpy)_3](ClO_4)_2$, respectively. This reduced IPCE is most likely caused by a lower dye regeneration quantum yield by the high-

redox-potential cobalt mediators, owing to a smaller driving force for reduction of the oxidized dye (see the discussion in the SI).

In summary, preliminary DSSC testing showed that our new, high-redox-potential $[Co(dma\text{-}bpy)_3](ClO_4)_2$ mediator achieves significantly higher V_{oc} than $[Co(bpy)_3](ClO_4)_2$, and shows less recombination current. Overall efficiencies in these cells suffered from low photocurrents. However, significant improvements in photocurrent should be achievable by optimizing cell conditions. Mass transport limitations of the mediator could be significantly reduced by using a less viscous solvent[17] or through the use of sensitizers with higher extinction coefficients, which then allows for thinner TiO_2 films.[52] Furthermore, employing a sensitizer with a more positive redox potential should result in a higher dye regeneration quantum yield and, therefore, higher photocurrents.

5.4 Conclusions

We have synthesized and characterized three new, high-potential cobalt complexes and examined them as possible redox mediators for high-potential dye-sensitized solar cells. Multiple pieces of evidence indicate decreasing complex stabilities as the redox potentials increase. In the case of $[Co(cn\text{-}bpy)_3](ClO_4)_2$, these included multiple waves in the cyclic voltammetry analysis in acetonitrile solution, a color change upon addition of TBP indicating the formation of a new species, and direct NMR evidence of dissociated free cn-bpy ligand in acetonitrile solution at 25 °C, despite elemental analysis results indicating that the complex began with the expected 3:1 ligand-to-cobalt ratio. DSSC recombination currents followed the stability trends of the complexes as determined by NMR.

The above results reveal that the instability of the $[Co(me\text{-}bpy)_3](ClO_4)_2$ and $[Co(cn\text{-}bpy)_3](ClO_4)_2$ complexes make them poor choices as mediators in DSSCs. In addition, these two complexes were limited by much lower solubilities than typical mediator concentrations in DSSCs, though the selection of different counterions could likely alleviate this. The $[Co(dma\text{-}bpy)_3](ClO_4)_2$ complex showed superior stability vs that of even $[Co(bpy)_3](ClO_4)_2$ despite having a more positive redox potential. Preliminary DSSC testing also indicates that further testing of this complex is warranted for more optimized, high-potential DSSC studies.

Our findings highlight the importance of examining the stabilities of novel mediator complexes, especially high-potential complexes, for DSSC applications. The NMR quantification of free, dissociated ligand used in this study is a quick, direct experiment to determine an approximate stability constant. The complex instabilities found herein also show the importance of designing ligand structures alternative to bipyridine. Indeed, it was likely no mistake that many of the higher-potential cobalt complexes which have already been studied possess phenanthroline, terpyridine, and other more strongly coordinating ligands.[15] Moving forward, a focal point should be toward clathrochelating ligands that can retain extremely high stabilities even with highly electron-withdrawing groups. Some examples of cobalt complexes with highly coordinating ligands are already beginning to appear in the literature.[53,54] The present studies support that direction for future DSSC research.

REFERENCES

(1) Desilvestro, J.; Grätzel, M.; Kavan, L.; Moser, J.; Augustynski, J. Highly Efficient Sensitization of Titanium Dioxide. *J. Am. Chem. Soc.* **1985**, *107*, 2988–2990.

(2) O'Regan, B.; Grätzel, M. A Low-Cost, High-Efficiency Solar Cell Based on Dye-Sensitized Colloidal TiO_2 Films. *Nature* **1991**, *353*, 737–740.

(3) Grätzel, M. Conversion of Sunlight to Electric Power by Nanocrystalline Dye-Sensitized Solar Cells. *J. Photochem. Photobiol. Chem.* **2004**, *164*, 3–14.

(4) Hagfeldt, A.; Boschloo, G.; Sun, L.; Kloo, L.; Pettersson, H. Dye-Sensitized Solar Cells. *Chem. Rev.* **2010**, *110*, 6595–6663.

(5) Giribabu, L.; Kanaparthi, R. K.; Velkannan, V. Molecular Engineering of Sensitizers for Dye-Sensitized Solar Cell Applications. *Chem. Rec.* **2012**, *12*, 306–328.

(6) Argazzi, R.; Murakami Iha, N. Y.; Zabri, H.; Odobel, F.; Bignozzi, C. A. Design of Molecular Dyes for Application in Photoelectrochemical and Electrochromic Devices Based on Nanocrystalline Metal Oxide Semiconductors. *Coord. Chem. Rev.* **2004**, *248*, 1299–1316.

(7) Robertson, N. Optimizing Dyes for Dye-Sensitized Solar Cells. *Angew. Chem. Int. Ed.* **2006**, *45*, 2338–2345.

(8) Hamann, T. W.; Jensen, R. A.; Martinson, A. B. F.; Ryswyk, H. V.; Hupp, J. T. Advancing Beyond Current Generation Dye-Sensitized Solar Cells. *Energy Environ. Sci.* **2008**, *1*, 66–78.

(9) Elliott, C. M. Dye-Sensitized Solar Cells: Out with Both Baby and Bathwater. *Nat. Chem.* **2011**, *3*, 188–189.

(10) Hamann, T. W. The End of Iodide? Cobalt Complex Redox Shuttles in DSSCs. *Dalton Trans.* **2012**, *41*, 3111–3115.

(11) Hao, F.; Dong, P.; Luo, Q.; Li, J.; Lou, J.; Lin, H. Recent Advances in Alternative Cathode Materials for Iodine-Free Dye-Sensitized Solar Cells. *Energy Environ. Sci.* **2013**, *6*, 2003–2019.

(12) Huang, S. Y.; Schlichthörl, G.; Nozik, A. J.; Grätzel, M.; Frank, A. J. Charge Recombination in Dye-Sensitized Nanocrystalline TiO_2 Solar Cells. *J. Phys. Chem. B* **1997**, *101*, 2576–2582.

(13) Nusbaumer, H.; Moser, J.-E.; Zakeeruddin, S. M.; Nazeeruddin, M. K.; Grätzel, M. $Co^{II}(dbbip)_2^{2+}$ Complex Rivals Tri-Iodide/Iodide Redox Mediator in Dye-Sensitized Photovoltaic Cells. *J. Phys. Chem. B* **2001**, *105*, 10461–10464.

(14) Mathew, S.; Yella, A.; Gao, P.; Humphry-Baker, R.; Curchod, B. F. E.; Ashari-Astani, N.; Tavernelli, I.; Rothlisberger, U.; Nazeeruddin, M. K.; Grätzel, M. Dye-Sensitized Solar Cells with 13% Efficiency Achieved through the Molecular Engineering of Porphyrin Sensitizers. *Nat. Chem.* **2014**, *6*, 242–247.

(15) Feldt, S. M.; Lohse, P. W.; Kessler, F.; Nazeeruddin, M. K.; Grätzel, M.; Boschloo, G.; Hagfeldt, A. Regeneration and Recombination Kinetics in Cobalt Polypyridine Based Dye-Sensitized Solar Cells, Explained Using Marcus Theory. *Phys. Chem. Chem. Phys.* **2013**, *15*, 7087–7097.

(16) Sapp, S. A.; Elliott, C. M.; Contado, C.; Caramori, S.; Bignozzi, C. A. Substituted Polypyridine Complexes of Cobalt(II/III) as Efficient Electron-Transfer Mediators in Dye-Sensitized Solar Cells. *J. Am. Chem. Soc.* **2002**, *124*, 11215–11222.

(17) Nelson, J. J.; Amick, T. J.; Elliott, C. M. Mass Transport of Polypyridyl Cobalt Complexes in Dye-Sensitized Solar Cells with Mesoporous TiO_2 Photoanodes. *J. Phys. Chem. C* **2008**, *112*, 18255–18263.

(18) Nazeeruddin, M. D. K.; Kalyanasundaram, K.; Grätzel, M.; Patrick Sullivan, B.; Morris, K. One-Pot Synthesis of Tetrahydronium Tris(4,4′-Dicarboxylato-2,2′-Bipyridine)-Ruthenium(II) Dihydrate. *Inorg. Synth.* **1998**, *32*, 181–186.

(19) Bos, K. D.; Kraaijkamp, J. G.; Noltes, J. G. Improved Synthesis of 4,4′-Disubstituted-2,2′-Bipyridines. *Synth. Commun.* **1979**, *9*, 497–504.

(20) Burfield, D. R.; Smithers, R. H. Desiccant Efficiency in Solvent Drying. 3. Dipolar Aprotic Solvents. *J. Org. Chem.* **1978**, *43*, 3966–3968.

(21) Coppinger, G. M. Preparations of N,N-Dimethylamides. *J. Am. Chem. Soc.* **1954**, *76*, 1372–1373.

(22) Baxter, P. N. W.; Connor, J. A. Bipyridinedicarbonitrile Complexes of Molybdenum and Tungsten. *J. Organomet. Chem.* **1988**, *355*, 193–196.

(23) Kiselev, E.; Agama, K.; Pommier, Y.; Cushman, M. Azaindenoisoquinolines as Topoisomerase I Inhibitors and Potential Anticancer Agents: A Systematic Study of Structure–Activity Relationships. *J. Med. Chem.* **2012**, *55*, 1682–1697.

(24) Ondersma, J. W.; Hamann, T. W. Measurements and Modeling of Recombination from Nanoparticle TiO_2 Electrodes. *J. Am. Chem. Soc.* **2011**, *133*, 8264–8271.

(25) Ashbrook, L. N.; Elliott, C. M. Dye-Sensitized Solar Cell Studies of a Donor-Appended Bis(2,9-Dimethyl-1,10-Phenanthroline) Cu(I) Dye Paired with a Cobalt-Based Mediator. *J. Phys. Chem. C* **2013**, *117*, 3853–3864.

(26) Ondersma, J. W.; Hamann, T. W. Impedance Investigation of Dye-Sensitized Solar Cells Employing Outer-Sphere Redox Shuttles. *J. Phys. Chem. C* **2010**, *114*, 638–645.

(27) Ashbrook, L. N.; Elliott, C. M. Sulfide Modification of Dye-Sensitized Solar Cell Gold Cathodes for Use with Cobalt Polypyridyl Mediators. *J. Phys. Chem. C* **2014**, *118*, 16643–16650.

(28) Díaz-Torres, R.; Alvarez, S. Coordinating Ability of Anions and Solvents Towards Transition Metals and Lanthanides. *Dalton Trans.* **2011**, *40*, 10742–10750.

(29) Koh, T. M.; Nonomura, K.; Mathews, N.; Hagfeldt, A.; Grätzel, M.; Mhaisalkar, S. G.; Grimsdale, A. C. Influence of 4-Tert-Butylpyridine in DSCs with $Co^{II/III}$ Redox Mediator. *J. Phys. Chem. C* **2013**, *117*, 15515–15522.

(30) Beck, M. T.; Nagypál, I. *Chemistry of Complex Equilibria*; Williams, D. R., Ed.; Halsted Press: New York, 1990.

(31) Irving, H.; Mellor, D. H. The Stability of Metal Complexes of 1,10-Phenanthroline and Its Analogues. Part I. 1,10-Phenanthroline and 2,2′-Bipyridyl. *J. Chem. Soc. Resumed* **1962**, 5222–5237.

(32) Brisig, B.; Constable, E. C.; Housecroft, C. E. Metal-Directed Assembly of Combinatorial Libraries—Principles and Establishment of Equilibrated Libraries with Oligopyridine Ligands. *New J. Chem.* **2007**, *31*, 1437–1447.

(33) Makrlík, E.; Vaňura, P. Stability Constants of tris(2,2′-Bipyridine) Complexes of Fe^{2+}, Co^{2+}, Ni^{2+}, Cu^{2+} and Zn^{2+} in 1,2-Dichloroethane Saturated with Water. *Colloids Surf.* **1992**, *68*, 195–197.

(34) Note, the same effect was not observed for $[Co(bpy)_3](ClO_4)_2$, but quantification of changes in free bpy concentration were difficult due to the overlap of the free bpy NMR peaks with the broadened TBP signals.

(35) Wang, P.; Zakeeruddin, S. M.; Moser, J. E.; Nazeeruddin, M. K.; Sekiguchi, T.; Grätzel, M. A Stable Quasi-Solid-State Dye-Sensitized Solar Cell with an Amphiphilic Ruthenium Sensitizer and Polymer Gel Electrolyte. *Nat. Mater.* **2003**, *2*, 402–407.

(36) Liu, Y.; Jennings, J. R.; Huang, Y.; Wang, Q.; Zakeeruddin, S. M.; Grätzel, M. Cobalt Redox Mediators for Ruthenium-Based Dye-Sensitized Solar Cells: A Combined Impedance Spectroscopy and Near-IR Transmittance Study. *J. Phys. Chem. C* **2011**, *115*, 18847–18855.

(37) Scott, M. J.; Nelson, J. J.; Caramori, S.; Bignozzi, C. A.; Elliott, C. M. Cis-Dichloro-bis(4,4‘-Dicarboxy-2,2-bipyridine)osmium(II)-Modified Optically Transparent Electrodes: Application as Cathodes in Stacked Dye-Sensitized Solar Cells. *Inorg. Chem.* **2007**, *46*, 10071–10078.

(38) The careful reader will notice that dark currents published by Feldt *et al.*[15] are about 1 order of magnitude larger than those in the present study. This is easily explained, as it has already been shown that the diffusion coefficient of a cobalt complex within TiO_2 is about 1 order of magnitude smaller in gBL than in acetonitrile.[17]

(39) Gerischer, H. Charge Transfer Processes at Semiconductor-Electrolyte Interfaces in Connection with Problems of Catalysis. *Surf. Sci.* **1969**, *18*, 97–122.

(40) Fabregat-Santiago, F.; Mora-Seró, I.; Garcia-Belmonte, G.; Bisquert, J. Cyclic Voltammetry Studies of Nanoporous Semiconductors. Capacitive and Reactive Properties of Nanocrystalline TiO_2 Electrodes in Aqueous Electrolyte. *J. Phys. Chem. B* **2003**, *107*, 758–768.

(41) Boschloo, G.; Fitzmaurice, D. Spectroelectrochemical Investigation of Surface States in Nanostructured TiO_2 Electrodes. *J. Phys. Chem. B* **1999**, *103*, 2228–2231.

(42) Bisquert, J.; Fabregat-Santiago, F.; Mora-Seró, I.; Garcia-Belmonte, G.; Barea, E. M.; Palomares, E. A Review of Recent Results on Electrochemical Determination of the Density of Electronic States of Nanostructured Metal-Oxide Semiconductors and Organic Hole Conductors. *Inorganica Chim. Acta* **2008**, *361*, 684–698.

(43) Vandermolen, J.; Gomes, W. P.; Cardon, F. Investigation on the Kinetics of Electroreduction Processes at Dark TiO_2 and $SrTiO_3$ Single Crystal Semiconductor Electrodes. *J. Electrochem. Soc.* **1980**, *127*, 324–328.

(44) Salvador, P.; Gutiérrez, C. Mechanisms of Charge Transfer at the Semiconductor-Electrolyte Interface I. Kinetics of Electroreduction at Dark of $Fe(CN)_6^{3-}$ and $IrCl_6^{2-}$ in Aqueous Solution on a Sintered Nb-doped n-$SrTiO_3$ Electrode: Influence of pH. *J. Electrochem. Soc.* **1984**, *131*, 326–336.

(45) Bisquert, J.; Zaban, A.; Salvador, P. Analysis of the Mechanisms of Electron Recombination in Nanoporous TiO_2 Dye-Sensitized Solar Cells. Nonequilibrium Steady-State Statistics and Interfacial Electron Transfer via Surface States. *J. Phys. Chem. B* **2002**, *106*, 8774–8782.

(46) Vrachnou, E.; Grätzel, M.; McEvoy, A. J. Efficient Visible Light Photoresponse Following Surface Complexation of Titanium Dioxide with Transition Metal Cyanides. *J. Electroanal. Chem. Interfacial Electrochem.* **1989**, *258*, 193–205.

(47) Bard, A. J.; Faulkner, L. R. *Electrochemical Methods: Fundamentals and Applications*; 2nd ed.; John Wiley & Sons, Inc.: Hoboken, NJ, 2001.

(48) Mosconi, E.; Yum, J.-H.; Kessler, F.; Gómez García, C. J.; Zuccaccia, C.; Cinti, A.; Nazeeruddin, M. K.; Grätzel, M.; De Angelis, F. Cobalt Electrolyte/Dye Interactions in Dye-Sensitized Solar Cells: A Combined Computational and Experimental Study. *J. Am. Chem. Soc.* **2012**, *134*, 19438–19453.

(49) Liu, Y.; Jennings, J. R.; Zakeeruddin, S. M.; Grätzel, M.; Wang, Q. Heterogeneous Electron Transfer from Dye-Sensitized Nanocrystalline TiO_2 to $[Co(bpy)_3]^{3+}$: Insights Gained from Impedance Spectroscopy. *J. Am. Chem. Soc.* **2013**, *135*, 3939–3952.

(50) Gaddie, R. S.; Moss, C. B.; Elliott, C. M. Cyclic Voltammetric Study of Cobalt Poly-4-*t*-Butylpyridine Ligand Complexes on Glassy Carbon Electrodes: Electrolyte Dependence and Mechanistic Considerations. *Langmuir* **2013**, *29*, 825–831.

(51) Jiang, R.; Anderson, A.; Barnes, P. R. F.; Xiaoe, L.; Law, C.; O'Regan, B. C. 2000 Hours Photostability Testing of Dye Sensitised Solar Cells Using a Cobalt Bipyridine Electrolyte. *J. Mater. Chem. A* **2014**, *2*, 4751–4757.

(52) Feldt, S. M.; Gibson, E. A.; Gabrielsson, E.; Sun, L.; Boschloo, G.; Hagfeldt, A. Design of Organic Dyes and Cobalt Polypyridine Redox Mediators for High-Efficiency Dye-Sensitized Solar Cells. *J. Am. Chem. Soc.* **2010**, *132*, 16714–16724.

(53) Kashif, M. K.; Axelson, J. C.; Duffy, N. W.; Forsyth, C. M.; Chang, C. J.; Long, J. R.; Spiccia, L.; Bach, U. A New Direction in Dye-Sensitized Solar Cells Redox Mediator Development: In Situ Fine-Tuning of the Cobalt(II)/(III) Redox Potential through Lewis Base Interactions. *J. Am. Chem. Soc.* **2012**, *134*, 16646–16653.

(54) Kashif, M. K.; Nippe, M.; Duffy, N. W.; Forsyth, C. M.; Chang, C. J.; Long, J. R.; Spiccia, L.; Bach, U. Stable Dye-Sensitized Solar Cell Electrolytes Based on Cobalt(II)/(III) Complexes of a Hexadentate Pyridyl Ligand. *Angew. Chem. Int. Ed.* **2013**, *52*, 5527–5531.

VI. SUMMARY

This dissertation has presented several studies concerning the use of photoelectrochemical cells that employ molecular light-harvesting materials for the collection of solar energy and its conversion to electrical or chemical energy. The main project described in Chapters II–IV involves the development of water-oxidizing photoelectrochemical cells with two different architectures: organic thin-film photoelectrolysis cells (OTF-PECs) and dye-sensitized metal oxide photoelectrolysis cells (DS-PECs). A secondary project described in Chapter V involved dye-sensitized solar cells (DSSCs) for the collection of solar energy and its conversion to electrical energy.

Chapter II provided important background knowledge and a comprehensive review of literature systems that have achieved photoelectrochemical oxidation of water to O_2 using organic light-harvesting materials. Major conclusions from this review are that (i) the use of interfacial layers appear to be key to enhance the efficiency of charge separation and to decrease the rate of recombination of charge carriers. (ii) Interfacial nanostructuring appears to be a promising strategy to enhance light-harvesting efficiency, allowing for thicker films to collect more light while keeping the domain size of the organic material low. (iii) A variety of strategies have been used to deposit a variety of water-oxidation catalysts (WOCatalysts) in different systems, which can greatly affect the electronic coupling (and therefore the efficiency of charge transfer) between the catalyst and dye for regeneration, as well as between the catalyst and substrate for recombination. There is, as of yet, no clear "best method" for catalyst loading, and the best method is likely to vary with system architecture. However, it has been shown in both architectures that the use of appropriate interfacial layers can help to slow electron scavenging by the catalyst. Finally, (iv) the

long-term stability of organic light-harvesting materials in water-oxidizing PECs has yet to be demonstrated in *any* system to date, and therefore remains to be an important unknown.

Chapter III described the development of a first-generation water-oxidizing photoanode composed of a perylene diimide thin film with photoelectrochemically deposited cobalt oxide WOCatalyst. This anode represents the first and only example in the literature of successful water oxidation by an organic thin-film without the use of an interfacial layer. In characterizing the device performance, it was determined that the largest performance-limiting efficiencies were the charge-transport efficiency (limited by low exciton dissociation efficiency and/or high charge recombination) and the light-harvesting efficiency (limited by the exciton diffusion length, and therefore the thickness of the organic film). It was proposed that the efficiency of a second-generation device might be improved by the use of an appropriate interfacial layer to aid in exciton dissociation and charge separation from the organic thin-film. Alternatively, it was proposed that a dye-sensitized metal oxide architecture might improve both the charge-separation and charge-transport efficiency as well as the light-harvesting efficiency.

Chapter IV described preliminary studies for the use of the same perylene diimide molecule in a dye-sensitized metal oxide architecture. For this study, nanostructured films of three different metal oxides (TiO_2, SnO_2, and WO_3) were prepared and characterized, then studied as substrates for dye sensitization. It was found that surface acidity played a large role in dye loading kinetics and saturation, with the best results on TiO_2, with the most basic surface, and practically no dye loading on WO_3, with the most acidic surface. However, the negative electrochemical potential of the TiO_2 conduction band relative to SnO_2 resulted in lower photocurrent for dyed TiO_2 than dyed SnO_2, as a result of poor charge injection efficiency from the photo-excited dye.

Optimized dying conditions and SnO_2 film thickness allowed for a light-harvesting efficiency >99%, or a >8-fold improvement relative to the first-generation OTF-PEC architecture. When DS-PEC anodes were tested in aqueous solution in the presence of hydroquinone sacrificial reductant, an absorbed-photon-to-current efficiency of 13% was found, which was a >2-fold improvement relative to the first-generation OTF-PEC architecture. However, when cobalt oxide WOCatalyst was deposited by the same photoelectrochemical method as used in the previous system, it did not result in enhanced photocurrent, but instead *decreased* photocurrent. Controls and open-circuit photovoltage measurements indicated that the cobalt was likely deposited directly on the SnO_2 surface, where it could enhance recombination by scavenging electrons from the SnO_2 conduction band. Therefore, proposed directions for future study include (i) alternative conditions for catalyst deposition (for example, lower pH where the SnO_2 surface will become positively charged in order to coulombically repel Co^{2+}), (ii) alternative catalyst preparation and loading strategies (for example, pre-formed cobalt oxide nanoparticles with lengthy, aliphatic anchoring ligands to space the catalyst away from the SnO_2 surface), and (iii) further study of interfacial layers to space the catalyst away from the SnO_2 surface (for example, insulating alumina deposited by atomic layer deposition).

Finally, Chapter V described a secondary project involving solar energy collection and conversion to electrical energy by dye-sensitized solar cells. Specifically, the goal was to increase the voltage (and therefore the overall power conversion efficiency) of DSSCs by studying alternative, high-potential redox mediator such as organometallic cobalt complexes. The redox potentials of the complexes were varied by synthetically incorporating different electron-withdrawing groups onto bidentate bipyridine ligands. Characterization of the resultant cobalt complexes confirmed that such ligands successfully shifted their redox potentials positively, but

also showed evidence for decreased complex stability as the redox potential was shifted more positively due to ligand lability. This instability resulted in high recombination currents in assembled DSSCs. Therefore, future studies were proposed to prepare electron-withdrawing, but also higher-chelating ligands for cobalt complexes that should allow for high redox potential but also high stability.

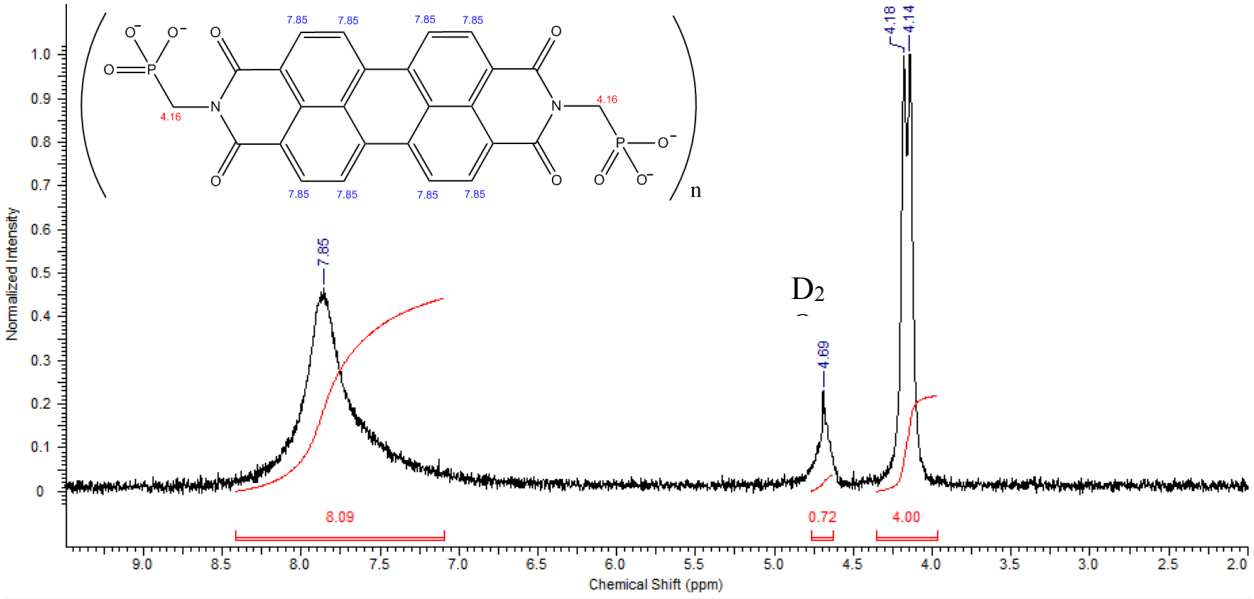

Figure S3.1 ^{1}H-NMR of K_4[PMPDI−4H] (300 MHz in D_2O/NaOD, 64 transients, wet1D solvent suppression). Note the highly broadened aromatic protons, likely due to aggregation, n > 1.[1,2]

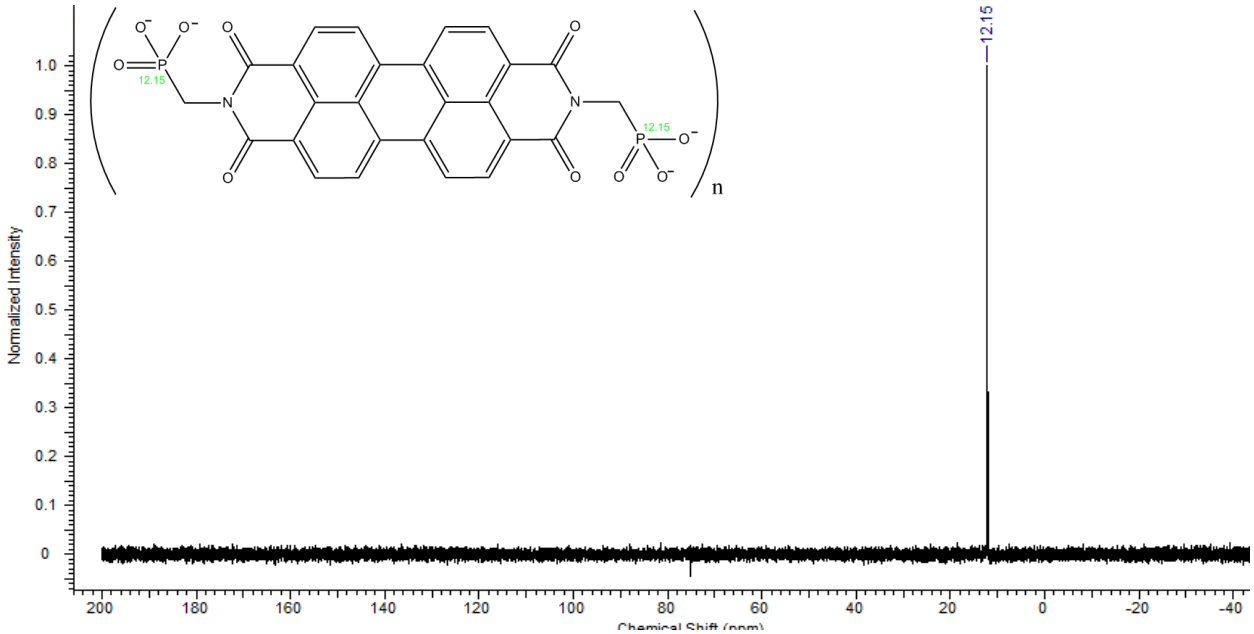

Figure S3.2 ^{31}P-NMR of K_4[PMPDI−4H] (300 MHz in D_2O/NaOD, 512 transients, proton-decoupled).

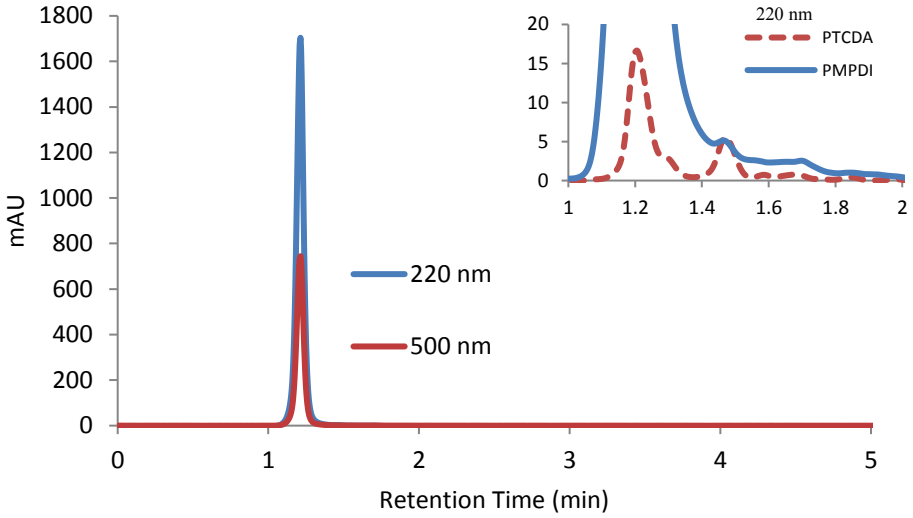

Figure S3.3 HPLC trace and integration results of PMPDI. Solvent: 75% 50 mM NH_4OH, 25% CH_3CN; Flow rate: 3.5 mL/min; Column: Hamilton PRP-1, 7.0 x 305mm, 100 Å pore size. The inset shows a zoomed-in view of the tail of the 220 nm PMPDI signal, and shows that the tail peaks are consistent with trace PTCDA starting material.

It is possible that the PMPDI sample contained trace PTCDA as leftover starting material, (though it was not detectable by NMR). It is also possible that the PMPDI product began to degrade to PTCDA under the chromatography conditions. PMPDI does gradually degrade to PTCDA under highly basic conditions (over tens of minutes in 1 M NaOH, as confirmed by UV–Vis).

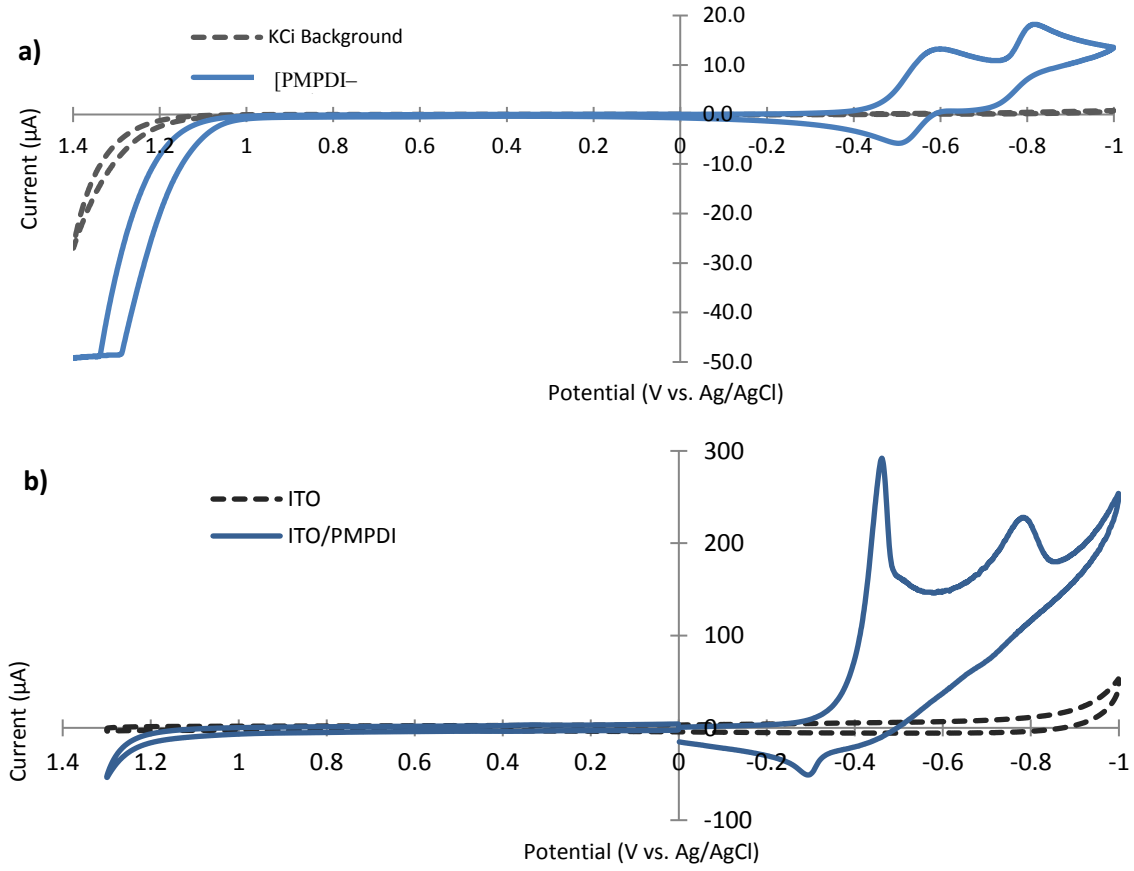

Figure S3.4 Cyclic voltammograms of background and (a) $PMPDI^{4-}$ (aq) in 0.1 M pH 10 potassium carbonate buffer, diamond working electrode, 25 mV/s scan rate (actual species is $[PMPDI{-}4H]^{4-}$ at this pH, see Fig. S3.6), and (b) PMPDI on ITO in 0.1 M pH 7 potassium phosphate buffer, 100 mV/s (actual species is K2-PMPDI at this pH, see Fig. S3.6).

To further investigate the origin of the catalytic anodic wave in Fig. S3.4a, the concentration of oxygen was followed in solution during bulk electrolysis experiments at 1.4 V vs. Ag/AgCl in pH 10 potassium carbonate buffer solutions with and without $PMPDI^{4-}$ (aq), using high surface area glassy-carbon foam electrodes. When PMPDI was present, current densities were generally lower than the same electrode in the buffer alone (a result opposite of the CV experiment above) suggesting an interference with the electrode surface, possibly caused by precipitation of the oxidized PMPDI caused by reduced solubility. Also, the faradaic efficiencies for detected oxygen were much lower when PMPDI was present in solution (average 5% with PMPDI vs. 27%

without), which also indicates some deactivation of the electrode. We therefore conclude that the oxidation wave in the CV of PMPDI may be caused by degradative PMPDI oxidation, or by some PMPDI-assisted oxidation reaction with products other than dioxygen.

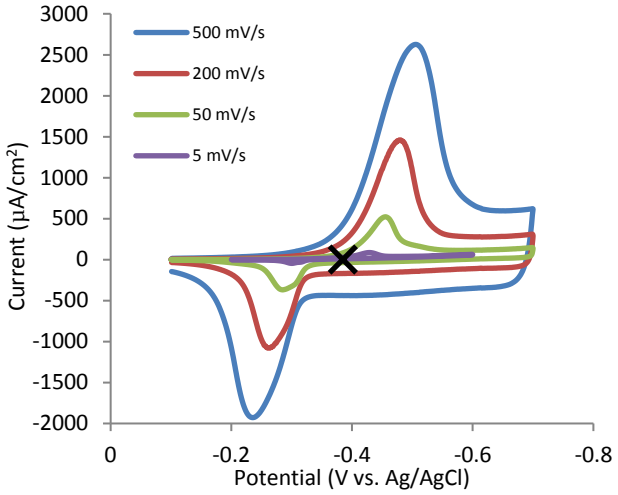

Figure S3.5 Scan rate dependence of the cyclic voltammograms of a PMPDI film on ITO in 0.1 M KPi buffer, pH 7 (actual species is K2-PMPDI at this pH, see Fig. S3.6). The black "**X**" indicates the average reduction onset potential of −0.39 V vs. Ag/AgCl, calculated by extrapolating the linear portion of each reductive wave to the intercept.

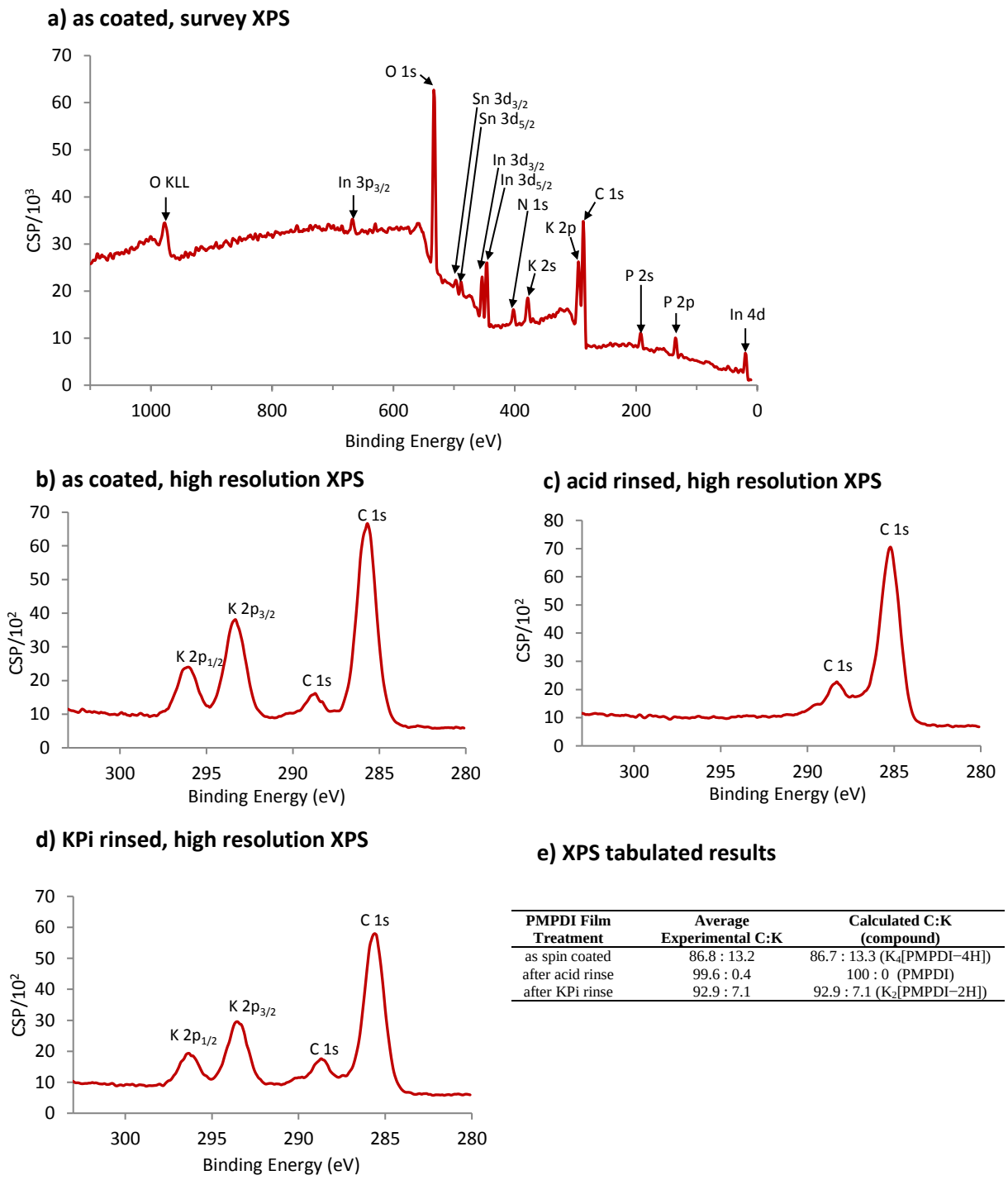

PMPDI Film Treatment	Average Experimental C:K	Calculated C:K (compound)
as spin coated	86.8 : 13.2	86.7 : 13.3 (K_4[PMPDI−4H])
after acid rinse	99.6 : 0.4	100 : 0 (PMPDI)
after KPi rinse	92.9 : 7.1	92.9 : 7.1 (K_2[PMPDI−2H])

Figure S3.6 (a) XPS survey spectrum of a PMPDI film on ITO untreated after spin coating, as well as high resolution XPS spectra of ITO/PMPDI films as coated (b), after submerging 1 minute in 50/50 2 M HCl/ethanol and rinsing with DI water (c), and then after submerging 1 minute in 0.1 M pH 7 KPi buffer and rinsing with DI water (d). High-resolution spectra were used to calculate the C:K ratio of the films. Results (averaged from 3 separate experiments) are tabulated in (e) and compared to calculated values for various levels of PMPDI protonation, thus providing evidence for the protonation state of PMPDI after each phase of treatment.

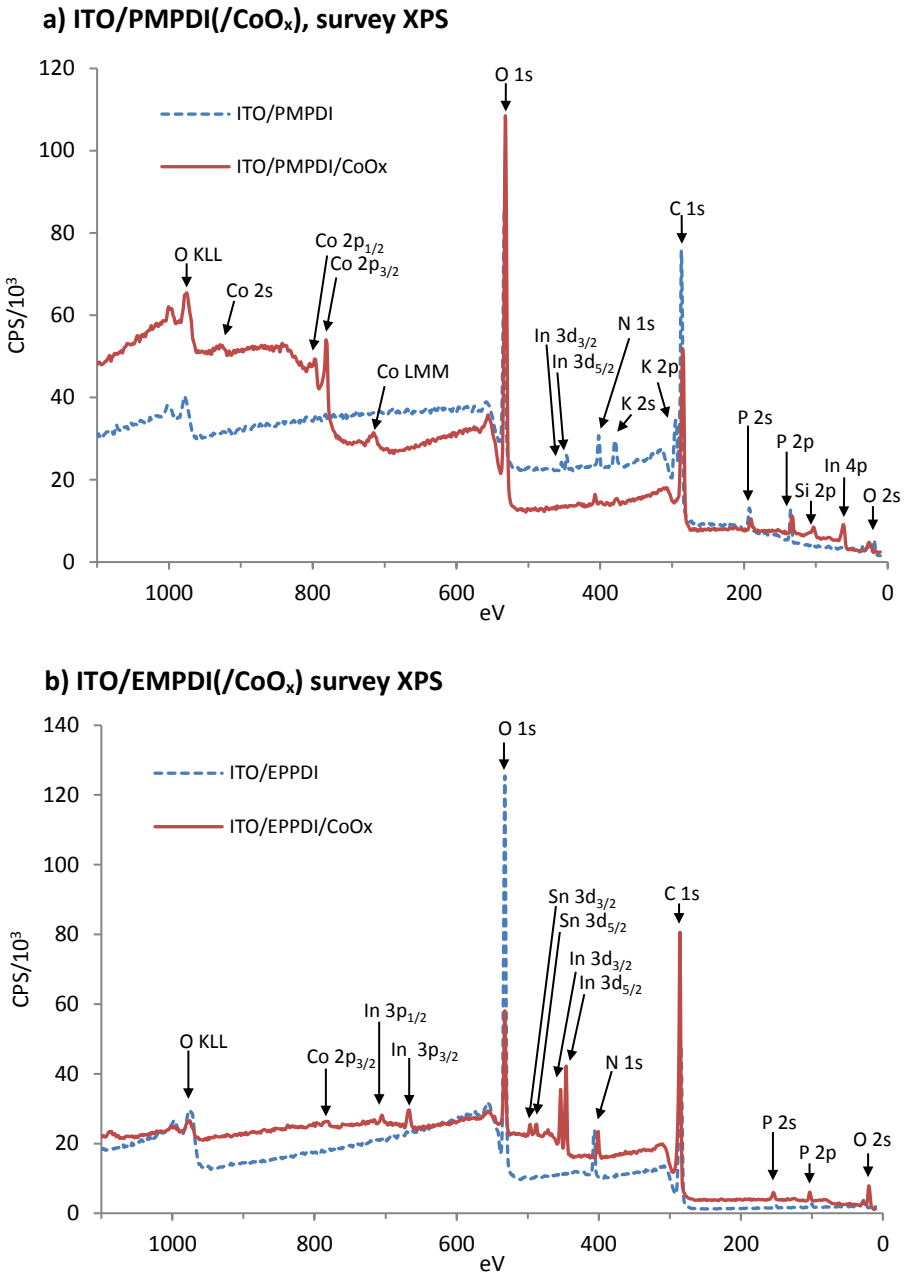

Figure S3.7 (a) XPS of an ITO/PMPDI film before and after CoO_x deposition and rinsing. The presence of cobalt remaining on the film is clear. (b) ITO/EPPDI before and after CoO_x deposition and rinsing. Only trace cobalt is detected.

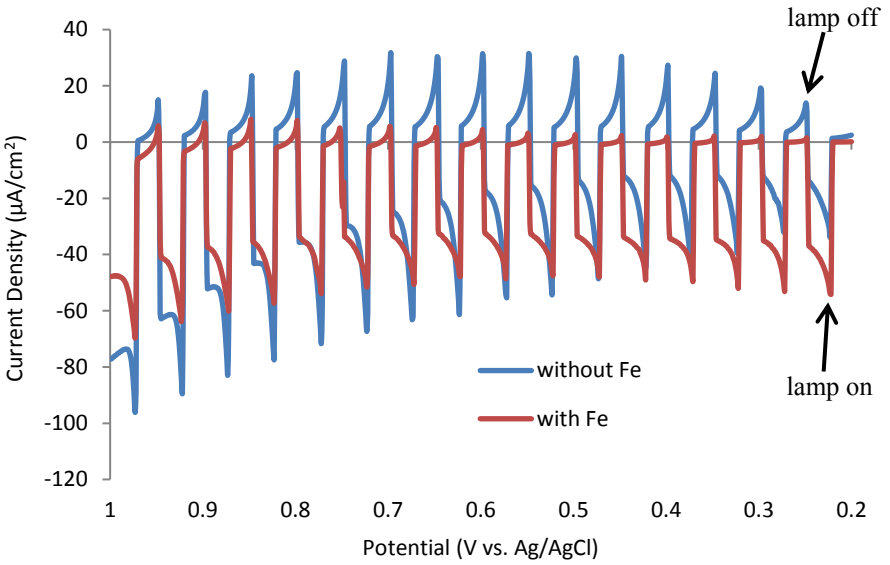

Figure S3.8 ITO/PMPDI/CoO_x photocurrent transients with (red line), and without (blue line), added ~1 mM $K_4Fe(CN)_6$ in 0.1 M pH 7 potassium phosphate buffer, 5 mV/s scan rate starting at 0 V, 5 second transients, approximately 100 mW/cm^2 illumination intensity (315-710 nm). We associate the cathodic current spikes with a performance-limiting recombination between the hole reservoir (i.e., oxidized CoO_x or water oxidation intermediates) with electrons in the PMPDI film. This recombination rate appears to compete with the rate of water oxidation, but not with the oxidation of $Fe^{II}(CN)_6^{4-}$, as the cathodic spikes are greatly reduced when iron is present.

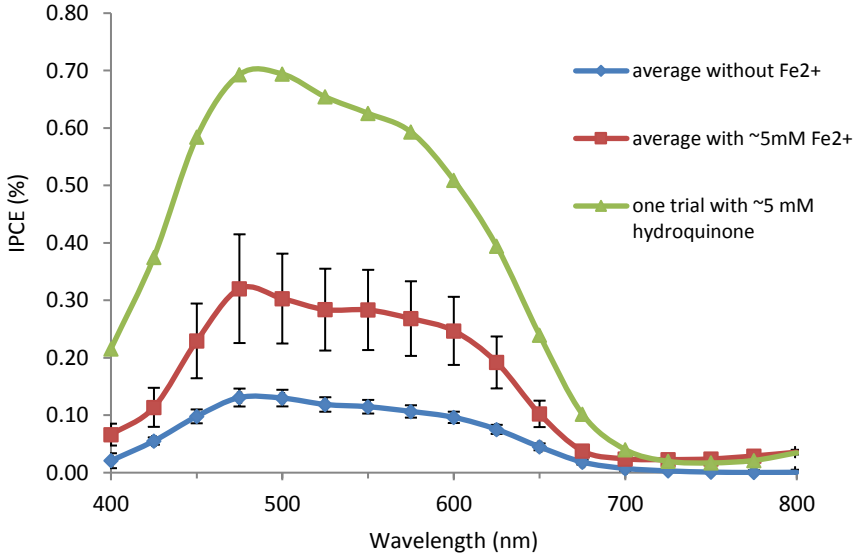

Figure S3.9 Average IPCE for three ITO/PMPDI/CoO_x anodes without (blue) and with (red) added $K_4Fe(CN)_6$ (≈ 5 mM), as well as one trial (green) with added hydroquinone (≈ 5 mM). Experiments were performed in a two-compartment photoelectrochemical cell separated by a glass frit, filled with 0.1 M pH 7 potassium phosphate buffer degassed with argon, using a two-electrode setup with platinum wire counter electrode.

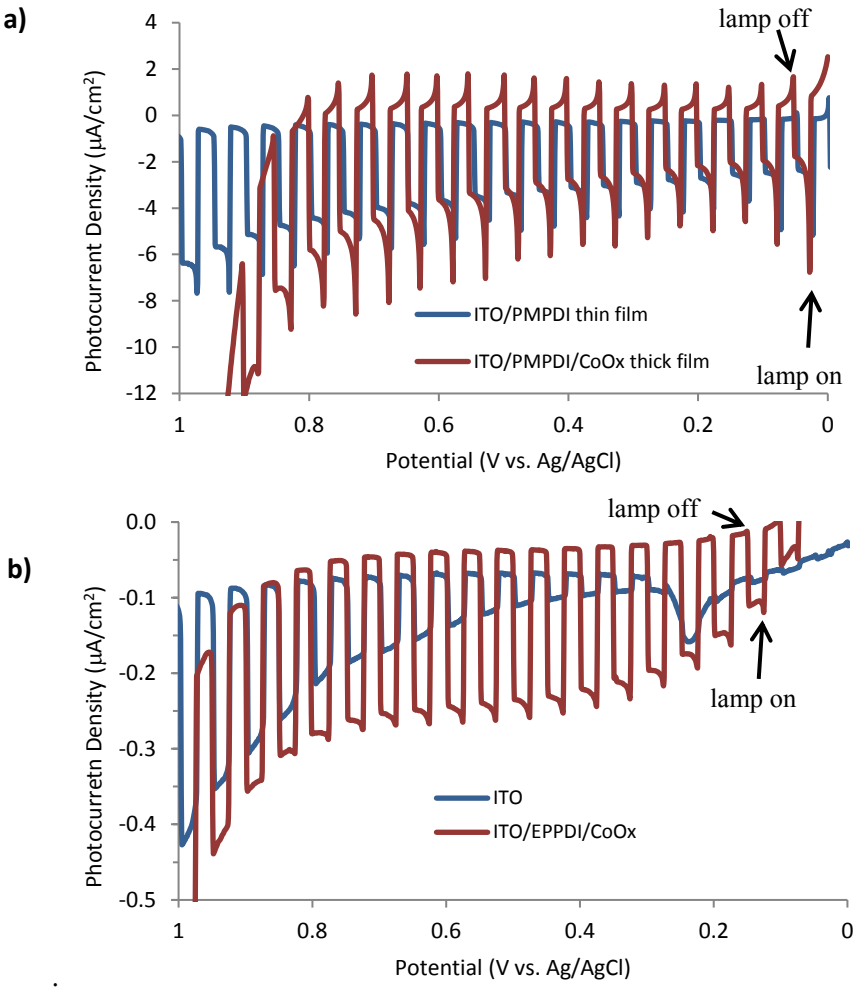

Figure S3.10 (a) Photocurrent transients of an ITO/PMPDI/CoO_x anode employing a thicker, drop-coated PMPDI film (red line). For comparison, photocurrent transients of a typical ITO/PMPDI thin, spin-coated film *without* CoO_x are shown (blue line). (b) Photocurrent transients of an ITO/EPPDI/CoO_x anode (red line). For comparison, photocurrent transients of a naked ITO anode are shown (blue line). All transients were run in 0.1 M pH 7 potassium phosphate buffer solution, 5 mV/s scan rate starting at 0 V, Ag/AgCl reference and Pt wire counter electrodes.

These results show that ITO/PMPDI/CoO_x anodes perform significantly worse when employing thick, drop-cast PMPDI films than the thinner spin-cast films. The presence of cathodic current spikes indicate the presence of CoO_x catalyst, which means that the low photocurrents are likely due to increased exciton recombination in the bulk of the film. In contrast, the lack of cathodic spikes from the ITO/EPPDI/CoO_x anode help to indicate that the catalyst was not

successfully deposited. The very low magnitude of photocurrents could also indicate that the EPPDI film are not in good electrical contact with the ITO substrate.

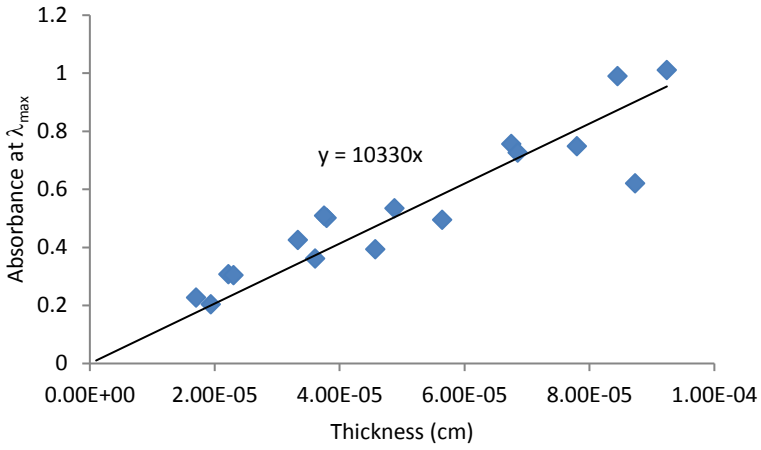

Figure S3.11 Absorption at λ_{max} (UV–Vis) vs. film thickness (optical profilometry) of thick, drop-cast PMPDI films on glass for the estimation of the absorption coefficient of PMPDI films.

Several thick films of PMPDI were prepared by drop casting on glass slides and evaporation under air on a rotary table. Films thus prepared showed poor uniformity, so the absorption spectra were recorded in a grid pattern across the film surface. A razor blade was then used to scrape a channel through the film in the center of each grid region, and the film thickness was determined by measuring the step height between the substrate (bottom of the channel) and the film surface using a ZeMetrics ZeScope Optical Profiler . The film thickness and absorbance at the λ_{max} for each grid region were then plotted in the above graph, and the yielding $\alpha \approx 10{,}000$ cm^{-1} from the slope of the best-fit line. This α value is roughly half of those found in the literaure[50] for films of other PDI derivatives, but this is not necessarily unexpected for a number of reasons: 1) our PMPDI films were formed by drop casting from solution, whereas those in the literature were formed by vacuum vapor deposition,[50] and 2) our films are anionic, and contain large potassium counter ions (deposited as K4-PMPDI under these conditions). Under working

conditions, our films are submerged in pH 7 buffer solution, protonating the film to the K2-PMPDI state and thus shrinking the film further. One of the above thick PMPDI films was submerged in 0.1 M pH 7 KPi buffer and re-analyzed, yielding film thicknesses that were about half of the original, K4-PMPDI films, and an $\alpha \approx 20{,}000\ cm^{-1}$. This value was used to estimate the thicknesses of thinner, spin-cast films.

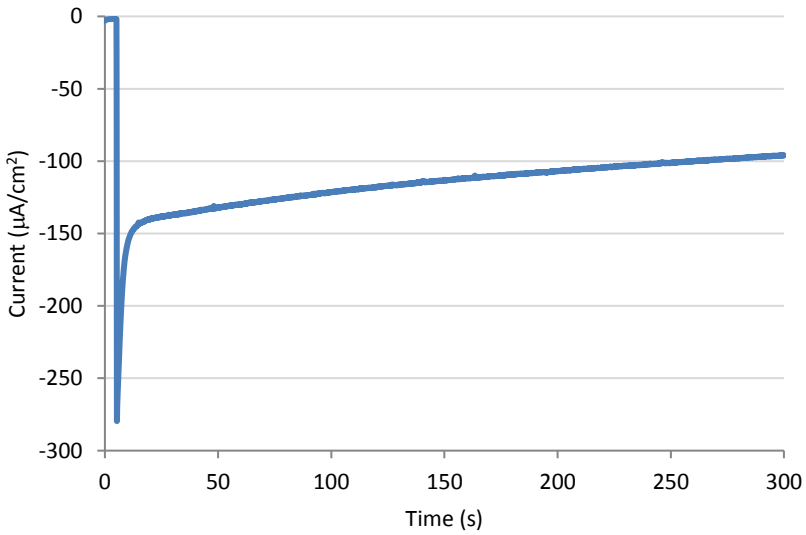

Figure S3.12 A representative example of the gradual photocurrent decay during a water electrolysis experiment of a typical ITO/PMPDI/CoO_x experiment, showing the gradual deactivation of the anode.

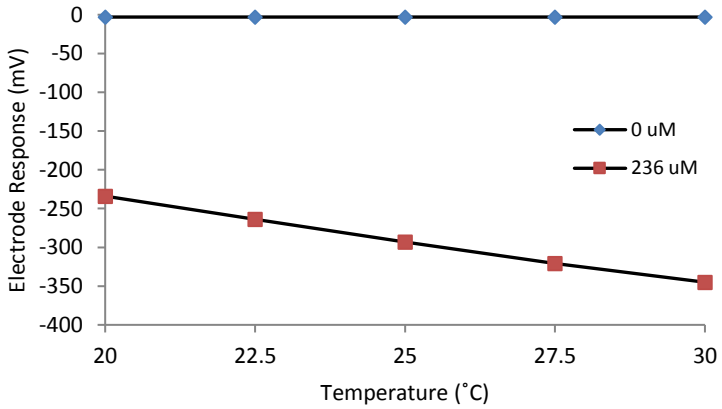

Figure S3.13 A representative calibration of the Clark electrode response as a function of temperature and dissolved oxygen concentration.

Standard solutions were 0.1 M Na_2SO_3[48] (0 %, 0 μM dissolved oxygen) or water vortexed

in air for at least 30 minutes before testing (20.9%, 236 μM dissolved oxygen, accounting for local air pressure). Each solution was suspended in a water bath on a magnetic stirrer/hotplate. The stirring rate was gradually increased until the detector response was independent of the stir rate. The detector response in each standard solution was recorded at regular intervals while the temperature was gradually increased.

Early controls using the above standard solutions as well as oxygen-saturated solution (bubbled with oxygen gas) confirmed that the Clark electrode shows a linear response to dissolved oxygen concentration between 20 and 30 ˚C. It should be noted that the solubility of oxygen in water decreases as temperature increases. Controls showed that, under the stirring rates used, the concentration of dioxygen in a super-saturated solution did not appreciably change (i.e., excess O_2 did not leave solution) during the 5 minute timescale of subsequent water oxidation experiments. It should be noted that even if small amounts of oxygen did escape solution, it would result in a low calculated value for the faradaic efficiency of water oxidation.

Characterization data for N,N'-bis(1-ethylpropyl)-3,4,9,10-perylenediimide (EPPDI)

The perylene diimide derivative EPPDI was synthesized according to the literature.[47] FT-IR (Nicolet SX-60 FT-IR spectrometer with ATR-ZnSe): 2965 cm^{-1} m, 2934 w, 2876 w, 1696 s, 1647 s, 1592 s, 1576 s, 1506 w, 1457 w, 1434 w, 1405 m, 1393 w, 1383 w, 1333 s, 1301 w, 1247 m, 1208 w, 1196 w, 1177 w, 1159 w, 1121 w, 1086 m, 975 w, 960 w, 929 w, 906 w, 852 m, 806 s, 789 w, 783 w, 759 s, 745 m, 706 w. ^{1}H-NMR (300 MHz Varian Inova) ($CDCl_3$): δ = 0.95 (t, 12H), 2.12 (m, 8H), 5.08 (m, 2H), 8.68 (2d, 8H). Elemental Analysis: Calculated for $C_{34}H_{30}N_2O_4$ (found): 76.96% C (75.84), 5.70% H (5.66), 5.28% N (5.34).

REFERENCES

(1) Marcon, R. O.; Brochsztain, S. Characterization of Self-Assembled Thin Films of Zirconium Phosphonate/Aromatic Diimides. *Thin Solid Films* **2005**, *492*, 30–34.

(2) Rodríguez-Abreu, C.; Aubery-Torres, C.; Solans, C.; López-Quintela, A.; Tiddy, G. J. T. Characterization of Perylene Diimide Dye Self-Assemblies and Their Use As Templates for the Synthesis of Hybrid and Supermicroporous Nanotubules. *ACS Appl. Mater. Interfaces* **2011**, *3*, 4133–4141.

(3) Tamizhmani, G.; Dodelet, J. P.; Cote, R.; Gravel, D. Photoelectrochemical Characterization of Thin Films of Perylenetetracarboxylic Acid Derivatives. *Chem. Mater.* **1991**, *3*, 1046–1053.

(4) Falck, D. Amperometric Oxygen Electrodes. *Curr. Sep.* **1997**, *16*, 19–22.

(5) Demmig, S.; Langhals, H. Very Soluble and Photostable Perylene Fluorescent Dyes. *Chem. Ber.* **1988**, *121*, 225–230.

APPENDIX II. SUPPORTING INFORMATION FOR CHAPTER IV

S4.1 Discussion on the Selection of MO_x Materials and Specific Preparation Methods

TiO_2 (anatase) is by far the most studied nanoparticle metal oxide (MO_x) film material for both dye-sensitized solar cells (DSSCs)[1,2] and water splitting, dye sensitized photoelectrolysis cells (WS-DSPECs),[3,4] which makes it an obvious starting point for our studies. However, literature examples exist where perylene derivatives do not have sufficient driving force to photo-inject electrons into the conduction band of TiO_2.[5] Therefore, it is of interest to study other semiconductor materials with E_{CB} positive of that for TiO_2. Other commonly studied, single-metal oxide semiconductors for DSSC and water splitting applications that also have E_{CB} positive of TiO_2 include Fe_2O_3, SnO_2, and WO_3.[6,7] Fe_2O_3, with a bandgap of 2.1 eV, will absorb wavelengths shorter than ~600 nm,[7] and would therefore compete with our PMPDI dye for light absorption.[8] For this reason, Fe_2O_3 was not considered as a semiconductor material for this study. Also relevant is a recent paper by Ronconi *et al*. in which they studied the performance of a cationic perylene diimide (PDI) dye in dye-sensitized photoelectrolysis cells (DS-PECs) on TiO_2, SnO_2, and WO_3 nanoparticle films, finding the best performance on WO_3.[9] It is therefore of interest to compare their results to our own studies using our anionic PDI dye, N,N´-bis(phosphonomethyl)-3,4,9,10-perylenediimide (PMPDI).[8]

Given that TiO_2 films are commonly studied, a variety of TiO_2 nanoparticle pastes are commercially available for the formation of mesoporous nanoparticle films. Studies of DSSC performance as a function of nanocrystalline TiO_2 particle size have found optimal performance for particles that were about 20 nm in diameter,[10,11] due to a balance between dye loading and charge collection efficiency. That is, smaller particle sizes result in higher surface area films, which

improves dye adsorption, but also allows for higher rates of recombination of injected electrons.[10,11] To our knowledge, no such studies have been done for water-splitting DS-PECs, but we predict that a similar trend should hold, with 20 nm particles being the most efficient, because of the similar function and device architectures for both types of devices. Therefore, we chose to begin our studies with a commercial TiO_2 paste from Solaronix, composed of 15–20 nm anatase particles.

SnO_2 has been well-studied in DSSC applications as an alternative semiconductor to TiO_2 for a number of reasons reviewed previously.[12] First, the more positive E_{CB} of SnO_2 relative to TiO_2 allows the use of dye sensitizers with more positive LUMO energy levels. Second, the electron mobility of SnO_2 is significantly higher than that of anatase TiO_2. However, SnO_2-based DSSCs have been shown to suffer from slightly lower dye loading (relative to TiO_2) of sensitizers with acidic anchor groups. As for particle sizes, Chappel and Zaban found improved DSSC performance for SnO_2 anodes after hydrothermally growing particles from 4 nm to 18 nm.[13] Nanoparticle SnO_2 films have also been studied as anode materials in dye-sensitized photoelectrolysis devices.[9,14–16] For our studies, we chose to start with a commercial SnO_2 nanopowder with average particle size of 18 nm (according to specific surface area by gas adsorption analysis), and formed a paste by slight alteration of a published formulation.[14]

Nanostructured WO_3 films have been studied primarily for (photo)electrocatalysis, electrochromic, and gas sensing devices,[17–19] though a few papers have dye-sensitized this material for DSSC[20,21] and WS-DSPEC[9] applications. Unfortunately, we were unable to find a commercial source for WO_3 nanoparticles in our target size range of about 20 nm. We note that a few papers exist which have studied the effect of WO_3 film particle sizes on photoelectrolysis or gas detection

performances,[22–26] usually finding better performance for somewhat larger particles. However, none of these studies are directly relevant to DSSC or WS-DSPEC devices.

Nanostructured WO_3 films have been prepared by a variety of methods, which have been reviewed in the literature.[18,27,28] The preparation method can strongly influence particle size and shape. We chose to narrow our search to sol–gel/hydrothermal methods, with the advantage of cheap scalability, and because TiO_2 nanoparticles for DSSC applications are typically formed by such routes[29] and tend to result in spherical nanoparticles. A recent review of nanostructured WO_3 films for water splitting applications contains a table listing water oxidation photocurrents from a variety of WO_3 films.[18] Of the films prepared by sol−gel methods, a paste formulation by Meda *et al*.[30] showed the highest photocurrents when accounting for the reported film thickness.[30] This also happens to be the same procedure used to prepare WO_3 films in the Ronconi *et al*. study mentioned above,[9] wherein they found that WO_3 was the best performing MO_x film for sensitization with a dicationic PDI dye. For these reasons, we chose the Meda *et al*. WO_3 preparation procedures for our studies.

S4.2 Experimental Details for the Preparation of MO_x Films

S4.2a Preparation of TiO_2 films. The film substrates were conductive fluorine-doped tin oxide (FTO) on glass (TEC 15, Hartford Glass). The glass was cut into 5x7 cm slides, then each piece was scored on the non-conductive side to make 10 (1.2 x 2.5 cm) sections, with two leftover (1 x 2.5 cm) junk pieces. Each glass was then cleaned by soaking in a large crystallization dish containing saturated KOH in isopropanol for 30 min, thoroughly rinsing with DI water, then with ethanol, and allowed to air-dry. Scotch Magic tape (Cat. # 810, 54 ± 1 μm thick according to optical

profilometry) was placed on two parallel sides of each glass slide, securing the slide to the benchtop and forming a channel for doctor-blading.

TiO_2 paste was purchased from Solaronix (Ti-Nanoxide T/SP, reported 18 wt % TiO_2 anatase nanoparticles, 15−20 nm diameter, in terpineol with organic binder) and used as received. For doctor blading, ~0.25 mL of the paste was collected by plastic syringe and deposited onto the end of an FTO substrate in a line perpendicular to the Scotch tape spacers, taking care to avoid any bubbles in the paste. A clean glass stir rod was used to spread the paste across the entire channel using one smooth motion, creating a film. The slide was covered with a petri dish and allowed to settle for 3−5 min to reduce any surface irregularities. After settling, the tape was removed and the slide was placed in a small benchtop furnace (Thermolyne 1300). According to the paste manufacturer's recommendations, the film was gradually heated (~30 °C/min) to 475 °C under air and held at temperature for 30 min to evaporate the solvent, burn off the organic binder, and allow the TiO_2 nanoparticles to sinter together to form a mesoporous film. After calcination, heat was turned off and the furnace door was gradually opened to allow the film to slowly cool (≤1 °C/s). Once cool, the slide was removed and cleaved into individual anodes using glass-nipping pliers.

S4.2b Preparation of SnO_2 Films. A paste of SnO_2 nanoparticles was prepared by slight modification of a published precedure,[14] using a commercial SnO_2 nanopowder (tin(IV) oxide, NanoArc©, Alpha Aesar, Lot Analysis: 99.6% SnO_2, 47 m^2/g specific surface area (SSA) by BET analysis, 18 nm average particle size according to SSA and 6.95 g/cm^3 density). Using a plastic spatula, 800 mg of white SnO_2 powder was weighed into a 20 mL scintillation vial. Next, 1.0 mL of glacial acetic acid (ACS grade, Mallinckrodt) was added as a peptization agent. A Teflon-coated magnetic stir bar was added and used for mixing so that the acid completely wetted the SnO_2 powder, forming a grey paste. The wetted powder was aged in an ultrasonic water bath (Branson

2510) for 5 min. Next, 4.0 mL of water (nanopure, 18 MΩ) was added and the solution was again mixed by stir bar. The mixture was then homogenized using a QSonica Q125 ultrasonic liquid microprocessor (1/8'' probe, held at continuous 80% amplitude for 5 min) to form an opaque, white suspension. Note, an ultrasonic probe (not just an ultrasonic bath) was necessary to sufficiently break up particles to achieve transparent SnO_2 films.

Next, 1.16 g of polyethyleneglycol bisphenol A epichlorohydrin copolymer (PEG-BAE), (Sigma, M_w = 15,000–20,000), was added in small pieces while mixing by stir bar. This PEG-BAE serves as a stabilizing/thickening agent. Once all the PEG-BAE had visibly dissolved, one drop (20 mg) of Triton X-100 (octyl phenoxy polyethoxyethanol, Sigma) was added to aid adhesion to the glass substrate, and the vial was sealed and stirred overnight before use. *The final paste formulation should be ~11 wt % SnO_2, 15 wt % acetic acid, 17 wt % PEG-BAE, and 57 wt % water*. We note that the original paste formulation[14] used about 6 wt % polyethylene glycol (M_w = 20,000 and 100,000) as stabilizer and thickening agent. We chose to use a higher wt % of PEG-BAE for our paste for consistency between our SnO_2 paste and the WO_3 paste described below. Pastes were stored in a sealed vial with continuous magnetic stirring for up to 3 weeks, with no detectable change in film transparency.

As described above for TiO_2, films were formed by doctor blading the paste onto clean FTO glass between one thickness of Scotch tape spacers (later referred to as "1-Scotch" films). Thicker films were prepared using multiple thickness of Scotch tape, where noted. The film was covered with a petri dish to prevent dust contamination and allowed to settle for 5 min to reduce any surface irregularities (if films rested long enough to begin to air-dry, the surface became tacky and resulted in a less transparent films after sintering). After settling, the tape was removed, the slide was placed in the furnace, and the temperature was gradually increased (~30 °C/min) to 450

°C under air and held at temperature to sinter for 1 h. After calcination, heat was turned off and the furnace door was gradually opened to allow the film to slowly cool (≤1 °C/s).

We note that we also tried an alternative SnO_2 paste formulation, starting with the same commercial SnO_2 nanopowder, but following a published procedure for TiO_2 that uses ethyl cellulose as a stabilizer/thickening agent and α-terpineol as solvent.[31] Such pastes should ideally be stable for longer, up to years,[31] because the higher viscosity of the mixture should prevent aggregation of the particles. Such pastes had a higher wt % of SnO_2 (~20 wt %), but a lower wt % of ethyl cellulose stabilizer. Films resulting from the use of such pastes had a lower thickness per single layer (as determined by optical profilometry, see below) than the previously described, water-based pastes. This may be due to differences in film porosity. Preliminary testing of dyed films of comparable thickness and otherwise identical conditions revealed that films prepared from the α-terpineol-based paste formulation achieved slightly lower photocurrents than the above water-based paste.

S4.2c Preparation of WO_3 Films. As noted in the main text, we chose a nano-WO_3 paste formulation from the literature[30] because of its superior water oxidation photocurrents, when accounting for film thickness, compared to other formulations.[18] Unfortunately, we were unable to reproduce the specific paste formulation ("Synt-2" from the Meda *et al*. paper)[30] based on the provided experimental details alone (see below).

Following the published precedure[30] (at 30% scale), 0.84 g of oxalic acid dihydrate (Crystal—Technical grade, Fisher)—that is, 0.60 g of the equivalent non-hydrate—was added to a weighed, 20 mL scintillation vial with magnetic stir bar, followed by 1.5 mL of water (18 MΩ, nanopure). The vial was capped and stirred on a sand bath at 60 °C to allow the acid to dissolve. Meanwhile, 1.68 g $Na_2WO_4 \cdot 2H_2O$ (ACS reagent 99%, Sigma-Aldrich)—that is, 1.50 g of the

equivalent non-hydrate, Na_2WO_4—was dissolved with magnetic stirring in 30 mL of nanopure water in a 100 mL beaker. While rapidly stirring (not specified[30]), 6 mL of concentrated HCl (12.1 M, Certified ACS Plus grade, Fisher) is to be "rapidly added"[30] to form condensed tungstic acid species, $WO_3 \cdot xH_2O$. Additional details from a previous patent[32] by the same research group clarifies that "rapidly added" likely means dropwise, at a rate of ~1 drop/s. During the acid addition, a light-yellow precipitate with a gel-like consistency forms. (According to Freedman[33], such an acidification at room temperature leads to $WO_3 \cdot 2H_2O$, which can be washed with neutral water to remove NaCl without peptization of the solid. By contrast, acidification at 100 °C formed $WO_3 \cdot 1H_2O$, which required washing with 0.1 M HCl to avoid peptization.[33]) As soon as the HCl addition was complete, the mixture was transferred to a plastic, 50 mL centrifuge tube and the solid precipitate was separated from solution (by centrifugation at 4000 rpm for 3 min[32]), discarding the solution.

The fine, light-yellow solid was washed 3 times with ~15 mL of nanopure water in the same centrifuge tube. For each wash, the solid was completely suspended by a glass stir rod, and the solution was vigorously shaken by hand for 60 s before centrifugation (again, 4000 rpm for 3 min) and subsequently discarding the wash solution. After washing, the wet precipitate (~4 mL volume) was added *portionwise* (specified in the patent[32]) by plastic spatula to the above oxalic acid solution at 60 °C to form a transparent colloidal solution. For all attempts, a stable transparent solution was not achievable at the reported concentration of tungsten species, even with trials using more than the reported amount of oxalic acid. During, or soon after the portionwise WO_3 additions, the solution would grow opaque yellow, indicating the aggregation of condensed tungstic acid species. Interestingly, the published procedure[30] lists twice the amount of Na_2WO_4 starting material (5 g) as compared to the previous patent[32] (2.5 g) despite otherwise very similar

conditions. Upon contacting the corresponding author, they confirmed that *the published,*[30] *"5 g" mass was actually a typo, and should be "2.5 g" of* Na_2WO_4.

Taking this typo into account, we repeated the above synthesis exactly (still at 30% scale), except now using 0.84 g of $Na_2WO_4 \cdot 2H_2O$—that is, 0.75 g of the equivalent non-hydrate, Na_2WO_4. With this change, transparent, colorless, colloidal solutions were consistently obtained after dissolving the washed tungstic acid solid in the oxalic acid solution. For the next step, the colloidal solution was weighed and polyethyleneglycol bisphenol A epichlorohydrin copolymer (PEG-BAE), (Sigma, M_w = 15,000–20,000), as a stabilizer and thickener, was added to solution in small pieces in a 1:5, PEG-BAE-to-solution weight ratio, and stirred to dissolve. The exact mass of PEG-BAE varied with each preparation, due to variable loss of $WO_3 \cdot 2H_2O$ during washing steps, but was typically 1.08 ± 0.08 g. Once all PEG-BAE had visibly dissolved, 3 drops (60 mg) of Triton X-100 (octyl phenoxy polyethoxyethanol, Sigma) was added to aid adhesion to the glass substrate, and the vial was sealed and stirred overnight before use. *The final paste formulation should be approximately 18 wt %* WO_3*, 19 wt % oxalic acid, 17 wt % PEG-BAE, and 46 wt % water*. Note, these values assume 100% recovery of WO_3 and do not account for the mass of water from the wet $WO_3 \cdot xH_2O$ precipitate, and are therefore a very rough approximation. The true formulation almost certainly has a higher wt % water. Such prepared pastes gradually grew more yellow and opaque over 3 days stirring at room temperature, but remained transparent for many weeks if stored unstirred in a refrigerator.

Films were formed by doctor blading the paste onto FTO between one thickness of Scotch tape spacers (unless noted otherwise) as described above for TiO_2 paste. WO_3 films were not allowed a settling time to alleviate surface irregularities, because oxalic acid would often begin to crystallize as the film dried at room temperature. Instead the tape was quickly removed and the

slide was placed in the furnace at 100 °C to dry for 10 min (following the reported procedure[30]). Next, the temperature was gradually increased at ~30 °C/min (heating rate was not originally specified[30,32]) to 550 °C under air and held at temperature to sinter for 1 h. After calcination, heat was turned off and the furnace door was gradually opened to allow the film to slowly cool (≤1 °C/s, not specified[30]).

Unfortunately, following the published sintering parameters consistently results in WO_3 films that have some degree of opacity caused by cracks throughout the film (see Fig. S4.1 and SEM images in Fig. S4.4). A leading hypothesis for the cause of the film cracking is the shrinkage of the paste as different components are evaporated or burned off. Attempts to avoid film cracking by lowering the temperature ramp rate to 10 °C/min had no effect. In order to determine the temperatures at which the most mass is lost from the paste during sintering, thermogravimetric analysis (TGA) was performed on the WO_3 paste using a TA Instruments TGA 2950 Thermogravimetric Analyzer under air flow and using a 10 °C/min heating ramp rate (Fig. S4.2).

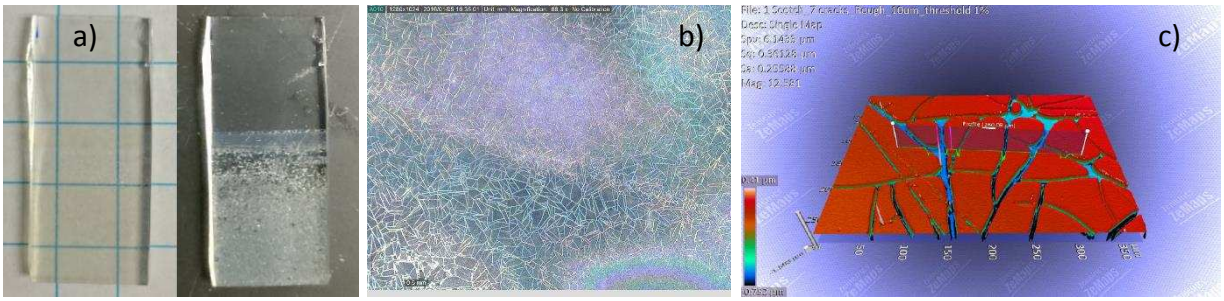

Figure S4.1 (a) photograph of a representative WO_3 film on FTO glass, viewed both on a grid paper to show transparency of the film and the black benchtop to show the opacity caused by film cracks; (b) digital microscope image of the film cracks; (c) optical profilometry image of film cracks.

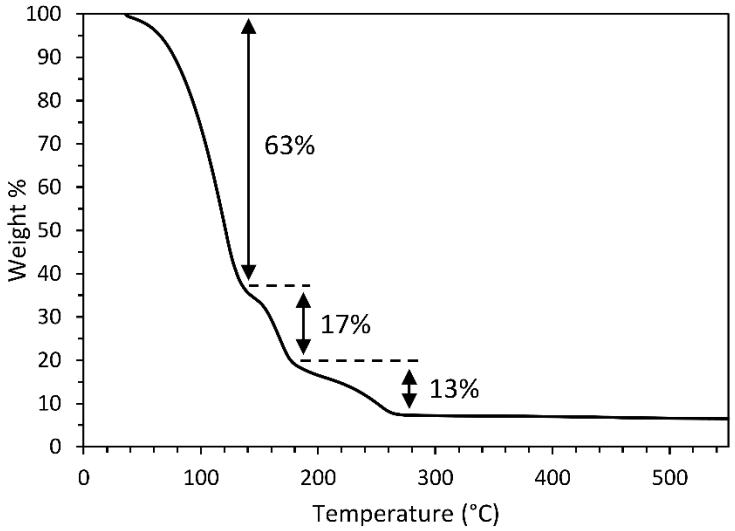

Figure S4.2 TGA plot of the WO_3 paste. Experiment was performed under 50 mL/min air flow with a 10 °C/min ramp rate.

As a final attempt to eliminate film cracking, a new WO_3 film was prepared by ramping the furnace temperature at ~15 °C/min, but also using ramp rests at the major mass loss temperatures observed by TGA: ramped to 100 °C and held for 30 min; ramped to 150 °C and held for 30 min; ramped to 225 °C and held for 15 min; ramped to 400 °C and held for 15 min; finally, ramped to 550 °C and held for 1 h. After sintering, the furnace door was opened gradually to allow slow cooling at ≤30 °C/min. This new furnace ramping procedure had no effect on the resulting films, which were cracked just as before.

Given the above troubles, we also tried an alternative WO_3 nanoparticle paste/film prep published by Santato *et al*.[34] These films have shown the second-highest photocurrents, when accounting for film thickness, compared to other formulations.[18] Unfortunately, these published procedures also have very poor experimental details, though a few additional details are available in a patent by the same group.[35] Briefly, an aqueous solution of Na_2WO_4 is run through a proton exchange column and eluted into stirring ethanol to prevent agglomeration of tungstic acid species. The solution is then concentrated by rotary evaporation, and a PEG stabilizer is added. In our

attempts to repeat this procedure, colloidal solutions became opaque yellow, indicating condensed $WO_3 \cdot xH_2O$ species, during or soon after the concentration step. Even so, one such opaque paste still formed transparent, crack-free WO_3 films on FTO after the doctor blade/sinter procedure. While the photocurrents of bare WO_3 films from this prep in pH 7, 0.1 M potassium phosphate (KPi) buffer were significantly higher than films prepared by the Meda *et al*. method,[30] subsequent testing (dying, alumina-treatment, dye-related photocurrents) showed no advantages over the above WO_3 films prepared by the Meda *et al*.[30]

S4.3 Characterization of MO_x Films

S4.3a Powder XRD of MO_x Films to Determine Crystallite Domain Size and Crystal Phase. Thin film XRD spectra were collected for each MO_x film (prepared with 1 thickness of Scotch tape) on FTO and on glass substrates (microscope slides) using a Bruker D-8 Discover Diffractometer (Cu $K_{\alpha 1}$ radiation, λ=1.54060 Å) with the source set to 40 kV and 40 mA and using a 0.6 mm source slit, 0.1 mm divergence slit, and 0.2 mm antiscatter slit. Scans were performed from 20 or 30–80° (2θ), 0.02° step size, and 1 s/step. Diffraction spectra were analyzed using Diffrac^{plus} Evaluation Package software. Estimations of the crystallite domain size were determined from the most intense diffraction peaks' full width at half maximum using the software's built-in equation, S4.1:

$$LC = \frac{180}{\pi} \cdot \frac{k \cdot \lambda}{\cos\theta \cdot \sqrt{FWHM^2 - s^2}} \qquad \text{(S4.1)}$$

where *LC* is the crystallite size domain, *k* is the Scherrer constant, taken as 0.94 according to the original Scherrer formulation,[36] λ is the wavelength of x-ray radiation, θ is the angle of the diffraction peak, *FWHM* is the diffraction peak's full width at half maximum (2θ), and *s* is the

instrument broadening (2θ), determined to be 0.11° by measuring the FWHM of peaks from a BaF_6 standard (NIST SRM 660c) tested under the same conditions.

The resulting XRD spectra for each MO_x film are shown in Fig. S4.3. Where possible, spectra are shown for films on glass substrate, in order to eliminate any potential peak broadening by overlap with peaks originating from the FTO substrate. We note that, for TiO_2 and SnO_2 films, there was no distinguishable difference between the XRD spectra of films annealed on glass vs FTO, and only a small difference (≤0.6 nm) in the calculated crystallite size domains. In the case of WO_3 films on glass, additional XRD peaks appeared which were consistent with sodium tungsten oxide, $Na_2W_3O_{10}$ (not shown). Such peaks were not present when the same WO_3 paste was prepared on FTO substrates, as shown in Fig. S4.2c. The most likely explanation for this

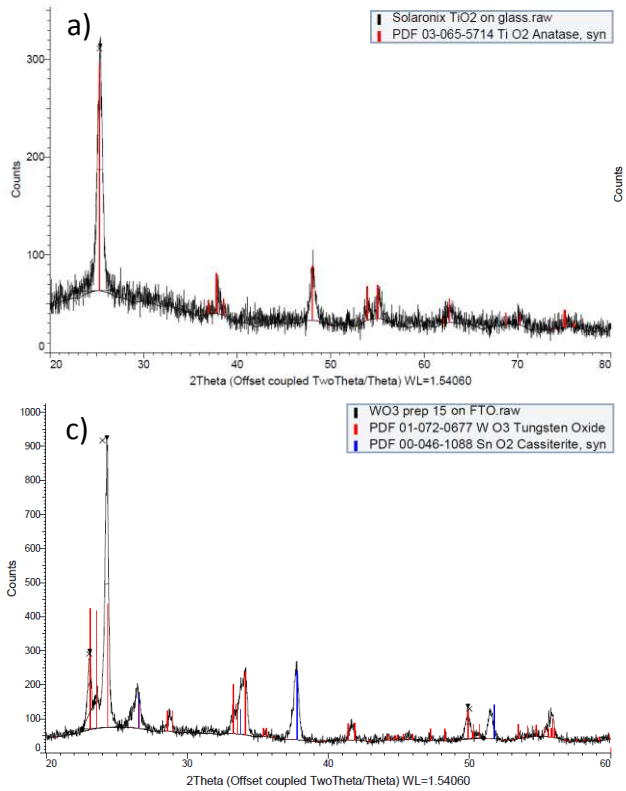

d)

Sample	Peak (°2θ)	FWHM (°2θ)	k	s (°2θ)	LC (nm)
TiO_2 on glass	25.345	0.596	0.94	0.11	14.5
SnO_2 on glass	26.600	0.511	0.94	0.11	17.1
WO_3 on FTO	24.314	0.277	0.94	0.11	33.4

Figure S4.3 Powder XRD spectra of sintered nanoparticle films including (a) TiO_2 on glass, (b) SnO_2 on glass, and (c) WO_3 on FTO. Included in each spectrum is the best-fitting PDF file. Also, (d) is a table showing data used in the calculation of the crystallite domain size for each MO_x.

observation is that sodium ions from the glass substrate (soda glass, 14% Na_2O) diffuse into the WO_3 film during sintering, which used a higher maximum temperature than for TiO_2 and SnO_2 films.

As shown in Fig. S4.3, TiO_2 films on glass were well fit by PDF file number 03-065-5714 for anatase TiO_2 with a tetragonal crystal system (as were TiO_2 films on FTO, not shown). SnO_2 films on glass were well fit by PDF file number 00-041-1445 for Cassiterite SnO_2 with a tetragonal crystal system (as were SnO_2 films on FTO). The WO_3 film on FTO is generally well fit by PDF pattern number 01-072-0677 for WO_3 in the monoclinic crystal system. However, the peak at 23.6°, corresponding to the (020) crystal plane, is significantly lower intensity than expected, and the peak at 24.3°, corresponding to the (200) crystal plane, is significantly higher intensity than expected. A similar XRD spectrum has been previously observed for nanocrystalline WO_3 films on FTO by Santato *et al*.[34] This group found that their WO_3 films (prepared by a similar sol–gel method, but using an ion-exchange column for acidification of tungstate) showed preferred crystallographic orientation: the three peaks from 23–25° (2θ) were significantly higher intensity than other peaks, and gained intensity from low to high angle.

S4.3b SEM of MO_x Films to Determine Morphology and Particle Size. Scanning electron microscopy images were obtained for each MO_x film in order to characterize the film and particle morphology and to determine particle sizes by a second technique. Images were obtained in house using a JEOL JSM-6500F field emission scanning electron microscope (FESEM), using 15 kV accelerating voltage and 10 mm working distance. Images were obtained at multiple magnifications for each film, shown below in Fig. S4.4. It is clear from the images at 100X and 1,000X magnifications that TiO_2 films were the most uniform. SnO_2 films contain small cracks up to tens of microns in length, whereas WO_3 films had large cracks which were microns wide

and networked across the whole film surface. These large cracks throughout the WO_3 films were the cause of some opacity due to light scattering (see Fig. S4.1 above).

Images at the 10,000X magnification level reveal that TiO_2 films and WO_3 films (in regions between cracks) were quite homogeneous, while SnO_2 films appear somewhat more porous. Finally, images between 100,000 and 200,000X magnification reveal a significant variation in particle sizes and morphologies between films. TiO_2 particles appear to be mostly spheroidal, and with a relatively narrow size distribution. SnO_2 particles are less well defined, and appear to have a larger distribution of sizes. Finally, WO_3 particles are significantly larger and less spherical than both TiO_2 and SnO_2.

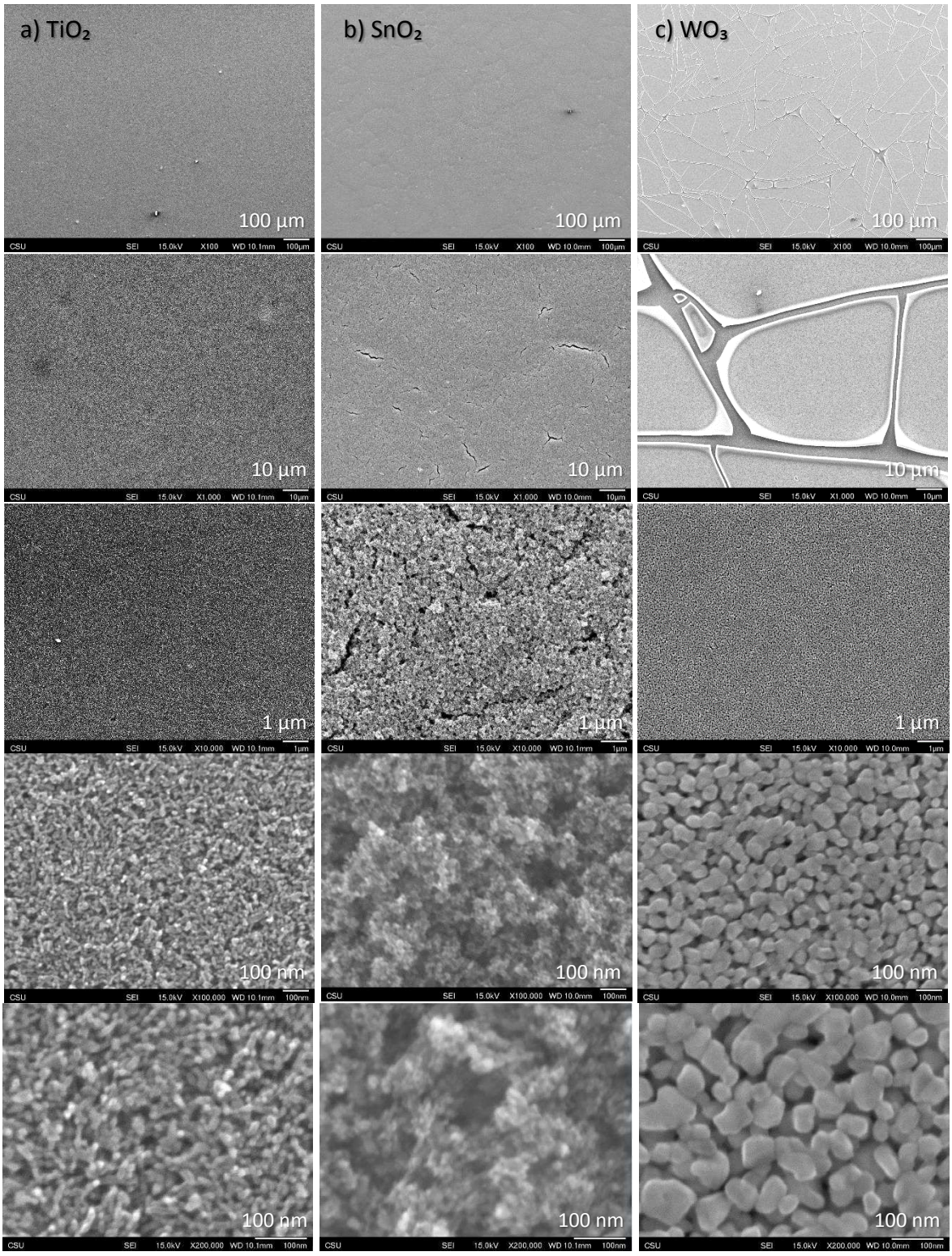

Figure S4.4 FESEM images of each sintered MO_x film at multiple magnifications (scale bars shown in lower right corner of each image) to show both film and particle morphology. Column (a) TiO_2, (b) SnO_2, (c) WO_3.

The images taken at 200,000X magnification were analyzed to obtain an estimate of particle size distribution, average size, and standard deviation. This was done using Paint.NET free image-editing software. First, the scale bar from each image was used to calibrate the pixel scale (2.13 pixels = 1 nm, 4.54 square pixels = 1 nm^2). Next, the area of individual particles were estimated from each image by drawing an ellipse around each particle shape and using the "magic wand" selection tool to measure the pixel area of each ellipse. These individual particle areas were recorded in Microsoft Excel and converted to nm^2. To determine the average diameter of each individual particle, the diameter of a circle with an equivalent area to each measured ellipse was calculated. Finally, Excel's Analysis ToolPak Add-In was used to convert the lists of particle diameters to Histogram data, and also analyzed by Descriptive Statistic to determine the mean and standard deviation of the average particle diameters. The results are shown in Fig. S4.5 below.

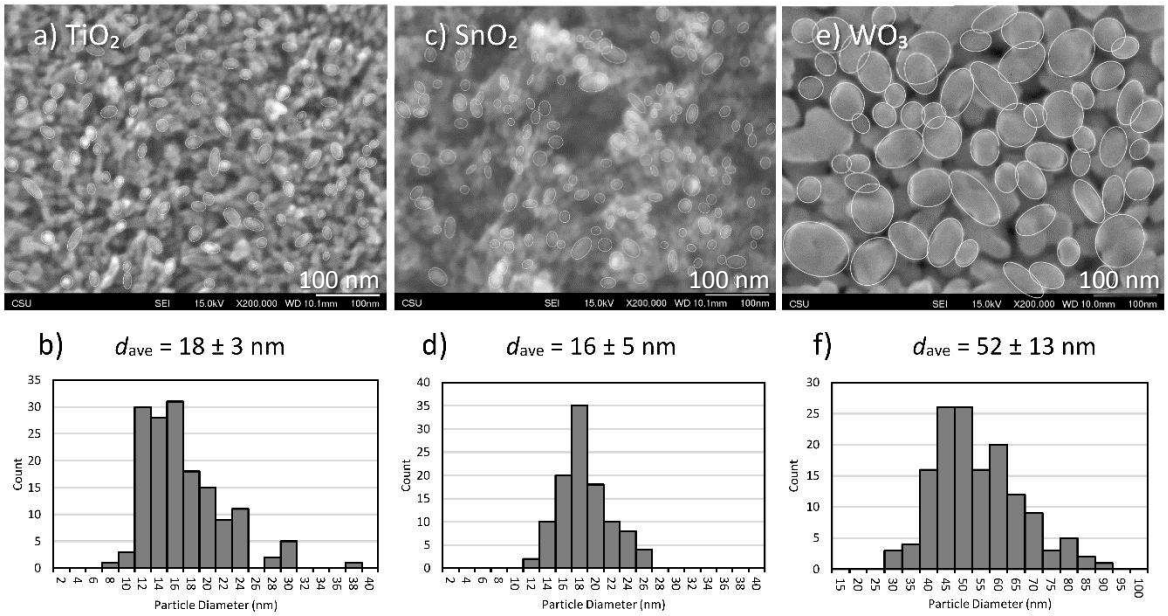

Figure S4.5 Particle size analysis from SEM images and corresponding average particle diameter, standard deviation, and average particle diameter distribution for sintered films of TiO_2, (a) and (b), respectively; for SnO_2, (c) and (d), respectively; and for WO_3, (e) and (f), respectively.

S4.3c Optical Profilometry of MO_x Films to Determine Film Thickness. Using a razor blade, a channel was slashed through the center of each MO_x film. A ZeScope optical profilometer was used to measure the film thickness by determining the step height at several locations across the razor channel for each MO_x, yielding an average thickness and experimental standard deviation. Whenever possible, measurements were taken in Robust Scan mode. However, Robust Scan mode gave poor results for SnO_2 films (possibly owing to the rougher surface for SnO_2 films, see Figure S4.6) so scans were taken in Film Scan mode, which gave better, but still noisy results. Profiles for WO_3 films also revealed the cracks responsible for film opacity caused by light scattering.

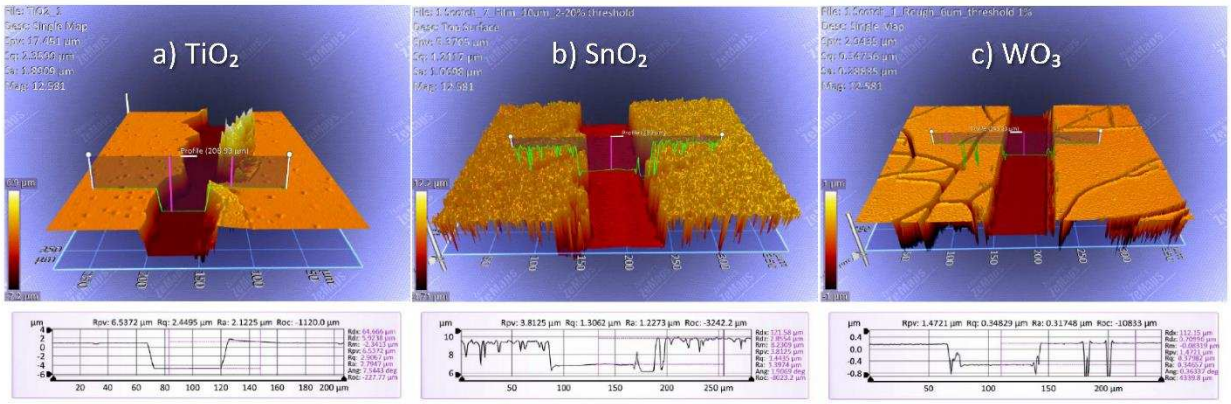

Figure S4.6 Representative optical profilometry 3D maps and corresponding height profiles for estimation of film thicknesses for (a) TiO_2, (b) SnO_2, and (c) WO_3.

S4.3d Photocurrent Transients of Bare MO_x Films to Estimate E_{CB}. As described by Beranek,[37] the conduction band edge (E_{CB}) of semiconducting, nanoparticle MO_x films can be estimated by a "Photocurrent Onset Measurement" method. For this technique, the MO_x film is submerged in the electrolyte of interest, and illuminated with light sufficient for bandgap excitation. This illumination generates excited electron and hole pairs within the MO_x. The band bending of the n-type semiconductors, in this case, should drive photo-generated holes in the valence band towards the MO_x/electrolyte interface where oxidation reactions can occur with a

suitable redox species in solution. At the same time, photo-generated electrons in the conduction band can diffuse through the MO_x film until they are collected at the MO_x/FTO interface. This process is then measured as an anodic (photo)current.

If the potential (that is, the Fermi energy) of the underlying FTO substrate is scanned in the cathodic direction, the driving force for collection of the conduction band electrons is decreased. Once the flat band potential is reached, there is no driving force for charge collection, and photocurrents should become zero. An important assumption is that the flatband potential is very close in energy to E_{CB}, as is true for doped, n-type semiconductors such as TiO_2. Therefore, the E_{CB} can be estimated by performing a current–voltage scan under interrupted illumination (photocurrent transients), and then determining *photocurrent onset potential*, or the potential at which the photocurrent decays to zero if scanned in the cathodic direction. An important note is that the electrolyte should be purged with an inert gas prior to the experiment, because oxygen dissolved in solution can scavenge photo-generated electrons. Indeed, even with gas purging, values of E_{CB} determined by this method are often anodically shifted.[37]

Therefore, photocurrent onset measurements were performed for three anodes of each MO_x film. The electrolyte solution was 10 mL of pH 7, 0.1 M KPi buffer in a 20 mL scintillation vial, and was degassed for 1 h with Ar before testing to remove dissolved O_2. During testing, the MO_x anode was lowered into the vial and submerged into solution deep enough to cover the whole MO_x film. These films were left in solution for as short a time as possible before testing was begun, usually less than 2 min. The vial also contained a Ag/AgCl (3 M NaCl) reference electrode and a Pt wire counter electrode. During testing, the Ar bubbler needle was withdrawn to just above the solution surface. After each experiment was completed, the needle was lowered back into solution to continue degassing for at least 5 min before the next experiment was begun.

Photocurrent onset measurements were performed by illuminating the cell in 10 s intervals of white light from a 65 W Xe arc lamp (for these tests, the KG3 bandpass filter—as used in other photoelectrochemical experiments—was left in place to avoid heating the solution from infrared radiation, but the 400 nm long-pass filter was removed to allow bandgap excitation of the MO_x semiconductors). During the light transients, the MO_x films were scanned in the cathodic direction at 2 mV/s. The scan windows were +0.2 to −0.8 V for TiO_2, +0.6 to −0.4 V for SnO_2, and +0.7 to −0.3 V vs Ag/AgCl for WO_3. Only the data from the first photocurrent onset experiment was analyzed for each new, previously unused MO_x anode, because the measured photocurrent onset potential shifts anodically with each repeated experiment. The simplest explanation for this observation is that O_2 is generated in solution by photo-generated holes during testing, which then scavenges photo-generated electrons and shorts the photocurrent. However, extended buffer degassing times did not shift the measured photocurrent onsets back in the cathodic direction for repeated scans, which seems to rule out this hypothesis.

After testing, the surface area of each MO_x film was determined from a digital image of the film atop a ruler. Using this measured area, photocurrents were converted to current densities. The photocurrent onset potential was defined—to avoid possible error caused by measuring by eye alone—as the potential at which the maximum photocurrent (measured at the end of the first transient of each scan) had decayed to 5% of its original value. We note that defining the onset potential in this way results in a very slight anodic shift of the measured values, but decreases error bars. Representative data from photocurrent onset measurements for each MO_x are provided in Fig. S4.7. The average photocurrent onset potential and standard deviation for three films of each MO_x material are summarized in Table 4.1 of the main text.

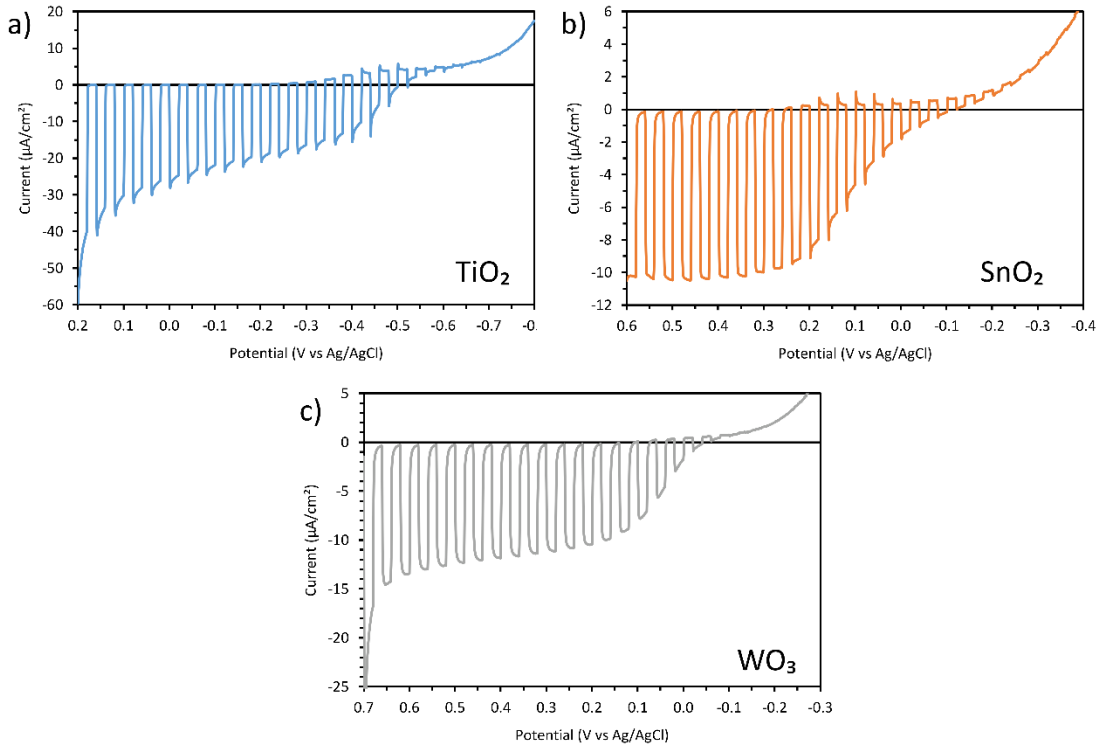

Figure S4.7 Photocurrent transient experiments for sintered MO_x nanoparticle films consisting of (a) TiO_2, (b) SnO_2, and (c) WO_3, taken in argon-degassed, pH 7, 0.1 M KPi buffer solution. Scans were taken in the cathodic direction with a 2 mV/s scan rate and 10 s light transients. Light from a Xe arc lamp was directed through a KG3 bandpass filter (315–710 nm), measuring 60 mW/cm².

S4.4 Estimation of PMPDI Energy States

The energies of a dye's HOMO and LUMO can be estimated by the electrochemical oxidation and reduction potentials ($E_{1/2}^{+/0}$ and $E_{1/2}^{0/-}$, respectively, in V) of the dye in the ground state as measured by cyclic voltammetry.[2] However, the electrochemical potential of the dye in the excited state, $E^{+/}$*, is often more positive than $E_{1/2}^{0/-}$ because of vibrational relaxation and solvent shell reorganization, for example. That is to say, the neutral, excited dye (D*) is often a less powerful reductant than the reduced dye in the ground state (D^-). This distinction is important when considering photochemical reactions. For example, in order for D* to inject an electron into the conduction band of a metal oxide substrate, that metal oxide must have electronic states that energetically overlap with D*.

In DSSC studies, the excited state energy, $E^{+/*}$ (eV), is usually estimated as[1,2]

$$E^{+/*} \approx qE_{1/2}{}^{+/0} - E_{0\text{-}0} \quad \text{(S4.2)}$$

where q is the elementary charge and $E_{0\text{-}0}$ is the energy (eV) of the transition between the lowest vibrational energy level of the electronic ground state ($E_{0,0}$) and the lowest vibrational energy level of the electronic excited state ($E_{1,0}$).[1,2] $E_{0\text{-}0}$ is often estimated from the wavelength at which the normalized absorption and emission spectra overlap by the Plank Equation:

$$E(\text{eV}) = hc/\lambda = 1239.8\ \text{eV}\cdot\text{nm} / \lambda(\text{nm}) \quad \text{(S4.3)}$$

Unfortunately, we have not been able to measure $E^{+/0}$ for PMPDI due the limiting solvent window in aqueous solutions (Fig. S4.8a) and to PMPDI's limited solubility in organic solvents.

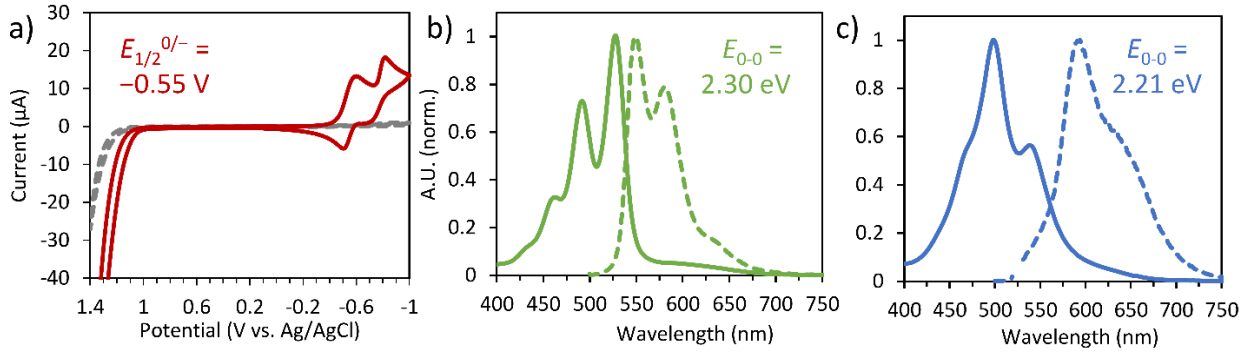

Figure S4.8 (a) Cyclic voltammograms of PMPDI (solid red trace) and the solvent background (dashed grey trace) in Ar-degassed 0.1 M carbonate buffer (pH 10) using a diamond working electrode, Pt wire counter electrode, Ag/AgCl reference electrode, and 25 mV/s scan rate. While the oxidation wave, $E_{1/2}{}^{+/0}$, for PMPDI is expected to be beyond the solvent window, a catalytic oxidative current of unknown origin was observed with PMPDI. (b) Normalized absorption and emission spectra for ~0.5 mM PMPDI dissolved in ethylene glycol and (c) nanopure water. Note the vibronic structure of the absorption spectra are consistent with monomeric PMPDI in ethylene glycol and dissolved aggregated dimer in water.[38,39] Fluorescence spectra were collected on a Horiba Jobin-Yvon FluoroLog-3 Spectrofluorometer, using 495 nm excitation in ethylene glycol and 525 nm excitation in water.

However, our measured $E_{0\text{-}0}$ of 2.2–2.3 eV (Fig. S4.8b,c) is approximately equal to electrochemical band gaps ($qE_{1/2}{}^{+/0} - qE_{1/2}{}^{0/-}$) typically found for PDIs,[40] which are typically insensitive to the N-substitution of the molecule. Importantly, the same observation of $E_{0\text{-}0}$ being approximately equal

to the electrochemical band gap was also recently observed for a series of perylene dyes by Lindquist *et al.*[41] This suggests that $E_{1/2}^{0/-}$ is likely a good approximation for the reducing power of PMDPI*, and we can estimate the HOMO ($E_{1/2}^{+/0}$) of PMPDI as:

$$E_{1/2}^{+/0} \approx E_{1/2}^{0/-} + E_{0\text{-}0}/q = -0.55 \text{ V vs Ag/AgCl} + 2.2 \text{ V} = +1.65 \text{ V vs Ag/AgCl} \qquad \text{(S4.4)}$$

S4.5 Illumination Setup for Photoelectrochemical Experiments

A 65 W Xe arc lamp was used as a white light source for photoelectrochemical experiments. Such arc lamps are generally considered to be decent approximations of the terrestrial solar spectrum in the visible wavelength range, but their output spectrum extends farther into the UV than the solar spectrum, and contains high intensity spikes in the IR region.[42] To compensate for these discrepancies, we directed the lamp beam through a visible wavelength bandpass filter (Thorlabs, KG3, ~315–710 nm) to cut off the IR region, as well as a 400-nm long-pass filter. The use of such filters also has the advantage of minimizing cell heating, and largely eliminating direct bandgap excitation of the MO_x films employed in these studies.

In order to closely approximate the visible region of the terrestrial solar spectrum, we calculated the effect of directing the Air Mass (AM) 1.5 G reference solar irradiance spectrum[43] (100 mW/cm²) through the above two filters, then scaled the filtered spectrum to match the original (unfiltered) intensities in the visible region (Fig. S4.8). The integrated irradiance resulting from the filtered and scaled spectrum contains 44.5 mW/cm². Therefore, we set up our testing station to closely approximate the irradiance of the AM 1.5 G spectrum in the visible region by directing our Xe arc lamp through the above two filters, then adjusting the beam focus and cell location until an incident irradiance of 44.7 mW/cm² was achieved, as measured by a ThorLabs S302A thermal power sensor. This light source was used for all photoelectrochemical experiments unless noted

otherwise. Importantly, control experiments with higher light intensity (still through the KG3 and long-pass filters) did not significantly improve photocurrent for SnO_2/PMPDI anodes.

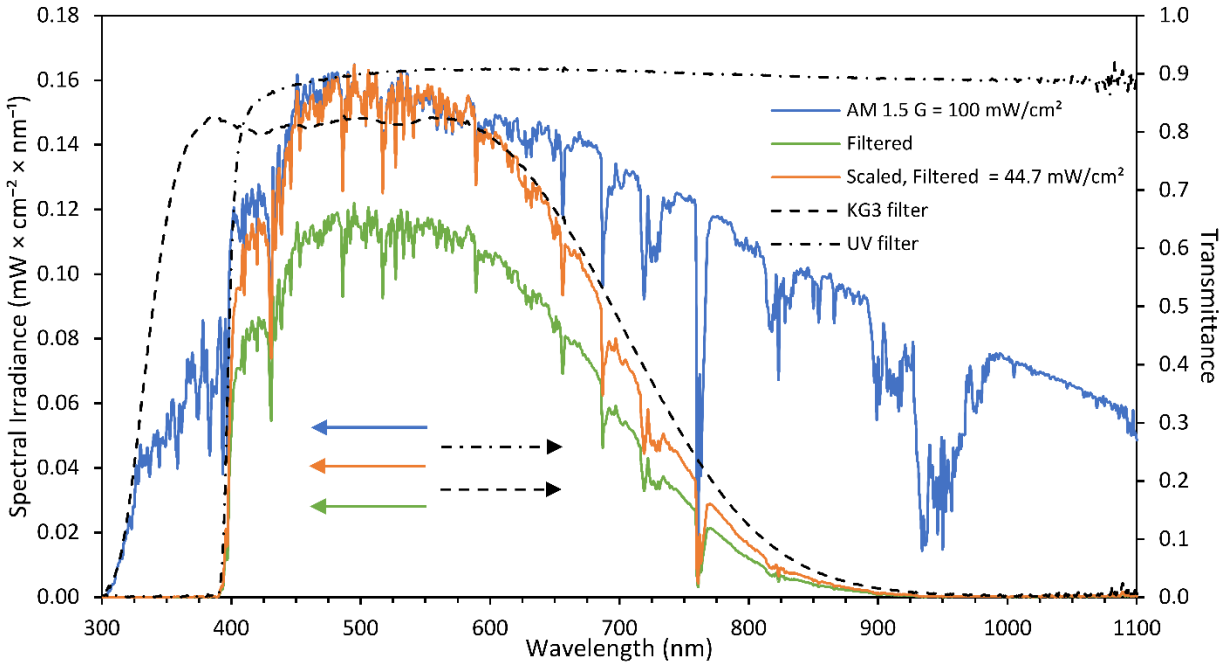

Figure S4.9. Calculating the irradiance needed to closely approximate the visible region of the AM 1.5 G solar spectrum after passing through a band-pass filter (KG3, ~315–710 nm) and UV filter (400 nm long-pass).

S4.6 Supplemental Photoelectrochemical Experiments for TiO_2 and SnO_2 Anodes

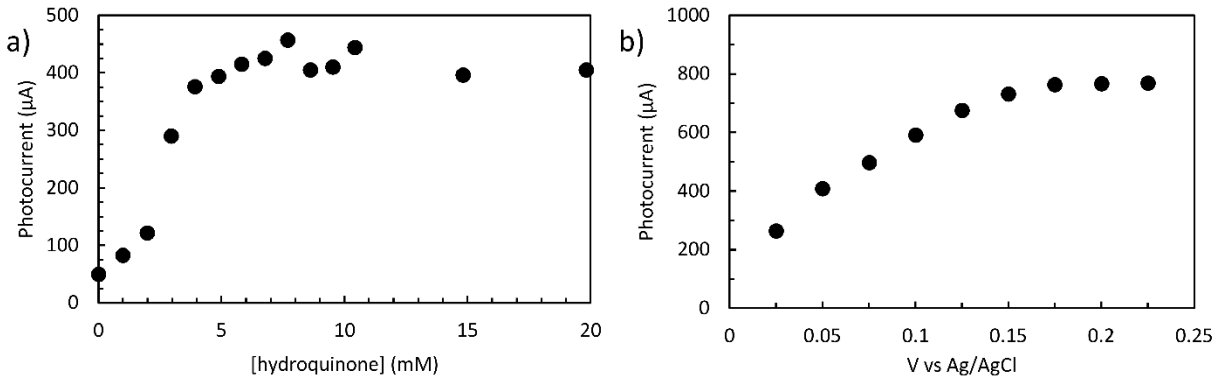

Figure S4.10 Photocurrent using a 2-Scotch SnO_2 film dyed for 48 h from ~0.5 mM aqueous PMPDI solution at 90 °C. Photocurrent was measured in pH 7, 0.1 M KPi buffer solution, illuminated with the lamp described above for 10 s on/off transients over 2 min, plotting the photocurrent (light current−dark current) of the last transient. (a) Concentration dependence of H_2Q: Between experiments, a solution of 200 mM H_2Q in 0.1 M KPi was added a drop at a time to obtain gradually increasing [H_2Q]. The working electrode was held at +0.05 V vs Ag/AgCl during transients. (b) Potential dependence: The potential of the working electrode was held at varying potentials during photocurrent transients while submersed in buffer containing 20 mM H_2Q.

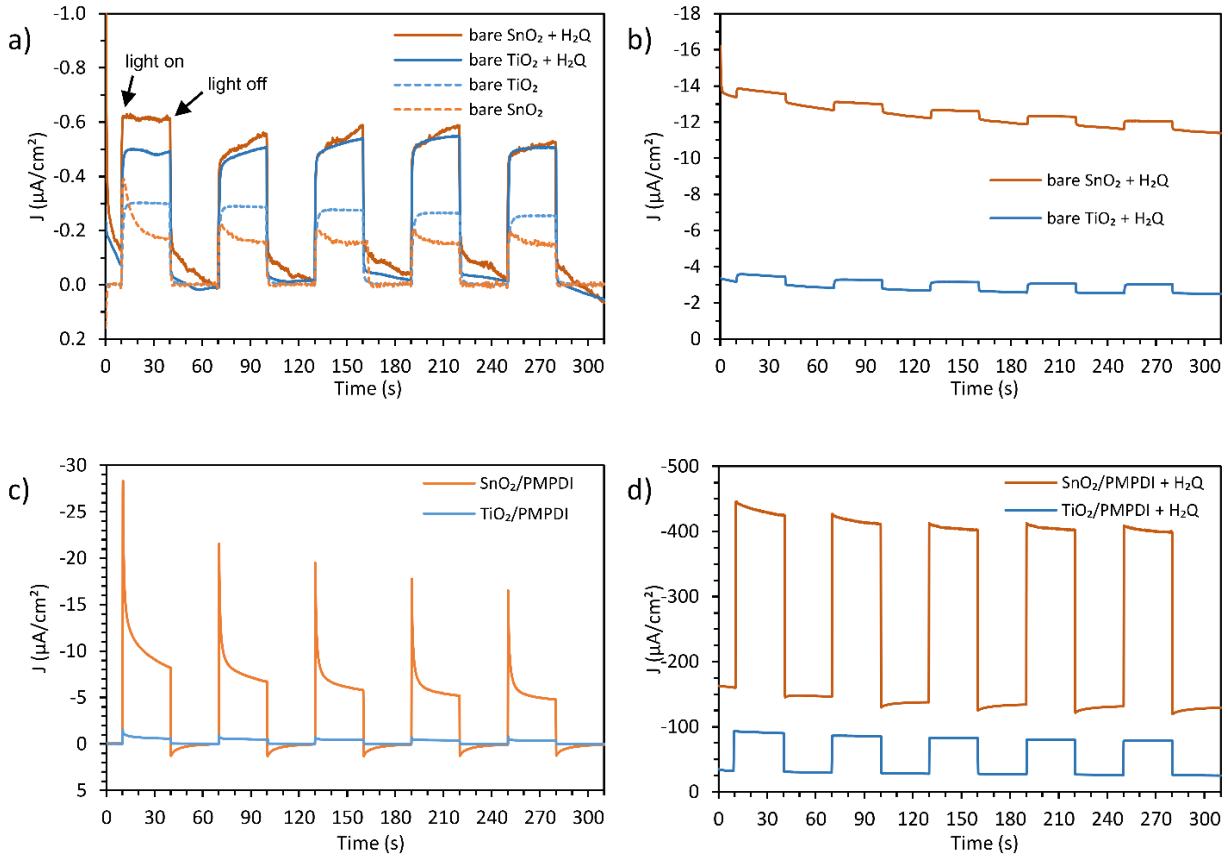

Figure S4.11 Control experiments showing anodic current density–time (*J*–*t*) traces with 30 s light transients for TiO_2 (blue) and SnO_2 (orange) films (1-Scotch thickness) both with (solid lines) and without (dashed lines) 20 mM H_2Q in pH 7, 0.1 M KPi buffer and held at +0.2 V vs Ag/AgCl. (a) Bare (undyed) MO_x nanoparticle films with and without H_2Q. Traces with H_2Q are plotted with dark currents subtracted for convenient comparison; (b) Bare films with H_2Q *without* dark currents subtracted; (c) Dyed films without H_2Q,; (d) Dyed films with H_2Q, as shown in Fig. 4.3 of the main text, but *without* dark currents subtracted. Note that anodic currents are given a negative sign according to the American convention, but are plotted in the positive direction to illustrate photocurrent.

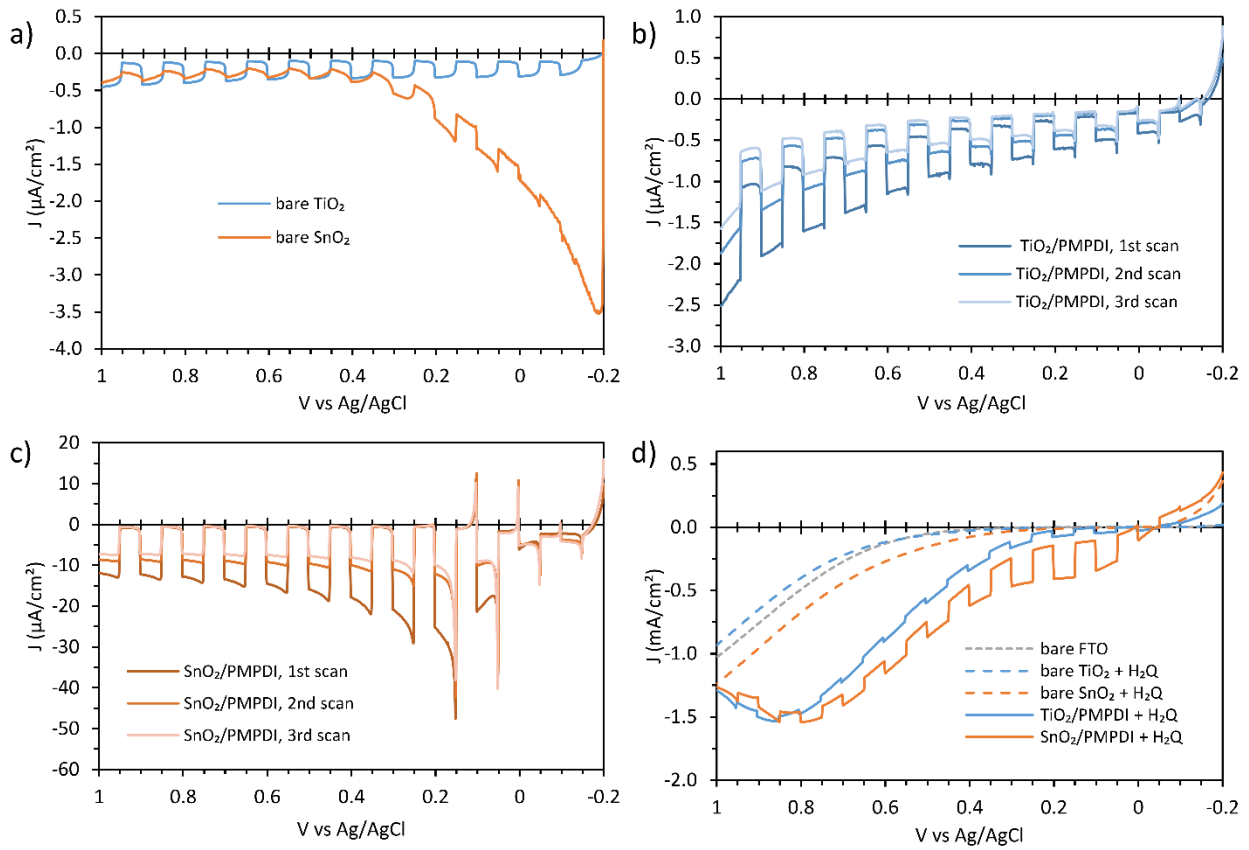

Figure S4.12 Current density–voltage (*J–V*) traces, plotted according to the American voltammogram convention (anodic currents have a negative sign), with 5 s light transients for TiO_2 (blue) and SnO_2 (orange) films (1-Scotch thickness) in pH 7, 0.1 M KPi buffer and scanned from −0.2 to +1.0 V vs Ag/AgCl with a scan rate of 10 mV/s. Illumination was provided with a Xe arc lamp approximating the AM1.5 visible spectrum. (a) Control experiment showing *J–V* transients of bare films without H_2Q; (b) Control experiment showing the effect of repeated J-V transient scans for the same TiO_2/PMPDI film; (c) Control experiment showing the effect of repeated J-V transient scans for the same SnO_2/PMPDI film; (d) Control experiment showing the effect of J-V transient scans on bare and dyed TiO_2 and SnO_2 films in the presence of 20 mM H_2Q.

S4.6a Interpretation of *J–V* Traces for MO_x/PMPDI Anodes. As discussed in Section S4.3d above, when the potential applied to the FTO substrate is equal to or negative of the conduction band (CB) edge of the MO_x nanoparticle film, there is no thermodynamic driving force for charge collection and no photocurrent is expected. As such, photocurrent for TiO_2 and TiO_2/PMPDI is observed throughout the whole potential window in Fig. S4.12 (E_{CB} for TiO_2 =

−0.51 V vs Ag/AgCl, Fig. S4.7a). For SnO_2 (E_{CB} = −0.16 V vs Ag/AgCl, Fig. S4.7b), the scan in Fig. S4.12a begins just above the conduction band, and therefore populates CB states with electrons. As the scan continues in the positive direction, these SnO_2 CB electrons are collected from the film and appear as a broad anodic background wave until a potential of approx. +0.3 V vs Ag/AgCl is reached (Fig. S4.12a,c).

We note that for SnO_2/PMPDI anodes (Fig. S4.12c) we consistently observe sharp current transient spikes (both anodic and cathodic) centered at approximately +0.1 V vs Ag/AgCl. Such current spikes are also present, though less pronounced, on bare SnO_2 anodes (Fig. S4.7b), which indicates that the current spikes are not attributable to PMPDI alone. Furthermore, the current spikes are independent of the scan direction and the solvent used to dye the film (formamide, ethylene glycol, and nanopure water were tested). To further probe this observation, we studied the SnO_2 density of states by cyclic voltammetry,[44] Fig. S4.13. The trace shows a clear capacitance peak at +0.06 V vs Ag/AgCl, consistent with the potential where photocurrent transient spikes are observed. A similar peak has been observed in the capacitance traces of bare TiO_2 nanoparticle films (at more negative potentials, consistent with the more negative CB of TiO_2), and have been attributed to mono-energetic, sub-bandgap (surface) trap states.[44] Such TiO_2 trap states have been proposed as recombination centers which degrade DSSC performance.[45–48] Mono-energetic surface traps in SnO_2 nanoparticle films have also been proposed as recombination centers,[49] but have been much less studied. Regardless, such SnO_2 recombination centers are currently our best hypothesis for the cause of the observed photocurrent transient spikes.

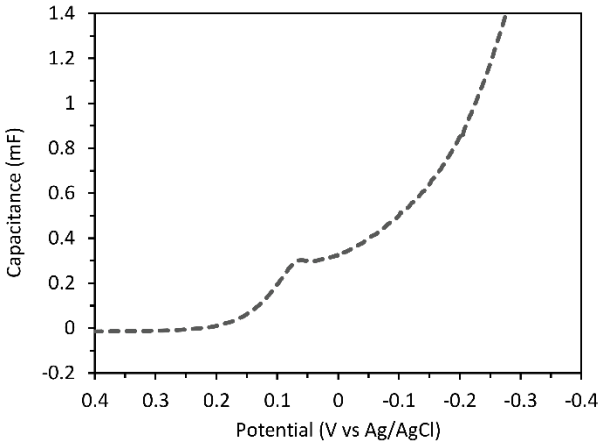

Figure S4.13 SnO_2 chemical capacitance estimated by linear sweep voltammetry of a bare nano-SnO_2 film on FTO in pH 7, 0.1 M KPi buffer, using a Pt wire counter electrode, Ag/AgCl reference electrode, and 100 mV/s scan rate. Capacitance was calculated by dividing the measured current by the scan rate.[44]

Referring back to the *J*–*V* transients for SnO_2/PMPDI in Figure S4.12c, as the potential of the FTO substrate is scanned positive of the MO_x CB, the steady-state photocurrent quickly grows to a maximum value at approx. +0.2 V vs Ag/AgCl, then gradually decays over time as the scan continues. When the *J*–*V* scan is immediately repeated for the same anode, the steady-state photocurrent at potentials higher than +0.2 V vs Ag/AgCl reaches a constant, potential-independent value. This time-dependent decay in both photocurrent spikes and steady-steady photocurrent for SnO_2/PMPDI at a constant +0.2 V vs Ag/AgCl over 4 min is also apparent in Figure S4.11c. We interpret this gradual decay in photocurrent as a gradual change related to the SnO_2 surface state. Recently, the Mallouk group have proposed that proton intercalation into TiO_2 is responsible for the rapid drop in photocurrent observed in the first few minutes of testing for most dye-sensitized, water-oxidizing photoanodes.[50,51] These intercalated protons then stabilize injected electrons near the surface and enhance recombination by back-electron transfer to the photo-oxidized dye.[51]

S4.7 SnO_2/PMPDI Performance Optimization Experiments

S4.7a Alternative Dying Conditions. In order to improve dye loading saturation and kinetics on SnO_2 films (see Fig. 4.3 of the main text), we chose to study alternative dying solvents and conditions. We had originally chosen to dye from formamide solvent because the UV–vis absorbance spectrum of PMPDI in that solvent looked the least aggregated (that is, it exhibited clear vibronic structure,[39,52] see Fig. S4.8b for example) at least at low concentrations. Moving forward, we tested the solubility of PMPDI (fully protonated form) in a variety of solvents: unbuffered nanopure water, methanol, ethanol, isopropanol, formamide, acetonitrile, ethylene glycol, dimethylsulfoxide, and 1-methyl-2-pyrrolidinone. We also tested combinations of 50/50 water/organic solvent, with negligible improvement in solubility. We found that PMPDI was most soluble (darkest solutions, though often aggregated) in water, DMSO, formamide, and ethylene glycol. Comparing the kinetics of SnO_2-dying from these 4 solvents indicated that both water and ethylene glycol solutions were faster than formamide (raw data not shown). Notably, freshly-dissolved PMPD (acid form) in water was pH ~4, which could result in a positively-charged SnO_2 surface (with its isoelectric point of 4–5)[53–55] to coulombically attract the negatively charged phosphonate groups of PMPDI. Repeated use of the aqueous dye solution resulted in a rise in pH and a drop in dye-loading efficiency.

Further improvements in dying kinetics were achieved by increasing the dying temperature, following literature precedent.[9,56–58] It was found that SnO_2 films dyed from 90 °C ethylene glycol or water dye solutions reached dye saturation within ~24h, a significant improvement over the 3 weeks required for room temperature formamide solutions (Fig. 4.3 of the main text). Figure S4.14a below displays the absorbance spectra of PMPDI on 2-Scotch SnO_2 films (see Sec. S4.7b below) after dying from ethylene glycol (green traces) or water (blue traces)

solutions for varying times. In Fig. S4.14b, the spectra are converted to absorptance (1 – Transmittance = light harvesting efficiency, LHE). Notably, with these improved dying conditions, PMPDI was able to reach an LHE >90% from ~440–560 nm, and >99% from 475–500 nm.

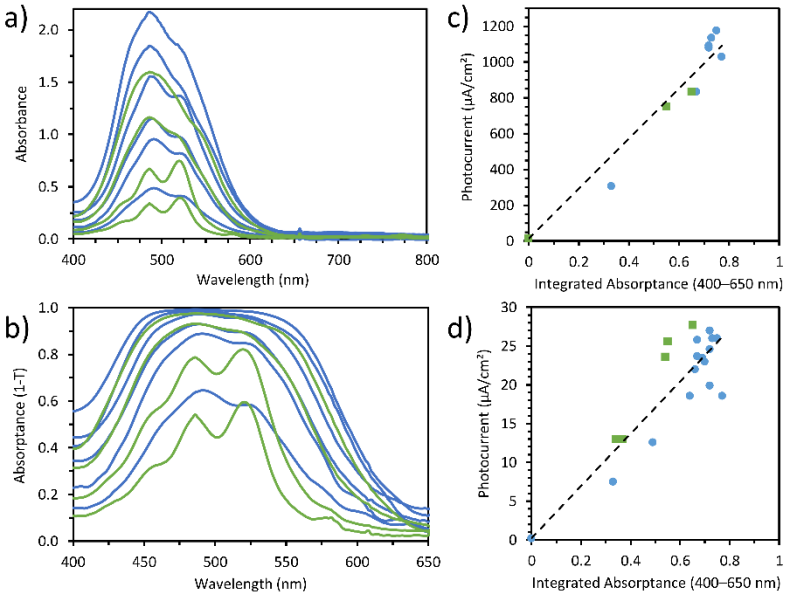

Figure S4.14 SnO_2/PMPDI photocurrent as a function of dye loading. (a) PMPDI absorbance spectra (spectrum of bare SnO_2 subtracted). Spectra are for films dyed from 0.5 mM PMPDI in ethylene glycol solvent (green) or water (blue) at 90 °C, dyed for varying amounts of time up to 24h. (b) Traces in (a) converted to absorptance (1−T) in order to calculate integrated absorptance (light harvesting efficiency) within the displayed wavelength window. (c) Steady-state photocurrent density at +0.2 V vs Ag/AgCl in the presence of 20 mM H_2Q in pH 7 KPi buffer (as measured at the end of a 5 min *J–t* experiment such as that shown in Fig. S4.11d, for example) vs the integrated light absorptance by PMPDI dye in the region of 400–650 nm. Green squares correspond to films dyed from ethylene glycol solution, while blue circles correspond to films dyed from water solution. (d) Same as (c), but with photocurrent measured in the *absence* of 20 mM H_2Q.

SnO_2/PMPDI anodes with varying dye loading were photoelectrochemically characterized by measuring current–time (*J–t*) transients such as those shown in Fig. S4.11(c) and (d). Anodes were submerged in pH 7, 0.1 M KPi buffer and illuminated by a Xe arc lamp calibrated to match the visible portion of the AM1.5G solar spectrum (see Sec. S4.5). Figures S4.14(c) and (d) plot the steady-state photocurrent with added 20 mM H_2Q sacrificial reductant (c) and without H_2Q (d), plotted versus the integrated absorptance within the wavelength window of 400–650 nm.

Restated, Figures S4.14(c) and (d) plot photocurrent vs PMPDI's overall light-harvesting efficiency within the window shown in Fig. S4.14b. Clearly, both with and without H_2Q, photocurrent is strongly correlated to the integrated absorptance of PMPDI. With H_2Q, SnO_2/PMPDI films with the highest dye loadings achieve photocurrent of ~1,100 μA/cm². In the absence of H_2Q, SnO_2/PMPDI anodes still exhibit photocurrent (the origin of which is still uncertain, given the lack of added WOCatalyst), which reaches ~25 μA/cm² for the highest dye loadings.

Aside from enhanced dying kinetics, the ethylene glycol and water dying solvents were of interest for an additional reason. The UV–vis absorbance spectrum of PMPDI dissolved in ethylene glycol exhibits vibronic structure that suggests the dye is molecularly dissolved as opposed to dissolved aggragates[38,39] (see Fig. S4.8b). By contrast, the spectrum of PMPDI in water is consistent with soluble dimers[38,39] (Fig. S4.8c). These solution spectra are unchanged at 90 °C. The UV–vis spectra of PMPDI on SnO_2 in Figures S4.14(a) and (b) suggest that the aggregation character is retained, at least when PMPDI is kept at low dye loadings (low dying time); at the lowest dye loadings, the spectra of PMPDI on SnO_2 dyed from ethylene glycol (green traces) retain vibronic structure that suggests mostly monomeric dye, whereas the vibronic structure for spectra dyed from water (blue traces) resemble that of the dimer. However, as dye loading increases (longer dying times) the spectra for PMPDI on SnO_2 loaded from either solvent begin to broaden and the vibronic structure degrades, suggesting higher degrees of PMPDI aggregation on the SnO_2 surface.

Dye aggregation on the MO_x surface in DSSCs and DS-PECs often results in lower performance, because the dye aggregation often allows non-radiative relaxation pathways that compete with electron injection into the conduction band of the MO_x substrate.[2,41,59–61] As a result,

the charge-injection efficiency is often lower when aggregates are present.[2,41,59–61] This may account for the observation in Fig. S4.14d, wherein SnO_2/PMPDI anodes dyed from ethylene glycol (green data points, less aggregation) generally showed higher photocurrent than those dyed from water (blue data points, more aggregation). Consistently, the effect was less pronounced at higher dye loading, where even the anodes dyed from ethylene glycol showed UV–vis spectra indicative of aggregation. An alternative hypothesis is that ethylene glycol co-adsorbs to the SnO_2 surface, and could possibly act as a barrier to recombination with redox species in solution, or could become oxidized itself. To remove this variable, *all subsequent studies were done on anodes dyed from water*.

S4.7b Varying SnO_2 Film Thickness. In order to optimize the light-harvesting efficiency of SnO_2/PMPDI anodes, we performed studies to vary the thickness of the SnO_2 film. Thicker films were prepared by doctor blading the SnO_2 paste between multiple layers of Scotch Magic tape (Cat. # 810, 54 ± 1 μm thick according to optical profilometry), or by coating multiple layers into one Scotch spacer, drying in between each layer at 120 °C for 10 min. After spreading the paste, the tape spacers were removed and the anodes were transferred to a furnace, where the temperature was gradually increased (~30 °C/min) to 450 °C under air and held at temperature to sinter for 1 h. After calcination, heat was turned off and the furnace door was gradually opened to allow the film to slowly cool (≤1 °C/s). The resultant varied SnO_2 film thicknesses were measured by optical profilometry. Results are shown in Fig. S4.15a. Film thicknesses increased approximately linearly with the number of scotch tape spacers, or the number of layers spread between 1 layer of scotch tape. Films prepared by multiple Scotch tape spacers were slightly thicker than those prepared by multiple paste depositions within 1-Scotch spacer. Films with

thickness >8 μm tended to crack/flake, giving rise to the diminished average thickness and larger error bars.

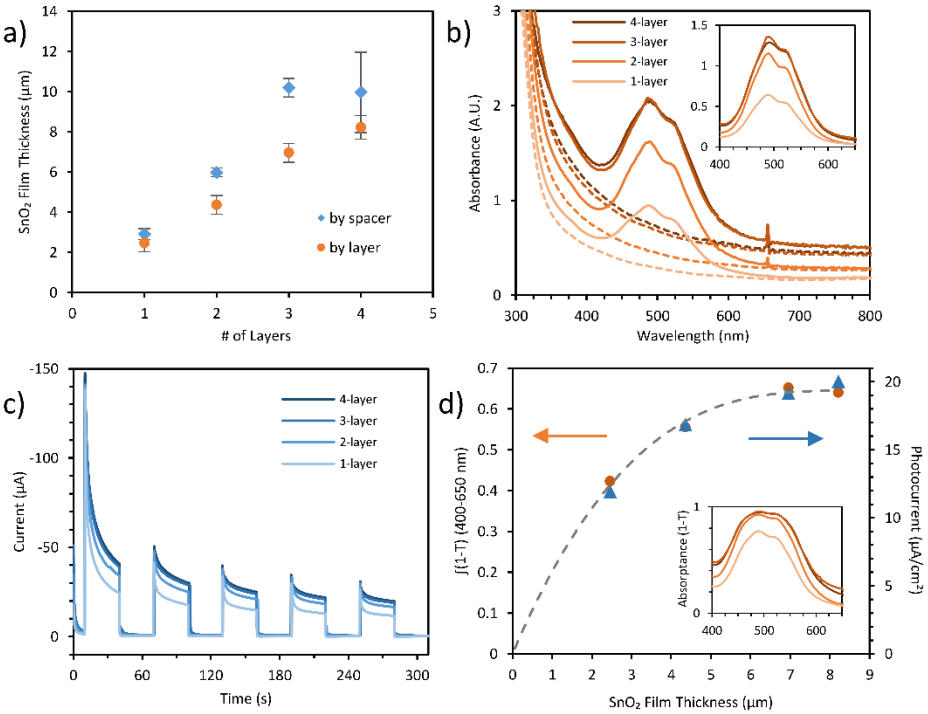

Figure S4.15 Varying SnO_2 film thickness. (a) SnO_2 film thickness (after sintering, as measured by optical profilometry) as a function of the number of Scotch tape spacers used during doctor blading (blue diamonds), or the number of layers of SnO_2 paste spread between 1 layer of Scotch tape (orange circles). (b) UV–vis spectra of bare SnO_2 films (dashed lines) of varying thickness, and after dying with PMPDI (solid lines). Films were dyed 24 h from ~0.3 M PMPDI in water at 90 °C. The inset shows the absorbance spectra of PMPDI alone (spectra of bare SnO_2 films were subtracted). (c) Anodic *J–t* traces with 30 s light transients for SnO_2/PMPDI films of varying thickness, held at +0.2 V vs Ag/AgCl in pH 7, 0.1 M KPi (no H_2Q sacrificial reductant). (d) PMPDI integrated absorptance (1−T) in the range of 400–650 nm (orange circles, see inset) and steady-state photocurrent (blue triangles) plotted vs SnO_2 film thickness. Dotted line is added to guide the eye.

SnO_2 films of varying thickness were dyed from ~0.3 mM PMPDI in water at 90 °C for 24h. Longer dying times did not enhance dye loading. After dying, films were soaked for 1 min in nanopure water to rinse away any non-adsorbed dye, and were allowed to air dry. UV–vis absorbance spectra were recorded for bare and dyed films of varying thickness, which are shown in Fig. S4.15b. The inset shows absorbance by PMPDI (bare film subtracted) on different film

thicknesses, and shows that light absorption is approximately saturated for the 3-layer film (~7 μm thickness).

Photocurrent–time (*J*–*t*) transients were measured for the SnO_2/PMPDI films of varying thickness in pH 7, 0.1 M KPi buffer (without H_2Q), held at +0.2 V vs Ag/AgCl. Results are shown in Fig. S4.15c, demonstrating that photocurrent saturates at higher film thicknesses. By converting the PMPDI absorbance spectra to *absorptance* spectra (1 – Transmittance, see the inset of Fig. S4.15d), we can calculate the integrated absorptance for each dyed film within the wavelength window of 400–650 nm. Restated, the area under each PMPDI absorptance curve in the inset of Fig. S4.15d represents the overall light-harvesting efficiency of the dye in that wavelength window. Finally, plotting both the steady-state photocurrent and the PMPDI integrated absorptance as a function of SnO_2 film thickness (Fig. S4.15d) demonstrates that photocurrent is strongly correlated with the dye's integrated absorptance, and both saturate by ~6 μm SnO_2 film thickness. Fortunately, this thickness was reproducibly produced by using 2 Scotch tape spacers to doctor blade the SnO_2 paste (Fig. S4.15a). Therefore, this "2-Scotch" method was used for all subsequent experiments.

S4.7c Preliminary Al_2O_3 Overlayer Testing. Alumina overlayers were deposited by the method of Ichinose *et al.*[62] following adaptations by Liberatore *et al.*[63] Specifically, a 0.1 M solution of aluminum(III) isopropoxide was prepared in an N_2-filled glovebox: a 20 mL scintillation vial (previously dried in an oven at 150 °C) was rinsed twice with anhydrous isopropanol (*i*-PrOH, Sigma, 99.5%, Sure/Seal cap, reported <30 ppm water), then 200 mg of aluminum isopropoxide (Al(*i*-PrO)$_3$, Sigma, ≥99.99% trace metals basis) was weighed into the vial, followed by 10 mL of anhydrous isopropanol by plastic syringe. The vial was capped, wrapped in Parafilm, and removed from the glove box (Palomares *et al.*[64] stated that solutions of

aluminum isobutoxide were air-stable once dissolved). The solution was agitated in a sonicating water bath until there was no visible solid, then heated on a sand bath to 60 °C without stirring. Note, all such solutions were slightly opaque, likely indicating that the solid aluminum isopropoxide starting material had reacted with trace water to form insoluble Al_2O_3 before being brought into the glove box. Therefore, solutions were centrifuged before use to collect the fine solids at the bottom.

Following the procedures of Palomares *et al.*,[64] sintered MO_x films were pretreated by exposure to water vapor (films on ITO were held above a vial of water at 60 °C) for 1 min, then dried in a furnace at 120 °C for 10 min. This step is presumably to ensure the presence of metal-aquo or metal-hydroxide groups on the surface to react with the Al(*i*-PrO)$_3$. The MO_x films were transferred directly from the 120 °C furnace to the Al(*i*-PrO)$_3$ solution at 60 °C for 10 min, one or two at a time (back to back, thus preventing alumina deposition on the glass substrate as well). After treatment, films were immediately rinsed by dipping in a vial of anhydrous *i*-PrOH to remove any unreacted Al(*i*-PrO)$_3$. Finally, films were placed in a furnace and gradually heated (~30 °C/min) to 400 °C and held at that temperature for 20 min, presumably burning off any residual organics (iPrO ligand) and to complete oxidation of the layer to form Al_2O_3. After slowly cooling (≤60 °C/min), films were placed in PMPDI dye solutions.

Theoretically, this method is expected to deposit a monolayer or less of alumina onto the MO_x film surface after one round of reaction between Al(*i*-PrO)$_3$ and surface hydroxyl groups.[62] With care, we were able to use this method to produce highly uniform alumina overlayers, with no alteration of the nano-MO_x film apparent to the eye (Fig. S4.16) and no change to the MO_x UV–vis absorbance spectrum (Fig. S4.17a). Therefore, the Al_2O_3 overlayer does not alter the light absorption or scattering properties of the substrate. We note that if the Al(*i*-PrO)$_3$ solution was not

centrifuged prior to use, and if MO_x films were rinsed after treatment with non-anhydrous iPrOH, then the resulting alumina overlayer was often visibly 'splotchy', likely due to the deposition of Al_2O_3 particle aggregates.

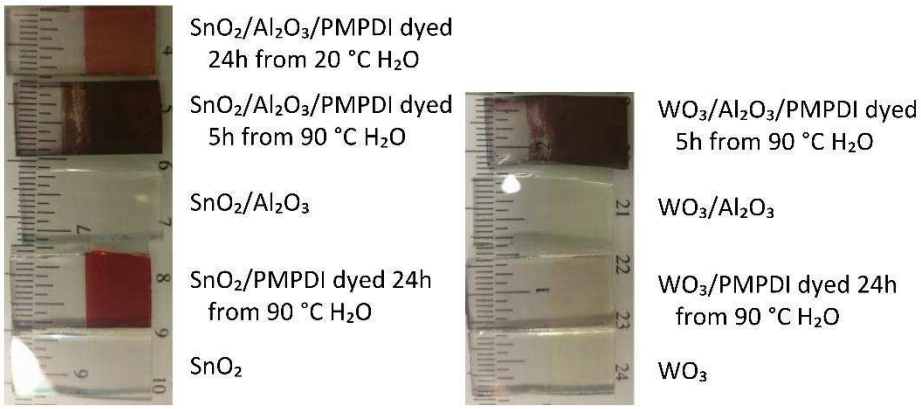

Figure S4.16 Photographs of various SnO_2 ("2-Scotch", ~6 μm thick) and WO_3 ("1-Scotch", ~0.75 μm thick) films in FTO substrates, both before and after alumina treatment and dying under various stated conditions.

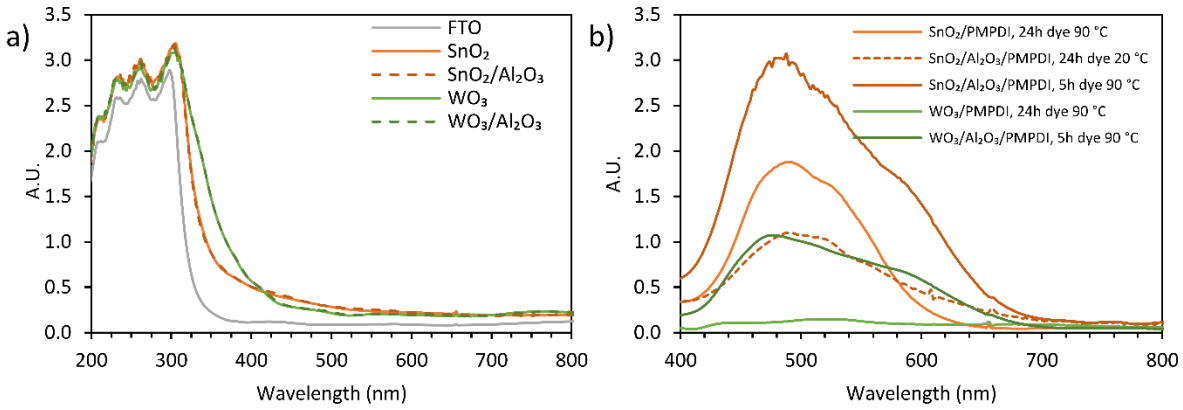

Figure S4.17 (a) UV–visible spectra of bare FTO and FTO coated with bare (un-dyed) SnO_2 (orange) and WO_3 (green) films ("2-Scotch", ~6 μm thick; "1-Scotch", ~0.75 μm thick, respectively) both before (solid line) and after (dashed line) deposition of alumina overlayer. (b) Visible absorbance spectra of PMPDI adsorbed on SnO_2 (orange) or WO_3 (green) films after dying from water solvent under the stated conditions. Absorbance spectra from the bare MO_x films were subtracted from the spectra taken of the respective MO_x/PMPDI films. Note that absorbance spectra are not corrected for the different thicknesses of the MO_x films.

The successful surface treatment of SnO_2 and WO_3 films is evident by the altered kinetics and saturation level of PMPDI dye loading (Figures S4.16 and S4.17b). Untreated SnO_2 films

reached PMPDI saturation (~1.9 A.U. at the λ_{max}) after ~24h of dying from 0.5 mM PMPDI in 90 °C water. By contrast, SnO_2/Al_2O_3 films reached saturation (~3.0 A.U. at the λ_{max}) after <5h of dying under the same conditions. The broadened and absorbance spectrum and red-shifted absorption onset of PMPDI on SnO_2/Al_2O_3 also indicates that PMPDI is more aggregated on this surface. Furthermore, PMPDI could be adsorbed on SnO_2/Al_2O_3 even at room temperature, reaching a lower saturation (~1.0 A.U. at the λ_{max}) within 24h (for comparison, untreated SnO_2 reached only 0.77 A.U. after 72 h under the same conditions), though higher aggregation was still evident by the red-shifted absorption onset. Importantly, alumina treatment also allowed for the loading of PMPDI on WO_3 films, reaching saturation of ~1.0 A.U. (note these WO_3 films were significantly thinner than SnO_2) within 5 h at 90 °C.

Fig. S4.18 provides *J–V* transient experiments which show the effect of the alumina overlayer on photocurrent, both before and after dying. Both untreated bare SnO_2 and SnO_2/Al_2O_3 films reach saturated photocurrent of ~0.1 μA/cm² in pH 7 buffer at potentials positive of ~0.0 V vs Ag/AgCl. SnO_2/PMPDI without alumina treatment and dyed for 24h from 90 °C water solution reached saturated photocurrent of ~20 μA/cm² at potentials positive of ~0.2 V vs Ag/AgCl (Fig. S4.18a). By contrast, SnO_2/Al_2O_3/PMPDI dyed from hot water for 5 h reached saturated photocurrent of only ~5.5 μA/cm² under the same conditions, despite significantly enhanced dye loading compared to the un-treated SnO_2/PMPDI film (Fig. S4.18b). Hypotheses for the lower photocurrent for SnO_2/Al_2O_3/PMPDI despite higher dye loading include (i) that the high dye aggregation (indicated by red-shifted absorbance onset, Fig. S4.18b) on alumina-treated films results in enhanced non-radiative relaxation of the dye before injection can occur;[2,41,59–61] (ii) that dye aggregates were deposited in more than a monolayer, and therefore much of the dye was not at the surface of the MO_x for light-induced electron injection; and (iii) that the tunneling barrier

introduced by the Al_2O_3 overlayer significantly decreases the injection efficiency from photo-excited PMPDI.[49,65]

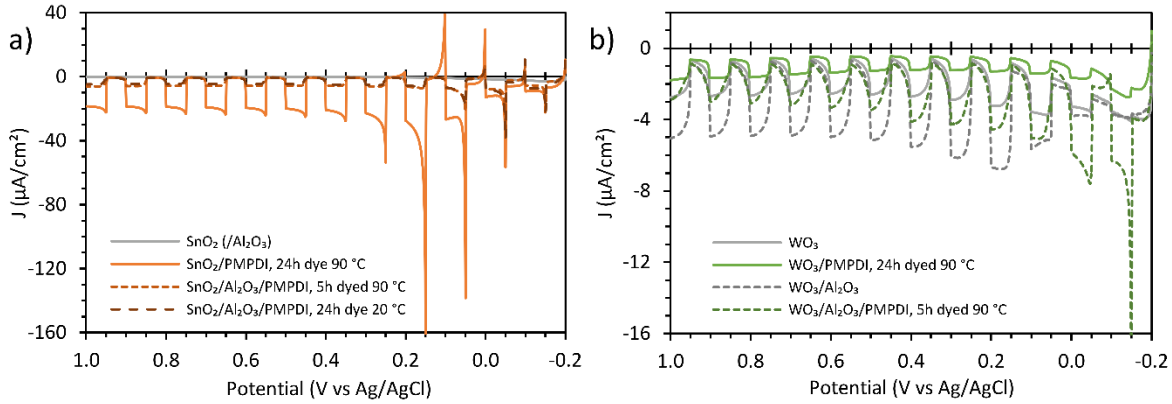

Figure S4.18 Current density–voltage (*J*–*V*) traces for anodes with and without Al_2O_3 overlayer treatment for SnO_2 (a) and WO_3 (b). Grey traces indicate bare MO_x films and colored traces indicate dyed films, solid traces indicate films without Al_2O_3, and dashed traces indicate films with Al_2O_3 overlayer treatment. *J*–*V* traces were obtained in pH 7, 0.1 M KPi buffer and scanned from +1.0 to −0.2 V vs Ag/AgCl with a scan rate of 10 mV/s. Illumination was provided with a Xe arc lamp approximating the AM 1.5 visible spectrum. All scans were recorded immediately following a 5 min *J*–*t* transient experiment such as that shown in Fig. S4.11c.

To test the above aggregation-based hypotheses, an SnO_2/Al_2O_3 film was also dyed from room temperature water, reaching saturation within 24 h, with a lower saturation than un-treated SnO_2 dyed from hot water and still more aggregated (Fig. S4.18b). Photocurrent was barely different from the SnO_2/Al_2O_3/PMPDI anode dyed from hot water despite significantly less dye loading, reaching saturated photocurrent of ~4 μA/cm² at potentials positive of +0.2 V vs Ag/AgCl (Fig. S4.18a). This is consistent with the hypothesis that much of the dye on SnO_2/Al_2O_3/PMPDI prepared from hot solution is aggregated away from the SnO_2 surface. Finally, an SnO_2/Al_2O_3 anode was also dyed from room temperature ethylene glycol for 5 days. This anode reached the same dye saturation as that dyed from room temperature water (~1 A.U. at the λ_{max}), but had less aggregation (no red-shifted absorbance onset, data not shown). In *J*–*V* experiments, this anode

reached saturated photocurrent of only ~3 μA/cm² at potentials positive of +0.2 V vs Ag/AgCl, thus indicating that photocurrent was not improved by a lower degree of aggregation.

A similar trend was found for WO_3 films. For bare films, the deposition of an Al_2O_3 overlayer actually enhanced photocurrent from ~2 μA/cm² to ~4 μA/cm² (Fig. S4.18b), possibly due to enhanced stability of the WO_3 in pH 7 buffer. However, photocurrent was halved after dye loading for both treated and untreated WO_3 films. This may indicate that adsorbed PMPDI has a poor injection efficiency into WO_3 and also pacifies the surface towards whatever electrochemical reaction takes place on the bare film, or possibly that the WO_3 film corrodes during the dying process.

In summary, the deposition of an Al_2O_3 overlayer on MO_x anodes significantly enhanced PMPDI dye loading kinetics and saturation, but resulted in decreased photocurrent relative to un-treated MO_x/PMPDI films. It has previously been shown that Al_2O_3 overlayers can significantly decrease the rate of photo-injection from excited dye, especially as the overlayer thickness increases, again due to the introduction of a thicker electron-tunneling barrier.[49,65] Therefore, our remaining hypotheses for the lack of a photocurrent enhancement effect by our single cycle of Al_2O_3 treatment include: (i) more than the expected monolayer of Al_2O_3 was deposited by the solution-based, dip-coat process used herein, or (ii) the injection efficiency of our specific PMPDI is significantly lower than previously-studied dyes in systems employing a single alumina overlayer, so that the addition of a tunneling barrier had a more pronounced effect on injection efficiency.

Consistent with hypothesis (i) above, it has been suggested that overlayers prepared by solution methods such as that employed herein can have non-uniform thickness,[65] and therefore we might expect improved results with more uniform overlayers (which can be prepared by atomic

layer deposition,[66] for example), either used before dye adsorption or afterwards to partially encapsulate the dye.[60] Consistent with hypothesis (ii) are previous studies which have shown that injection is slower and injection efficiency is lower for dyes such as PMPDI that can aggregate[2,41,59–61] or that employ a non-conjugated spacer groups between the anchors and chromophore[65,67] such as phosphonomethyl groups of PMPDI, due to poor electronic coupling. Thereby, we would expect improved performance by changing the dye structure to include conjugated and short linker groups between the perylene core and the anchor group.

S4.8 Oxygen Quantification by Generator–Collector Method

To determine if observed photocurrent was the result of photoelectrochemical water oxidation catalysis, O_2 in solution was quantified by a Generator–Collector (G–C) method.[68,69] This technique has improved sensitivity relative to a Clark electrode due to its higher collection efficiency (detection of O_2 by electrochemical reduction), but lower selectivity due to its lack of an oxygen-selective membrane as in a Clark electrode. This method uses two working electrodes in a sandwich configuration, with the photoanode (Generator) as the first working electrode (W1) facing a second working electrode (Collector, W2). While original Collector electrodes were Pt,[68] Meyer *et al*. showed that FTO was also usable.[69]

We began by testing the potential-dependent response of a planar FTO electrode in aqueous buffer with differing amounts of dissolved oxygen (Fig. S4.19 below). Multiple cycles of cyclic voltammetry (CV) were performed in pH 7, 0.1 M KPi buffer that was degassed with Ar for 15 min (blue trace), then repeated after degassing with air for 5 min (orange trace), then repeated again after degassing with O_2 for 5 min (grey trace). Consistent with previous results,[70] reductive current at the FTO electrode above −0.3 V vs Ag/AgCl increased with increasing concentration of

dissolved oxygen. Reduction currents were nearly saturated at potentials negative of the peak at −0.60 V vs Ag/AgCl, consistent with O_2 reduction. Therefore, a potential of −0.65 V vs Ag/AgCl was chosen for subsequent G–C studies with FTO as the Collector electrode.

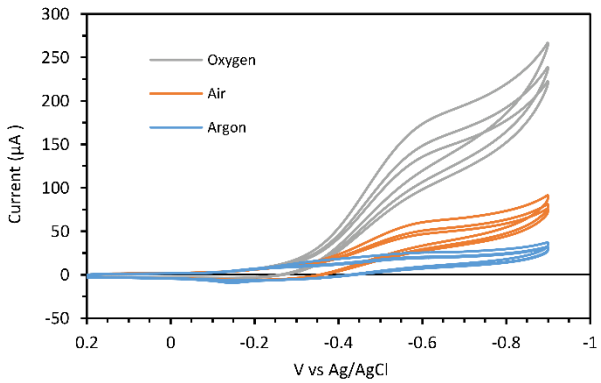

Figure S4.19 Cyclic voltammograms of an FTO working electrode in pH 7, 0.1 M KPi buffer degassed 15 min with argon (blue), 5 min air (orange), then 5 min O_2 (grey). Scan rate was 100 mV/s.

Subsequently, we assembled a G–C testing configuration by attaching a copper tape electrical contact to the top (FTO) portion of an FTO/SnO_2/PMPDI (Generator) anode, then masked the top and bottom FTO portions (where there was no SnO_2/PMPDI film) with un-stretched Parafilm (reported 130 µm thick). Copper tape was attached to the top of a bare FTO (Collector) electrode of similar size. The two electrodes were sandwiched together, with the Parafilm spacers preventing contact between the electrodes or the two Cu tape contacts (see the G–C schematic in Fig. S4.20a below). The two electrodes were then wrapped together with two thin, long strips of stretched Parafilm. This way, two sides of the G–C sandwich were open to allow diffusion of solution into and out of the cell.

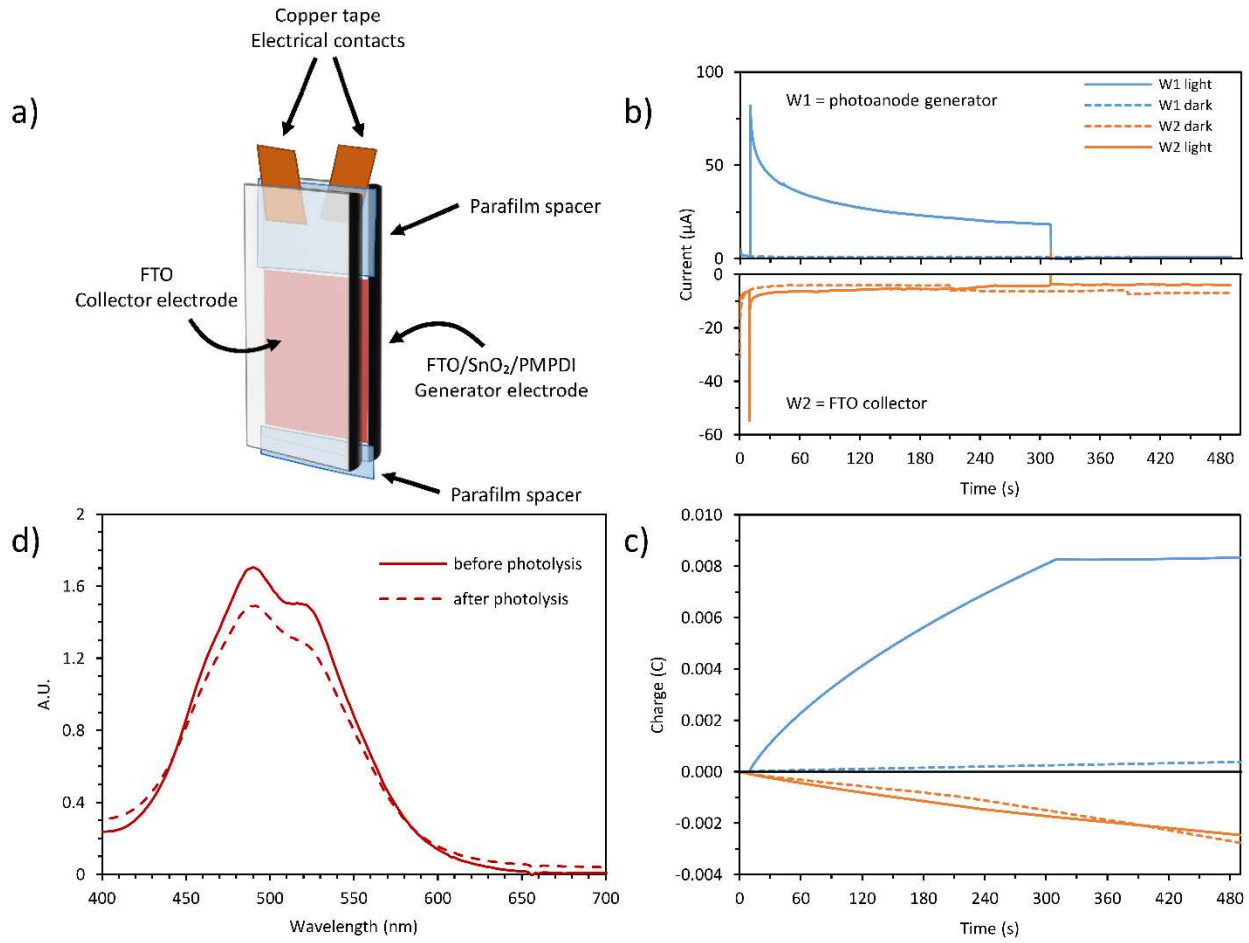

Figure S4.20 (a) Schematic representation of a G–C electrode configuration. The FTO/SnO_2/PMPDI Generator electrode is sandwiched against a bare FTO collector electrode with Parafilm spacers above and below the SnO_2/PMPDI film to prevent contact. Both electrodes have Cu tape as electrical contacts for connection of alligator clips. (b) Current measured at the Generator (upper, blue traces) and Collector (lower, orange traces) held a +0.2 V vs Ag/AgCl, and −0.65 V vs Ag/AgCl, respectively, in pH 7, 0.1 M KPi buffer degassed with Ar for 15 min. Solid line traces were illuminated from 10–310 s. Dashed lines were subsequently measured in the dark as a baseline. (c) Integrated current–time traces from (b) used to calculate faradaic efficiency. (d) UV–vis absorbance spectra of PMPDI (spectrum of bare SnO_2 was subtracted) before and after 10 min of photolysis.

Once assembled, the G–C cell was submerged in solution in a two-compartment photoelectrochemical cell with a working compartment made from 1 × 1.5 cm^2 pyrex rectangular tubing with a working volume of ~5 mL and separated from the auxiliary compartment by a medium porosity glass frit. The cell was filled with pH 7, 0.1 M KPi buffer solution which was degassed with Ar for at least 30 min. The Ag/AgCl (3 M NaCl) reference electrode was placed

near the G–C cell in the working compartment, and a Pt wire counter electrode in the auxiliary compartment. Argon was flowed over the top of solution throughout experiments. Electrochemical testing was controlled with a CH Instruments 750D bipotentiostat, using amperometric current–time experiments. Current was measured at the Generator (SnO_2/PMPDI) and Collector (FTO) electrodes held at +0.2 V and −0.65 V vs Ag/AgCl, respectively, for 490 s trials. First, the G–C cell was illuminated from the back (substrate) side of the SnO_2/PMPDI electrode from 10–310 s, using a Xe arc lamp calibrated to closely match the visible portion of the AM1.5 standard solar spectrum (see Sec. S4.5). Subsequently, and without moving the cell, the experiment was repeated in the dark.

An example current–time trace from a G–C cell is provided in Fig. S4.20b. Photocurrent measured at the SnO_2/PMDPI Generator electrode was consistent with previous measurements (see Fig. 4.5c of the main text), with steady-state photocurrent decaying from ~50 to 20 μA/cm² during 5 min of photolysis. Currents at the Collector electrode were above zero throughout the experiment, even in the dark. This likely indicates trace O_2 or other impurities in solution. Current–time traces were integrated to determine the charge passed (Q) at each electrode (Fig. S4.20c). Subtraction of charge passed in the dark (dashed lines) from charge passed during illumination (solid lines) allows for the calculation of charge attributable to photoelectrochemical processes ($Q_{photo)}$ such as water oxidation. Notably, Q_{photo} at the collector electrodes were very small, indicating minimal O_2 production by the SnO_2/PMPDI (see below).

In order to calculate the collection of efficiency of the same G–C cell, the current–time traces were repeated in the presence of H_2Q sacrificial reductant (following literature precedent).[69] This step was done *second* in order to prevent contamination of trace H_2Q during O_2-testing. To do this, the electrolyte was removed from the cell by pipet (without moving any of the electrodes),

and replaced with Ar-degassed pH 7, 0.1 M KPi *plus 20 mM H_2Q*. The current-time measurements were then repeated in the light and dark. The collector efficiency, η_{coll}, was calculated as:

$$\eta_{coll} = \frac{Q_{photo}(Generator, H_2Q)}{-Q_{photo}(Collector, H_2Q)} \quad \text{(S4.5)}$$

using the charge passed (Q_{photo}) at the end of illumination, 310 s. An average η_{coll} of 92 ± 3% was found from our experiments. Finally, the collector efficiency can be used to calculate the overall faradaic efficiency for water oxidation, η_F, as:

$$\eta_F = \frac{Q_{photo}(Generator)}{-Q_{photo}(Collector)} \times \eta_{coll} \quad \text{(S4.6)}$$

again using the charge passed at the end of illumination, 310 s, measured prior to H_2Q addition. Our experiments for SnO_2/PMPDI anodes yielded average faradaic efficiency for O_2 production (or other reducible products) of **$1 \pm 2\%$**. This means that, within experimental error, practically none of the photocurrent observed at SnO_2/PMPDI anodes can be attributable to O_2 evolution.

S4.8a PMPDI Concentration Calculations for Stability Estimation. Given the above hypothesis that photocurrent from SnO_2/PMPDI anodes (without catalyst) in aqueous solutions originates from oxidative decomposition of PMPDI, we estimated the amount of PMPDI on a given anode. The molar extinction coefficient of PMPDI in water solution was determined to be ~22,000 $M^{-1}cm^{-1}$ (or 2.2 $M^{-1}\mu m^{-1}$) at the λ_{max} of 500 nm. The SnO_2/PMPDI anode tested in Fig. S4.20b had Abs_{max} of 1.7 using a 2-Scotch SnO_2 film (6.0 μm thickness). Assuming that the extinction coefficient is roughly the same for PMPDI adsorbed on SnO_2 as in aqueous solution, we get a value of ~0.13 M PMPDI, or 0.13 mol PMPDI per L of SnO_2 film volume. (Typical optimized values ranged from 0.13 to 0.16 M PMPDI on SnO_2). Typical dimensions for SnO_2/PMPDI films were ~1.3 cm^2 × 6.0 μm, giving a volume of 7.8×10^{-4} cm^3 or 7.8×10^{-7} L. Therefore, the amount of dye on our anode was (0.13 mol/L) × (7.8×10^{-7} L) = 1.0×10^{-7} mol

PMPDI. Using Avogadro's constant, we get (1.0×10^{-7} mol) × (6.02×10^{23} molec./mol) ≈ **6.0×10^{16} molecules PMPDI** in this SnO_2 film.

As shown in Fig. S4.20c, this SnO_2/PMPDI anode passed a photo-generated charge, Q_{photo}, of 0.0080 C over 5 min of uninterrupted photolysis. Given that a coulomb is equal to 6.24×10^{18} electrons, approximately 5.0×10^{16} electrons were passed during this 5 min of photolysis. Thus, 0.83 electrons were passed per PMPDI molecule on the film. Subsequently, an additional 5 min of photolysis was carried out wherein photocurrent settled to a steady-state of ~15 μA (data not shown), and an additional Q_{photo} of 0.0050 C was passed, giving a total of **8.1×10^{16} electrons passed**. Therefore, approximately 1.4 electrons were passed for every molecule of PMPDI in the film, sufficient to perform at least a 1-electron oxidation of all PMPDI or a 2-electron oxidation of 67% of the PMPDI. Meanwhile, the UV–vis absorbance spectrum of the SnO_2/PMPDI anode was taken before and after this 10 min of photolysis, and is shown in Fig. S4.20d. The change in absorbance at the λ_{max} is consistent with a loss of only 12% of the PMPDI by desorption or degradation.

In summary, more charge is passed during 10 min of photolysis than the approximated number of molecules of PMPDI on the SnO_2 film, and photocurrent remained stable beyond this time. Meanwhile, the UV–vis absorbance spectra of the film before and after photolysis indicates only 12% loss of PMPDI. This clearly indicates that the majority of photocurrent cannot be attributed to decomposition of PMPDI, nor to O_2 production by water oxidation. Therefore, the last remaining hypothesis for the origin of photocurrent is the oxidation of water to H_2O_2, or the oxidation of solution impurity species such as Cl^- leached from the reference electrode or trace metal impurities from the buffer, for example.

S4.9 IPCE Measurements for SnO_2/PMPDI

Action spectra were collected using a testing apparatus consisting of a Xe arc lamp (Oriel model 66002, calibrated to approximately match the AM1.5 reference power in the visible region), power supply (Oriel model 68700), monochromator (Oriel Cornerstone 130, model 7400), and a CH Instruments 630D potentiostat. Experiments were run in the same two-compartment photoelectrochemical cell as previous experiments, with FTO/SnO_2/PMPDI working electrode and Ag/AgCl reference electrode in the working compartment and Pt wire counter electrode in the auxiliary compartment. The face of the cell was pressed against an aperture defining an illuminated area of 0.385 cm^2. To collect the action spectra, the electrodes were held at +0.2 V vs Ag/AgCl while the incident monochromatic light (~3 nm bandwidth) was scanned from 400 to 700 nm in 25 nm steps. Photocurrent, I_{ph}, was measured at each wavelength step by recording three 15 s light transients, subtracting the dark current from the light current at the end of each transient, and averaging the three values. The incident lamp power at each wavelength step, P_{mono}, was recorded through the same aperture using a Thorlabs silicon standard power sensor, model S120B, in order to calculate the final incident-photon-to-current efficiency (IPCE) values. The calculation was performed according to the equation:[71]

$$\mathrm{IPCE}(\lambda) = \frac{I_{\mathrm{ph}}(\mathrm{mA}) \times 1239.8\ (\mathrm{V{\cdot}nm})}{P_{\mathrm{mono}}(\mathrm{mW}) \times \lambda(\mathrm{nm})} \tag{S4.7}$$

A representative photocurrent action spectrum for an optimized SnO_2/PMPDI anode in pH 7, 0.1 M KPi buffer is provided in Fig. S4.21, showing the three current–time transients at each illumination wavelength (plotted by the American convention with anodic photocurrent plotted in the negative direction). Notably, there is small photocurrent present throughout the whole scan, even at high (red) wavelengths where PMPDI does not absorb light. This low photocurrent may originate from excitation of intra-bandgap SnO_2 defect states, for example. In the wavelength

range where PMPDI absorbs light (~400–600 nm), photocurrents are slightly larger and take on the spike behavior that was previously observed in polychromatic *J*–*t* and *J*–*V* transient experiments at +0.2 V vs Ag/AgCl (see Figures S4.11 and S4.12, for example). We note that, given the O_2 detection results above, the origin of photocurrent is not O_2 generation, and is currently unknown. The current spike behavior likely results from rapid injection from photo-excited PMPDI, followed by a buildup of oxidized PMPDI at the surface as a result of poor charge transfer to solution, given the lack of a sacrificial reductant or WOCatalyst. The result is a decay to a low steady-state current where charge injection and back-electron transfer are at kinetic equilibrium.

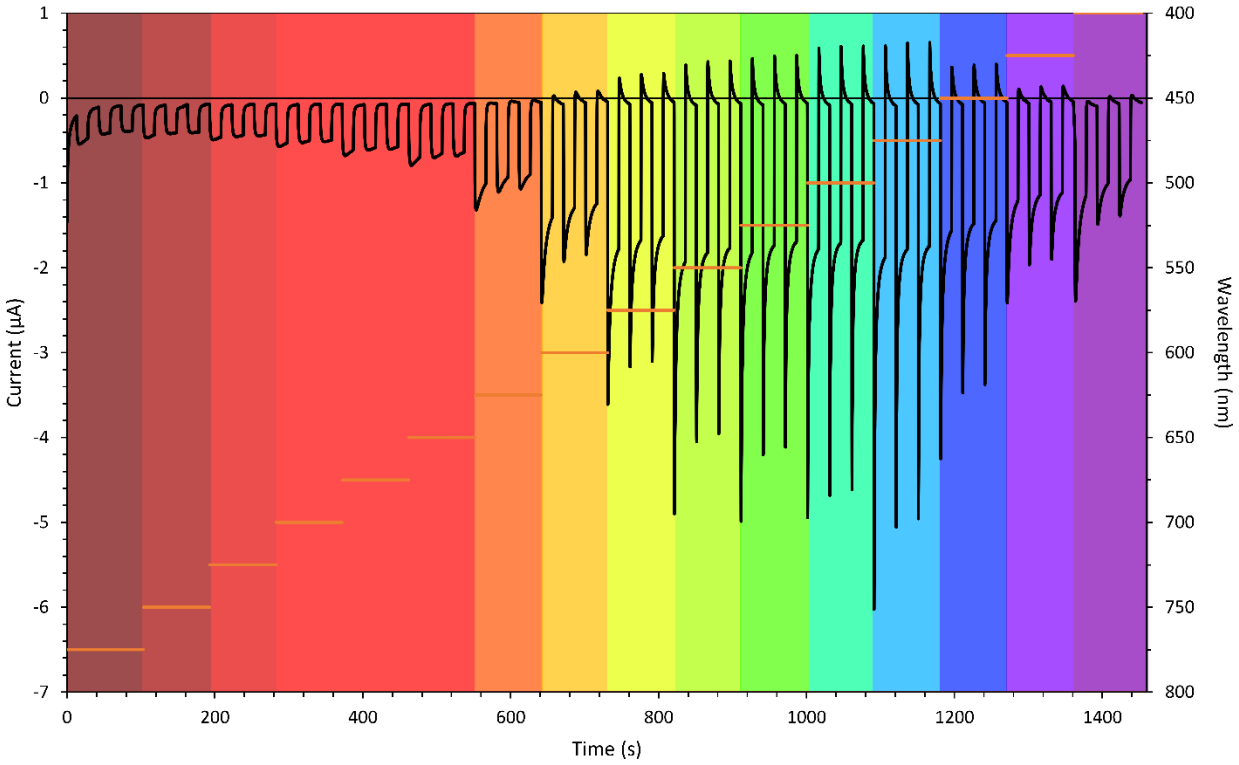

Figure S4.21 Transient Photocurrent–time traces from a representative SnO_2/PMPDI anode in pH 7, 0.1 M KPi buffer**.** Anode was held at +0.2 V vs Ag/AgCl and illuminated with a Xe arc lamp approximating 1 sun illumination through a monochromator. For each wavelength step, three 15 s transients were performed. There was a short, ~30–60 s break between each wavelength measurement while the cell was held in the dark at open-circuit.

Photocurrent action spectra were also collected in the presence of 20 mM H_2Q sacrificial reductant. A plot from one representative SnO_2/PMPDI anode is shown in Fig. S4.22. Again, similar to polychromatic *J*–*t* and *J*–*V* transient experiments in the presence of H_2Q (Figures S4.11 and S4.12), photocurrent was much higher in magnitude and showed much less spike-like behavior than without H_2Q. This suggests much more efficient regeneration of photo-oxidized PMPDI, allowing for rapid turnover to absorb additional photons. There was slight drift in the overall dark current during each scan, though the photocurrent magnitudes were quite stable over time and with repeated transients.

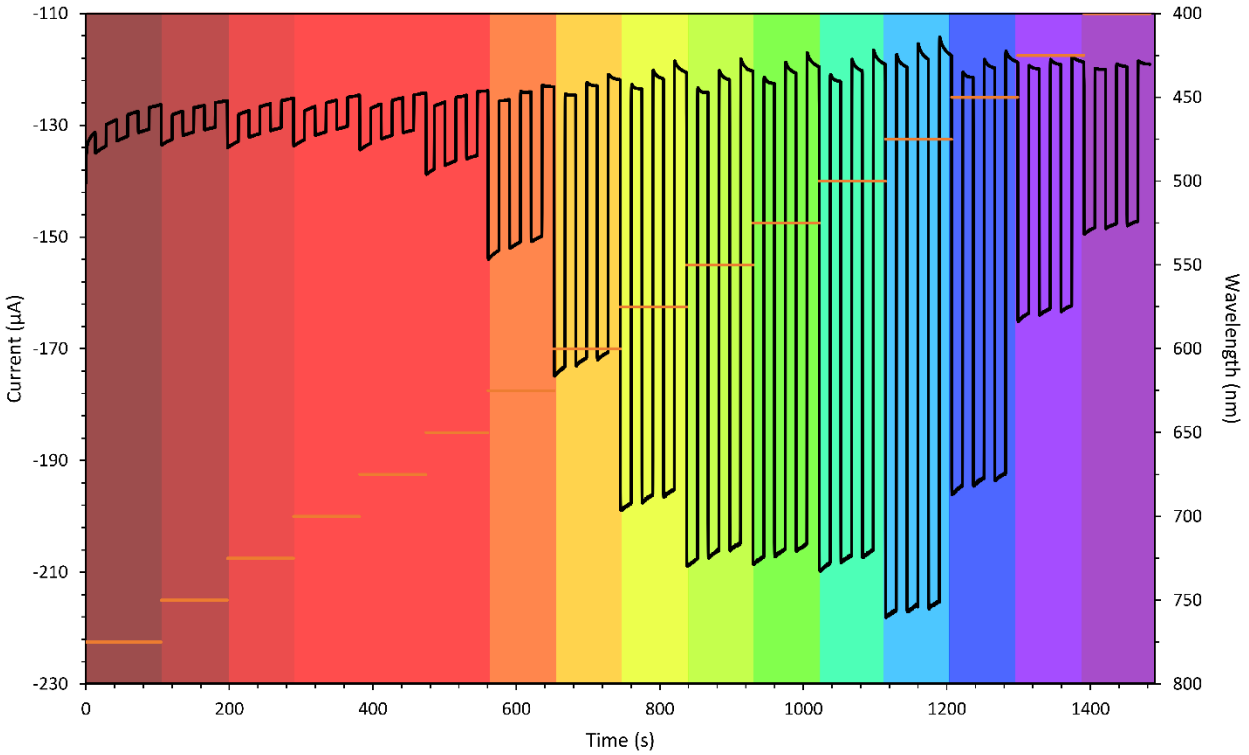

Figure S4.22 Transient Photocurrent–time traces from a representative SnO_2/PMPDI anode in pH 7, 0.1 M KPi buffer *with 20 mM H_2Q*. Anode was held at +0.2 V vs Ag/AgCl and illuminated with a Xe arc lamp approximating 1 sun illumination through a monochrometer. For each wavelength step, three 15 s transients were performed. There was a short, ~30–60 s break between each wavelength measurement while the cell was held in the dark at open-circuit.

Subsequently, photocurrents at each wavelength were used to calculate the IPCE spectra by equation S4.7. Resulting spectra are shown in Fig. S4.23 for SnO_2/PMPDI anodes without, (a), and with, (b), H_2Q.

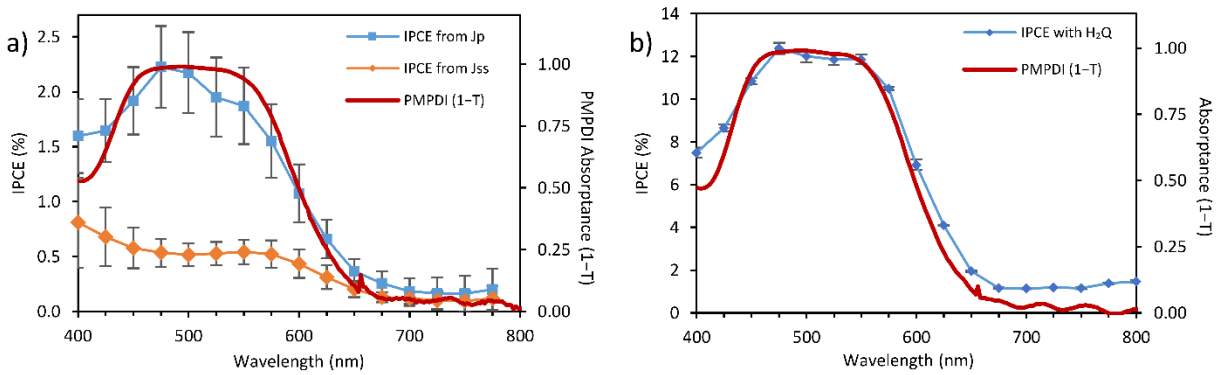

Figure S4.23 IPCE values calculated for SnO_2/PMPDI in pH 7, 0.1 M KPi in the absence (a) and in the presence (b) of 20 mM H_2Q. IPCE values in (a) were calculated from the peak photocurrent values, J_p (blue squares) or from the steady-state current, J_{ss} (orange diamonds), and are compared to the absorptance spectrum of PMPDI (light absorbance and scattering from bare SnO_2 is subtracted). Error bars represent the standard deviation obtained from (a) 4 different anodes (11 transient measurements) taken both from low-to-high wavelengths and high-to-low wavelength, and (b) two different anodes (5 transient measurements).

Notably, the gradual decay of photocurrent over time in the absence of H_2Q (Fig. S4.11c, for example) resulted in relatively large error bars (Fig. S4.23a, note that action spectra were recorded both from high-to-low and from low-to-high wavelengths to avoid a systematic error). In contrast, the stable photocurrent observed in the presence of H_2Q resulted in much smaller error bars. Without H_2Q, IPCE data calculated (incorrectly)[71] from *peak* photocurrent (spike) values were a relatively good match for the absorptance spectrum of PMDPI (Fig. S4.23a, blue square data), whereas IPCE data calculated (correctly)[71] from the *steady-state* photocurrent values were a poor match (Fig. S4.23a, orange diamond data). This observation is not well understood, but may be a result of recombination-limited current or of the specific (unknown) oxidation reaction that is taking place.

Importantly, the IPCE spectrum for SnO_2/PMPDI films in the *presence* of H_2Q is a close match to the absorptance spectrum of the PMPDI (Fig. S4.23b). We note that *all* IPCE points recorded at 400 nm are higher than expected from the absorptance spectrum of PMPDI. This likely indicates a photocurrent contribution from direct light absorption by SnO_2 (see the absorption spectrum of bare SnO_2 in Fig. S4.17a). The maximum IPCE of 12.4 ± 0.3% for optimized SnO_2/PMPDI anodes in the presence of H_2Q is far from the ~86% achieved by top DSSCs,[72] likely due to poor injection efficiency caused by dye aggregation[2,41,59–61] and poor electronic coupling through the phosphonomethyl anchor group.[65,67]

REFERENCES

(1) Ardo, S.; Meyer, G. J. Photodriven Heterogeneous Charge Transfer with Transition-Metal Compounds Anchored to TiO_2 Semiconductor Surfaces. *Chem. Soc. Rev.* **2009**, *38*, 115–164.

(2) Hagfeldt, A.; Boschloo, G.; Sun, L.; Kloo, L.; Pettersson, H. Dye-Sensitized Solar Cells. *Chem. Rev.* **2010**, *110*, 6595–6663.

(3) Swierk, J. R.; Mallouk, T. E. Design and Development of Photoanodes for Water-Splitting Dye-Sensitized Photoelectrochemical Cells. *Chem. Soc. Rev.* **2013**, *42*, 2357–2387.

(4) Yu, Z.; Li, F.; Sun, L. Recent Advances in Dye-Sensitized Photoelectrochemical Cells for Solar Hydrogen Production Based on Molecular Components. *Energy Environ. Sci.* **2015**, *8*, 760–775.

(5) Brennaman, M. K.; Norris, M. R.; Gish, M. K.; Grumstrup, E. M.; Alibabaei, L.; Ashford, D. L.; Lapides, A. M.; Papanikolas, J. M.; Templeton, J. L.; Meyer, T. J. Ultrafast, Light-Induced Electron Transfer in a Perylene Diimide Chromophore-Donor Assembly on TiO_2. *J. Phys. Chem. Lett.* **2015**, *6*, 4736–4742.

(6) Grätzel, M. Photoelectrochemical Cells. *Nature* **2001**, *414*, 338–344.

(7) Krol, R. van de; Liang, Y.; Schoonman, J. Solar Hydrogen Production with Nanostructured Metal Oxides. *J. Mater. Chem.* **2008**, *18*, 2311–2320.

(8) Kirner, J. T.; Stracke, J. J.; Gregg, B. A.; Finke, R. G. Visible-Light-Assisted Photoelectrochemical Water Oxidation by Thin Films of a Phosphonate-Functionalized Perylene Diimide Plus CoO_x Cocatalyst. *ACS Appl. Mater. Interfaces* **2014**, *6*, 13367–13377. http://pubs.acs.org/doi/abs/10.1021/am405598w.

(9) Ronconi, F.; Syrgiannis, Z.; Bonasera, A.; Prato, M.; Argazzi, R.; Caramori, S.; Cristino, V.; Bignozzi, C. A. Modification of Nanocrystalline WO_3 with a Dicationic Perylene Bisimide: Applications to Molecular Level Solar Water Splitting. *J. Am. Chem. Soc.* **2015**, *137*, 4630–4633.

(10) Chou, T. P.; Zhang, Q.; Russo, B.; Fryxell, G. E.; Cao, G. Titania Particle Size Effect on the Overall Performance of Dye-Sensitized Solar Cells. *J. Phys. Chem. C* **2007**, *111*, 6296–6302.

(11) Xue, Z.; Zhang, W.; Yin, X.; Cheng, Y.; Wang, L.; Liu, B. Enhanced Conversion Efficiency of Flexible Dye-Sensitized Solar Cells by Optimization of the Nanoparticle Size with an Electrophoretic Deposition Technique. *RSC Adv.* **2012**, *2*, 7074–7080.

(12) Wang, H.; Rogach, A. L. Hierarchical SnO_2 Nanostructures: Recent Advances in Design, Synthesis, and Applications. *Chem. Mater.* **2014**, *26*, 123–133.

(13) Chappel, S.; Zaban, A. Nanoporous SnO_2 Electrodes for Dye-Sensitized Solar Cells: Improved Cell Performance by the Synthesis of 18 Nm SnO_2 Colloids. *Sol. Energy Mater. Sol. Cells* **2002**, *71*, 141–152.

(14) Brennan, B. J.; Durrell, A. C.; Koepf, M.; Crabtree, R. H.; Brudvig, G. W. Towards Multielectron Photocatalysis: A Porphyrin Array for Lateral Hole Transfer and Capture on a Metal Oxide Surface. *Phys. Chem. Chem. Phys.* **2015**, *17*, 12728–12734.

(15) Alibabaei, L.; Sherman, B. D.; Norris, M. R.; Brennaman, M. K.; Meyer, T. J. Visible Photoelectrochemical Water Splitting into H_2 and O_2 in a Dye-Sensitized Photoelectrosynthesis Cell. *Proc. Natl. Acad. Sci.* **2015**, *112*, 5899–5902.

(16) Poddutoori, P. K.; Thomsen, J. M.; Milot, R. L.; Sheehan, S. W.; Negre, C. F. A.; Garapati, V. K. R.; Schmuttenmaer, C. A.; Batista, V. S.; Brudvig, G. W.; van der Est, A. Interfacial Electron Transfer in Photoanodes Based on phosphorus(V) Porphyrin Sensitizers Co-Deposited on SnO_2 with the Ir(III)Cp* Water Oxidation Precatalyst. *J. Mater. Chem. A* **2015**, *3*, 3868–3879.

(17) Deb, S. K. Opportunities and Challenges in Science and Technology of WO_3 for Electrochromic and Related Applications. *Sol. Energy Mater. Sol. Cells* **2008**, *92*, 245–258.

(18) Liu, X.; Wang, F.; Wang, Q. Nanostructure-Based WO_3 Photoanodes for Photoelectrochemical Water Splitting. *Phys. Chem. Chem. Phys.* **2012**, *14*, 7894–7911.

(19) Zhi-guang, Y.; Jun, W.; Li, F.; Ya-nan, W. U.; Lang, Z. Study on the Preparation and Application of Nanostructured Tungsten Trioxide. *Appl. Chem. Ind.* **2015**, *44*, 707–710.

(20) Zheng, H.; Tachibana, Y.; Kalantar-zadeh, K. Dye-Sensitized Solar Cells Based on WO_3. *Langmuir* **2010**, *26*, 19148–19152.

(21) Ayouchi, R.; Bhattacharyya, S. R.; Barrado, J. R. R.; Schwarz, R. Tungsten Trioxide Nanostructured Electrodes for Organic Dye Sensitised Solar Cells. *Int. J. Nanotechnol.* **2014**, *11*, 869.

(22) Hyun-Wook Ryu; Kyung-Hee Park; In-Chun Kim; Kwang-Jun Hong; Woo-Sun Lee; Jin-Seong Park. Synthesis and Characterization of WO_3 Nanopowders and Their Electrical Properties. *J. Korean Phys. Soc.* **2003**, *42*, L727–L730.

(23) Hong, S. J.; Jun, H.; Borse, P. H.; Lee, J. S. Size Effects of WO_3 Nanocrystals for Photooxidation of Water in Particulate Suspension and Photoelectrochemical Film Systems. *Int. J. Hydrog. Energy* **2009**, *34*, 3234–3242.

(24) Amano, F.; Ishinaga, E.; Yamakata, A. Effect of Particle Size on the Photocatalytic Activity of WO_3 Particles for Water Oxidation. *J. Phys. Chem. C* **2013**, *117*, 22584–22590.

(25) Arutanti, O.; Ogi, T.; Nandiyanto, A. B. D.; Iskandar, F.; Okuyama, K. Controllable Crystallite and Particle Sizes of WO_3 Particles Prepared by a Spray-Pyrolysis Method and Their Photocatalytic Activity. *AIChE J.* **2014**, *60*, 41–49.

(26) Memar, A.; Phan, C. M.; Tade, M. O. Controlling Particle Size and Photoelectrochemical Properties of Nanostructured WO_3 with Surfactants. *Appl. Surf. Sci.* **2014**, *305*, 760–767.

(27) Bignozzi, C. A.; Caramori, S.; Cristino, V.; Argazzi, R.; Meda, L.; Tacca, A. Nanostructured Photoelectrodes Based on WO_3: Applications to Photooxidation of Aqueous Electrolytes. *Chem. Soc. Rev.* **2013**, *42*, 2228–2246.

(28) Zhu, T.; Chong, M. N.; Chan, E. S. Nanostructured Tungsten Trioxide Thin Films Synthesized for Photoelectrocatalytic Water Oxidation: A Review. *ChemSusChem* **2014**, *7*, 2974–2997.

(29) Ito, S.; Murakami, T. N.; Comte, P.; Liska, P.; Grätzel, C.; Nazeeruddin, M. K.; Grätzel, M. Fabrication of Thin Film Dye Sensitized Solar Cells with Solar to Electric Power Conversion Efficiency over 10%. *Thin Solid Films* **2008**, *516*, 4613–4619.

(30) Meda, L.; Tozzola, G.; Tacca, A.; Marra, G.; Caramori, S.; Cristino, V.; Bignozzi, C. A. Photo-Electrochemical Properties of Nanostructured WO_3 Prepared with Different Organic Dispersing Agents. *Sol. Energy Mater. Sol. Cells* **2010**, *94*, 788–796.

(31) Ito, S.; Chen, P.; Comte, P.; Nazeeruddin, M. K.; Liska, P.; Péchy, P.; Grätzel, M. Fabrication of Screen-Printing Pastes from TiO_2 Powders for Dye-Sensitised Solar Cells. *Prog. Photovolt. Res. Appl.* **2007**, *15*, 603–612.

(32) Angiuli, F.; Argazzi, R.; Caramori, S.; Bignozzi, C. A. A Method for Preparing Nanocrystalline Transparent Films of Tungsten Oxide. WO2007094019 (A1), August 23, 2007.

(33) Freedman, M. L. The Tungstic Acids. *J. Am. Chem. Soc.* **1959**, *81*, 3834–3839.

(34) Santato, C.; Odziemkowski, M.; Ulmann, M.; Augustynski, J. Crystallographically Oriented Mesoporous WO_3 Films: Synthesis, Characterization, and Applications. *J. Am. Chem. Soc.* **2001**, *123*, 10639–10649.

(35) Augustynski, J.; Ulmann, M.; Solarska, R. Manufacturing Method. WO2005103329 (A2), November 3, 2005.

(36) Scherrer, P. Bestimmung der Größe und der inneren Struktur von Kolloidteilchen mittels Röntgenstrahlen. *Nachrichten Von Ges. Wiss. Zu Gött. Math.-Phys. Kl.* **1918**, *1918*, 98–100.

(37) Beranek, R. (Photo)electrochemical Methods for the Determination of the Band Edge Positions of TiO_2-Based Nanomaterials. *Adv. Phys. Chem.* **2011**, *2011*, 1–20.

(38) Ford, W. E. Photochemistry of 3,4,9,10-Perylenetetracarboxylic Dianhydride Dyes: Visible Absorption and Fluorescence of the Di(glycyl)imide Derivative Monomer and Dimer in Basic Aqueous Solutions. *J. Photochem.* **1987**, *37*, 189–204.

(39) Chen, Z.; Stepanenko, V.; Dehm, V.; Prins, P.; Siebbeles, L. D. A.; Seibt, J.; Marquetand, P.; Engel, V.; Würthner, F. Photoluminescence and Conductivity of Self-Assembled $\pi-\pi$ Stacks of Perylene Bisimide Dyes. *Chem. – Eur. J.* **2007**, *13*, 436–449.

(40) Lee, S. K.; Zu, Y.; Herrmann, A.; Geerts, Y.; Müllen, K.; Bard, A. J. Electrochemistry, Spectroscopy and Electrogenerated Chemiluminescence of Perylene, Terrylene, and Quaterrylene Diimides in Aprotic Solution. *J. Am. Chem. Soc.* **1999**, *121*, 3513–3520.

(41) Lindquist, R. J.; Phelan, B. T.; Reynal, A.; Margulies, E. A.; Shoer, L. E.; Durrant, J. R.; Wasielewski, M. R. Strongly Oxidizing Perylene-3,4-Dicarboximides for Use in Water Oxidation Photoelectrochemical Cells. *J. Mater. Chem. A* **2016**, *4*, 2880–2893.

(42) Fundamentals of Xenon Arc Lamps. http://zeiss-campus.magnet.fsu.edu/articles/lightsources/xenonarc.html (accessed May 18, 2016).

(43) Reference Solar Spectral Irradiance: Air Mass 1.5. http://rredc.nrel.gov/solar/spectra/am1.5/ (accessed May 18, 2016).

(44) Bisquert, J.; Fabregat-Santiago, F.; Mora-Seró, I.; Garcia-Belmonte, G.; Barea, E. M.; Palomares, E. A Review of Recent Results on Electrochemical Determination of the Density of Electronic States of Nanostructured Metal-Oxide Semiconductors and Organic Hole Conductors. *Inorganica Chim. Acta* **2008**, *361*, 684–698.

(45) Vandermolen, J.; Gomes, W. P.; Cardon, F. Investigation on the Kinetics of Electroreduction Processes at Dark TiO_2 and $SrTiO_3$ Single Crystal Semiconductor Electrodes. *J. Electrochem. Soc.* **1980**, *127*, 324–328.

(46) Salvador, P.; Gutiérrez, C. Mechanisms of Charge Transfer at the Semiconductor-Electrolyte Interface I. Kinetics of Electroreduction at Dark of $Fe(CN)_6^{3-}$ and $IrCl_6^{2-}$ in Aqueous Solution on a Sintered Nb-doped n-$SrTiO_3$ Electrode: Influence of pH. *J. Electrochem. Soc.* **1984**, *131*, 326–336.

(47) Bisquert, J.; Zaban, A.; Salvador, P. Analysis of the Mechanisms of Electron Recombination in Nanoporous TiO_2 Dye-Sensitized Solar Cells. Nonequilibrium Steady-State Statistics and Interfacial Electron Transfer via Surface States. *J. Phys. Chem. B* **2002**, *106*, 8774–8782.

(48) Ondersma, J. W.; Hamann, T. W. Measurements and Modeling of Recombination from Nanoparticle TiO_2 Electrodes. *J. Am. Chem. Soc.* **2011**, *133*, 8264–8271.

(49) Prasittichai, C.; Hupp, J. T. Surface Modification of SnO_2 Photoelectrodes in Dye-Sensitized Solar Cells: Significant Improvements in Photovoltage via Al_2O_3 Atomic Layer Deposition. *J. Phys. Chem. Lett.* **2010**, *1*, 1611–1615.

(50) Swierk, J. R.; McCool, N. S.; Saunders, T. P.; Barber, G. D.; Mallouk, T. E. Effects of Electron Trapping and Protonation on the Efficiency of Water-Splitting Dye-Sensitized Solar Cells. *J. Am. Chem. Soc.* **2014**, *136*, 10974–10982.

(51) McCool, N. S.; Swierk, J. R.; Nemes, C. T.; Saunders, T. P.; Schmuttenmaer, C. A.; Mallouk, T. E. Proton-Induced Trap States, Injection and Recombination Dynamics in Water-Splitting Dye-Sensitized Photoelectrochemical Cells. *ACS Appl. Mater. Interfaces* **2016**, *8*, 16727–16735.

(52) Gallaher, J. K.; Aitken, E. J.; Keyzers, R. A.; Hodgkiss, J. M. Controlled Aggregation of Peptide-Substituted Perylene-Bisimides. *Chem. Commun.* **2012**, *48*, 7961–7963.

(53) Parks, G. A. The Isoelectric Points of Solid Oxides, Solid Hydroxides, and Aqueous Hydroxo Complex Systems. *Chem. Rev.* **1965**, *65*, 177–198.

(54) Kosmulski, M. The pH-Dependent Surface Charging and the Points of Zero Charge. *J. Colloid Interface Sci.* **2002**, *253*, 77–87.

(55) Kosmulski, M. pH-Dependent Surface Charging and Points of Zero Charge II. Update. *J. Colloid Interface Sci.* **2004**, *275*, 214–224.

(56) Tennakone, K.; Kumara, G. R. R. A.; Kottegoda, I. R. M.; Perera, V. P. S. An Efficient Dye-Sensitized Photoelectrochemical Solar Cell Made from Oxides of Tin and Zinc. *Chem. Commun.* **1999**, 15–16.

(57) Kumara, G. R. R. A.; Tennakone, K.; Perera, V. P. S.; Konno, A.; Kaneko, S.; Okuya, M. Suppression of Recombinations in a Dye-Sensitized Photoelectrochemical Cell Made from a Film of Tin IV Oxide Crystallites Coated with a Thin Layer of Aluminium Oxide. *J. Phys. Appl. Phys.* **2001**, *34*, 868.

(58) Fukai, Y.; Kondo, Y.; Mori, S.; Suzuki, E. Highly Efficient Dye-Sensitized SnO_2 Solar Cells Having Sufficient Electron Diffusion Length. *Electrochem. Commun.* **2007**, *9*, 1439–1443.

(59) Mishra, A.; Fischer, M. K. R.; Bäuerle, P. Metal-Free Organic Dyes for Dye-Sensitized Solar Cells: From Structure: Property Relationships to Design Rules. *Angew. Chem. Int. Ed.* **2009**, *48*, 2474–2499.

(60) Kamire, R. J.; Materna, K. L.; Hoffeditz, W. L.; Phelan, B. T.; Thomsen, J. M.; Farha, O. K.; Hupp, J. T.; Brudvig, G. W.; Wasielewski, M. R. Photodriven Oxidation of Surface-Bound Iridium-Based Molecular Water-Oxidation Catalysts on Perylene-3,4-Dicarboximide-Sensitized TiO_2 Electrodes Protected by an Al_2O_3 Layer. *J. Phys. Chem. C* **2017**, *121*, 3752–3764.

(61) Giribabu, L.; Kanaparthi, R. K.; Velkannan, V. Molecular Engineering of Sensitizers for Dye-Sensitized Solar Cell Applications. *Chem. Rec.* **2012**, *12*, 306–328.

(62) Ichinose, I.; Senzu, H.; Kunitake, T. Stepwise Adsorption of Metal Alkoxides on Hydrolyzed Surfaces : A Surface Sol-Gel Process. *Chem. Lett.* **1996**, *25*, 831–832.

(63) Liberatore, M.; Burtone, L.; Brown, T. M.; Reale, A.; Carlo, A. D.; Decker, F.; Caramori, S.; Bignozzi, C. A. On the Effect of Al_2O_3 Blocking Layer on the Performance of Dye Solar Cells with Cobalt Based Electrolytes. *Appl. Phys. Lett.* **2009**, *94*, 173113.

(64) Palomares, E.; Clifford, J. N.; Haque, S. A.; Lutz, T.; Durrant, J. R. Slow Charge Recombination in Dye-Sensitised Solar Cells (DSSC) Using Al_2O_3 Coated Nanoporous TiO_2 Films. *Chem. Commun.* **2002**, 1464–1465.

(65) Guo, J.; She, C.; Lian, T. Effect of Insulating Oxide Overlayers on Electron Injection Dynamics in Dye-Sensitized Nanocrystalline Thin Films. *J. Phys. Chem. C* **2007**, *111*, 8979–8987.

(66) van Delft, J. A.; Garcia-Alonso, D.; Kessels, W. M. M. Atomic Layer Deposition for Photovoltaics: Applications and Prospects for Solar Cell Manufacturing. *Semicond. Sci. Technol.* **2012**, *27*, 074002.

(67) Asbury, J. B.; Hao, E.; Wang, Y.; Lian, T. Bridge Length-Dependent Ultrafast Electron Transfer from Re Polypyridyl Complexes to Nanocrystalline TiO_2 Thin Films Studied by Femtosecond Infrared Spectroscopy. *J. Phys. Chem. B* **2000**, *104*, 11957–11964.

(68) Zhao, Y.; Swierk, J. R.; Megiatto, J. D.; Sherman, B.; Youngblood, W. J.; Qin, D.; Lentz, D. M.; Moore, A. L.; Moore, T. A.; Gust, D.; *et al.* Improving the Efficiency of Water Splitting in Dye-Sensitized Solar Cells by Using a Biomimetic Electron Transfer Mediator. *Proc. Natl. Acad. Sci. U. S. A.* **2012**, *109*, 15612–15616.

(69) Ashford, D. L.; Sherman, B. D.; Binstead, R. A.; Templeton, J. L.; Meyer, T. J. Electro-assembly of a Chromophore–Catalyst Bilayer for Water Oxidation and Photocatalytic Water Splitting. *Angew. Chem.* **2015**, *127*, 4860–4863.

(70) Kent, C. A.; Concepcion, J. J.; Dares, C. J.; Torelli, D. A.; Rieth, A. J.; Miller, A. S.; Hoertz, P. G.; Meyer, T. J. Water Oxidation and Oxygen Monitoring by Cobalt-Modified Fluorine-Doped Tin Oxide Electrodes. *J. Am. Chem. Soc.* **2013**, *135*, 8432–8435.

(71) Chen, Z.; Dinh, H. N.; Miller, E. *Photoelectrochemical Water Splitting: Standards, Experimental Methods, and Protocols*; SpringerBriefs in Energy; Springer New York: New York, NY, 2013.

(72) Mathew, S.; Yella, A.; Gao, P.; Humphry-Baker, R.; Curchod, B. F. E.; Ashari-Astani, N.; Tavernelli, I.; Rothlisberger, U.; Nazeeruddin, M. K.; Grätzel, M. Dye-Sensitized Solar Cells with 13% Efficiency Achieved through the Molecular Engineering of Porphyrin Sensitizers. *Nat. Chem.* **2014**, *6*, 242–247.

APPENDIX III. SUPPORTING INFORMATION FOR CHAPTER V

S5.1 Discussion on Ligand Syntheses

2,2'-Bipyridine-4,4'-bis(N,N-dimethylcarboxamide) (dma-bpy). A Chemical Structure search of dma-bpy on SciFinder.cas.org reveals that the ligand has a CAS registry number (220833-72-7). However, the patent reference on record for its synthesis describes the synthesis of the di*ethyl*amide derivative instead.[1] Therefore, the synthesis of the di*methyl*amide derivative is, to the best of our knowledge, previously unpublished. The synthesis described in the above patent involves reaction of 2,2'-bipyridine-4,4'-dicarboxylic acid with thionyl chloride to form the acid chloride, followed by reaction with diethylamine in toluene.[1] A precise extension of these published conditions to form dma-bpy would require di*methyl*amine as the precursor, but di*methyl*amine is a gas under ambient conditions which would make the synthesis unnecessarily complex. Instead, in the present work, the acid chloride was refluxed in distilled, dried DMF, which is known to decompose to dimethylamine during reflux, and which therefore serves as a precedented precursor to form dimethylamide products.[2]

2,2'-Bipyridine-4,4'-dicarbonitrile (cn-bpy). To the authors' knowledge, there are three published syntheses for the exact 2,2'-bipyridine-4,4'-dicarbonitrile ligand molecule.[3–5] Of these, the oldest procedure reported the highest yield of 88% using a dehydration reaction between 2,2'-bipyridine-4,4'-dicarboxamide starting material and $POCl_3$ as the dehydrating agent.[3] The two published procedures for the synthesis of the 2,2'-bipyridine-4,4'-dicarboxamide starting material both involve the reaction of carboxylic ester precursors with anhydrous ammonia gas.[6,7] In order to avoid this expensive reagent we chose to start with the much more reactive acid chloride, which was then added to a concentrated aqueous ammonia solution (hoping that the reaction would be

much faster with ammonia than water, since ammonia is the stronger nucleophile). Separation of the desired amide product from its carboxylic acid byproducts was foreseen to be a problem, as both compounds are extremely insoluble due to strong π stacking and hydrogen bonding interactions in their corresponding solids. Fortunately, we found that the carboxylic acid could be selectively dissolved in excess ammonia solution by deprotonation, and that the amide preferentially precipitates when the crude solid is dissolved in hot DMF. Using these purification techniques, the desired amide product was typically collected in a 56% yield. Previously unpublished (to our knowledge) IR absorbance frequencies of the purified 2,2'-bipyridine-4,4'-dicarboxamide are reported in the main text.

With the primary amide product in hand, we followed the literature procedure for its dehydration to the dicarbonitrile using $POCl_3$ dehydrating agent.[3] Unfortunately, this published procedure did not contain sufficient details to successfully complete the reaction, as repeated attempts yielded only the amide starting material after workup (hydrolysis of $POCl_3$, neutralization, and extraction with chloroform). Using additional workup details found in a published reaction for a close analogue (specifically, evaporating off excess $POCl_3$ before quenching, quenching with ice instead of water, neutralizing with NH_3 (aq), and extracting with chloroform),[8] an average yield of 71% was attained. The necessity for additional workup details to achieve the final ligand illustrate that the nitrile can be hydrolyzed back to the amide under the high heat and highly acidic conditions present when excess $POCl_3$ reagent is not removed before quenching.

S5.2 UV–Vis Characterization of Cobalt Complexes

UV–visible spectrophotometry was performed using an Agilent 8453 UV–visible spectrophotometer. The instrument was blanked using neat acetonitrile in an appropriate quartz cuvette. Samples were prepared in acetonitrile (EMD, OmniSolv grade) and diluted as necessary to obtain adequate spectra. Spectra are shown in Figure S5.1, and calculated molar extinction coefficients are provided in Table S5.1. The strong absorption bands in the UV region (Figure S5.1a) are consistent with light absorption from the bipyridine ligands (see below). Weaker peaks or shoulders from these bands extended into the visible region (Figure S5.1b), and very weak absorption features were present at higher wavelengths (Figure S5.1c), both of which may originate from Co^{2+} d–d transitions.[9]

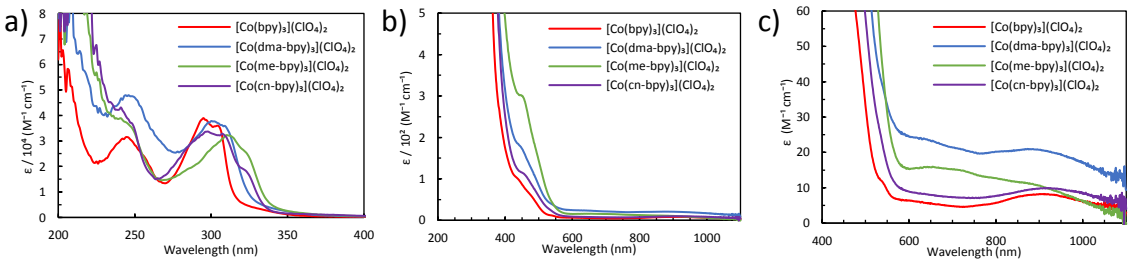

Figure S5.1 UV–vis spectra of the four cobalt complexes studied herein in acetonitrile: (a) 0.1 mM complexes in a 2 mm quartz cuvette, (b) and (c) 5 mM complexes in a 5 mm quartz cuvette.

Table S5.1 UV–Vis Data for Cobalt Complexes Studied Herein in Acetonitrile.

complex	*λ (nm)*	*ε (M^{-1} cm^{-1})*	*λ (nm)*	*ε (M^{-1} cm^{-1})*	*λ (nm)*	*ε (M^{-1} cm^{-1})*	*λ (nm)*	*ε (M^{-1} cm^{-1})*
$[Co(bpy)_3](ClO_4)_2$	245	3.2×10^4	295	3.9×10^4	450	0.90×10^2	910	8
$[Co(dma\text{-}bpy)_3](ClO_4)_2$	245	4.8×10^4	300	3.8×10^4	450	1.8×10^2	885	24
$[Co(me\text{-}bpy)_3](ClO_4)_2$	240	3.9×10^4	310	3.2×10^4	450	3.0×10^2	650	16
$[Co(cn\text{-}bpy)_3](ClO_4)_2$	240	4.2×10^4	297	3.4×10^4	450	1.2×10^2	920	11

One observation from the spectra in Figure S5.1a is that the band centered at 300 nm for the $[Co(cn\text{-}bpy)_3](ClO_4)_2$ complex showed a shoulder at longer wavelengths, which was not present in the spectra of any of the other complexes studied. Because the $[Co(cn\text{-}bpy)_3](ClO_4)_2$ complex is the least stable, we hypothesized that this shoulder may be evidence for dissociated cn-bpy ligand. The control UV–spectrum of free cn-bpy ligand was not consistent with this shoulder (see Figure S5.2a below). It is still possible that the shoulder could originate from a $[Co(cn\text{-}bpy)_2(solv)_2]^{2+}$ species, though this hypothesis was not tested.

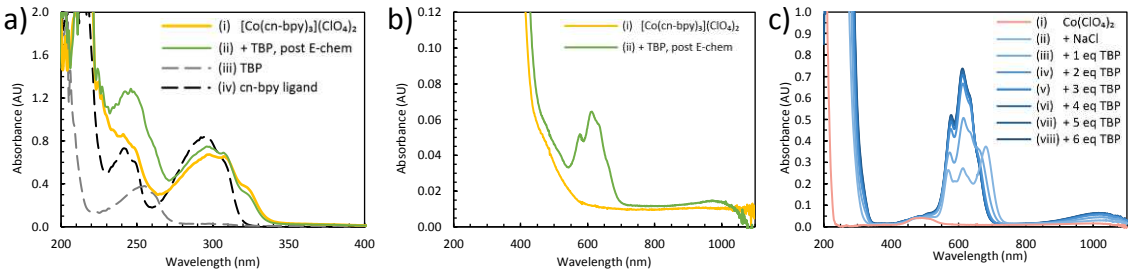

Figure S5.2 UV–vis spectra of $[Co(cn\text{-}bpy)_3](ClO_4)_2$ in acetonitrile, as well as various controls:
(a) UV region in a 2 mm quartz cuvette of (i) 0.1 mM $[Co(cn\text{-}bpy)_3](ClO_4)_2$; (ii) 0.1 mM $[Co(cn\text{-}bpy)_3](ClO_4)_2$, 1.5 mM TBP, 10 mM $LiClO_4$ after performing electrochemistry and aging overnight; (iii) 1 mM TBP control; (iv) 0.3 mM free cn-bpy ligand.
(b) Spectra in a 5 mm quartz cuvette of (i) 1.0 mM $[Co(cn\text{-}bpy)_3](ClO_4)_2$, 100 mM $LiClO_4$ (solution was yellow); (ii) 1.0 mM $[Co(cn\text{-}bpy)_3](ClO_4)_2$, 100 mM $LiClO_4$, 15 mM TBP after performing electrochemistry and aging overnight (solution was green).
(c) Spectra in a 5 mm quartz cuvette of a control solution consisting of (i) 5 mM $Co(ClO_4)_2$, and (ii) the same solution after adding 1.0 mg of NaCl (saturated), and (iii)–(viii) after adding 1–6 molar equiv TBP (vs cobalt).

As discussed in the main text, a solution color change from yellow to green was observed for the $[Co(cn\text{-}bpy)_3]^{2+}$ complex after adding TBP and performing electrochemistry (both in acetonitrile and γ-butyrolactone solutions). To better characterize this change, we recorded the UV–vis spectra for each of the complexes in this study as several changes were made to the solutions. For all complexes, *no* significant change in the absorption spectra shown in Figure S5.1 were observed after (i) adding 100 mM $LiClO_4$ supporting electrolyte, (ii) after performing cyclic

voltammetry (Figure 5.2 of the main text), (iii) after adding one molar equivalent of 4-*tert*-butylpyridine (TBP) (of course, an increased absorbance in the UV region was observed, consistent with the spectrum of TBP in acetonitrile, see Figure S5.2a below), (iv) after repeating cyclic voltammetry in the presence of TBP, or (v) after aging the solutions overnight with the added 1 molar equivalent of TBP.

The solution color change to green was only observed for the $[Co(cn\text{-}bpy)_3]^{2+}$ complex, and only after adding a large molar excess of TBP (one drop) and performing electrochemistry. Figure S5.2 below characterizes the changes in the absorbance spectrum responsible for this color change. In the UV region, the band centered at ~240 nm grows, consistent with absorption from free TBP. The color change appears to originate from the appearance of an absorption feature with peaks at 575 and 610 nm, and shoulders at ~635 and 660 nm (Figure S5.2b). Knowing that this absorption feature only appeared after both adding TBP and performing electrochemistry, we set out to probe its origin. We hypothesized that either water or NaCl may be responsible, leaching into solution from the aqueous saturated sodium calomel reference electrode (SSCE) used during cyclic voltammetry. Indeed, the absorbance feature in Figure S5.2b was very closely reproduced by a control experiment in which NaCl and then TBP were added to a $Co(ClO_4)_2$ solution in acetonitrile at room temperature (Figure S2c) resulting in bright blue solutions. Separate controls involving controlled water additions had no effect.

The ultimate absorbance feature of Figure S5.2c very closely matches a previously published spectrum for tetrahedral $Co(py)_2Cl_2$ in pyridine (py) solution,[10] as well as the absorbance peak values published for the same complex in $CHCl_3$ solution.[11] Therefore, we propose that the color change from yellow to green observed for $[Co(cn\text{-}bpy)_3]^{2+}$solutions after addition of TBP and performing electrochemistry originates from the dissociation of cn-bpy ligand, leading to the

ultimate formation of a small percentage of a brightly blue colored $Co(TBP)_2(Cl)_2$ species. We remind the reader that this exact byproduct would not form in a DSSC mediator solution due to the lack of chloride ions. Furthermore, the only significance we assign to the formation of this byproduct is that it was one of the first indications that our new $[Co(cn\text{-}bpy)_3]^{2+}$ complex is unstable.

S5.3 Determination of CoL_3 Equilibrium Constants by NMR

Benzene was chosen as an internal standard for quantitative NMR because it was readily available in high purity. We note that benzene is not an ideal internal standard because it is volatile and its proton signal can overlap with some of the bipyridine signals. However, the vapor pressures of benzene and acetonitrile are very similar, meaning they should evaporate at similar rates. Therefore, any evaporation during sample preparation should not significantly alter the concentration of the internal standard. We also performed experiments using 1,3,5-trimethoxybenzene as an internal standard, which is nonvolatile and its proton signal is shifted upfield away from bipyridine peaks.[12] However, the quantitative NMR results were no better with regard to the observed error bars.

NMR samples were prepared by weighing out each complex into a 1 dram shell vial. To each vial was added 500.0 μL of a previously prepared stock solution of 5.0 mM benzene in d_3-acetonitrile by glass syringe. Samples were agitated by sonication to dissolve all solid, and the solutions were transferred into NMR tubes (5 mm, thin wall, 7", 500 MHz rating) by glass pipette. ^{1}H NMR spectra were recorded on a Varian Inova 400 MHz NMR. Signals from bpy ligands bound to paramagnetic cobalt(II) were evident between 10 and 95 ppm as shown in Figure S5.3, and have previously been fully assigned.[13] For quantitative NMR, spectra were recorded between −0.5 and 9.5 ppm with 64 to 128 transients, 1 s relaxation delay, 45 degree pulse angle, at 25 °C. After

taking the NMR spectrum for each sample, samples were diluted with additional 5.0 mM benzene in d_3-acetonitrile in 250 μL portions by glass syringe. Samples were inverted several times to mix, allowed to equilibrate for at least 30 min, and the spectrum was collected again.

Quantitative NMR data were processed according to Bharti and Roy[14]:

1) Prior to Fourier Transform, an exponential window function was applied to the FID data with a line broadening value of 1.0 Hz to improve the S/N and resolution of the spectrum.
2) FID data was zero filled to a factor of 2.
3) Fourier Transform.
4) Manual phase correction.
5) Manual baseline correction.
6) Manual peak integration. When integrating, the relative area of the benzene internal standard peak was set at 50. If it was known that other bpy peaks overlapped with benzene, the average area of the other respective peaks (free ligand or Co^{3+} ligands) were obtained and their area added to the 50 value of benzene.
7) Concentrations were calculated using the straightforward formula from Wallace:[15]

$$\frac{Moles\ of\ component}{Moles\ of\ reference} = \frac{Integral\ (component\ signal)}{Integral\ (reference\ signal)} \times \frac{Number\ of\ protons\ per\ mole\ from\ reference\ signal}{Number\ of\ protons\ per\ mole\ from\ component\ signal} \quad \text{(S5.1)}$$

Quantitative NMR spectra are shown in Figures S5.6–S5.9, and data from quantitative NMR is summarized in Table S5.2.

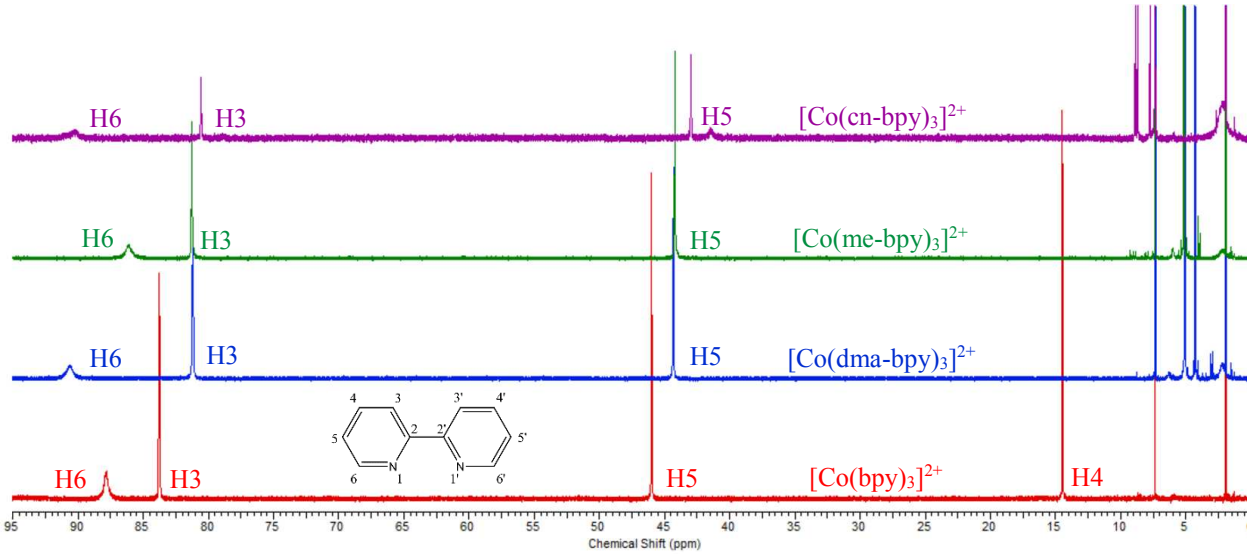

Figure S5.3 ^{1}H NMR spectra of cobalt(II) complexes in d_3-acetonitrile solutions containing benzene as an internal standard ($\delta_{benzene}$ = 7.3 ppm).

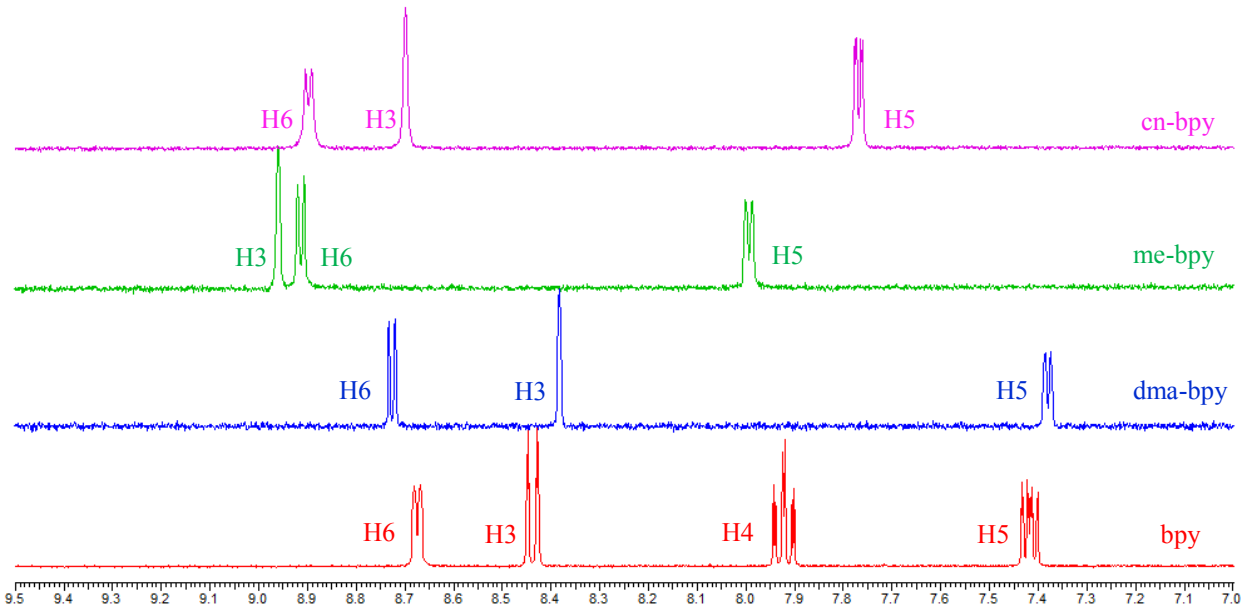

Figure S5.4 ^{1}H NMR spectra of free ligands, for reference, in d_3-acetonitrile.

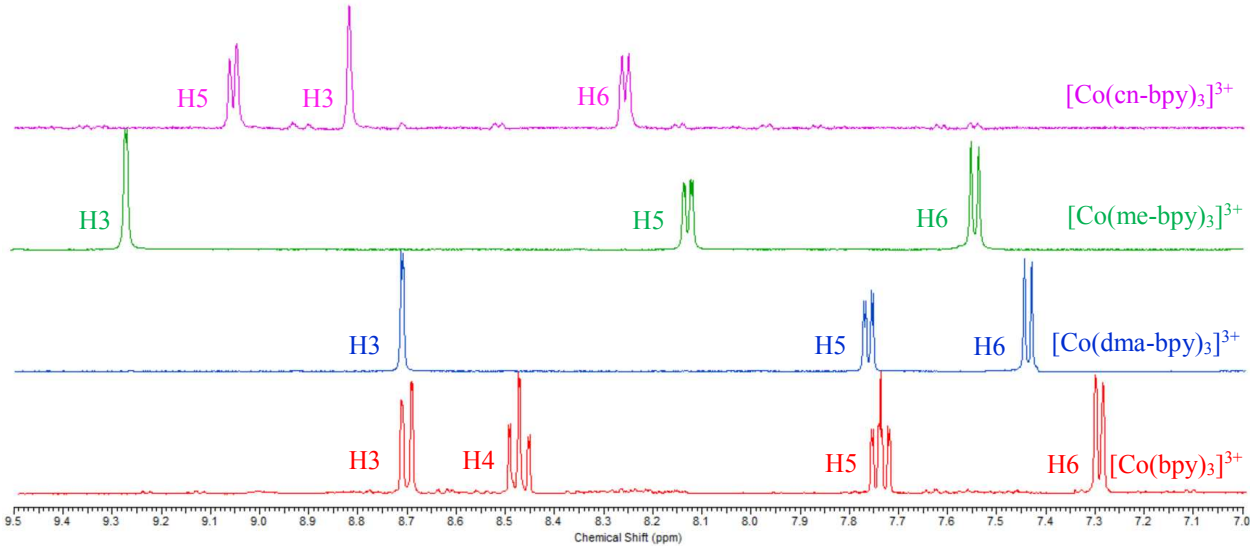

Figure S5.5 ^{1}H NMR spectra of cobalt(III) complexes, for reference, in d_3-acetonitrile. Note, these complexes were oxidized in situ using $NOBF_4$, and contained benzene as an internal reference. The benzene peak ($\delta \approx 7.3$ ppm) was removed from each spectrum for clarity.

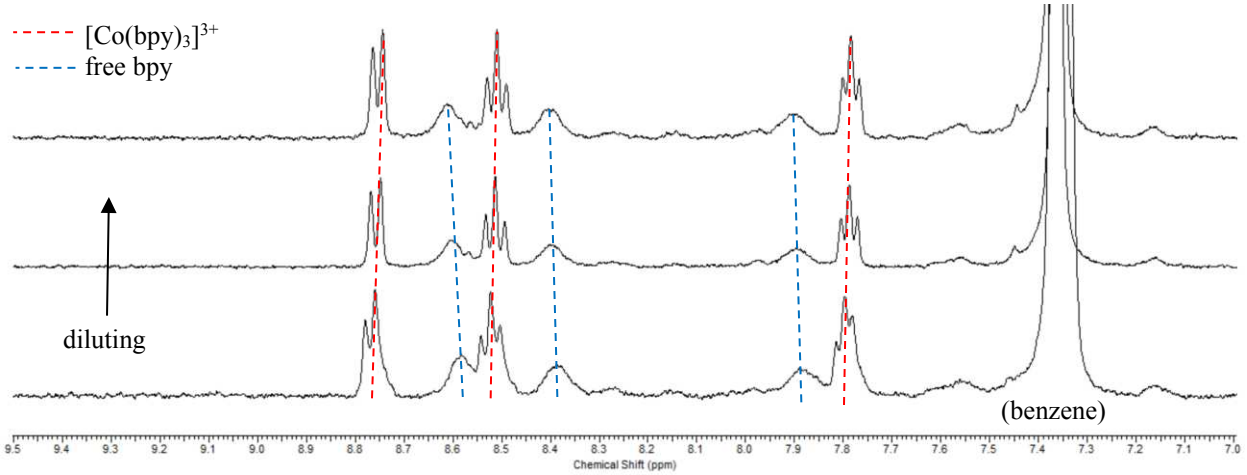

Figure S5.6 Aromatic region of ^{1}H NMR of $[Co(bpy)_3](ClO_4)_2$ in d_3-acedonitrile with benzene internal standard. Note that peaks shift as the sample is diluted because of the changing concentration of paramagnetic cobalt(II), so specific chemical shifts are not as helpful in assigning peaks as are the splitting patterns. The splitting patterns of the peaks marked with red dotted lines match that of a trace $[Co(bpy)_3]^{3+}$ impurity. Peaks marked with blue dotted lines are not resolved enough to see splitting patterns, but their chemical shifts converge toward those shown in Figure S5.2 for free bpy ligand as the sample is diluted.

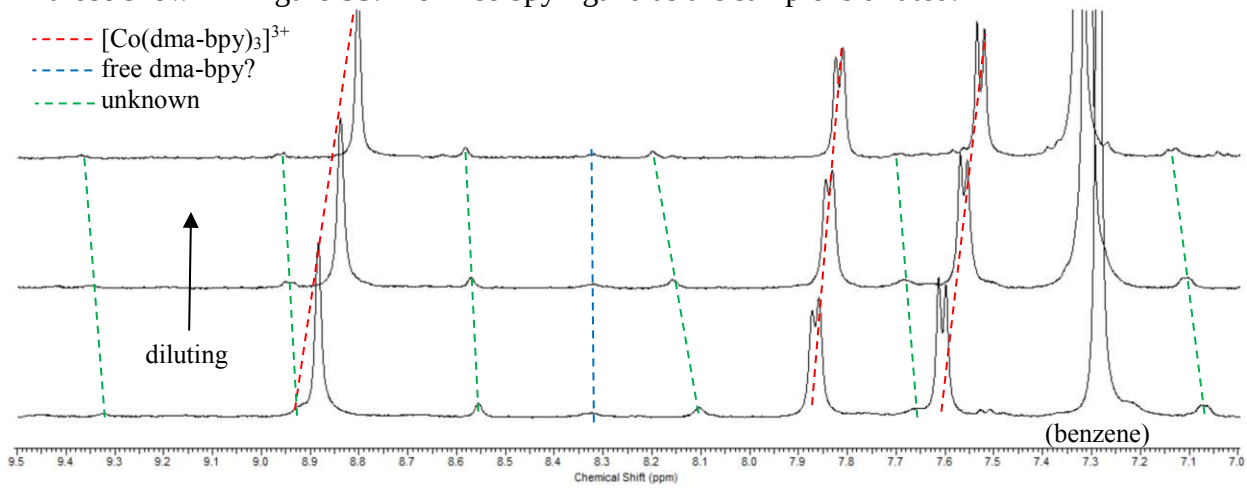

Figure S5.7 Aromatic region of ^{1}H NMR of $[Co(dma\text{-}bpy)_3](ClO_4)_2$ in d_3-acedonitrile with benzene internal standard. Note that peaks shift as the sample is diluted because of the changing concentration of paramagnetic cobalt(II), so specific chemical shifts are not as helpful in assigning peaks as are the splitting patterns. The splitting patterns of the peaks marked with red dotted lines match that of a trace $[Co(dma\text{-}bpy)_3]^{3+}$ impurity. Peaks marked with green dotted lines have not been identified. Note from Figures S5.2 and S5.3 that the signal for H6 of free dma-bpy ligand overlaps with the signal for H3 of $[Co(dma\text{-}bpy)_3]^{3+}$, and the signal for H5 of free dma-bpy ligand overlaps with the benzene internal standard. Not shown, the methyl protons off free dma-bpy and those of $[Co(dma\text{-}bpy)_3]^{3+}$ also overlap. However, spiking experiments with free dma-bpy indicated that a small peak just above $\delta = 8.3$ ppm is consistent with H3 of the free dma-bpy ligand. The fact that only one signal from free dma-bpy was not overlapped by other peaks makes this assignment much less confident than other samples. However, the lack of any larger peak for H3 of free dma-bpy illustrates that this complex is clearly the most stable of those studied.

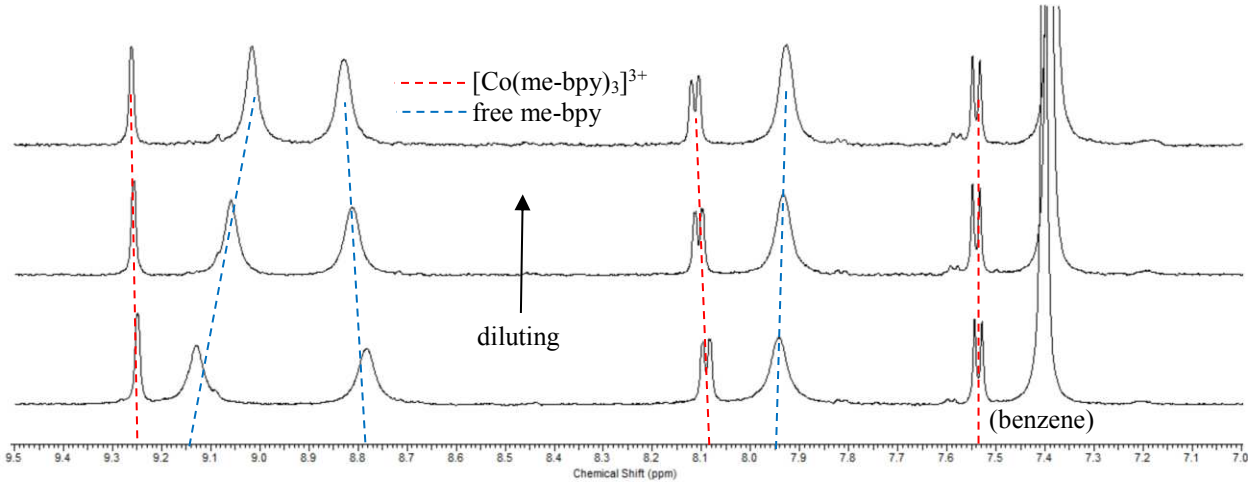

Figure S5.8 Aromatic region of ^{1}H NMR of $[Co(me\text{-}bpy)_3](ClO_4)_2$ in d_3-acedonitrile with benzene internal standard. Note that peaks shift as the sample is diluted because of the changing concentration of paramagnetic cobalt(II), so specific chemical shifts are not as helpful in assigning peaks as are the splitting patterns. The splitting patterns of the peaks marked with red dotted lines match that of a trace $[Co(me\text{-}bpy)_3]^{3+}$ impurity. Peaks marked with blue dotted lines are not resolved enough to see splitting patterns, but their chemical shifts converge towards those shown in Figure S5.2 for free me-bpy ligand as the sample is diluted.

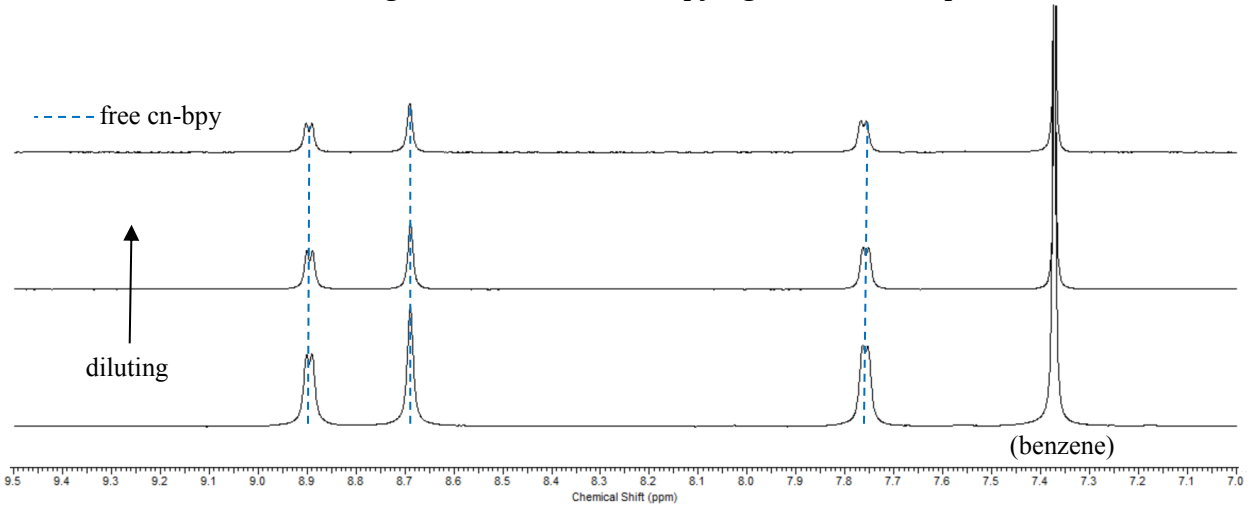

Figure S5.9. Aromatic region of ^{1}H NMR of $[Co(cn\text{-}bpy)_3](ClO_4)_2$ in d_3-acedonitrile with benzene internal standard. Note that peaks do not appear to shift as the sample is diluted, likely because of the low starting concentration of the sample as necessitated by its low solubility in acetonitrile. As a result, the changing concentration of paramagnetic cobalt(II) as the sample is diluted is very small relative to the other samples. The splitting patterns and chemical shifts of the peaks marked with blue dotted lines are consistent with free cn-bpy ligand, as shown in Figure S5.2.

Table S5.2 NMR Data and Calculated K_3 Stability Constants. Subscripts *i* and *e* Indicate Initial and Equilibrium Concentrations, Respectively.

	$[CoL_3]_i$ (M)	Detected $[CoL_3]^{3+}$ (M)	% $[CoL_3]^{3+}$	Detected $[L]_e$ (M)	Calculated $[CoL_3]_e$ (M)	% dissoc. ligand	Calc. K_3 (M^{-1})	Ave K_3 (std dev)
$[Co(bpy)_3]^{2+}$	0.0736	0.00020	0.28	0.00036	0.0733	0.49	5.7×10^5	
	0.0591	0.00019	0.33	0.00037	0.0587	0.63	4.3×10^5	4.6×10^5
	0.0494	0.00019	0.39	0.00035	0.0490	0.71	4.0×10^5	(0.7×10^5)
$[Co(dma\text{-}bpy)_3]^{2+}$	0.0999	0.00096	0.96	0.00013[a]	0.0998	0.13	5.9×10^6	
	0.0716	0.00073	1.0	0.00011[a]	0.0715	0.15	5.9×10^6	8×10^6
	0.0527	0.00056	1.1	0.00007[a]	0.0527	0.13	1.2×10^7	(3×10^6)
$[Co(me\text{-}bpy)_3]^{2+}$	0.0513	0.00041	0.81	0.00235	0.0490	4.6	8.86×10^3	
	0.0344	0.00028	0.81	0.00181	0.0326	5.3	9.94×10^3	9.2×10^3
	0.0256	0.00021	0.83	0.00164	0.0240	6.4	8.91×10^3	(0.5×10^3)
$[Co(cn\text{-}bpy)_3]^{2+}$	0.0052	ND	ND	0.00643	NA	125	NA	
	0.0034	ND	ND	0.00516	NA	152	NA	NA
	0.0025	ND	ND	0.00403	NA	158	NA	

[a] Not definitively known to be free dma-bpy ligand

As discussed in the main text, sequential equilibrium constants of ligand (L) coordinating to a metal cation (M) are defined below.[16]

$$\mathrm{M} + \mathrm{L} \rightleftharpoons \mathrm{ML}, \; K_1 = \frac{[ML]}{[M][L]} \tag{S5.2}$$

$$\mathrm{ML} + \mathrm{L} \rightleftharpoons \mathrm{ML_2}, \; K_2 = \frac{[ML_2]}{[ML][L]} \tag{S5.3}$$

$$\mathrm{ML_2} + \mathrm{L} \rightleftharpoons \mathrm{ML_3}, \; K_3 = \frac{[ML_3]}{[ML_2][L]} \tag{S5.4}$$

It was assumed that, upon dissolution, CoL_3 complexes equilibrate only into species present in eq S5.4. The K_3 stability constants were calculated by eq S5.4 using the detected equilibrium concentration of free ligand, $[L]_e$, and the calculated equilibrium concentration of complex ($[CoL_3]_e = [CoL_3]_i - [L]_e$), and assuming $[ML_2]_e = [L]_e$.

In the case of $[Co(cn\text{-}bpy)_3]^{2+}$ it is clear that the above assumption does not hold, because the amount of detected free cn-bpy ligand was greater than the initial concentration of complex. In this case, a simplification was made by assuming that 100% of the initial $[Co(cn\text{-}bpy)_3]^{2+}$ complex dissociated a ligand to form $[Co(cn\text{-}bpy)_2]^{2+}$. Therefore, any free ligand detected in excess of the

initial concentration of $[Co(cn\text{-}bpy)_3]^{2+}$ was assumed to be present due to a second dissociation event, and the K_2 stability constant was calculated by eq S5.3. These simplified calculations are included in Table S5.3, and an average $\log(K_2)$ value of 3.1 was calculated. It was previously found that for $[Co(bpy)_3]^{2+}$ in aqueous solution, the ratio $\log(K_2/K_3)$ was 0.8.[17] Assuming the same ratio holds for this complex in acetonitrile, then K_3 for $[Co(cn\text{-}bpy)_3]^{2+} \approx 200$. The standard deviation calculated for K_2 was extrapolated for K_3.

Table S5.3 Calculated Values and K_2 and K_3 Stability Constants for $[Co(cn\text{-}bpy)_3]^{2+}$. See Discussion Below.

	$[CoL_2]_i$ (M)	*Detected $[CoL_3]^{3+}$ (M)*	*% $[CoL_3]^{3+}$*	*Detected $[L]_e$ (M)*	*Calculated $[CoL_2]_e$ (M)*	*% dissoc. ligand*	*Calc. K_2 (1/M)*	*Ave K_2 (std dev)*	*Calc K_3[a] (std dev)*
$[Co(cn\text{-}bpy)_2]^{2+}$	0.0052	ND	ND	0.00128	0.0039	24.9	2.36×10^3		
	0.0034	ND	ND	0.00175	0.0017	51.5	5.36×10^2	1.1×10^3	2×10^2
	0.0025	ND	ND	0.00149	0.0011	58.4	4.79×10^2	(0.9×10^3)	(1×10^2)

[a] Ref. 17 found $\log(K_2/K_3) = 0.8$ for $[Co(bpy)_3]^{2+}$, see discussion below

S5.4 Recombination Modeling

The kinetics of heterogeneous electron transfer at semiconductor electrodes is commonly described by a Marcus–Gerischer model.[18] This model assumes isoenergetic electron transfer governed by the Frank–Condon principle, and accounts for overlap between the distributions of electronic states in the electrode and those of the reactants in solution. For a deeper understanding and background on recombination modeling in DSSCs, the reader is directed to several earlier publications.[19–21]

Distributions of Electronic States. We begin by describing different types of electronic states in the TiO_2 nanoparticle film. As with any semiconductor, TiO_2 has a density of states making up the conduction band. However, due to the high surface area of nanocrystalline films, surface states become much more influential, and result in localized trap states within the band

gap of the film.[22] If we assume that the electrons in trap states are in equilibrium with electrons in the conduction band, then the occupancy of trap states at a given energy E can be calculated by the Fermi–Dirac function:

$$f(E - E_{\mathrm{F}}) = \frac{1}{1+\exp[(E-E_{\mathrm{F}})/k_{\mathrm{B}}T]} \tag{S5.5}$$

where E_{F} is the Fermi energy and $k_{\mathrm{B}}T$ is the thermal voltage (about 25 meV at room temp). When $E - E_{\mathrm{F}}$ is much larger than $k_{\mathrm{B}}T$, eq S5.5 can be simplified to the Boltzmann approximation, and the volume concentration of occupied conduction band states is given by:

$$n_{\mathrm{cb}}(E_{\mathrm{F}}) = N_{cb} \exp\left[\frac{E_{\mathrm{cb}}-E_{\mathrm{F}}}{k_{\mathrm{B}}T}\right] \tag{S5.6}$$

where N_{cb} is the effective number density of states of the conduction band and E_{cb} is the energy of the lower edge of the conduction band.

The literature has described an exponential distribution of trap states tailing off below the TiO_2 conduction band edge by:[23]

$$g_{\mathrm{t,exp}}(E) = \frac{N_{\mathrm{t,exp}}}{k_{\mathrm{B}}T_0} \exp\left[\frac{E-E_{\mathrm{cb}}}{k_{\mathrm{B}}T_0}\right] \tag{S5.7}$$

where $N_{\mathrm{t,exp}}$ is the number density of the exponential distribution of trap states, and T_0 is a tailing parameter with temperature units which defines the tail shape of the distribution curve. In addition, there has been evidence of "monoenergetic" surface trap states modeled by a Gaussian function:[21,24,25]

$$g_{\mathrm{st,me}}(E) = \frac{N_{\mathrm{st,me}}}{\sqrt{2\pi\sigma^2}} \exp\left[\frac{-(E-E_{\mathrm{st,me}})^2}{2\sigma^2}\right] \tag{S5.8}$$

where $N_{\mathrm{st,me}}$ is the number density of monoenergetic surface trap states, σ is the standard deviation defining the width of the function, and $E_{\mathrm{st,me}}$ is the mean potential of the states. The total volume concentration of occupied trap states as a function of E_{F} is then:

$$n_t(E_{\mathrm{F}}) = \int_{-\infty}^{E_{\mathrm{cb}}} f(E - E_{\mathrm{F}}) g_{\mathrm{t}}(E)\, dE \tag{S5.9}$$

As stated above, this model assumes that electrons in trap states are in equilibrium with electrons in the conduction band, and therefore their occupancies can be described by Fermi statistics. Bisquert et al. have shown that, in the case of deeper trap states, this assumption will only be valid if the rate of de-trapping to the conduction band is very fast relative to the rate of mediator reduction directly from the trap.[26] We have no evidence to support or refute that this condition is met, but we note that it is made more likely when working with dyed anodes, as the dye sterically blocks the TiO_2 surface and should reduce the rate of trap state recombination relative to de-trapping.

Next we must define the density of unoccupied (acceptor) states for the redox mediator. The concentration density of states function for acceptor electronic states in solution (the oxidized form of the redox mediator) is given by:[18]

$$D_{\mathrm{ox}}(E) = C_{\mathrm{ox}} W_{\mathrm{ox}}(\lambda, E) dE \tag{S5.10}$$

where C_{ox} is the concentration of the oxidized form of the mediator in solution, and W_{ox} is the probability density function which is dependent on both electron energy (E) and the reorganization energy (λ) of the specific redox couple. The energy levels of mediator species in solution are widely distributed due to fluctuations in the solvent shell surrounding each species. W_{ox} can be defined from Marcus theory, and has the form of a normalized Gaussian function as a result of treating solvent shell fluctuations as a harmonic oscillator:[19]

$$W_{\mathrm{ox}}(\lambda, E) = \frac{1}{\sqrt{4\pi\lambda k_{\mathrm{B}} T}} \exp\left[\frac{-\left(E - E^0_{\mathrm{redox}} + \lambda\right)^2}{4\lambda k_{\mathrm{B}} T}\right] \tag{S5.11}$$

where E^0_{redox} is the standard potential of the redox couple.

Recombination Rate. According to Gerischer, the electron transfer event will depend on the level of interaction between the electrode surface and the reactant in solution.[19] If we assume a weak interaction (that is, mediator ligands are strongly bound and prevent significant overlap of

electronic wave functions between the cobalt complex and the TiO_2 surface), the recombination rates, U_i, between various TiO_2 electron states (i = cb; st,exp; st,me) and the oxidized form of the mediator in solution are given by:

$$U_{\mathrm{cb}}(E_{\mathrm{F}}) = k_{\mathrm{et}} V_f n_{\mathrm{cb}}(E_{\mathrm{F}}) D_{\mathrm{ox}}(E_{\mathrm{cb}}) \tag{S5.12}$$

$$U_{\mathrm{st,exp}}(E_{\mathrm{F}}) = k_{\mathrm{et}} C_{\mathrm{ox}} V_f \int_{-\infty}^{E_{\mathrm{cb}}} f(E - E_{\mathrm{F}}) g_{\mathrm{t,exp}}(E) W_{\mathrm{ox}}(E)\, dE \tag{S5.13}$$

$$U_{\mathrm{st,me}}(E_{\mathrm{F}}) = k_{\mathrm{et}} C_{\mathrm{ox}} \int_{-\infty}^{E_{\mathrm{cb}}} f(E - E_{\mathrm{F}}) g_{\mathrm{st,me}}(E) W_{\mathrm{ox}}(E)\, dE \tag{S5.14}$$

$$U_{\mathrm{tot}}(E_{\mathrm{F}}) = U_{\mathrm{cb}}(E_{\mathrm{F}}) + U_{\mathrm{st,exp}}(E_{\mathrm{F}}) + U_{\mathrm{st,me}}(E_{\mathrm{F}}) \tag{S5.15}$$

where k_{et} is the electron transfer rate constant (assumed to be the same for each of the different mediator complexes, and regardless of the type of surface state from which the electron originates), and V_f is the volume fraction of populated TiO_2 states which are close enough to the surface to be captured by mediator states in solution.[21]

As for the specific parameters used for recombination modeling, a previous publication by Ondersma and Hamann compiled most of the required data, either from previous literature or calculated from their own measurements.[21] Because the TiO_2 anodes used in this study were prepared similarly, and because dark current experiments also followed very similar conditions, many of the parameters were adopted from that work. Exceptions include the E^0_{redox} values, which were measured by cyclic voltammetry in this work. All other potential values were adjusted to the SSCE reference used in this study as opposed to a Ag/AgCl reference ($E_{\mathrm{V\ vs\ SSCE}} = E_{\mathrm{V\ vs\ Ag/AgCl}} - 0.045$ V). Ondersma and Hamann also included a volume fraction, V_f, which accounts for the fraction of electrons in TiO_2 which are close enough to the particle surface to participate in electron transfer.[21] The V_f used in our model was adjusted for our larger, 37 nm TiO_2 particles, as opposed to the 20 nm particles used in that study. A list of parameters used are provided in Table S5.4, and

a copy of the Excel spreadsheet used to generate the model data is also provided. Modeling results are provided in Figure 5.6 of the main text.

Table S5.4. Parameters Used for Recombination Modeling.

parameter	value
E^0_{redox}, Co(dma-bpy)$_3$ *(V vs. SSCE)*	0.392
E^0_{redox}, Co(me-bpy)$_3$ *(V vs. SSCE)*	0.503
E^0_{redox}, Co(cn-bpy)$_3$ *(V vs. SSCE)*	0.688
E_{cb} *(V vs. SSCE)*	−0.745
$E_{st,me}$ *(V vs. SSCE)*	−0.205
N_{cb} *(cm^{-3})*	8 x 10^{20}
N_{exp} *(cm^{-3})*	1.73 x 10^{19}
N_{me} *(cm^{-3})*	4.86 x 10^{17}
T (K)	295
T_0 *(K)*	850
k_{et} *(cm^4 s^{-1})*	6 x 10^{-17}
σ (eV)	0.08
λ (eV)	1.41
C_{ox} *(molec cm^{-3})*	1.20 x 10^{19}
V_f	0.15

S5.5 Additional Electrochemical Characterization of Cobalt Complexes

The unusual dark current behavior observed for the [Co(cn-bpy)$_3$](ClO$_4$)$_2$ complex (Figures 5.5 and 5.7 of the main text) caused one of our reviewers to ask if we could perform cyclic voltammetry over a larger potential range than Figure 5.2 of the main text, in order to check for possible redox-active impurities. The full potential range that is likely to affect an operating DSSC is that between the potential of the cathode (pinned at the redox potential of the mediator redox couple)[27] and the potential of the anode (the quasi Fermi energy of electrons in the TiO$_2$), which could feasibly reach as far negative as the conduction band edge of the TiO$_2$. This latter value is generally cited as −0.5 V vs NHE, or −0.74 V vs SSCE, the reference electrode used in this study.

We prepared solutions of each of our cobalt complexes in γ-butyrolactone (gBL) containing 100 mM $LiClO_4$ supporting electrolyte. Voltammetry was run on 1.0 mL of solution in a 1 dram shell vial using a gold working electrode (0.0314 cm^2), SSCE reference, and platinum wire counter electrode. Before testing each solution, the working electrode was polished with a DI water slurry of alumina polishing powder (0.3 μm), rinsed with DI water, cleaned by sonication in ethanol for 30 s, and allowed to air dry. In order to reach sufficiently negative potentials, the solutions were degassed (bubbling argon) for ≥15 min prior to testing. Resulting voltammograms are shown below in Figure S5.10.

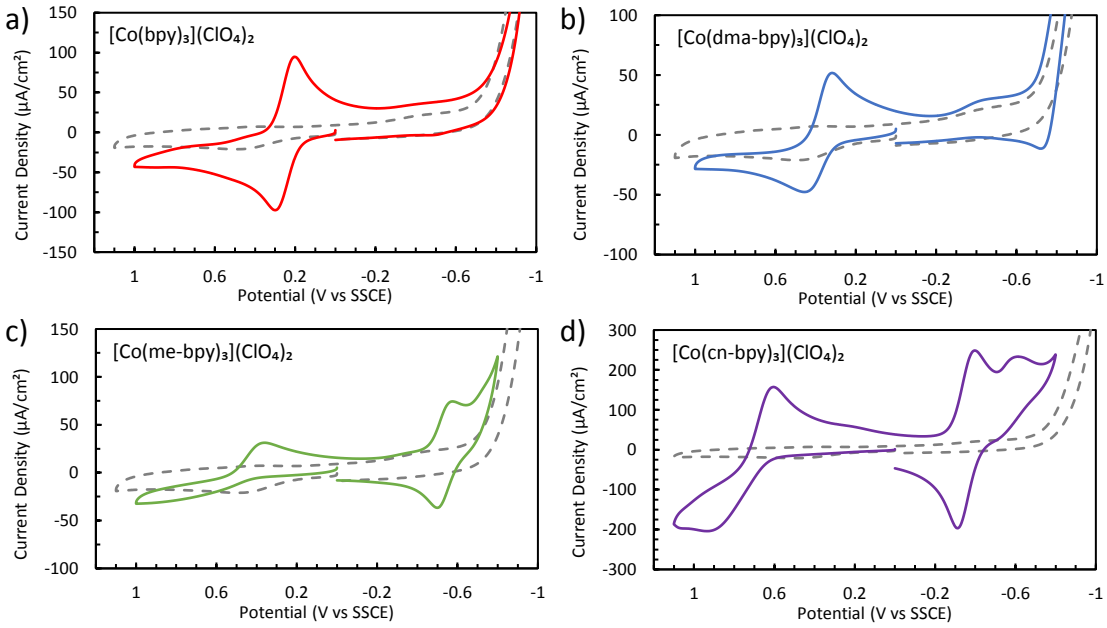

Figure S5.10 Cyclic voltammograms of the four cobalt complexes studied herein in gBL with 100 mM $LiClO_4$: (a) 1 mM $[Co(bpy)_3](ClO_4)_2$, red; (b) 1 mM $[Co(dma\text{-}bpy)_3](ClO_4)_2$, blue; (c) 1 mM $[Co(me\text{-}bpy)_3](ClO_4)_2$, green; (d) 5 mM $[Co(cn\text{-}bpy)_3](ClO_4)_2$, purple. The CV of the blank electrolyte is included in each figure as a grey dashed line.

Each voltammogram in Figure S5.10 shows a redox wave for the $Co^{2+/3+}$ couple at potentials positive of 0 V vs SSCE. As the complexes' redox potentials grow more positive (from Fig. S5.10a to S5.10d), redox waves for the $Co^{1+/2+}$ couple begin to occur within the solvent window. Importantly, for the $[Co(cn\text{-}bpy)_3](ClO_4)_2$ complex, the $Co^{1+/2+}$ couple has an $E_{1/2}$ of

approximately −0.35 V vs SSCE. There is a second, less reversible wave further negative with $E_{1/2}$ approximately −0.58 V vs SSCE. This result is similar to that in Figure 5.2 of the main text. Under those conditions ($[Co(cn\text{-}bpy)_3](ClO_4)_2$ in acetonitrile electrolyte) a second, less reversible wave was observed for the $Co^{2+/3+}$ redox couple instead of the $Co^{1+/2+}$ couple. These results, taken together, are consistent with a slightly higher complex stability for $[Co(cn\text{-}bpy)_3]^{n+}$ in gBL relative to acetonitrile, but which still dissociates a cn-bpy ligand after reduction. Furthermore, this interpretation is consistent with the other main results of this study, that is, direct evidence for ligand dissociation in acetonitrile solution by NMR, as well as indirect evidence by UV–vis for a new complex forming, both in acetonitrile and gBL solutions.

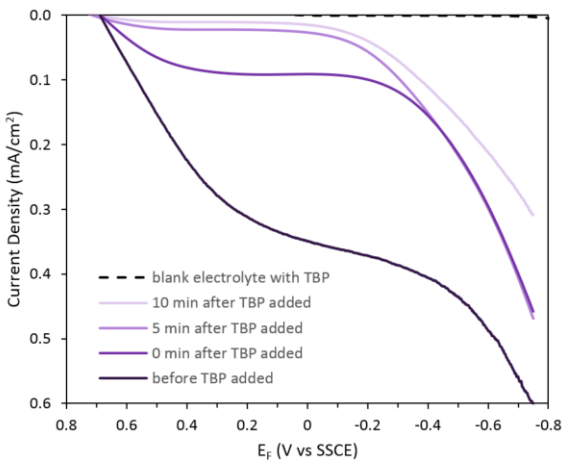

Figure S5.11 Dark currents on a Z907-sensitized photoanode as a function of time after adding 200 mM TBP to the bulk mediator solution containing 40 mM $[Co(cn\text{-}bpy)_3](ClO_4)_2$, half of which was oxidized to Co^{3+} with a stock solution of $NOBF_4$, and 100 mM $LiClO_4$ in gBL solvent. Anode was pretreated in 200 mM TBP, 100 mM $LiClO_4$ gBL solution overnight before testing. Cell was disassembled, rinsed, and blotted dry with a Kimwipe in between each experiment. A precipitate formed in the bulk mediator solution over time, coinciding with the decrease in potential-independent current. The scan rate was 50 mV/s.

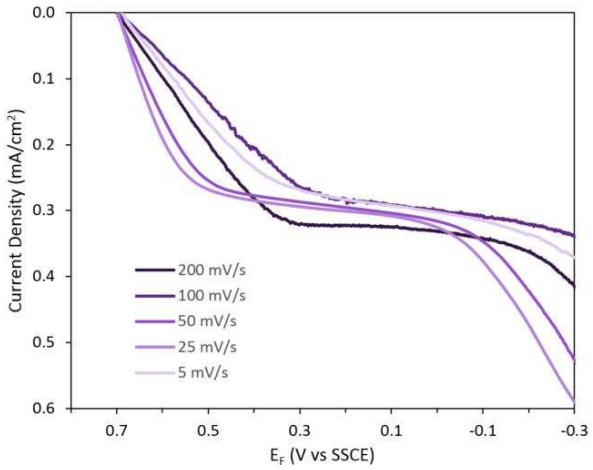

Figure S5.12 Dark currents on a Z907-sensitized photoanode as a function of scan rate. Mediator solution contained 40 mM $[Co(cn\text{-}bpy)_3](ClO_4)_2$, half of which was oxidized to Co^{3+} with a stock solution of $NOBF_4$, and 100 mM $LiClO_4$ in gBL solvent. Experiments were performed consecutively without disassembly of the cell.

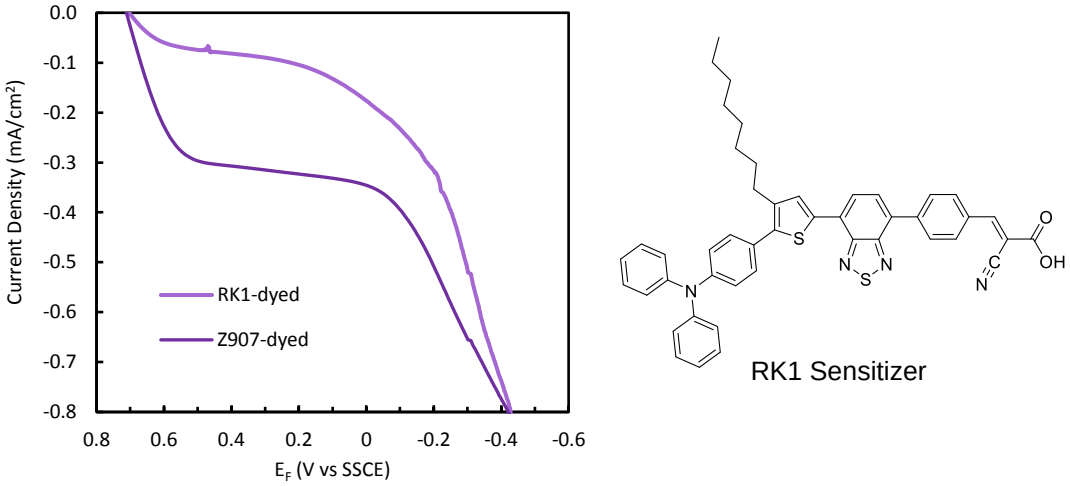

Figure S5.13 Dark currents on Z907 or RK1-sensitized photoanodes (averaged current from two cells each), and the molecular structure of RK1. Mediator solution contained 40 mM $[Co(cn\text{-}bpy)_3](ClO_4)_2$, half of which was oxidized to Co^{3+} with a stock solution of $NOBF_4$, and 100 mM $LiClO_4$ in gBL solvent. Averaged current is shown from two anodes of each dye. Scan rates were 50 mV/s.

S5.6 Preliminary DSSC Testing of New Cobalt Complex Mediators

Cobalt mediator solutions were prepared with 150 mM $[Co(L)_3](ClO_4)_2$, 200 mM lithium trifluoromethanesulfonate (LiTriflate) (Aldrich, 96%, stored in desiccator), and 200 mM TBP in gBL. During preparation, enough of a stock solution of $NOBF_4$ (0.2 M in gBL) was added in order to oxidize 10% (15 mM) of the mediator to Co^{3+}. Z907-dyed anodes and gold cathodes were prepared as described in the Experimental Section of the main text, under the *DSSC Dark Current Testing* subheading. Prior to testing, Z907 anodes were pretreated by soaking for 30 min in a gBL solution of 200 mM LiTriflate and 200 mM TBP.[28] Mediator solutions of $[Co(cn\text{-}bpy)_3](ClO_4)_2$ were not tested in DSSC due to its poor stability as determined in this study. Other factors such as its lower solubility and precipitation upon addition of TBP would have made its DSSC performance incomparable to the other mediators studied herein.

Electrodes were arranged in a sandwich configuration, with the photoanode clamped with the glass side against the 0.385 cm^2 aperture of a custom-built cell holder. The edges of the anode were masked with 25 μm Kapton spacers, against which the cathode was pressed and held with a screw clamp. Mediator solution was drawn into a glass pipette tip, which was placed against the top of the photoanode and drawn into the cell by capillary action. After DSSC tests were completed (see below), the cell was disassembled and each peace rinsed with acetonitrile and dabbed dry with a Kimwipe. The cell was then reassembled, and the next mediator solution was introduced for testing. The photoanode was not removed from the cell holder in between tests, ensuring that the exact same area was tested with each mediator, eliminating fluctuations in DSSC performance that could be caused by lateral variations in TiO_2 thickness or dye loading.

DSSC testing was performed in a two-electrode configuration using a Keithley 2400 SourceMeter controlled by a virtual instrument in Labview 8.2 software. The cell was illuminated

through a 400 nm high-pass cutoff filter, then through the 0.385 cm^2 cell holder aperture by a 100 W Oriel xenon arc lamp (calibrated to closely match the AM1.5 solar irradiance after passing through a Thorlabs KG5 330–665 bandpass filter, in order to compensate for the higher IR irradiance of the lamp when compared to the AM1.5 spectrum). Cells were allowed to equilibrate in the light under open circuit for 20 min prior to performing a battery of tests, performed in the order: *J–V* curve, dark current, open-circuit voltage decay (OCVD), current transient, and IPCE. For *J–V* curves and dark current measurements, potentials were applied from −900 to 100 mV vs the cathode with 50 mV/s scan rate. For OCVD and current transient experiments, a Pentax camera with the back cover removed was utilized as a shutter. For incident photon-to-current efficiency (IPCE) measurements, light was passed through an Oriel 1/8 M Cornerstone monochromator, controlled by the Labview software. The light power through the monochromator was recorded across the range 400–800 nm in 10 nm steps using a silicon standard power sensor (Thorlabs S120B). The subsequent DSSC photocurrent at each respective wavelength was used to calculate IPCE values.

DSSC testing results are shown below in Figure S5.14, and *J–V* results are summarized in Table S5.5. First, we would like to point out that these cells are highly unoptimized, but should serve adequately for general comparisons between mediator complexes. Figure S5.14a shows the *J–V* curves for $[Co(bpy)_3](ClO_4)_2$ mediator as a control, and for our new, high-redox potential complexes $[Co(dma\text{-}bpy)_3](ClO_4)_2$ and $[Co(me\text{-}bpy)_3](ClO_4)_2$. As indicated in Table S5.5, neither of the new complexes reach efficiencies higher than the $[Co(bpy)_3](ClO_4)_2$ control. The performance of both new mediator complexes is significantly limited by a low short-circuit current density (J_{sc}) value. The J_{sc} for $[Co(dma\text{-}bpy)_3](ClO_4)_2$ is more than 2 times lower, and that for $[Co(me\text{-}bpy)_3](ClO_4)_2$ is nearly 10 times lower than for the $[Co(bpy)_3](ClO_4)_2$ control. Importantly,

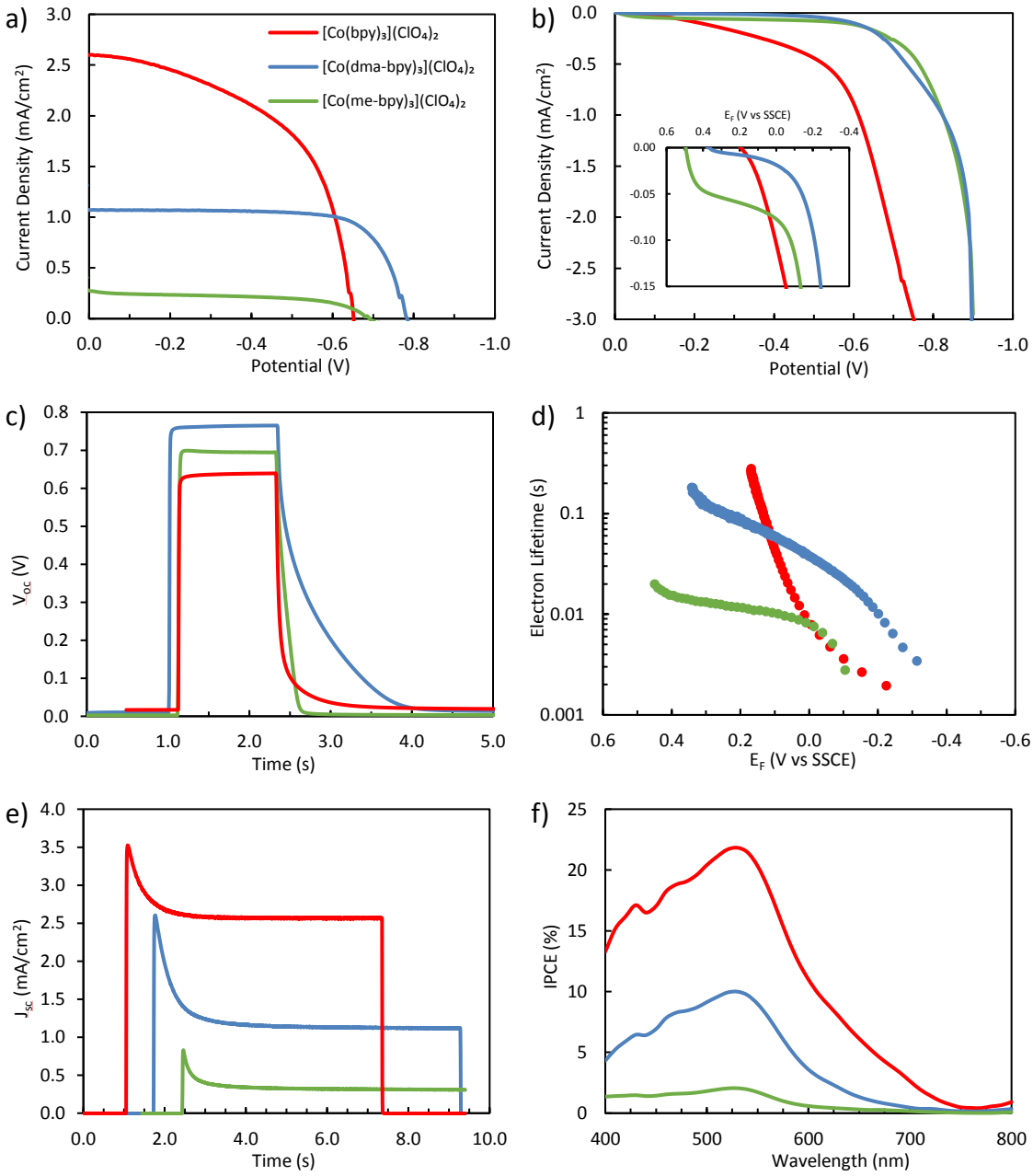

Figure S5.14 DSSC testing results of Z907-sensitized anodes and mediator containing 135 mM $[Co(L)_3]^{2+}$, 15 mM $[Co(L)_3]^{3+}$, 200 mM LiTriflate, and 200 mM TBP in gBL. Red curves indicate $[Co(bpy)_3](ClO_4)_2$ mediator, blue curves indicate $[Co(dma\text{-}bpy)_3](ClO_4)_2$ mediator, and green curves indicate $[Co(me\text{-}bpy)_3](ClO_4)_2$ mediator. (a) *J*–*V* curves; (b) dark current curves (the inset has been expanded to view lower current onsets, and the *x* axis has been converted to TiO_2 quasi-Fermi energy); (c) OCVD curves; (d) TiO_2 electron lifetimes; (e) current transients; (f) IPCE curves.

Table S5.5 Key DSSCs data employing Z907-sensitized anodes and cobalt mediator solutions studied herein.

	$E_{1/2}$ (mV vs SSCE)	V_{oc} (mV)	J_{sc} (mA/cm^2)	FF	Efficiency (%)	$1-(J_{ss}/J_p)^a$
$[Co(bpy)_3](ClO_4)_2$	220	650	2.60	0.538	0.909	0.27
$[Co(dma\text{-}bpy)_3](ClO_4)_2$	392	785	1.07	0.735	0.619	0.57
$[Co(me\text{-}bpy)_3](ClO_4)_2$	503	690	0.277	0.530	0.101	0.63

[a] See discussion below.

cells with both new mediators *did* show an improved open-circuit voltage (V_{oc}) compared to $[Co(bpy)_3](ClO_4)_2$. The $[Co(dma\text{-}bpy)_3](ClO_4)_2$ mediator has an $E_{1/2}$ that is 172 mV more positive than that of $[Co(bpy)_3](ClO_4)_2$, and cells with $[Co(dma\text{-}bpy)_3](ClO_4)_2$ were able to achieve a V_{oc} that was 135 mV higher. On the other hand, the $[Co(me\text{-}bpy)_3](ClO_4)_2$ mediator has an $E_{1/2}$ that is 283 mV more positive than that of $[Co(bpy)_3](ClO_4)_2$, but cells with this mediator were only able to achieve a V_{oc} that was 40 mV higher.

Figure S5.14b shows dark current densities for each mediator solution. As shown by the inset, the $[Co(bpy)_3](ClO_4)_2$ control has a much higher slope for the current onset than our two new complexes. As discussed in the main text, this is likely due to the lack of additional functional groups on the bpy ligands, resulting in stronger electronic overlap between the mediator and the TiO_2 as well as faster mass transport through solution. Interestingly, both new high-redox-potential complexes exhibit initial dark currents that are nearly potential independent (saturation dark current). Notably, the saturation dark current for $[Co(me\text{-}bpy)_3](ClO_4)_2$ has a much larger magnitude under these conditions (135 mM Co^{2+}, 15 mM Co^{3+}) than for the same complex under the conditions of Figure 5.5 in the main text (20 mM Co^{2+}, 20 mM Co^{3+}). This suggests that the saturation dark current is proportional to the initial Co^{2+} concentration, not Co^{3+}. Interestingly, Co^{2+} should be much more labile, but Co^{3+} should be the species responsible for dark recombination current. Perhaps small amounts of the Co^{2+} complex lose a bipyridine ligand, which is replaced with some other ligand species that is then retained upon oxidation to Co^{3+}.

OCVD curves for each mediator complex are shown in Figure S5.14c. Decay in the V_{oc} indicates depopulation of electronic states in TiO_2 through recombination with Co^{3+} complex in solution. Consistent with their initial recombination rates (dark current slopes at onset, Figure S5.14b), voltage decays the fastest with $[Co(bpy)_3](ClO_4)_2$ mediator, followed by $[Co(me\text{-}bpy)_3](ClO_4)_2$, then $[Co(dma\text{-}bpy)_3](ClO_4)_2$. OCVD curves can be converted to TiO_2 electron lifetimes according to Zaban et al.,[29] as shown in Figure S5.14d. The shapes of the lifetime curves may suggest recombination originating primarily from TiO_2 conduction band states for $[Co(bpy)_3](ClO_4)_2$, but more contribution from TiO_2 surface trap states for $[Co(dma\text{-}bpy)_3](ClO_4)_2$ and $[Co(me\text{-}bpy)_3](ClO_4)_2$ mediators.[20]

Current transients for each mediator complex are shown in Figure S5.14e. Upon illumination, cells reach a peak current density (J_p) which should be proportional to the light intensity, but then quickly decay to a steady-state current (J_{ss}) consistent with the J_{sc} from *J*–*V* measurements.[30] Such current decays indicate a mass-transport-limited current, governed by the rate of transport of the oxidized mediator to the cathode.[30] Table S5.5 compares the percentage of current loss due to mass transport ($(1 - (J_{ss}/ J_p))$) between mediator complexes. The $[Co(bpy)_3](ClO_4)_2$ control showed about a 30% current loss due to mass transport, while the $[Co(dma\text{-}bpy)_3](ClO_4)_2$ and $[Co(me\text{-}bpy)_3](ClO_4)_2$ mediators showed double this loss, consistent with their larger size.

IPCE curves for each mediator complex are shown in Figure S5.14f. Generally, IPCE values for $[Co(dma\text{-}bpy)_3](ClO_4)_2$ mediated cells were less than half of those using the $[Co(bpy)_3](ClO_4)_2$ control, and those for $[Co(me\text{-}bpy)_3](ClO_4)_2$ were nearly 10 times lower. Such experiments measure very small photocurrents under monochromatic light illumination, and therefore preclude mass transport limitations. Instead, a cell's IPCE depends on its light harvesting

efficiency, the quantum yield for electron injection from the excited sensitizer into the TiO_2 conduction band, and the electron collection efficiency.[31] The dye's quantum efficiency for electron injection is not expected to vary due to a change in mediator. Therefore, differences in IPCE between these cobalt complexes are likely caused by differences in light harvesting efficiency and electron collection efficiency.

As shown in Figure S5.14d, recombination is slower (electron lifetimes are longer) for $[Co(dma\text{-}bpy)_3](ClO_4)_2$ compared to $[Co(bpy)_3](ClO_4)_2$ at more negative electron potentials, but faster at more positive electron potentials. In the case of $[Co(me\text{-}bpy)_3](ClO_4)_2$, recombination is approximately the same or faster than for $[Co(bpy)_3](ClO_4)_2$ at all positive electron potentials, which likely contributes to its significantly lower IPCE by reducing the electron collection efficiency. Light harvesting efficiency could be reduced either by competing light absorption by the mediator or by poor regeneration efficiency of the oxidized dye by the Co^{2+} mediator. As shown Figure S5.1b, the cobalt complexes do have a visible light absorption shoulder between 400–550 nm (the molar extinction coefficient for this band is largest for the $[Co(me\text{-}bpy)_3](ClO_4)_2$ complex), and so competitive visible light absorption by the mediators may be a factor. Perhaps more importantly, a recent study by Feldt et al. found that a driving force of 400 meV for oxidized dye regeneration by cobalt mediators was required to achieve an efficient dye regeneration quantum yield.[32] With the ground state redox potential for Z907 at 0.76 V vs SSCE,[32] our $[Co(dma\text{-}bpy)_3](ClO_4)_2$ mediator has ~370 mV of driving force, and $[Co(me\text{-}bpy)_3](ClO_4)_2$ only ~260 mV of driving force for dye regeneration. Extrapolating from the results of Feldt et al., we would expect regeneration quantum yields of ~0.88 and 0.78, respectively for our mediator complexes.

REFERENCES

(1) Donovan, R. J.; Morgan, R. J. Imidazolium Cations, Processes for Their Preparation, and Uses Therefor. US5874587 (A), February 23, 1999.

(2) Coppinger, G. M. Preparations of N,N-Dimethylamides. *J. Am. Chem. Soc.* **1954**, *76*, 1372–1373.

(3) Baxter, P. N. W.; Connor, J. A. Bipyridinedicarbonitrile Complexes of Molybdenum and Tungsten. *J. Organomet. Chem.* **1988**, *355*, 193–196.

(4) Stanek, J.; Caravatti, G.; Capraro, H. G.; Furet, P.; Mett, H.; Schneider, P.; Regenass, U. S-Adenosylmethionine Decarboxylase Inhibitors: New Aryl and Heteroaryl Analogs of Methylglyoxal Bis(guanylhydrazone). *J. Med. Chem.* **1993**, *36*, 46–54.

(5) Losse, S.; Görls, H.; Groarke, R.; Vos, J. G.; Rau, S. One-Step Synthesis of 4,4′-Dicyano-2,2′-Bipyridine and Its Bis(4,4′-Di-Tert-Butyl-2,2′-bipyridine)ruthenium(II) Complex. *Eur. J. Inorg. Chem.* **2008**, *2008*, 4448–4452.

(6) Maerker, G.; Case, F. H. The Synthesis of Some 4,4'-Disubstituted 2,2'-Bipyridines. *J. Am. Chem. Soc.* **1958**, *80*, 2745–2748.

(7) Sigal, G.; Tjiong, H.; Dong, L.; Masood, A.; Titmas, R. ECL Labels Having Improved Non-Specific Binding Properties, Methods of Using and Kits Containing the Same. WO03002974 (A2), January 9, 2003.

(8) Kiselev, E.; Agama, K.; Pommier, Y.; Cushman, M. Azaindenoisoquinolines as Topoisomerase I Inhibitors and Potential Anticancer Agents: A Systematic Study of Structure–Activity Relationships. *J. Med. Chem.* **2012**, *55*, 1682–1697.

(9) Meissler, G. L.; Tarr, D. A. Electronic Spectra of Coordination Compounds. In *Inorganic Chemistry*; Pearson Education, Inc.: New Jersey, 2004; pp. 388–408.

(10) Kojima, K.; Saida, M.; Donoue, M.; Matsuda, J. Pressure and Temperature Effects on Octahedral-Tetrahedral Equilibria in Pyridine Solutions of Some Cobalt(II) Halides. *Bull. Chem. Soc. Jpn.* **1983**, *56*, 684–688.

(11) King, H. C. A.; Körös, E.; Nelson, S. M. 1039. The Co-Ordination Number of Transition-Metal Ions. Part I. The Thermodynamics of Some Tetrahedral–Octahedral Configuration Equilibria in Solution: Complexes of Cobalt(II) with Pyridine and 2-Methylpyridine. *J. Chem. Soc. Resumed* **1963**, 5449–5459.

(12) Pauli, G. F.; Gödecke, T.; Jaki, B. U.; Lankin, D. C. Quantitative ^{1}H NMR. Development and Potential of an Analytical Method: An Update. *J. Nat. Prod.* **2012**, *75*, 834–851.

(13) Brisig, B.; Constable, E. C.; Housecroft, C. E. Metal-Directed Assembly of Combinatorial Libraries—Principles and Establishment of Equilibrated Libraries with Oligopyridine Ligands. *New J. Chem.* **2007**, *31*, 1437–1447.

(14) Bharti, S. K.; Roy, R. Quantitative ^{1}H NMR Spectroscopy. *TrAC Trends Anal. Chem.* **2012**, *35*, 5–26.

(15) Wallace, T. Quantitative Analysis of a Mixture by NMR Spectroscopy. *J. Chem. Educ.* **1984**, *61*, 1074.

(16) Beck, M. T.; Nagypál, I. *Chemistry of Complex Equilibria*; Williams, D. R., Ed.; Halsted Press: New York, 1990.

(17) Irving, H.; Mellor, D. H. The Stability of Metal Complexes of 1,10-Phenanthroline and Its Analogues. Part I. 1,10-Phenanthroline and 2,2′-Bipyridyl. *J. Chem. Soc. Resumed* **1962**, 5222–5237.

(18) Bard, A. J.; Faulkner, L. R. A Model Based on Distributions of Energy States. In *Electrochemical Methods: Fundamentals and Applications*; John Wiley & Sons, Inc.: Hoboken, NJ, 2001; pp. 124–130.

(19) Gerischer, H. Charge Transfer Processes at Semiconductor-Electrolyte Interfaces in Connection with Problems of Catalysis. *Surf. Sci.* **1969**, *18*, 97–122.

(20) Bisquert, J.; Zaban, A.; Greenshtein, M.; Mora-Seró, I. Determination of Rate Constants for Charge Transfer and the Distribution of Semiconductor and Electrolyte Electronic Energy Levels in Dye-Sensitized Solar Cells by Open-Circuit Photovoltage Decay Method. *J. Am. Chem. Soc.* **2004**, *126*, 13550–13559.

(21) Ondersma, J. W.; Hamann, T. W. Measurements and Modeling of Recombination from Nanoparticle TiO_2 Electrodes. *J. Am. Chem. Soc.* **2011**, *133*, 8264–8271.

(22) Hagfeldt, A.; Grätzel, M. Light-Induced Redox Reactions in Nanocrystalline Systems. *Chem. Rev.* **1995**, *95*, 49–68.

(23) Fabregat-Santiago, F.; Mora-Seró, I.; Garcia-Belmonte, G.; Bisquert, J. Cyclic Voltammetry Studies of Nanoporous Semiconductors. Capacitive and Reactive Properties of Nanocrystalline TiO_2 Electrodes in Aqueous Electrolyte. *J. Phys. Chem. B* **2003**, *107*, 758–768.

(24) Boschloo, G.; Fitzmaurice, D. Spectroelectrochemical Investigation of Surface States in Nanostructured TiO_2 Electrodes. *J. Phys. Chem. B* **1999**, *103*, 2228–2231.

(25) Bisquert, J.; Fabregat-Santiago, F.; Mora-Seró, I.; Garcia-Belmonte, G.; Barea, E. M.; Palomares, E. A Review of Recent Results on Electrochemical Determination of the Density of Electronic States of Nanostructured Metal-Oxide Semiconductors and Organic Hole Conductors. *Inorganica Chim. Acta* **2008**, *361*, 684–698.

(26) Bisquert, J.; Zaban, A.; Salvador, P. Analysis of the Mechanisms of Electron Recombination in Nanoporous TiO_2 Dye-Sensitized Solar Cells. Nonequilibrium Steady-State Statistics and Interfacial Electron Transfer via Surface States. *J. Phys. Chem. B* **2002**, *106*, 8774–8782.

(27) Scott, M. J.; Nelson, J. J.; Caramori, S.; Bignozzi, C. A.; Elliott, C. M. Cis-Dichloro-bis(4,4‘-Dicarboxy-2,2-bipyridine)osmium(II)-Modified Optically Transparent Electrodes: Application as Cathodes in Stacked Dye-Sensitized Solar Cells. *Inorg. Chem.* **2007**, *46*, 10071–10078.

(28) Ondersma, J. W.; Hamann, T. W. Impedance Investigation of Dye-Sensitized Solar Cells Employing Outer-Sphere Redox Shuttles. *J. Phys. Chem. C* **2010**, *114*, 638–645.

(29) Zaban, A.; Greenshtein, M.; Bisquert, J. Determination of the Electron Lifetime in Nanocrystalline Dye Solar Cells by Open-Circuit Voltage Decay Measurements. *ChemPhysChem* **2003**, *4*, 859–864.

(30) Nelson, J. J.; Amick, T. J.; Elliott, C. M. Mass Transport of Polypyridyl Cobalt Complexes in Dye-Sensitized Solar Cells with Mesoporous TiO_2 Photoanodes. *J. Phys. Chem. C* **2008**, *112*, 18255–18263.

(31) Grätzel, M. Solar Energy Conversion by Dye-Sensitized Photovoltaic Cells. *Inorg. Chem.* **2005**, *44*, 6841–6851.

(32) Feldt, S. M.; Lohse, P. W.; Kessler, F.; Nazeeruddin, M. K.; Grätzel, M.; Boschloo, G.; Hagfeldt, A. Regeneration and Recombination Kinetics in Cobalt Polypyridine Based Dye-Sensitized Solar Cells, Explained Using Marcus Theory. *Phys. Chem. Chem. Phys.* **2013**, *15*, 7087–7097.

LIST OF ABBREVIATIONS

General Abbreviations

ALD	atomic layer deposition
AM1.5G	air mass 1.5 global standardized solar irradiance
APCE	absorbed photon-to-current efficiency
BBL	poly(benzimidazobenzophananthroline)
CNT	carbon nanotube
Cp*Ir	a class of WOCatalysts based on the [Cp*Ir(κ^2-ppy)Cl] structural motif
CV	cyclic voltammetry, cyclic voltammogram
D–A	sensitizer dye composed of electron-donor and acceptor functional groups
D-π-A	sensitizer dye composed of electron-donor and acceptor functional groups separated by a π-conjugated bridge
DS-PEC	dye-sensitized photoelectrolysis cell
DSSC	dye-sensitized solar cell
FTO	fluorine-doped tin oxide coated glass
g-C_3N_4	graphitic carbon nitride (polyheptazine) (see Fig. 2.23)
HER	hydrogen-evolving reaction
HOMO	highest occupied molecular orbital
H_2Q	hydroquinone, 1,4-dihydroxybenzene
IEP	isoelectric point
IPCE	incident photon-to-current efficiency
ITO	indium-tin oxide coated glass
KPi	potassium phosphate buffer (inorganic)
K1-PMPDI	monopotassium salt of PMPDI
K2-PMPDI	dipotassium salt of PMPDI
K4-PMPDI	tetrapotassium salt of PMPDI
LHE	light-harvesting efficiency
LUMO	lowest unoccupied molecular orbital
MO_x	metal oxide
MWCNT	multi-walled carbon nanotube
Nf	Nafion
NHE	normal hydrogen electrode
NP	nanoparticle
n-SC	n-type semiconductor
OCVD	open-circuit (photo)voltage decay
OER	oxygen-evolving reaction
OPV	organic photovoltaic
OSC	organic semiconductor
OTF	organic thin-film
Pc	a phthalocyanine derivative
PDI	a perylene diimide derivative
PEC	photoelectrolysis cell

Pi	inorganic phosphate
PMI	a perylene monoimide derivative
p/n-PEC	tandem photoelectrolysis cell with n-SC photoanode and p-SC photocathode
Por	a porphyrin derivative
PPy	poly(pyrrole)
p-SC	p-type semiconductor
PTTh	poly(terthiophene)
PV	photovoltaic
P3HT	poly(3-hexylthiophene)
RHE	reversible hydrogen electrode
Ru–bda	a class of WOCatalysts based on the [Ru(bda)(pic)$_2$] structural motif
Ru–pdc	a class of WOCatalysts based on the [Ru(pdc)(pic)$_3$] structural motif
SC	semiconductor
SCE	saturated calomel electrode
SSCE	saturated sodium calomel electrode
SCLJ	semiconductor–liquid junction
SubPor	a subporphyrin derivative
WOC	water-oxidation catalysis
WOCatalyst	water-oxidation catalyst
WS-PEC	water-splitting photoelectrolysis cell
XPS	X-ray photoelectron spectroscopy
XRD	X-ray diffraction

Variables

A	electrode area
c	speed of light (m/s)
C^*	bulk concentration of a redox species (M)
e	elementary charge of an electron (C)
E_{appl}	applied potential (V)
E_{CB}	electrochemical potential of a semiconductor conduction band (V)
E_F	Fermi energy (V)
$E_{F,n}$	quasi-Fermi energy of electrons under illumination (V)
$E_{F,p}$	quasi-Fermi energy of holes under illumination (V)
E_g	bandgap energy (V)
E_{rxn}	electromotive force of a cell reaction (V)
E_{VB}	electrochemical potential of a semiconductor valence band (V)
$E_{1/2}$	reversible half-wave potential from cyclic voltammetry (V)
F	Faraday constant (eN_A)
h	Plank constant (eV·s)
i_l	diffusion-limited current, as in cyclic voltammetry (A)
J	current density (μA/cm²)
m	mass transfer coefficient, as in cyclic voltammetry (cm/s)
n	number of electrons transferred in an electrochemical process
V_{oc}	open-circuit photovoltage (V)
ΔE_p	peak separation of a cyclic voltammogram (V)

ΔG	free energy change (kJ/mol)
η_{STH}	solar-to-hydrogen conversion efficiency (%)
λ	photon wavelength (m or nm) or reorganization energy (eV)

Specific Molecules

CoPc	cobalt(II) phthalocyanine (see Fig. 2.7)
Cp*Ir	a Cp*Ir-type catalyst derivatized with a carboxylic acid anchor group (see Fig. 2.13)
Cp*Ir-Sil	a Cp*Ir-type catalyst with phenylene spacer and silatrane anchor group (see Fig. 2.19)
DMF	N,N-dimethylformamide
D–A	an all-organic donor–acceptor sensitizer dye (see Fig. 2.20)
D-π-A	an all-organic donor–π bridge–acceptor sensitizer dye (see Fig. 2.21)
EPPDI	N,N′-bis(1-ethylpropyl)-3,4,9,10-perylenediimide
H_2Pc	phthalocyancine (see Fig. 2.5)
IrIr	a dimeric Ir catalyst (see Fig. 2.19)
MnPor	5,10,15,20-tetra(4-sulfonophenyl)porphyrin (see Fig. 2.8)
PCBM	[6,6]-phenyl-C_{61}-butyric acid methyl ester (see Fig.s 2.9, 2.10)
PMI	a peryelene-3,4-dicarboximide dye derivate (see Fig. 2.19)
PMPDI	N,N'-bis(phosphonomethyl)-3,4,9,10-perylenediimide (see Fig. 2.11)
PTCBI	3,4,9,10-perylene tetracarboxylic bis(benzimidazole) (see Fig.s 2.5, 2.7)
PTCDA	3,4,9,10-perylene tetracarboxylic dianhydride (see Fig. 2.9)
RK1	an all-organic DSSC dye (see Fig. S5.13)
Ru–bda1	the Ru–bda type catalyst portion of a molecular dyad (see Fig. 2.15)
Ru–bda2	a Ru–bda type catalyst with an aliphatic anchor linking group (see Fig. 2.16)
Ru–bda3	a Ru–bda type catalyst with phosphonate anchor group (see Fig. 2.21)
Ru–pdc1	a Ru–pdc type catalyst with a pdc anchor group (see Fig. 2.20)
Ru-ZnP	covalent molecular dyad with a Zn-Por dye and Ru–bda type catalyst (see Fig. 2.15)
SubPor	a subporphyrin dye derivative with push–pull molecular engineering (see Fig. 2.16)
TBP	4-*tert*-butylpyridine
TEPDI	(N,N'-bis(2-(trimethylammonium)-ethylene)-3,4,9,10-perylenediimide (see Fig. 2.18)
ZnPc	Zinc(II) phthalocyanine (see Fig. 2.17)
ZnPor1	a Zn-porphyrin sensitizer dye (see Fig. 2.13)
ZnPor2	the Zn-porphyrin dye portion of a molecular dyad (see Fig. 2.15)
Z907	a Ru-based DSSC dye (see Fig. 5.4)
gBL	γ-butyrolactone
***t*-BuOH**	*tert*-butanol

Organometallic Ligands

bda	2,2'-bipyridine-6,6'-dicarboxylate
bpy	2,2'-bipyridine

cn-bpy	2,2’-bipyridine-4,4’-dicarbonitrile (see Fig. 5.1)
dma-bpy	2,2’-bipyridine-4,4’- bis(N,N-dimethylcarboxamide) (see Fig. 5.1)
me-bpy	2,2’-bipyridine-4,4’-bis(methylester) (see Fig. 5.1)
pdc	2,6-pyridinedicarboxylate
pic	4-picoline
ppy	2-phenylpyridine